

University of Windsor

Scholarship at UWindor

Electronic Theses and Dissertations

Theses, Dissertations, and Major Papers

2004

Investigation of wear and scuffing behaviour of ferrous thermal spray coatings for aluminum engines.

Afsaneh Edrisy
University of Windsor

Follow this and additional works at: <https://scholar.uwindsor.ca/etd>

Recommended Citation

Edrisy, Afsaneh, "Investigation of wear and scuffing behaviour of ferrous thermal spray coatings for aluminum engines." (2004). *Electronic Theses and Dissertations*. 2513.
<https://scholar.uwindsor.ca/etd/2513>

This online database contains the full-text of PhD dissertations and Masters' theses of University of Windsor students from 1954 forward. These documents are made available for personal study and research purposes only, in accordance with the Canadian Copyright Act and the Creative Commons license—CC BY-NC-ND (Attribution, Non-Commercial, No Derivative Works). Under this license, works must always be attributed to the copyright holder (original author), cannot be used for any commercial purposes, and may not be altered. Any other use would require the permission of the copyright holder. Students may inquire about withdrawing their dissertation and/or thesis from this database. For additional inquiries, please contact the repository administrator via email (scholarship@uwindsor.ca) or by telephone at 519-253-3000ext. 3208.

NOTE TO USERS

Page(s) not included in the original manuscript and are unavailable from the author or university. The manuscript was scanned as received.

xiii-xvi

This reproduction is the best copy available.

UMI[®]

**INVESTIGATION OF WEAR AND SCUFFING BEHAVIOUR OF
FERROUS THERMAL SPRAY COATINGS
FOR ALUMINUM ENGINES**

by

AFSANEH EDRISY

**A Dissertation
Submitted to the Faculty of Graduate Studies and Research
through Engineering Materials in Partial Fulfillment of the Requirements
for the Degree of Doctor of Philosophy at the
University of Windsor**

**Windsor, Ontario, Canada
©Afsaneh Edrisy 2004**



Library and
Archives Canada

Bibliothèque et
Archives Canada

Published Heritage
Branch

Direction du
Patrimoine de l'édition

395 Wellington Street
Ottawa ON K1A 0N4
Canada

395, rue Wellington
Ottawa ON K1A 0N4
Canada

Your file Votre référence

ISBN: 0-612-96370-5

Our file Notre référence

ISBN: 0-612-96370-5

NOTICE:

The author has granted a non-exclusive license allowing Library and Archives Canada to reproduce, publish, archive, preserve, conserve, communicate to the public by telecommunication or on the Internet, loan, distribute and sell theses worldwide, for commercial or non-commercial purposes, in microform, paper, electronic and/or any other formats.

The author retains copyright ownership and moral rights in this thesis. Neither the thesis nor substantial extracts from it may be printed or otherwise reproduced without the author's permission.

AVIS:

L'auteur a accordé une licence non exclusive permettant à la Bibliothèque et Archives Canada de reproduire, publier, archiver, sauvegarder, conserver, transmettre au public par télécommunication ou par l'Internet, prêter, distribuer et vendre des thèses partout dans le monde, à des fins commerciales ou autres, sur support microforme, papier, électronique et/ou autres formats.

L'auteur conserve la propriété du droit d'auteur et des droits moraux qui protègent cette thèse. Ni la thèse ni des extraits substantiels de celle-ci ne doivent être imprimés ou autrement reproduits sans son autorisation.

In compliance with the Canadian Privacy Act some supporting forms may have been removed from this thesis.

Conformément à la loi canadienne sur la protection de la vie privée, quelques formulaires secondaires ont été enlevés de cette thèse.

While these forms may be included in the document page count, their removal does not represent any loss of content from the thesis.

Bien que ces formulaires aient inclus dans la pagination, il n'y aura aucun contenu manquant.


Canada

LIST OF SYMBOLS

A_n	Nominal contact area
A_r	Real contact area
C	Pre-exponential constant
d_{75}	Grain size in the coating tested at 75 N
d_i	Grain size in the undeformed coating
F	Normal load
F_{tr}	Transition load
H	Hardness
H_0	Hardness of the coating without contributions from grain boundaries
H_{75}	Hardness of the coating tested at 75 N
H_i	Initial hardness
k	Thermal conductivity
K	Wear coefficient
k_d	Thermal conductivity of the disk
k_p	Thermal conductivity of the pin
l	Equivalent diffusional length
m	Hall-Petch coefficient
Q	Activation energy for diffusion leading to oxide growth
q	Heat
R	Gas constant
R_c	Thermal resistance of the coating
R_d	Thermal resistance of the disk
R_s	Thermal resistance of the substrate
S	Sliding distance
T	Temperature
T_0	Reference temperature
T_b	Average surface temperature
v	Sliding speed
V_{Fe}	Volume fraction of Fe
V_{FeO}	Volume fraction of FeO
W	Wear rate
Z	Depth below the contact surface
μ	Coefficient of friction
ε	Magnitude of accumulate strain

"The virtue of the candle lies not in the wax that leaves its trace, but in its light."
ANTOINE DE SAINT-EXUPERY

ABSTRACT

The development of lightweight internal combustion engines using materials such as cast aluminum alloys represents one of the most significant technological developments in the automotive industry. These engines reduce weight, which in turn reduce fuel consumption and emission. However, poor wear resistance and low seizure load of unprotected Al-Si alloys are a major drawback for applications involving sliding contact in automotive engine blocks. The wear resistance of cast aluminum parts can be improved by depositing coatings on the sliding surfaces. In this respect, iron based coatings deposited through a thermal spray process may play an important role in improving wear resistances of aluminium parts used in the automotive industry. These coatings can be produced economically and be easily deposited on the curved surfaces in ambient air atmosphere. In this research, two promising thermal spray deposition processes were considered: These were i) plasma transfer wire arc thermal spraying (PTWA) process, and ii) high velocity oxy-fuel (HVOF) process. The research work presented in this dissertation primarily focussed on the wear behaviour of low carbon steel thermal spray coatings which were applied using PTWA and HVOF processes deposited on engine grade cast aluminum alloy substrates. The main objective of the work was to characterize the micromechanisms of wear that control the wear rates of the coatings. Several new wear mechanisms that were previously unknown in thermal spray coatings were identified. In addition, the effect of the environment on the wear performance of coatings was investigated. The importance of controlling the atmospheric conditions during the sliding contact of coated aluminum components was established.

Detailed analyses of compositions and microstructures of iron based coatings that were produced using PTWA and HVOF thermal deposition processes showed that the wear resistances of the coatings were sensitive to the production method. A model to calculate the friction induced contact temperature increase was developed and used to explain the differences in the wear rates of the coatings.

Wear maps for thermal sprayed coatings have been constructed for the first time. The wear maps constructed showed the wear rates as a function of the loading conditions (load and velocity). The potential industrial application of wear maps includes prediction of scuffing behaviour of lightweight engines coated by thermal spray coatings. A laboratory experimental method has been developed based on information provided on the wear maps to simulate the wear mechanisms seen in the scuffed engines.

*To
my dear parents, Akram and Iraj
for their endless encouragement and support.
and
my dear husband Reza
for his incomparable devotion and patience*

ACKNOWLEDGMENTS

I want to express my sincere thanks to Dr. A. T. Alpas for his encouragement, support and supervision. It was a great pleasure for me to conduct this dissertation under his supervision. I am also extremely grateful to Dr. T. Perry for his guidance and supervision.

I would like to extend my sincerest gratitude to my committee members for their useful comments that helped to improve the final copy of the dissertation. I would like to acknowledge Dr. R. Gaspar for his support and valuable advice throughout my graduate work.

My sincere thanks to Dr. Y T Cheng, of General Motors, for his valuable discussions and suggestions; Mr. J. Robinson for his technical assistance and Ms. B. Denomey for her most valuable administrative assistance. Special thanks are extended to Dr. A. R. Riahi for his helpful discussions and comments.

The financial support provided by NSERC (Natural Sciences and Engineering Research Council of Canada), General Motors of Canada Limited is greatly appreciated. In particular, I am very grateful for the NSERC Industrial Postgraduate Scholarship with General Motors (2001-2003).

I am extremely thankful to my parents and my sister "Elahe" for their love and encouragement; and my good friends Ali, Mitra, and Niloofar for their constant help and support.

TABLE OF CONTENTS

LIST OF SYMBOLS	(iii)
ABSTRACT	(iv)
DEDICATION	(vi)
ACKNOWLEDGEMENTS	(vii)
LIST OF FIGURES	(xii)
LIST OF TABLES	(xxvii)
 Chapter 1	
Introduction	1
 Chapter 2	
Literature Survey	6
2.1 General Introduction	6
2.2 Modes of Wear	8
2.2.1 Abrasive Wear	9
2.2.2 Rolling Contact Wear	9
2.2.3 Fretting Wear	10
2.2.4 Erosive Wear	10
2.2.5 Sliding Wear	10
2.3 Subsurface Zones Sliding Wear	12
2.4 Transfer and Mechanical Mixing	15
2.5 Archard Equation	15
2.6 Wear Maps and Their Applications	18
2.7 Surface Temperature in Dry Sliding Contact	21
2.8 Oxidation During Sliding Contact	24
2.9 Effect of Environmental Humidity	27
2.10 Tribological Aspects of Internal Combination Engines	28
2.11 Wear Resistant Materials for Internal Combustion Engines	28
2.11.1 Aluminum Alloys for Internal Combustion Engines	28
2.11.2 Material Matrix Composites	31
2.11.2.1 Mild and Ultra-mild Wear	32
2.11.2.2 Transition to Severe Wear	33
2.11.3 Thermal Spray Coatings	34
2.11.3.1 Wear Behaviour of Ferrous Thermal Spray Coatings	38
2.12 Friction and Wear of Internal Combustion Parts	39
2.12.1 Principles of Operations	39
2.12.2 Engine Types and Design Considerations	40
2.12.3 Pistons and Piston Ring Assembly	42
2.12.4 Engine Wear	43
 Chapter 3	
Materials and Experimental Methods	48
3.1 Coating Deposition Process	48
3.1.1 Fabrication of Plasma Transfer Wire Arc Low Carbon Steel Coatings (PTWA 1020 Coatings)	48
3.1.2 Fabrication of High Velocity Oxygen Fuel (HVOF) Low Carbon Steel Coatings	50

3.1.2.1	HVOF 1020 Coatings	50
3.1.2.2	HVOF 1020-2.5% Al Coatings	52
3.2	Laboratory Wear Testing Procedures	52
3.2.1	Description of the Pin-on-Disc Tribometer	52
3.2.2	Sample Preparation for Pin-on-Disc Tests and Measurements of Wear Rates	53
3.2.3	Description of Counterface Material	54
3.2.4	Sliding Contact Temperature Measurement	54
3.2.5	Measurements of Coefficient of Friction	55
3.2.6	Environmentally Controlled Wear Tests	55
3.2.6.1	Wear Test Under Controlled Humidity	55
3.2.6.2	Wear Tests Under Argon Atmosphere	55
3.2.7	Microhardness Measurements	56
3.3	Examination of Samples Worn Under the Laboratory Conditions	56
3.3.1	Scanning Electron Microscopy	56
3.3.1.1	Cross-Sectional SEM Metallography	57
3.3.1.2	Examination of Loose Debris Particles	57
3.3.2	Compositional Analysis by X-Ray diffraction Method	57
3.3.3	WYKO Automated Interferometer	58
Chapter 4	Results: Coating Microstructures, Pin-on-Disc Wear Tests, and Characterization of Worn Surfaces	64
4.1	Plasma Transferred Wire Arc Coating (PTWA 1020)	65
4.1.1	Microstructure, Composition and Properties	65
4.1.2	Pin-On-Disc Wear Test Results: Wear Rates Under Dry Atmosphere	67
4.1.3	SEM observations of Worn Surfaces	69
4.1.3.1	SEM Observations of the Samples Tested at Low Speeds	69
4.1.3.2	SEM Observations of the Samples Tested at High Speeds	71
4.1.4	X-ray Diffraction of Loose Debris Particles	73
4.1.5	SEM Observations of the Cross-Section Under the Worn Surface	75
4.1.6	Measurements of Temperature and Coefficients of Friction	75
4.1.7	Hardness of Worn Surfaces	76
4.1.8	Wear Rates Under Controlled Humidity Atmosphere	77
4.1.9	SEM Observations of Worn Surfaces Under Controlled Humidity	79
4.1.10	The effect of humidity on the Coefficient of Friction	80
4.1.11	Results of XRD Analysis	81
4.2	High Velocity Oxy-Fuel HVOF 1020 Coatings	82
4.2.1	Microstructure Composition and Properties	82

4.2.2	Pin-On-Disc Wear Test Results under Dry Atmosphere	82
4.2.3	SEM Observation of Worn Surfaces	84
4.2.4	X-Ray Diffraction of Loose Debris Particles	87
4.3	High Velocity Oxygen Fuel HVOF 1020-2.5% Al Coatings	88
4.3.1	Microstructure, Composition and properties	88
4.3.2	Pin-on-Disc Wear Test Results: Wear Rates Under Dry Atmosphere	88
4.3.3	SEM Observation of Worn Surfaces	90
Chapter 5	Discussion of the Results: Wear Mechanisms and Wear Maps	136
5.1	Mechanical Wear	140
5.1.1	Severe Plastic Deformation and Splat Tip Fracture	140
5.1.2	Splat Delamination through the Oxide Veins	141
5.2	Oxidational Wear	142
5.2.1	Comparison of Wear Rates Due to Oxidational Wear in PTWA 1020 and HVOF 1020 Coatings	144
5.2.2	The role of Surface temperature on Oxidational Wear	145
5.3	Surface Hardening during Wear	150
5.4	Polishing Wear	152
5.5	Wear Mechanism Maps for the Thermal Spray Coatings	153
5.5.1	Wear Map for PTWA 1020	154
5.5.2	Wear Map for HVOF 1020	156
5.5.3	Wear Map for HVOF 1020-2.5% Al	158
5.6	Temperature Maps for the Thermal Spray Coatings	161
5.7	Comparison of the Wear Map of Aluminum 356 with PTWA 1020 Coatings	162
Chapter 6	Engineering Applications:	
	Investigation of Scuffed Engines with Thermal Spray Coatings	177
6.1	Materials and Testing Methods	177
6.1.1	Scuffed Thermal Spray Coated Aluminum Engine	177
6.1.2	Race Track Procedures on the Corvette Engine	180
6.1.3	Cold Scuffed Engine testing procedures on the Saturn Engine	180
6.1.4	Metallographic Samples Preparation From the Scuffed Engines	181
6.1.5	Pin-On-Disc Wear Test Argon Atmosphere	183
6.2	Results	186
6.2.1	Scuffed Corvette Engines Bores	186
6.2.1.1	Optical Surface Profilometer Morphology	186
6.2.1.2	SEM Observations of The Face of Scuffed Corvette Engine Bores	187
6.2.1.3	SEM Observations of the Minor Face of the Scuffed Corvette Engine Bores	190
6.2.1.4	SEM Observations of the Piston Skirt	192
6.2.1.5	SEM Observations of the Top Piston Ring	193

6.2.2	SEM Observations of the Scuffed Engine Block	194
6.2.3	SEM Observations of the HVOF 1020-2.5% Al Coatings after Pin-On-Disc Wear Tests	195
6.2.4	SEM Observations of Cast Iron after Pin-On-Disc Wear Test	197
6.3	Analysis of Engine Scuffing Mechanisms	198
6.3.1	Consideration of Forces during the Engine Cycles	199
6.3.2	Transmission Electron Microscopy (TEM) From the Major Face of the Corvette Engine Bores	201
6.3.3	Correspondence Between the Mechanism in the Scuffed Engine And the Wear Map for HVOF 1020-2.5% A	203
 Chapter 7 Summary and Conclusions		232
 List of References		237
 List of Publications Resulting from this Work		250
 List of Conference Presentations Resulting from this Work		251
 VITA AUCTORIS		252

LIST OF FIGURES

CHAPTER II

Fig. 2.1	46
----------------	----

Three groups of the lightweight materials , which are being developed as alternatives to the cast iron liners in cast aluminum engines.

Fig. 2.2	47
----------------	----

Illustrates four strokes of internal combustion engines schematically: (1) the compression of air, (2) the raising of air temperature by the combustion of fuel, (3) the generation of energy from the heated air and the resultant expansion of pressure, and (4) exhaust of the gases.

CHAPTER III

Fig. 3.1	60
----------------	----

The PTWA set up used to coat inner surfaces of the cylinder bores. This set up is located at the General Motors Research and Development Centre, Warren, MI.

Fig. 3.2	61
----------------	----

Photograph showing a) The general view of the pin on disc tribometer. b) The sample holder and the pin.

Fig. 3.3	62
----------------	----

Schematic drawing showing the main components of the pin-on disc machine.

Fig. 3.4	63
----------------	----

This figure schematically shows the way that the worn sample was sectioned (AA'). This method provided a good way for the examination of the subsurface damage parallel to the sliding direction.

CHAPTER IV

Fig. 4.1	92
----------------	----

A typical secondary electron SEM image of the surface of the PTWA 1020 in the as deposited condition shows that the surface is very rough after the thermal deposition process.

Fig. 4.30	116
A back-scattered SEM micrograph of a PTWA 1020 sample worn at 50 N load and 0.5 m/s and 90% relative humidity. The polishing wear mechanism is active at this relative humidity level, but there is still evidence of fracture.	
Fig. 4.31.a	117
A variation of the coefficient of friction with the sliding distance at different humidity levels for the PTWA 1020 coatings tested at 5 N - 0.1m/s.	
Fig. 4.31.b	118
Variation of the coefficient of friction with the sliding distance at different humidity levels for the PTWA 1020 coatings tested at 50 N - 0.5m/s.	
Fig. 4.32	119
The average coefficient of friction of PTWA 1020 coatings for the wear tests performed under 50 N, 0.5 m/s loading condition as a function of humidity.	
Fig. 4.33	120
The XRD spectra of the PTWA 1020 wear debris collected from a constant load and a sliding speed of 50 N and 0.5 m/s, and different humidity of 50% with high wear rate, and 90% with low wear rate.	
Fig. 4.34	121
The fraction of the elemental iron content of debris of PTWA 1020 obtained from wear tests performed at 50 N and 0.5 m/s as a function of the relative humidity of the wear environment. The quantitative phase analysis was obtained from the Rietveld analyses with an accuracy of $\pm 0.5\%$. The iron content follows a similar trend as the wear rate.	
Fig. 4.35	122
Microstructure and composition of HVOF 1020 coatings: (a) is a back-scattered SEM micrograph showing the cross-sectional microstructure. The light areas labelled (b) in the micrograph are the steel splats, (see the EDS spectrum of (b)); the dark grey regions labelled (c) consist of Fe and O as shown in the EDS spectrum of (c); the black regions labelled (d) are the pores. Figure 4.35 (d) XRD spectrum of HVOF 1020 confirming the presence of iron and (FeO).	
Fig. 4.36	124

A variation of wear rates (mm^3/m) of the HVOF 1020 coatings is plotted as a function of sliding speed at several load levels of 5 N, 10 N, 25 N, 50 N and 75 N.

Fig. 4.37 125

(a) Secondary and (b) back-scattered SEM images of the worn surface of the HVOF 1020 coating tested at 10 N load and 0.5 m/s sliding speed after 5000 m sliding distance.

Fig. 4.38 126

A back-scattered SEM micrograph of the worn surface of the HVOF 1020 coating tested at 75 N load and 0.5 m/s shows severe plastic deformation on the sliding surfaces.

Fig. 4.39 126

A back-scattered SEM micrograph of the worn surface of the HVOF 1020 coating tested at 75 N load and 0.5 m/s shows severe deformation and fracture at the tip of the splats on the contact surface.

Fig. 4.40 127

A secondary SEM micrograph of the worn surface of the e HVOF 1020 coating tested at high load (75 N) and high sliding speed (2 m/s) after 5000 m sliding distance that shows a severely deformed and damaged surface associated with the cracks (marked with arrows) normal to the sliding direction.

Fig. 4.41 127

A back-scattered SEM micrograph of the HVOF 1020 coating tested at 50 N load and 2 m/s. The micrograph was taken from a region on the wear track, which shows evidence for surface oxidation during sliding.

Fig. 4.42 128

A low magnification back-scattered SEM image from the worn surface (on a tilted angle 60°) of the HVOF 1020 coatings tested at 50 N and 2 m/s shows that the worn surface has a high roughness along with scattered oxide patches.

Fig. 4.43 128

A secondary SEM image of the HVOF 1020 that shows the 7 μm thick oxide rich films that formed on the sliding surface of the coating tested at 75 N and 2 m/s after 5000 m sliding distance.

Fig. 4.44	129
Another example of the formation of the thick oxide layers of the HVOF 1020 during sliding at high loading conditions. The figure also shows cracking in the oxide film.	
Fig. 4.45	130
A secondary electron SEM image from the debris gathered from the HVOF 1020 tested under 75 N and 2.5 m/s shows the plate-like iron oxide debris.	
Fig. 4.46	131
Microstructure and composition of HVOF 1020-2.5% Al coatings: Figure 4.46.a is a back-scattered SEM micrograph showing the cross-sectional microstructure. The light areas labelled (b) the steel splats (see EDS spectrum of Figure 4.46.b); the medium grey regions labelled (c) are the iron oxide veins that consists of Fe and O as shown in the EDS spectrum of Figure 4.46.c ; the dark grey regions labelled (d) are inclusions consisting of Al, Fe and O as shown in the EDS spectrum of Figure 4.46.d ; the black regions labelled (e) are the pores.	
Fig. 4.47	133
The variation of the wear rates (mm^3/m) of the HVOF 1020- 2.5% Al coatings is plotted as a function of sliding speed at load levels of 5 N, 10 N, 25 N, 50 N and 75 N.	
Fig. 4.48	134
A back-scattered SEM micrograph was taken from the worn surface of the HVOF 1020-2.5% Al coating tested at 75 N and 2 m/s, which shows the scratches at low magnification.	
Fig. 4.49	134
A back-scattered SEM image that was taken from the worn surface of the HVOF 1020-2.5% Al coating tested at 75 N load and 0.2 m/s that shows that the metallic fragments were flattened and forged on the sliding surface.	
Fig. 4.50	135
A back-scattered SEM micrograph shows the fracture of the inclusions into the small particles, which can act as abrasive and scratch the sliding surfaces of HVOF 1020- 2.5% Al.	
Fig. 4.51	135

A secondary SEM micrograph (on a 60° angle) showing the morphologies of the worn surface of HVOF 1020-2.5%Al coatings tested at 75 N load and 2 m/s sliding speed. Iron oxide layers on the worn surface are about 1 µm thick.

CHAPTER V

Fig. 5.1	163
A schematic diagram illustrating the mechanism for deformation and fracture of steel splats. a) shows a cross-section of the unworn surface. b) shows a cross-section of plastically deformed splats elongated along the sliding direction. c) is a surface view showing fracture at the edges of the splats.	
Fig. 5.2	164
Rectangular PTWA 1020 sample of 10 mm wide and 25 mm in length with 1 mm in thickness were tested using a miniature three point bending jig. 4 mm diameter round pins were put in contact with the lower face of the aluminum substrate	
Fig. 5.3	164
The cross section of the PTWA 1020 coating after the three point bending test at the maximum load of 160 N shows a large perpendicular crack to the surface propagated through the coating into the substrate	
Fig. 5.4	165
A high magnification micrograph of the cross section of the PTWA 1020 presented in Fig. 5.3.	
Fig. 5.5	166
A back-scattered SEM micrograph from the cross section of the worn surface of HVOF 1020-2.5% Al shows the cracks propagated through the oxide veins and caused delamination of an entire iron splat adjacent to the contact surface. The same type of delamination wear was also observed in PTWA 1020. But the occurrence of this wear mechanism is rare.	
Fig. 5.6	167
Comparison of friction induced surface temperatures for PTWA 1020 and HVOF 1020 at different sliding speeds at 75 N load	
Fig. 5.7	168

TEM metallographic investigations on the longitudinal sections of the PTWA 1020 sample tested at 75 N and 2.5 m/s which showed surface hardening after wear. The microstructure is divided into three distinguished layers: 1) on the contact surface where the grain size is about 50 nm, and 2) adjacent to the layer where there is a substructure consisting of an elongated sub-grain and 3) undeformed coating.

Fig. 5.8169

Schematic diagrams illustrating a mechanism for polishing wear by chemical and mechanical mechanisms. a) a cross-section of the coating and the formation of the oxide film at high humidity. b) the detached hydrated iron oxide by counterface becomes entrapped in the spaces between the actual contact areas. c) The crests of asperities are removed and the surface becomes flat.

Fig. 5.9170

Wear map showing wear rates and mechanisms for PTWA 1020 thermal spray coatings in dry sliding against tool steel pin material. The coatings wear rates have units of 10^{-6} g/m. Experiments were conducted using the pin-on-disc geometry, at room temperature in air (RH=10%). (a-d) Typical SEM micrographs (backscattered electron (BSE)) of worn surface morphologies from Regimes I-IV.

Fig. 5.10171

Wear map showing wear rates and mechanisms for HVOF 1020 thermal spray coatings in dry sliding against tool steel pin material. The coatings wear rates have units of 10^{-6} g/m. Experiments were conducted using the pin-on-disc geometry, at room temperature in air (RH=10%). (a-c) Typical SEM micrographs of worn surface morphologies

Fig. 5.11172

(a) WYKO optical surface profilometer image from the worn surface of the HVOF 1020 coating tested at 75 N and 2 m/s shows the topographical features of the thick and rough oxide layers formed during sliding, (b) WYKO image from the worn surface of the PTWA 1020 coating tested at same loading condition shows uniform and protective oxide film on the sliding surface.

Fig. 5.12173

Wear map showing wear rates and mechanisms for HVOF 1020-2.5% Al thermal spray coatings in dry sliding against tool steel pin material. The coatings wear rates have units

of 10^{-6} g/m. Experiments were conducted using the pin-on-disc geometry, at room temperature in air (RH=10%).

Fig. 5.13 174

The surface (bulk) temperature map for the PTWA 1020 constructed on load vs. speed axes. The temperature map shows the temperature increase (in °C) on the sliding surface during the sliding at various combinations of load and velocity. The wear regimes are superimposed on the temperature map.

Fig. 5.14 175

The surface (bulk) temperature map for the HVOF 1020 constructed on load vs. speed axes. The temperature map shows the temperature increase (in °C) on the sliding surface during the sliding at various combinations of load and velocity. The wear regimes are superimposed on the temperature map.

Fig. 5.15 176

The comparative wear map of the PTWA 1020 coatings and the 356 Al alloy showing the degree of protection provided by the coatings to the aluminum surfaces. The numbers on the map are the ratios of the wear rates of PTWA 1020 to the wear rates of 356 Al alloys at the same loading conditions.

CHAPTER VI

Fig. 6.1 207

Schematic showing the four steps of the thermal spray deposition process used to coat the inner surfaces of the cylinder bores in internal combustion engines.

Fig. 6.2 208

(a) Photographs of the sectioned bore, (b) the major thrust surface of the bore of the corvette engine.

Fig. 6.3 209

3D surface profilometry image from the front face of the scuffed corvette engine showing the crosshatch hone marks on the surface.

Fig. 6.4 210

Surface profilometry image from the minor face of the scuffed corvette engine showing the hone marks that completely disappeared, and the scratches and wear scars on the surface.

Fig. 6.5211

(a) Surface profilometry 3D image from the major face of the scuffed corvette engine, showing the rough surfaces that are associated with the deep scratches and wear scars. (b) Plan view WYKO image of the major face, along with Y and X profiles of selected points as marked on the image.

Fig. 6.6213

Plan view secondary electron image taken from the surface of the major face of the middle part of the scuffed Corvette bore.

Fig. 6.7214

(a) Cross-sectional micrograph taken from the same area on the major thrust face (middle part of the bore). The micrograph shows 2-5 μm thick tribolayer on the sliding surface and extensive subsurface cracking. (b) High magnification of the back-scattered SEM image of the damaged surface region (area inside the rectangle) in Fig. 7.a shows a mechanically mixed tribolayer, evidence of plastic deformation and the flow beneath the tribolayer.

Fig. 6.8215

Secondary SEM micrograph taken from the major face of the corvette engine showing the shear stress from sliding of the rings or piston induced subsurface plastic deformation, which is unidirectional because all the visible microstructural elements were aligned in the same direction.

Fig. 6.9216

Back-scattered SEM image from the major face of the Corvette engine shows cracking in the inclusions identified rich in Fe, Al and O using EDS analysis technique and FeAlO_3 with the aid of a TEM.

Fig. 6.10217

Secondary electron SEM image of the longitudinal cross section from the major face of the Corvette engine shows how the surface layers were detached from sliding surfaces.

Fig. 6.11218

Cross-sectional secondary SEM image taken from the minor face 45 mm below the deck face showing no evidence of the tribolayer.

Fig. 6.12219

Photographs taken from two sides of the piston skirt in contact with (a) the major face and (b) the minor face of the cylinder bore.

Fig. 6.13220

a-b) Back-scattered electron SEM images with different magnifications taken from the side of the piston skirt in contact with the major face with the greatest damage showing the iron patches (light grey area) that were transferred from the HVOF 1020-2.5% Al coating on the cylinder bores.

Fig. 6.14221

Cross-sectional micrograph of the nitrate stainless steel top ring.

Fig. 6.15221

Back-scattered SEM micrograph of the centre of the damaged area of the ring showing the surface being cracked along a direction perpendicular to the sliding direction with scratches parallel to the sliding direction. There is also evidence of material transfer (dark region) to the surface of the ring.

Fig. 6.16222

EDS analysis of the dark area (seen in Fig. 15) showing the presence of elemental Al, Fe, O, and Cr elements in this area.

Fig. 6.17223

Secondary SEM micrograph taken from the edges of the severely damaged part of the top ring showing that chipping has occurred in this area.

Fig. 6.18223

Back-scattered SEM micrograph from the cross-section of the major side of the scuffed Saturn engine bore that shows subsurface cracks parallel to the surface. Some cracks extend to the surface. The figure also shows a missing part of a splat at the contact surface.

Fig. 6.19	224
Back-scattered SEM micrograph from the major side of the scuffed Saturn engine that shows cracking of the inclusions, and the crack in the deformed layer extending parallel to the contact surface.	
Fig. 6.20	224
Back-scattered SEM image from the cross-section of HVOF 1020-2.5% Al tested at 100 N load and 0.2 m/s speed under Ar atmosphere and boundary lubricated conditions to 15,000 m using a pin-on-disc tribometer that shows formation of a deformed layer, and cracks in the inclusions.	
Fig. 6.21	225
Back-scattered SEM image from the cross-section of HVOF 1020-2.5% Al tested at 100 N load and 0.2 m/s speed under Ar atmosphere and boundary lubricated conditions to 15,000 m using a pin-on-disc tribometer that shows extensive cracks in the inclusions, and a subsurface crack which reaches to the surface.	
Fig. 6.22	225
Back scattered SEM image from the cross-section of HVOF 1020-2.5% Al tested at 100 N load and 0.2 m/s speed under Ar atmosphere and boundary lubricated conditions to 15,000 m using a pin-on-disc tribometer that shows the highly deformed tribolayer fracture. This has led to the formation of loose debris during sliding.	
Fig. 6.23	226
Back-scattered SEM image from the cross-section of the cast iron tested at 100 N load and 0.2 m/s speed under Ar atmosphere and boundary lubricated conditions to 15,000 m using a pin-on-disc tribometer that shows no visible damage, and a deformed layer at the contact surface.	
Fig. 6.24	226
Back-scattered SEM image from the cross-section of the cast iron tested at 100 N load and 0.2 m/s speed under Ar atmosphere and boundary lubricated conditions to 15,000 m using a pin-on-disc tribometer that shows the typical type of damage.	
Fig. 6.25	227
Back-scattered electron image from the cross-section of the cast iron tested at 150 N load and 0.2 m/s speed under Ar atmosphere and boundary lubricated conditions using a pin-on-disc tribometer that shows elongated graphite flakes (marked on the micrograph).	

Fig. 6.26	227
High magnification of the back-scattered SEM image of the damaged surface region (area inside the rectangle in Fig. 25) shows elongated graphite flakes in detail. Extensive fracture of the iron near the contact surface is evident.	
Fig. 6.27	228
a) A free body diagram showing the forces during a combustion stroke, and (b) free body diagram during a compression stroke.	
Fig. 6.28	228
Variation of the cylinder pressure as a function of the crank angle, and major engine cycle events. EVC = Exhaust valve closing, IVC = Intake valve closing, EVO = Exhaust valve opening, and IVO = Intake valve opening.	
Fig. 6.29	229
TEM metallographic investigations on the longitudinal sections of the major face of the scuffed Corvette engine along with the corresponding selected area electron diffraction (SAED) pattern from the ultrafine region.	
Fig. 6.30	230
Schematic diagram shows the microstructure of the longitudinal sections of the major face of the scuffed Corvette engine. The microstructure is divided into two distinguished layers: 1) on the contact surface where the grain size is about 20 nm, and 2) adjacent to the layer where there is a substructure consisting of an elongated sub-grain of 200 - 300 nm in width and about 100 nm in thickness.	
Fig. 6.31	231
The high magnification TEM micrograph from the material layers immediately below the contact surface, namely about 0.2 μm below the surface of the scuffed Corvette engine that shows nano-size grain structure with an equiaxed morphology.	

LIST OF TABLES

Table 3.1	50
The plasma transfer wire arc (PTWA) processes parameters.	
Table 3.2	51
The high velocity oxy-fuel (HVOF) processes parameters	
Table 4.1	66
Microstructural characteristics of the PTWA 1020 coatings. Note that the volume fraction of constituents was computed using an image analysis system and Vickers hardness was measured using a load of 25 g.	
Table 4.2	74
Quantitative XRD phase analysis of the debris (in weight fraction) at three different loading conditions.	
Table 4.3	83
Microstructural characteristics of the HVOF 1020 coatings.	
Table 4.4	87
Quantitative XRD phase analysis of debris (weight percent) of the HVOF 1020 coatings tested at different loading conditions	
Table 4.5	89
Microstructural Characteristics of the HVOF 1020-2.5% Al Coatings.	
Table 5.1.a	138
Summary of metallographic observations of worn PTWA 1020 coatings at low loads ≤ 20 N.	
Table 5.1.b	139
Summary of metallographic observations on worn PTWA 1020 coatings at high loads ≥ 20 N.	

Table 5.2	148
------------------	-------	-----

The coefficients of friction of the PTWA 1020 and HVOF 1020 coatings measured at 75 N at different velocities.

Table 6.1	179
------------------	-------	-----

Properties of the LS1 engine

Table 6.2	180
------------------	-------	-----

Properties of the Saturn engine

Table 6.3	206
------------------	-------	-----

Methodology used to develop new laboratory test in order to determine the scuff resistance of the materials

CHAPTER I

INTRODUCTION

The automotive industry continues to allocate considerable resources to reduce vehicle mass and improve fuel economy. In this respect replacing the traditional use of cast iron in components such as engine block with ones made of cast aluminum alloys is becoming a viable cost-effective method for reducing the mass of automotive components. The wear resistances of cast aluminum parts used in moving component are not satisfactory and is currently improved by protecting the sliding surfaces with liners made of cast iron. This technology is not desirable from a manufacturing point of view. The lightweight alternatives of wear resistance surfaces include aluminum matrix composites that incorporate hard particles and/or graphite flakes. Aluminum matrix composite liners are not cost effective. Although the research and development work in on metal matrix composites have been continuing since mid 1980's, these materials have not found widespread applications as liners due to difficulties in their manufacturing processes and their high cost. A potential alternative is to coat the aluminum surfaces with a wear resistant coating. At the present time there are many technologies available to produce wear resistant coatings for aluminum but most of them are expensive and only found applications in the aerospace industry. The challenge that must be met in manufacturing wear resistance coatings is to obtain the required performance while minimizing the overall cost and manufacturing complexity. In this respect thermal spray coating deposition technologies are of significant interest for the automotive industry [1]. In general, the use of thermally sprayed coatings can be to provide resistance to heat,

wear, erosion and corrosion for the base materials. The coatings can be deposited in ambient atmosphere and have lower production costs compared to other deposition technologies.

Thermal spraying has been practiced since the early 1900s. The first patent in this area was for a technique using a flame as the heat source, which was patented by Schoop [2]. In the beginning the technique was limited to low melting point materials such as tin and lead, and was progressively extended to steel. Wire plasma spraying was developed to avoid unmelted particles in the spray jet. In this technique the wire feed stock was introduced into the plasma. Here again, the materials melting temperature was limited to 1500-1600 °C. In 1957, plasma spraying became accepted as an attractive option, at first, by the aeronautics industry, (NASA) and later by the aircraft industry. The development of the plasma jet method dramatically extended the technological possibilities to any material that could melt without decomposition. Later on, coating deposition under vacuum [3] or controlled atmosphere [4] made it possible to produce dense coatings with almost no oxidation. These coatings showed excellent bonding and cohesive strength. A recent development in surface fabrication by this method is the introduction of rotation of the spray gun which allows the inside surfaces of the engine blocks cylinders to be sprayed without having to rotate the part.

Thermal spray coatings have typically a layered microstructure that consists of splats separated by oxide veins. The literature on the wear behaviour of thermal spray coatings is very limited. The wear mechanism observed in thermal spray coatings is usually referred to as the splat delamination [5]. It has been reported that the splat delamination mechanism is due to the presence of 'weak links' caused by the oxide veins

in the coating microstructures [6, 7]. High wear rates were generally associated with the formation and propagation of subsurface cracks within the oxide veins, resulting in the removal of whole splats during the sliding process. With the exceptions of splat delamination and mechanisms related to the laminated microstructures of these coatings, there are several similarities between the wear behaviour of thermal spray low carbon steel coatings and low carbon steels. Since the focus of this work is on the wear mechanisms of ferrous thermal spray coatings it is appropriate to summarize the main points of wear research performed on iron and steel here. According to Welsh [8,9], when pins made of plain carbon steel (0.12 to 0.78% C) were rubbed against rings of the same material, at a critical sliding speed, which depended on the composition of steel tested, the high wear rates (severe wear) suddenly diminished to low values (mild wear). This was attributed to a self-induced quench hardening process, as a result of frictional heating of asperities. Archard [10], by studying the wear behaviour of 0.52% C steel in detail, found critical speeds at which the severe to mild wear transitions occurred for the tests carried on at two loads. It was shown that at those critical speeds the surface temperature was high enough for a ferrite to austenite phase transformation and subsequent quench hardening. Lim and Ashby [11] studied the wear of steels using a wear map approach; they classified the wear mechanisms by accounting for the frictional heating and calculating the flash temperatures for four mechanisms. As will be shown in this thesis, among these wear mechanisms observed, the oxidation-dominated wear and severe plastic deformation induced wear appear to be most closely related to the wear of thermal spray low carbon steel coatings. The work presented in this work provides a detailed metallographic characterization of the thermal spray coatings manufactured at the

General Motors Research and Development Center, Warren MI. The coatings were produced by two different thermal spray processes. The wear behaviour of the coatings was systematically investigated and the micromechanisms of wear were determined.

The thesis is organized into seven chapters including this one (Chapter I). Chapter II reviews wear phenomena in metallic systems in particular in ferrous materials. The relevant literature on the micromechanisms of wear processes and the microstructural changes that occur during wear are reviewed. An introduction to the literature on wear and scuffing of internal combustion engines is also given.

Chapter III describes the materials and experimental procedures used in this work. In this chapter the thermal spray deposition processes used for the production of the low carbon steel coatings are explained. Three coatings were fabricated using two different thermal spray processes. These were the plasma transfer wire arc (PTWA) deposition, and the high velocity oxy-fuel (HVOF) deposition processes. Experimental procedures, used to characterize the microstructures of the coatings as well as the details of the wear tests and subsequent metallographic analyses are described.

The presentation of the results arising from the experimental work, are divided according to the coatings studied. First, the chemical compositions and microstructures of PTWA 1020 coating are given, followed by wear test results. The results of HVOF 1020 and HVOF 1020-2.5% Al thermal spray coatings are presented in the same order.

The discussion of the experimental observations is presented in Chapter VI. The micromechanisms that control the wear rates in the thermal spray coatings are discussed. The role of the coatings microstructures as well as the role of the production processes used to fabricate the coatings on the wear behaviour of the coatings are discussed by

comparing the wear tests results of the PTWA 1020 and the HVOF 1020 coatings. Model to analyse friction induced surface temperature increase, generated during sliding wear is developed and used to explain the differences in the oxidative wear mechanisms of the coatings that showed different wear rates. The surface temperatures generated at different loads and velocities are summarized in the form of the temperature maps for each coating. Wear mechanisms and wear rates of the three thermal spray coatings, namely PTWA 1020, HVOF 1020, and HVOF 1020-2.5% Al coatings, are summarized in the form of the wear maps that are constructed separately for each coating

Chapter VI focuses on the engineering applications of the thermal spray coatings. Wear of actual engines in which thermal spray coatings were used as cylinder bore coatings are investigated. Micromechanisms responsible for scuffing damage in actual engines with bores coated with high velocity oxy-fuel (HVOF) 1020-2.5% Al low carbon steel thermal spray coating are studied using SEM, TEM, and other material characterization techniques. A methodology is developed in order to select a laboratory scale pin-on-disc type scuffing tests applicable to studying cold scuffing of coated engines. Strong correlations between the wear mechanisms in the scuffed engines and those that occurred in the laboratory wear tests were found. The conclusions and summary are given in Chapter VII.

CHAPTER II

LITERATURE SURVEY

In this section the existing literature on the micromechanisms of wear processes, in particular studies focussed on the micromechanisms of sliding wear is presented. Since the thermal spray coatings that are studied in this work are being developed for automotive engines, an introduction to the literature on the wear and scuffing of internal combustion engines is also given. The literature on the wear of thermal spray coatings is very limited. The previous studies on the sliding wear of these coatings together with the studies on their fabrication methods and microstructures are also reviewed in the current section.

2.1. GENERAL INTRODUCTION

Whenever two surfaces move over each other, wear occurs on one or both surfaces to a certain degree depending on the surface conditions. Wear is defined [12] as “damage to one or both surfaces, generally involving progressive loss of material”. In most cases, wear is detrimental, leading to increased clearances between the moving components. Unwanted freedom of movement and loss of precision may occur, often accompanied with increased noise and vibration. In machine elements this may lend itself to increased mechanical loading and an accelerated material removal rate, and sometimes may lead to scuffing and seizure.

The potential tribological applications of ferrous thermal spray coatings investigated in this dissertation are in internal combustion engines made of cast

aluminum. Lightweight aluminum engines commonly made of B 319 or A 356 are not sound tribological components but are susceptible to wear and scuffing. One of the principal objectives for the development of thermal spray coating is to provide wear resistant surfaces during the sliding contact of the cylinder bore and piston ring assembly. It is important to emphasize that wear is not a material property. It depends critically on the conditions under which the sliding contact occurs. The environment, the surface temperature, as well as the contact load (pressure) and relative motion speed are all important in determining the sliding wear rates. The role of these factors on the wear rates and mechanisms will be discussed in detail in the following sections.

Wear is one of the main components of tribology. The term tribology encompasses the science and technology of friction, wear, and lubrication. An excellent review of the history of tribology was presented by Zum Gahr [13]. The word tribology is in fact a very new term, which was first used in 1966 by a UK government committee. In 1986, the National Research Council of Canada [14] estimated that the losses due to wear amounted to \$5 billion per year. This is in broad agreement with the estimates made by other national committees that at least 1% of the gross national product might be saved with investment in tribology research. The savings arise from several sources. These include the reduction in energy consumption; savings in maintenance and replacement costs, saving in losses due to breakdowns etc.

One well established method of reducing friction, and often wear, is to lubricate the surfaces. The study of lubrication is very closely related to that of friction and wear. Indeed, even when an artificial lubricant is not added to a system, components of the atmosphere (especially oxygen and water vapour) often play a similar role. Therefore

their role must be considered in studying the interaction of the surfaces. Another way of reducing tribological costs is to select the most appropriate wear resistant material for the specific engineering components. In order to do this the micromechanisms of wear that occur in surfaces in sliding contact must be well characterized. This is because there is currently no reliable design equation that can be used in tribological material selection. A thorough understanding of the wear mechanisms is necessary in order to build these models from the microstructural point of view. Prior to reviewing these mechanisms it is instructive to review the “modes of wear”.

2.2. MODES OF WEAR

In an attempt to classify various forms of wear, a large number of terms related to describing features of worn surfaces and wear modes have been proposed [13, 15-25]. The different modes of wear observed in industrial practice can be broadly classified as follows:

- Abrasive Wear
- Rolling Contact Wear
- Fretting Wear
- Erosive Wear
- Sliding Wear

2.2.1. ABRASIVE WEAR

Abrasive wear occurs when a sharp particle or asperity penetrates a softer surface and scratches that surface or cuts a chip. There are two common types of abrasive wear. These are known as i) two-body abrasion, and ii) three-body abrasion. In two-body abrasion a rough hard surface slides against a relatively soft opposing surface and causes damage to the softer surface either by ploughing or micromachining it. Three-body abrasion involves action of rough hard particles trapped between the two sliding surfaces that cause the surfaces to be abraded [26]. The degree of surface damage is usually higher if the hardness difference between the particles and the contact surface is large. Literature on abrasive wear is more than the literature on other wear modes since this type of wear accounts for the majority of tribological failures. A detailed quantitative description of abrasive wear was first developed by Rabinovitch [27]. Materials aspects of abrasive wear are recently reviewed by Zum Gahr [13].

2.2.2. ROLLING CONTACT WEAR

This type contact mode between the surfaces of two solids is characterized by a rotational motion that occurs together with a transitional (sliding) motion. The rotational axes of both bodies are parallel to the contact area, and the vectors of velocity are of different magnitudes [13]. In practice, this type of wear is commonly seen in bearings.

2.2.3. FRETTING WEAR

The term fretting characterizes a small oscillatory motion between two solid surfaces in contact. The direction of the motion is usually, but not necessarily, tangential to the surfaces. The amplitude of the motion lies in a range typically between 1 and 100 μm . The surface degradation occurs as a result of repeated oscillations with small amplitude.

2.2.4. EROSIVE WEAR

In some situations, wear is caused by the action of hard particles striking the surface. These particles are either carried by a gas stream or by a flowing liquid. This type of wear mode is called solid particle erosion. Particle velocities in erosive wear commonly vary between 5 and 500 m/s. If the hard particles are carried by a liquid, the wear is termed slurry erosion [26]. In general, erosive wear is caused on solid bodies by the sliding or impacting action of solids, liquids, gases or a combination of these [13].

2.2.4. SLIDING WEAR

Sliding wear is defined as a motion between two moving bodies in relative motion with each other. The surface velocities of these two bodies in the common contact area are different and usually one of them is stationary [28]. Therefore, sliding wear refers to a wear mode generated by pure sliding without rolling or spinning. The term “adhesive

wear” is sometimes used to describe sliding wear but adhesion is only one of the several physical and chemical processes that are involved in sliding wear.

Sliding wear can be divided into two types [23, 26, 29, 30]: (a) Mild wear that usually occurs at low loads and sliding velocities; and (b) Severe wear, which is promoted by high temperatures, loads and velocities.

Sliding wear usually involves debris formation mechanisms such as delamination, subsurface fatigue, and oxidation [21, 30-32]. Material transfer from one surface to another, often accompany sliding wear, in particular in the severe wear regime. According to the earlier theories of sliding wear [33], when asperities come into contact, they adhere strongly to each other and form asperity junctions that become welded to each other. Subsequent separation of the surfaces takes place in the bulk of the softer asperities, which adhere to the harder surface [27]. Whenever material is removed from its original surface in this way, an adhesive wear fragment, or loose debris is created. Adhesion between the asperities is favoured by clean surfaces, by chemical and structural similarities between the sliding pairs [34]. The vacuum environment or inert atmospheric conditions also favour adhesion between the surfaces. However, it is difficult to prove adhesion at the asperity level as well as wear debris formation as a result of asperity fracture phenomena by metallographic and other surface characterization techniques. As pointed above, adhesion may not be considered as a mechanism itself other than a result of severe localized surface deformation.

The mechanisms of the debris formation are influenced by the severity of surface deformation and the stress and strain distributions in the material layers adjacent to the contact surfaces. In ceramics the material removal and debris formation during sliding is

mostly caused by brittle fracture as a result of inter-granular crack propagation [35, 36]. In ductile materials, where a subsurface crack growth occurs as a result of a void nucleation and propagation (e.g. at around second phase particles and precipitates), delamination of the highly strained subsurface layers becomes an important wear mechanism [37]. This mechanism may lead to the formation of plate-like or flaky debris particles [38]. It was suggested that when a local cyclic plastic deformation zone is present at the crack tip (possibly mode II, or shear type) fatigue crack propagation may occur leading also to the formation of flaky debris particles [39, 40, 41]. The fatigue crack propagation takes place in an elastic material. The plastically deformed region ahead of a growing crack is small compared to the total length of the crack. Therefore wear by fatigue many occur in brittle or quasi-brittle materials. In contrast in highly ductile materials damage accumulation processes and ductile failure as a result of subsurface delamination are more common. In these materials subsurface strains can reach levels of the order of 2-3 or higher. The nature of subsurface zones are examined in the next section.

2.4. SUBSURFACE ZONES IN SLIDING WEAR

It is well known that sliding friction may produce large amounts of plastic deformation in the material layers adjacent to contact surfaces [42-51]. Rice et al. [51] suggested that the material under the sliding surfaces can be examined in three separate zones. According to his description the farthest zone from the sliding contact is the original undeformed bulk material (zone 1). The next layer (zone 2) contains plastically deformed material, where the magnitudes of the plastic shear strains increase towards the

contact surface. Depending on the type of material, testing environment, and the nature of contact geometry, zone 2 may become harder or softer than the undeformed bulk material. In ductile materials, voids may develop within this zone. Cracks may nucleate in brittle materials. Heilman et al. [52] have observed a large rotational of grains in copper samples subjected to dry sliding. The rotation of the grains occurred about an axis normal to the sliding direction and parallel to the wear surface and extended to 20 microns in depth leading to the distortion of flow lines. At higher magnifications, it was observed that the flow lines consisted of a network of fine grains of small thickness elongated in the sliding direction. The aspect ratio of these grains increased on approaching the surface. By comparing the grain shape before and after the sliding, the magnitude of accumulated strains (ϵ) can be estimated as a function of depth. In most cases, the shear strain increases exponentially with decreasing depth and may be approximated by the expression [53]

$$\epsilon = \epsilon_{\text{Surface}} \exp(-AZ) \quad (2.1)$$

where Z is the depth below the contact surface.

For approximately 10 microns below the sliding surface, the plastic deformation is very severe. The heavily deformed grains are difficult distinguished from one another. TEM studies have shown that the microstructure at this depth consisted of a substructure with small dislocation cells. The cells are normally elongated in the sliding direction with a thickness of 0.3-0.5 microns [54-57]. The cell sizes decrease as the material gets closer to the contact surface and also there is an increase in the dislocation density from 10^8 cm^{-2} to 10^{10} cm^{-2} in the case of lubricated wear of aluminum under light load [58]. Ohmae et al.

[59] have observed equiaxed cells at depths greater than 5 microns, which may indicate extensive thermal recovery during sliding wear.

Zone 3 is a tribolayer, which forms on the contact surface and consists of a mechanical mixture of original specimen material counterface materials and oxides [59]. The tribolayers consist of either chemically mixed or mechanically mixed species coming from both surfaces. Chemical species from the counterface and from the test environment may diffuse into the contact surface and contribute to the formation of the tribolayers. Mechanical mixture may occur as a result of transfer and back transfer of species between the contacting surfaces. Riahi and Alpas [60] reported that in graphitic aluminum matrix composites, the mild wear rates were primarily controlled by the formation of the tribo-layers, which were mechanically mixed and oxidized surface layers on the contact surfaces. Given the high strains and strain rates generated during sliding contacts this process is sometimes regarded as equivalent to high-energy ball milling process. In some cases zone 3 appears homogeneous with a nanocrystalline microstructure [61]. The nanocrystalline structure was reported to be formed as a result of mechanical mixing [62].

Rigney and Hirth [63] developed a model for the source of friction during steady state sliding of metals. The model focussed on the plastic work done in the near-surface region, described in terms of work hardening, and recovery processes that took place during steady state sliding. Rosenfield [64] proposed a model of sliding wear by considering subsurface strain distribution to predict the flake thickness during sliding wear.

2.4. TRANSFER AND MECHANICAL MIXING

In dry sliding systems material transfer may occur from one sliding surface to another. This phenomenon has led to the idea that the formation of surface layers may reduce wear by reducing adhesion [60]. In some systems amorphous layers on the surface are produced by sliding, but in most cases a significant part of the tribolayer is composed of ultrafine grained crystalline material [54], varying from about 3 nanometers to several tens of nanometers. The ultrafine nature of the tribolayers, which are termed as mechanically mixed layers (MML) in Al-SiC composites was reported by Li and Tandon [65].

Rigney et. al [61, 66] observed that the wear debris collected from wear tests on the Cu, Cu-Ni, Cu-Al, Ni and Mo worn against steel, contained components from both materials in contact. The wear debris and the surface layers had similar ultrafine grain structure, and the same average composition. It has been shown that during sliding, back transfer of material to the counterface was very common [30]. Cocks [67] and Antler [68] have suggested that the preferential material transfer direction may depend not only on the material combination in the tribosystem but also on the geometry of the system. It was also shown that for similar metals, the rate of material transfer may be as high as 50-100 times that of dissimilar metal systems [30].

2.5. ARCHARD EQUATION

In dry sliding wear, it is often found that the wear rate changes with the sliding distance during the early stages of sliding due to the changes in the topography and

microstructure of the surfaces in contact. After the initial period of running, three types of wear curves have been observed.

i) The first type of wear curve shows a linear dependence of the volume or mass loss during wear to the sliding distance. This type of wear curve, with constant slope is commonly observed in the mild wear regime.

ii) In this type of wear, initially the wear rate is high so that the surfaces and debris appear to be metallic. The curve shows a transitional behaviour and the wear rate reduces to a lower steady value for the remainder of the test.

iii) The third type of wear curve depicts a transitional behaviour. Usually mild wear occurs first but after a certain sliding distance the wear rate increases suddenly to severe wear (e.g. [69]).

When the material does not show a wear transition and the amount of material loss remains constant, the wear rate can be regarded as the "equilibrium wear rate" [29] or "steady state wear rate". It should be noted that this is applicable to the mild wear rates only. Severe wear usually represents a condition of instability and wear rates usually increase with time often leading to seizure.

Many quantitative models for mild wear have been developed, but one of the simplest is given by Archard. Archard [59] first derived a theoretical expression (Linear Wear Law or Archard Equation), which predicts the rate of sliding wear W at a constant sliding speed as:

$$W = \frac{w}{S} = \frac{KF}{H} \quad (2.2)$$

Where 'w' is the wear volume, 'S' is the sliding distance, 'F' is the applied normal load, 'H' is the bulk hardness of the material subjected to wear in sliding contact, and K is a constant which is called the wear coefficient. The value of 'K' strongly depends on the sliding environment. For example, changes in the humidity of air can change the wear coefficient of brass by a factor of 100 [30].

Although the Archard equation is usually a good starting point to describe the wear rates, it should be used with caution. As noted before, the Archard equation is valid only for low loads up to some point at which the rate of wear may increase sharply. When the applied loads exceed this point, the wear coefficient K is no longer a constant, and may rise rapidly for small increases in load, until the onset of seizure (or welding of surfaces to each other).

The main limitation of the Archard equation arises from the fact that the equation assumes that the bulk hardness of the material at room temperature is the only materials property that controls the wear rate [71]. As discussed above, the bulk hardness cannot be regarded as the sole factor that influences the wear rates. The hardness of the surfaces change with the accumulation of surface strains during sliding. Friction induced surface temperature changes will also affect the hardness of the material layers near the contact surfaces. In fact, the existence of sudden transitions that depend on changing the surface conditions at critical loads and speeds makes it uncertain whether the phenomenological Archard equation can be used for design purposes over a wide range of load conditions [60, 72]. There is therefore a need to understand the wear behaviour of engineering materials from the microscopic point of view by characterizing the more fundamental microstructural changes as a function of the applied mechanical factors and environment.

In the past ten years or so the use of wear maps that show the wear rates in conjunction with the underlying mechanisms has become an accepted method of presenting laboratory scale wear data as a function of experimental conditions. The research done on the development of wear maps is summarized in the next section.

2.6. WEAR MAPS AND THEIR APPLICATIONS

Lim and Ashby [11] studied the sliding wear of steels and developed a wear map using the wear data they collected from the literature. The wear map that they constructed summarized the wear behaviour of the mild steel over a wide range of load and sliding velocity, identifying the dominant mechanism and showing the overall wear rate. The load and speed conditions corresponding to the operation of a primary wear mechanism that control the wear rates under these conditions were indicated on the wear map. The map is divided into different regions. These involved ultra mild wear at low speeds and loads, delamination wear at moderate loading conditions, mild and severe oxidational wear at high loads and speeds. The wear mechanisms were categorized by taking into account the effects of the coefficient of friction and friction induced temperature increases. The flash temperatures, i.e., the temperature reached at the tip of the asperities were calculated and these were used in modelling the oxidational wear mechanisms.

In 1988, Antoniou and Subramanian [73] developed a wear mechanism map for aluminium-silicon alloys by following the mapping method proposed by Lim and Ashby [11, 74]. They identified the wear mechanisms by direct observations of the worn surfaces of the aluminium alloy samples, the steel counterface, and the wear debris morphology. This map was however generic and did not indicate the effects of important

microstructural factors such as silicon particle size, volume fraction, and morphology on the wear rates.

Wang et. al. [75] constructed a wear mechanism map for dry sliding of an Al 6061 alloy reinforced with 20% SiC. The wear map showed a transition from mild to severe wear and showed that seizure occurred ultimately by increasing the loading condition. Mild wear was associated with oxidation of aluminium surfaces. The sliding surface of the aluminum was relatively smooth and the wear debris was small and brittle. It was suggested that at the severe wear regime, rapid surface degradation caused high wear rates.

Liu et. al. [76] constructed a qualitative wear mechanism map for Al alloys using wear data collected from the literature. Rohatgi et al. [77] were also involved in constructing wear maps of Al alloys. These alloys contained various solid lubricant particles such as graphite and hard particles such as zircon.

Another approach to the development of wear maps was adopted by Kato et al. [78] and consisted of empirical tests performed using pin on disc type wear testers over a wide variety of loads and speeds for the nitrided steel. The characterization of the wear debris produced during tests was used as the primary means for distinguishing between mild and severe wear regimes on load versus speed axes. It was shown that gas nitriding not only reduced the wear rate, but also expanded the mild wear region toward higher loads and sliding speeds.

Zhang and Alpas [69] studied the wear behaviour of a wrought aluminum alloy (6061) as a function of applied load and sliding speed. They also developed an empirical wear transition map constructed on load versus sliding speed axes for this aluminum

alloy, Al6061 sliding against SAE 52100 steel [69]. They have shown that the transition to severe wear was controlled by a critical temperature condition. They suggested that measured bulk temperatures could be used as a simple criterion to detect the onset of severe wear.

Wilson and Alpas [79] developed a wear map when the effects of applied load and speed on the wear behavior of an A356 Al alloy and A356 Al- 20% SiC composite were summarized. The role of SiC particle addition on the wear behavior of A356 Al was discussed. The experimentally determined load and sliding speed data were used to calculate the critical transition temperature to severe wear in A356 Al by assuming a relationship between asperity contact size and debris particle diameter.

Riahi and Alpas [80] developed a wear map for grey cast iron. According to the wear map constructed, transition boundaries between the mild to severe wear, and the ultra-mild to mild wear regimes were linear on the log load versus log velocity scale. They concluded that the transition from mild to severe wear occurred at constant sliding energy. An empirical equation was developed to show that the transition from mild to severe wear in grey cast iron occurred when the energy generated at the contact surfaces ($\mu F_n v$) reached a constant value.

Fracture of graphite flakes grouped to form a rosette type morphology, as well as fracture of the matrix at the “necks” formed between the graphite flakes and the contact surface led to the formation of large-size debris in the mild wear regime, which was otherwise dominated by oxidative wear [80].

In Summary, the literature survey indicates that the wear maps are useful tools to summarize wear rates as a function of operating conditions. These maps have been

constructed for aluminum and steel. In this research work the maps are constructed for ferrous coatings on aluminum alloys.

2.7. SURFACE TEMPERATURE IN DRY SLIDING CONTACT

When two surfaces are put in sliding motion against each other, almost 90% of the work done as a result of surface traction or friction is dissipated in the form of heat. The friction induced temperature increase almost always modify the mechanical and physical properties of the sliding surfaces, and may cause softening by recrystallization, surface oxidation, or may even result in melting. The highest temperature increase occurs at the tips of contacting asperities, which make up the true area of contact at the sliding interface. The instantaneous temperature increase of these contact points, which is named the flash temperature, is much higher than the average or 'bulk temperature' of the surface, especially at low loads and sliding velocities. Several research studies have been done to measure or predict contact surface temperatures [11, 81-83].

The bulk temperature or the temperature of the surface in a region 0-100 μm below the contact surfaces can be measured by inserting thermocouples inside the samples or using other methods. However, the flash temperatures, because of their very localized nature are extremely difficult to measure experimentally. The role of the experimentally determined contact surface temperature (bulk temperature) on the wear transition was studied by Zhang and Alpas [69] using miniature thermocouple probes positioned inside the specimens subjected to sliding wear. It was observed that in 6061 Al alloy the transition from mild to severe wear occurred when the bulk surface temperature T_b exceeded a critical temperature of 123 °C. This observation thus provided a practical

means by which the onset of severe wear for a given tribo-system can be predicted, using a single bulk temperature measurement for Al alloys sliding against steel.

Temperatures generated by sliding processes were first calculated by Jaeger [84] using a so called moving heat source analysis, in which the energy input is modelled as a plane heat source moving along the surface. In some analyses the energy input due to the plastic deformation of subsurface regions were taken into account [81]. Welsh [8,9] studied the sliding behaviour of plain carbon steel (0.12 to 0.78% C) pins against rings made of the same material. He observed that at a critical sliding speed the high wear rates suddenly diminished to low values. The critical sliding speed depended on the composition of steel. This was attributed to a self-induced quench hardening process, as a result of frictional heating of asperities [8, 9]. Archard's observations [10] indicated that critical speeds existed for the severe to mild wear transitions at two loads in 0.52% C steel. He showed that at those critical speeds the surface temperature was high enough for a ferrite-austenite transformation and a reduction in wear rates as a result of subsequent quench hardening.

Archard and Rowntree [82] modelled the temperature distribution at the surface and in the substrate region in sliding wear. They validated their model by comparing the surface temperatures with those necessary for producing a metallurgically transformed material, namely martensite, on steel surfaces as a result of a single rubbing contact.

Ashby et al. [73] developed a model by considering a pin-on-disc configuration. The heat, q , which is generated at the contact surface, per unit of nominal contact area A_n per second is given as

$$q = \frac{\mu F v}{A_n} \quad (2.3)$$

Considering that the temperature generated at the contact surface flows both into the pin (identified by subscript 1) and the disk (identified by subscript 2), the bulk temperature T_b is expressed as

$$T_b - T_0 = \Delta T = \frac{\mu F v}{A_n} \left[\frac{k_1}{l_{1b}} + \frac{k_2}{l_{2b}} \right]^{-1} \quad (2.4)$$

In this equation T_0 is the temperature at a distance sufficiently remote from the contact surface so that the effect of the friction induced temperature is negligible. k_1 and k_2 are the thermal conductivities of the material at the two surfaces and l_{1b} and l_{2b} are the two lengths. These are defined as equivalent diffusional lengths and described in reference [73]. They depend on the physical lengths of the pin and the disk but also on the geometry of heat flow, thermal contact resistance between the pin and clamp etc.

In the bulk temperature calculations the frictional heat was assumed to be injected uniformly across the nominal contact area A_n . To calculate the flash temperatures it was assumed that the heat generated at the contact surface entered the surface through the asperities, which are represented by the true contact area A_r . The average flash T_f temperature was expressed as:

$$T_f - T_n = \Delta T = \frac{\mu F v}{A_r} \left[\frac{k_1}{l_{1f}} + \frac{k_2}{l_{2f}} \right]^{-1} \quad (2.4)$$

Here T_n is the “sink” temperature. The heat flowing through the asperity contacts is reduced to the bulk temperature levels very quickly and thus the “sink” temperature is

equivalent to the bulk temperature. The distances l_{1f} and l_{2f} are called effective heat diffusion distances and they depend on the size of the asperities.

Wilson and Alpas [79] presented the temperature measurements in map form for A356 Al alloy and A356 Al-20% SiC composite against steel and compared them with their observed wear transitions. An interesting aspect of the temperature map for this tribological system was that the oxidation of the steel counterface that occurred at the onset of the transition temperature to severe wear (in the unreinforced A356) became an important factor in delaying the transition to severe wear in the composite. A layer of iron oxide with a low coefficient of friction was formed at the contact surface, and higher temperatures were needed to observe a transition to severe wear.

Quinn [85] studied the effect of flash temperature, which he called hot-spot temperature, on the unlubricated wear of steel using the same material pairs of low alloy and medium carbon steels. He showed that the hot spot temperature is an important variable in the wear of steel. This was attributed to the change in the surface oxidation characteristics of the contacting surfaces, which are examined in detail in the next section.

2.8. OXIDATION DURING SLIDING CONTACT

In general, the friction of pure metals sliding against themselves in air under unlubricated condition is determined by the presence of surface oxides. If the oxide film remains intact during sliding, a small amount of surface damage is expected to occur and the coefficient of friction (μ) of the oxide determines the average coefficient of friction of

the tribological system. In several metals the transition to severe wear is delayed because the protective oxide coating is retained over a wide range of load, while in others, where the oxide is fractured and removed at very light loads, the contact is always metallic and wear rates are usually high. The value of the μ may be low at higher loading conditions if the oxide film is thick and metallic contact between asperities is prevented. Otherwise if the oxide film is not continuous and metallic contact is allowed to occur, considerable surface damage and rapid wear take place.

A detailed review of oxidative wear of metals is given by Quinn [31, 32, 85]. Mild oxidative wear was defined [31] as a mechanism of wear in which protective oxide films are formed at the real areas of the contact at a given contact temperature [31]. When the oxide film reached a critical thickness, it broke up and eventually appeared as wear debris. It was shown that temperature plays an important role in determining the structure of the oxide film present, which in turn affected the wear properties of the sliding interface. Quinn [86] assumed that normal stress and shear stress applied during sliding contact had no effect on the oxides formed. The comparison that was made on the basis of this assumption revealed a good correlation between the oxide actually obtained in the wear experiments and those to be expected from the oxidation data of Davies et al. [87], and of Moreau and Bardolle [88]. In this comparison it was assumed that oxidation occurred at the hot-spot temperatures predicted from Archard's [82] curves for single contact wear conditions. Briefly, it was suggested that the oxide growth rates obeyed an Arrhenius equation:

$$r = C \exp\left(\frac{-Q}{RT}\right) \quad (2.5)$$

where 'r' is the rate constant for growth of the oxide film. 'T' can be taken as the flash temperature and 'R' is the gas constant. 'Q' is the activation energy for diffusion leading to oxide growth. 'C' is a pre-exponential constant. Quinn estimated the C values for the oxidation of mild steel at different temperatures. The calculations were made for both static oxidation and under sliding conditions. It was shown that for the temperature range 450 - 600° C, the value of "C" was $3.2 \times 10^{-2} \text{ (kg}^2\text{m}^{-4}\text{s}^{-1}\text{)}$ for static oxidation while this value was as high as 10^3 for oxidation induced by sliding contact. This indicates that oxidation under sliding conditions is much faster by a factor of (10^5) than would be expected from static oxidation.

Under static conditions, Fe_2O_3 is the equilibrium phase that forms under ambient conditions [89], however the temperature at the asperity contact area during sliding of steel at relatively low loads and speeds could easily reach 300 °C or above [11]. This could promote formation of Fe_3O_4 and FeO, although Fe_3O_4 grows under static conditions at above over 450 °C, and FeO above 600 °C [26, 31, 32].

Molgaard [90] studied oxide growth and oxide transfer phenomena in wear. He stated that an increase in the plasticity of the oxide layer, particularly if the layer contains FeO may cause a decrease in the wear rates.

Oxidational wear in aluminum alloys has been examined by Eyre [91]. Eyre studied sliding wear of aluminum alloys containing silicon, copper, iron and nickel against steels with different hardness, and grey cast iron samples. In all cases oxidative wear occurred at low loads and speeds. It was shown that the transition load between oxidational and metallic wear increased as the silicon and copper content increased. The work further showed that in the oxidational wear regime iron oxide was formed during

sliding transfer to the contact surface of the aluminum alloy from the counterface and created a complex surface containing AlFe and $\alpha\text{Al}_2\text{O}_3$. Fracture and spallation of the oxidized layer was the controlling wear mechanism under these conditions.

2.9. EFFECT OF ENVIRONMENTAL HUMIDITY

Lancaster [92] has reviewed the effect of environmental humidity on wear and friction of different materials and noted that the coefficient of friction of iron decreased with increasing humidity due to rust formation. The fretting of pure metals as a function of humidity was investigated by Goto and Buckley [93]. They found that fretting wear rates decreased at high humidity conditions; however, the maximum fretting wear occurred at a certain humidity. The wear of three different types of carbon steels at moderate humidity levels of 30–70% was investigated by Oh et al. [94]. The results showed a transition from severe to mild wear increasing the humidity. Papaphilippou et al. [95] studied the effect of humidity on the wear of cast iron. They attributed the low wear rate at high humidity to the less abrasive character of the debris.

Barnes et al [96] studied the influence of oxide films on the friction and wear of Fe-5%Cr alloy in unidirectional and reciprocating motions in controlled oxygen pressure. They reported that protective islands of compacted debris developed as the partial pressure of oxygen increased.

2.10. TRIBOLOGICAL ASPECTS OF INTERNAL COMBUSTION ENGINES

The research work presented in this dissertation is aimed at studying wear resistances of coatings that can be used to protect surfaces of the cylinder bores in internal combustion engines made of aluminum. It is therefore instructive to summarize the tribological aspects of the internal combustion engines.

2.11. WEAR RESISTANT MATERIALS FOR INTERNAL COMBUSTION ENGINES:

The automotive industry is interested in reducing vehicle weight to improve fuel economy. A significant weight saving is provided by replacing cast iron in engine blocks with cast aluminum alloys. In designing new engines with aluminum block, it is important that engine durability is not sacrificed for lighter weight. One essential area of concern is the cylinder bores. The cast aluminum alloys, 380, A319 and A356 (hypo-eutectic) that are currently used in engine block castings have poor tribological properties. The compromise that has been adopted at the present time is to insert cast iron sleeves, which solves the durability problem, but adds significant amount of weight and dimension to the bore area. Fig. 2.1 shows three groups of lightweight materials that are being developed as alternatives to cast iron liners in aluminum engine castings.

2.11.1. ALUMINUM ALLOYS FOR INTERNAL COMBUSTION ENGINES

One of the three options to reduce the scuffing and seizure tendency of aluminum engines is to use a different aluminum alloy than the conventional A319. These alloys

must possess high wear resistance at the expense of ease of castability and machinability characteristics of the A319. In view of the importance of Al-Si alloys as lightweight tribo-materials with potential widespread applications in the automotive industry, several investigations have been conducted on the sliding wear resistances of Al-Si alloys [69, 79, 97-101]. Engine components made of Al-Si alloys may suffer from scuffing during cold start and oil starvation periods. Scuffing that occurs under boundary lubrication [102-106], and dry sliding conditions [106-110] has been studied. Most of these investigations were limited to testing conditions that led to mild and/or severe types of wear. The results generally suggested that the wear resistance of Al-Si alloys was a weak function of the silicon content of the alloy [96, 97, 99]. Other studies indicated that the size and morphology of silicon particles affect the wear and scuffing resistance (e.g. [108]), and that the eutectic composition provided the best wear resistance [98, 100]. Therefore, microstructures and morphologies of Al-Si alloys have yet to be optimized to maximize the wear and scuffing resistance.

Several wear mechanisms have been reported in studies of aluminum and its alloys in dry sliding contact against steel surfaces. The observations of Shivanath et al. [111] are typical. They identified two wear mechanisms in Al-Si alloys: one oxidational and the other metallic. In the oxidational wear regime, wear rates were low, with the worn surfaces covered by a dark compacted transfer layer, presumed to consist of aluminum oxide and some transferred steel, although its exact nature was not investigated. The onset of metallic wear occurred above a characteristic load at which massive deformation of the aluminum alloy surface occurred, accompanied by the

formation of metal fragments, which tended to adhere to the steel counterface. Wear rates in this severe wear regime were at least an order of magnitude greater than those in the mild wear regime.

These observations are similar to those of Hirst and Lancaster [112] on the sliding wear of 99% pure Al against stellite, where a transition from mild (oxidational) to severe (metallic) wear occurred at a critical normal load. Several subsequent investigations on the wear of Al-Si alloys (e.g. [113-115]) have also discussed these two main wear mechanisms and the effects of the sliding parameters and alloy composition on transitions between them.

Recently, Wilson and Alpas [116] calculated flash temperatures in the mild wear regime for A356 Al using empirical seizure load and asperity size data and the equations developed by Ashby et al. [11]. The onset of metallic flake/plate debris formation was attributed to a critical flash temperature that was close to the critical bulk surface temperature ($T_{crit} = 125\text{ }^{\circ}\text{C}$) observed for bulk seizure and severe wear. The onset of flake/plate delamination wear can thus be thought of as a highly localized form of seizure occurring in the sliding contact zone. This phenomenon is different from the delamination mechanism [117, 118], which occurs under effectively isothermal sliding conditions with low frictional heating, and in which most of the wear debris also consists of plate-like particles.

Newly developed wear resistant aluminum alloys include:

- i) ALUSIL (~17% Si, 4% Cu, 1% Mg (close to the composition of A390)) made by Kolbenschmidt-Pierburg, and used by Audi and Volkswagen in some production engines;

- ii) LOKASIL, an aluminum metal matrix composite using a silicon pre-form in a high pressure die casting process, in production at Porsche for low volume applications; and
- iii) Silitek (>25% Si, Fe, Ni) produced by PEAK using the Osprey process, which is used by Mercedes as cylinder liners (all compositions given here are in weight percent). All alternative alloys currently in automotive production share the characteristic of being hypereutectic alloys containing >17% silicon.

At the present time there is very little information in the open literature on the wear mechanisms that operate in these new aluminum alloys.

2.11.2. METAL MATRIX COMPOSITES

Metal matrix composites have been developed over the past 30 years. The primary user of the metal matrix composites is the aerospace industry for airframe and spacecraft structures. More recently, the automotive, and electronic industries have been interested in these composites. Metal matrix composites can be classified into either continuous fibre composites or discontinuously reinforced composites. The reinforcements have been introduced into matrices of aluminum, magnesium, copper, titanium, nickel, nickel based super alloys, or various alloys of iron. The aluminum matrix composites are among those that have become broadly available. Discontinuously reinforced composites have become the most commonly used to date. Additions of SiC, Al₂O₃, ZrO₂, and other ceramic particles, fibers, and whiskers to Al alloys generally improve their wear and seizure resistance. However, it must be emphasized once more that wear resistance is not a material property and that the micromechanisms of wear

of metal matrix composites depend on the conditions under which they are tested or used in practice. Therefore, in studying the wear of metal matrix composites it is important to examine wear behaviour as a function of the applied mechanical factors.

2.11.2.1. MILD AND ULTRAMILD WEAR

Numerous investigations of the dry sliding wear of aluminum matrix composites against steels have reported significant increases in their wear resistance compared with unreinforced aluminum alloys. When contact loads and sliding speeds are kept very low, so that frictional heating effects are negligible, ceramic reinforcing particles tend to support the contact stresses. Subsurface plastic deformation and shear of the matrix alloy is prevented by the constraint introduced by the reinforcing phase. Hosking et al. [119] observed this effect by the sliding wear rates for a 2024 Al alloy reinforced with different amounts of Al_2O_3 particles. The wear rate falls significantly with increasing Al_2O_3 content. Composites containing larger Al_2O_3 particulates show greater wear resistance than alloys with smaller particulates and equivalent reinforcement content. The load support provided by particulate reinforcement in ultramild wear was also demonstrated by Zhang and Alpas [37] in sliding wear tests of 6061 Al-20 vol% Al_2O_3 against SAE 52100 bearing steel. At a low loading condition it was observed that the worn surface exhibited Al_2O_3 particulates standing proud of the matrix alloy.

Increasing the normal load to a level above which the reinforcement can no longer constrain the matrix alloy from shear deformation introduces damage mechanisms to the matrix [120]. Wang and Rack [121] studied the transition wear

behaviour of SiC particulate and SiC whisker-reinforced 7091 Al alloys in pin-on-disk dry sliding against 17-4 PH stainless steel disks at a constant contact load of 13 N (0.43 MPa nominal pressure). At sliding velocities below 1.2 m/s the wear rates of unreinforced 7091 Al and the 20 vol% SiC_p and SiC_w reinforced 7091 Al MMCs were of similar magnitude. The wear debris produced by both the composites and the unreinforced alloy below 1.2 m/s was dark in color and consisted of fine, equiaxed, predominantly metallic particulates, typical of that seen in the mechanical mixing/oxidation regime for aluminum alloys [69, 79]. Wang and Rack [121] suggested that the mechanism of wear under these conditions resulted from cracking by surface fatigue to produce the small metallic debris particles.

2.11.2.2. TRANSITION TO SEVERE WEAR

The transition to severe wear, associated with an increase in wear rate by a factor of 10-100, occurs in these materials when a critical surface temperature is reached. This critical temperature is raised, and thus the transition takes place at higher pressure and sliding speed in composites than in unreinforced aluminum alloys. In work by Alpas and Zhang [122], severe wear and seizure was initiated at a load of 98 N and sliding surface bulk temperature of 145 °C in dry sliding wear of Al-7% Si (A356 Al) against SAE 52100 bearing steel. No severe wear was observed in an A356 Al-20vol% SiC composite, which was tested up to a load of 150N, at which steady-state bulk surface temperatures of approximately 200 °C were measured. A similar result has been reported for an Al₂O₃ reinforced MMC based on Al-22% Si

the transition load for the MMC in dry sliding against steel at 1 m s^{-1} was more than three times that for the unreinforced matrix [123].

The presence of SiC in these composites can cause increased wear of traditional grey cast iron piston ring materials, leading to premature losses in engine compression and increased piston slap and scuffing effects. The use of piston rings with harder surfaces (e.g., plasma nitrided high Cr steels or Cr coatings) has reduced ring wear to within the range experienced by traditional cast iron rings in sliding contact against cast iron liners. Another factor preventing the widespread use of the metal matrix composites as cylinder liner at the present time is the high manufacturing cost of these materials. In this respect thermal spray coatings present themselves as viable alternatives.

2.11.3. THERMAL SPRAY COATINGS

Thermal spray processes offer an effective way of applying a thick or thin coating to surfaces. Thermal spraying is a group of process in which finely divided metallic and non-metallic materials are deposited in a molten or semi-molten state on a prepared substrate. Traditionally, the use of thermally sprayed coatings can be divided into two areas [124]. One is to protect structural steel work against corrosion or oxidation, an example being the application of zinc or aluminum (or their alloys) to provide sacrificial or barrier coatings. The other is to provide specific surface properties to mechanical components. These include resistance to wear often combined with resistance to corrosion or chemical attack, improved electrical or thermal properties. The coating material can be metals, cermets, oxides, ceramics, or combinations of these elements

including alloys and composites. The thermal spray coatings that are being developed for automotive applications are based on low carbon steel. Therefore the raw material is cost effective. They also have the advantage of being fabricated in air and deposited on curved surfaces.

The principle of thermal spraying is that the coating material is raised to its melting point and small particles are projected on to the prepared substrate (workpiece) by a high pressure gas, where they immediately quench and form a cohesive coating. The coating material may be in wire or powder form and the heat source maybe a combustion flame, a plasma jet or an arc struck between consumable wires or between a consumable and non consumable.

One popular thermal spraying technique, which uses combustion gases as a source of heat, is the high velocity oxy-fuel (HVOF) process [125, 126]. The combustion gases used are typically propane, propylene, methane or hydrogen mixed with oxygen. The high pressures and flow of the gases result in very high gas velocities and consequently, a particles travel at many times the speed of sound. The kinetic energy of the particle is released in the form of heat as it impacts the substrate. If the flow of gases is carefully controlled to ensure maximum combustion efficiency, which results in dense coatings with low oxide content [127, 128]

Plasma spray processes use an electric arc to heat gases to peak plasma temperatures of $>25,000$ K, producing plasma jet with temperature distributions of 3,000-15,000 K. At these temperatures, the plasma gases (Ar, H₂, He, or N₂) dissociate and ionize into an equilibrium mixture of ions and electrons, as energy is pumped into them by the confined arc discharge. This plasma state gives the process its capability to melt

any material with a stable melting point. In plasma transferred wire arc (PTWA), an arc is created between consumable and non-consumable electrodes. The molten droplets are accelerated towards the substrate by plasma and propellant gases.

The twin wire arc thermal spray process employs two wires that act as consumable electrodes and the arc provides the heat energy to melt them. Plasma spraying employs a high temperature plasma as the heat source (approximately 15,000 °C), to melt the coating materials, which is usually in powder form. This method is suitable for spraying refractory materials such as oxide ceramics.

HVOF processes typically have the highest particles velocities, but its gas temperatures limit the maximum particle temperatures achievable. Wire arc spray has lower processing temperatures and produces intermediate particle velocities but, due to its low gas temperatures, may be used for thermally sensitive substrate materials. Finally, plasma spray, with its high processing temperatures, is the most flexible with respect to materials. In addition, due to its ability to operate under inert gas conditions, it is commonly chosen for consolidating environmentally reactive materials. [129].

The microstructure of the coating generated by thermal spray processes can be best described as a layered structure consisting of "splats", resulting from flattening of the molten metal droplets as they hit the surface. The particles in a molten or plastic state impact on the substrate or previously deposited layer; the next particle impacting on an already completely solidified one. Thus thermo-mechanical properties of the coating depend not only on the way particles flattened and the resulting splats solidify and cool down, but also on the thermal history of the particles layering at the same location. These facts were studied in detail by McPherson [130]. The splat size in the coatings normally

varies from a few microns to hundreds of microns. However, it is difficult to clearly distinguish the splats in most of the thermal spray coatings since they are highly irregular in shape. During the spray process, as the splats stack up, they may entrap gas and/or air in the valleys of the roughened surface or between adjacent splats, thereby forming micropores upon solidification. Oxides are present in thermal spray coatings since particles oxidize easily in the flame. Oxide content is less when spraying is done in vacuum or under an inert gas cover. Oxides are usually present as a thin layer between splats and are considered to be the weakest link in the coatings. Unmelted particles are common in plasma spraying, especially when powder metal is used as feedstock [128-131]. Thus, thermally sprayed coatings have a structure markedly different from that of cast, wrought and powder metallurgy materials.

The mechanical properties of low carbon steel coatings produced by PTWA and HVOF processes were studied by Rabiei et al. [6]. Their investigation showed that the thin oxide layers between the splats had a local mode I type interfacial fracture toughness of only 0.2-1.0 MPa \sqrt{m} and slightly higher toughness in mode III loading.

Neiser et al. [132] investigated the oxidation of wire HVOF sprayed steel during the spray process. They found that oxidation of the top surface of flattened droplets is not the dominant oxidation mechanism. They used a model and analytically predicted a thickness of a few nanometers for FeO on the splat surface as it cools. However, experimental evidence showed that the oxide layers were typically 100 times thicker than the predicted value. They concluded from the oxide distributions that most of the oxide forms before the droplet impacts the substrate.

Hackett and Settles [133] have studied turbulent mixing of HVOF thermal spray and coating oxidation. They suggested that a hot boundary layer containing significant amount of oxygen envelopes the surface. They analyzed sprayed aluminum coatings and concluded that the coating oxide content results principally from oxidation after particle impact while the still hot coating is exposed to this boundary layer and the oxidation of spray particle in flight is a minor source of oxide inclusions. Matejicek et al. [134] investigated the effects of deposition temperature on the formation and properties of plasma sprayed molybdenum coatings. They found that with increasing temperature, the nature of the splat changes from irregular and fragmented towards round-shaped. The deposits formed at higher temperatures exhibited fewer pores and interlamellar voids.

Erickson et al [135] used scratch and bend tests to evaluate the cohesive strength of alumina plasma sprayed coatings. They reported that the investigated coatings tended to fracture along thermal cracks and pores rather than splat interfaces indicating that the former were the weakest links in the coatings.

2.11.3.1. WEAR BEHAVIOUR OF FERROUS THERMAL SPRAY COATINGS

Hartfield and Tung [7] used thermal sprayed cylinder liners and piston rings on a bench top wear tester to investigate the effect of microstructure on the wear behaviour of thermal spray coatings. They described the wear behaviour of several thermal spray coatings and compared them to a grey cast iron, 390 aluminum alloy, and a Nikasil coating. They reported that splat delamination was the common wear mechanism in thermal spray coatings. This was in the form of loss of entire splats adjacent to the contact surfaces. They found that porosity had a negative effect on the wear resistance.

However, unmelted particles did not appear to have an effect on the wear resistance. It has been reported that the low fracture toughness of the interfacial oxide could cause splat delamination upon frictional contact [6,7].

McCune et. al [136] used two thermal spraying methods, namely twin wire arc process and plasma transferred wire arc processes, using graphite filled cored wires with steel and nickel sheaths to develop wear and friction resisting surfaces on light weight materials such as cast aluminum alloys. They found that the overall carbon content of the coatings could not be maintained at the levels of the prepared cores. The improvement was achieved by encapsulation of graphite with nickel and using nitrogen as a propellant to minimize loss by oxidation. The coefficient of friction and wear characteristics of the coatings were investigated under dry sliding conditions to determine the effect of the graphite as a solid lubricant, and also a lubricated condition was used to simulate the ring/bore contact. They suggested that their results showed that the tribological behaviour of the coatings were similar to that of gray cast iron.

2.12. FRICTION AND WEAR OF INTERNAL COMBUSTION ENGINE PARTS

2.12.1. PRINCIPLES OF OPERATION

In an internal combustion engine, fuel is burned within the engine, and the combustion products serve as the mechanism that converts the latent energy of the fuel into mechanical energy. Principal features of internal combustion engines consist of following: (1) the compression of air, (2) the raising of air temperature by the combustion of fuel, (3) the generation of energy from the heated air and the resultant expansion of

pressure, and (4) exhaust of the gases [137,138]. Fig. 2.2 illustrates these steps schematically. For the intake stroke, the intake valve opens and the piston moves downward, drawing air and gasoline vapour into the cylinder. During the compression stroke, the intake valve closes, the piston moves upward, and compresses the mixture. During the power stroke, the ignition system produces a spark that ignites the mixture. As it burns, high pressure is created, which pushes the piston downward. For the exhaust stroke, the exhaust valve opens and the piston moves upward, forcing the burned gases from the cylinder. The interaction of the moving parts during the engine cycle results in a complex tribosystem.

The four-stroke cycle engine (Fig. 2.2) is based on the reciprocating piston principle and spark-ignition (Otto cycle). In spark-ignition engines, the fuel and air are mixed in either the carburetor or intake port (fuel injection) prior to entry into the combustion chamber. In compression-ignition engines, the intake system supplies only air, which is compressed before the fuel is injected into the combustion chamber. Four-stroke compression-ignition and spark-ignition engines are used in most automotive applications. Depending on the cylinder arrangement, four-stroke engines can be subcategorized as in-line, V (vee), opposed piston, and radial types [137-139].

2.12.2. ENGINE TYPES AND DESIGN CONSIDERATIONS

The most common engines in modern cars are in-line four-cylinder designs for smaller cars and in-line six-cylinder, V-6, and V-8 designs for larger cars. Smaller engines, both in terms of cylinder number and size (displacement), provide improved fuel economy. The displacement of modern passenger cars ranges, on average, from 1.6 to 5.7

Liquid-cooling passages are provided around the bore of each cylinder as well as in the hot regions of the combustion chambers and exhaust ports in the cylinder head. Modern pistons are generally made from aluminum alloys, but grey iron or malleable iron pistons are used in heavy-duty diesel applications. Crankshafts are usually made from cast iron (grey iron or ductile iron) or forged steel. Similarly, connecting rods are made from cast iron (malleable iron), conventional steel forgings, or powder metallurgy steel forgings. Detachable cylinder heads contain the inlet and exhaust valves (overhead valves). Some engines employ a single exhaust and inlet valve, while other designs feature three or four valves per cylinder. Exhaust gas is directed through short passages to the exhaust collector or manifold.

Fuel and air are delivered to the cylinder head by a compact inlet manifold, usually made from aluminum. Fuel management is provided by either a carburetor or an electronic fuel injection system. In most cases, feedback from an exhaust gas combustion sensor is used to provide precise control of the fuel/air ratio and to optimize the performance of the emission control system. Electronic ignition virtually eliminates the need for periodic ignition system maintenance [137].

Fuel economy goals have also resulted in strong interest in the understanding of engine friction and wear in the design of engine components with improved tribological performance. For example, recent studies have indicated that a 6.9 kPa mean effective pressure (MEP) reduction in engine friction yields a 1 to 2% fuel economy improvement in four-cylinder automobiles [139].

2.12.3. PISTONS AND PISTON RING ASSEMBLY

Among the many moving parts in an internal combustion engine, the piston and piston ring assembly are considered to be the components that contribute the most to total engine friction and wear. It is estimated that piston ring friction amounts to approximately 50 to 70% of the friction loss of the piston assembly, and that the piston assembly is responsible for about 25% to as much as 75% of total engine friction losses [131-133]. Most pistons for automotive applications are made from aluminum alloys. The acceptance of aluminum alloy pistons by gasoline engine manufacturers can be attributed to their lightweight and high thermal conductivity. Aluminum automotive pistons generally are permanent mould castings. The alloy most commonly used for passenger car pistons is 332.0-T5, an aluminum silicon alloy that has a good combination of foundry, mechanical, and physical characteristics, including low thermal expansion. Piston alloys for heavy duty engines include 336-T551, a low expansion alloy, and 242-T571 because of its higher thermal conductivity and superior properties at elevated temperatures [140]. Piston rings are mechanical devices used for sealing pistons. They are generally split-type, self expanding metal rings. When they are placed in the grooves of the piston and provided with a lubricant, a moving seal is formed between the piston and the cylinder bore (liner).

There are two types of piston rings: i) compression rings and ii) oil-control rings. Compression rings, generally two or more, are located near the top of the piston. Compression rings have to perform two basic functions gas sealing and oil control under the most hostile conditions, being exposed to high temperatures, high gas pressures, extreme stresses, impact, corrosion, and abrasion. They must be able to operate with a

minimum of lubrication and still provide service at low wear conditions. Therefore, the basic design considerations are efficient sealing, lightweight, and good material strength and minimum wear under elevated-temperature conditions [141]. Oil rings, generally one or more, are placed below the compression rings to prevent the passage of excessive lubricating oil into the combustion chamber, yet provide adequate lubrication for the compression rings. Major factors affecting this basic function are ring-bore contact pressure, ring-bore conformability, sliding surface characteristics, and drainage for the surplus oil. Other factors that influence oil ring design include amount of oil transported, oil viscosity, and engine operating and temperature conditions.

2.12.4. ENGINE WEAR

Normally, all reciprocating engines operate with lubrication. Oil of the wrong viscosity or oil that deteriorates in service may cause wear of cylinders, cylinder liners, rings, camshafts, and valve trains. The products of combustion of the fuel contain water vapour that carries potentially corrosive gases, such as oxides of sulfur, carbon, and nitrogen. If allowed to condense on engine parts, these oxides form acids and may cause excessive corrosive wear [142].

Other mechanisms associated with piston ring and cylinder liner wear include abrasive wear. Abrasion appears to be responsible for the normal mechanical wear that occurs in the majority of liners. In liners with a long wear life, corrosion is observed, this may contribute indirectly to increased abrasion. The combined action of abrasion and corrosion appears to produce a smooth surface with well defined graphite and a pitted and etched surface which may aid the retention of lubricant on the surface [142].

Both the type and extent of wear varies down the cylinder liner wall, to improve resistance to abrasive wear it may only be necessary to protect the cylinder liner for some distance just below the top dead centre position. Also an increase in corrosion resistance would be particularly significant over the middle of the liner.

The principal factors that influence wear of piston rings are speed, temperature, load, frequency of use, dirt, corrosion, surface finish, and quantity of lubricant [139]. Speed influences ring wear largely as a function of piston travel per kilometre. Tribological design weaknesses of rings, pistons, and cylinders become more evident as speed increases. Although radial face wear is the prime consideration, wear of ring and groove sides cannot be ignored. Engine speed affects side wear because it affects the acceleration forces on the rings [129]. Although high temperature occasionally causes wear by interfering with lubrication of cylinder surfaces, low temperature is a far more frequent source of excessive piston and ring wear. As coolant temperature falls below 65 °C, cylinder and ring wear increases rapidly because of corrosion caused by condensate that carries corrosive combustion products, as shown in Fig. 5 (c). When it is impossible to maintain proper temperature, lubricating oils that contain additives are helpful [139].

Engine load affects the wear rates of both cylinders and rings principally through its influence on temperature and corrosive wear. Engines in light load service generally have a high rate of corrosive wear. High loads do not generally cause wear problems unless design weaknesses cause scuffing because of distortion or destruction of the oil film by hot spots [139].

In engines, three wear mechanisms may operate either separately or together: abrasion, corrosion and scuffing. Scuffing is the most detrimental of the wear

mechanisms. Scuffing is local damage on the contact surface and defined differently by different researchers. Some researchers defined scuffed surfaces as those that were involved in sudden failure, and others described them as having grooves, marks of transferred material, transferred particles, and other physical features [69]. A roughening of surfaces by plastic flow whether or not there is material loss or transfer was defined by Ludema [143]. In this thesis scuffing is defined as local damage to the sliding surfaces either as a result of material transfer or as a result of scratching.

Of the several known mechanisms of wear, scuffing is among the least understood. Scuffing has been observed in gears, between cams and tappets, and between piston rings and cylinders [144, 145]. In the case of piston rings and cylinder liners, scuffing resistance is a function of surface roughness of the cylinder and the materials involved [146]. The scuffed surface characteristics are similar to those observed during running-in of piston rings, there is also considerable similarity to 'severe' metallic wear.

In summary the literature survey shows that in the area of wear of thermal spray composites there is a lot of room for basic research work. The wear mechanisms need to be characterized in a better way and related to the engine scuffing characteristics.

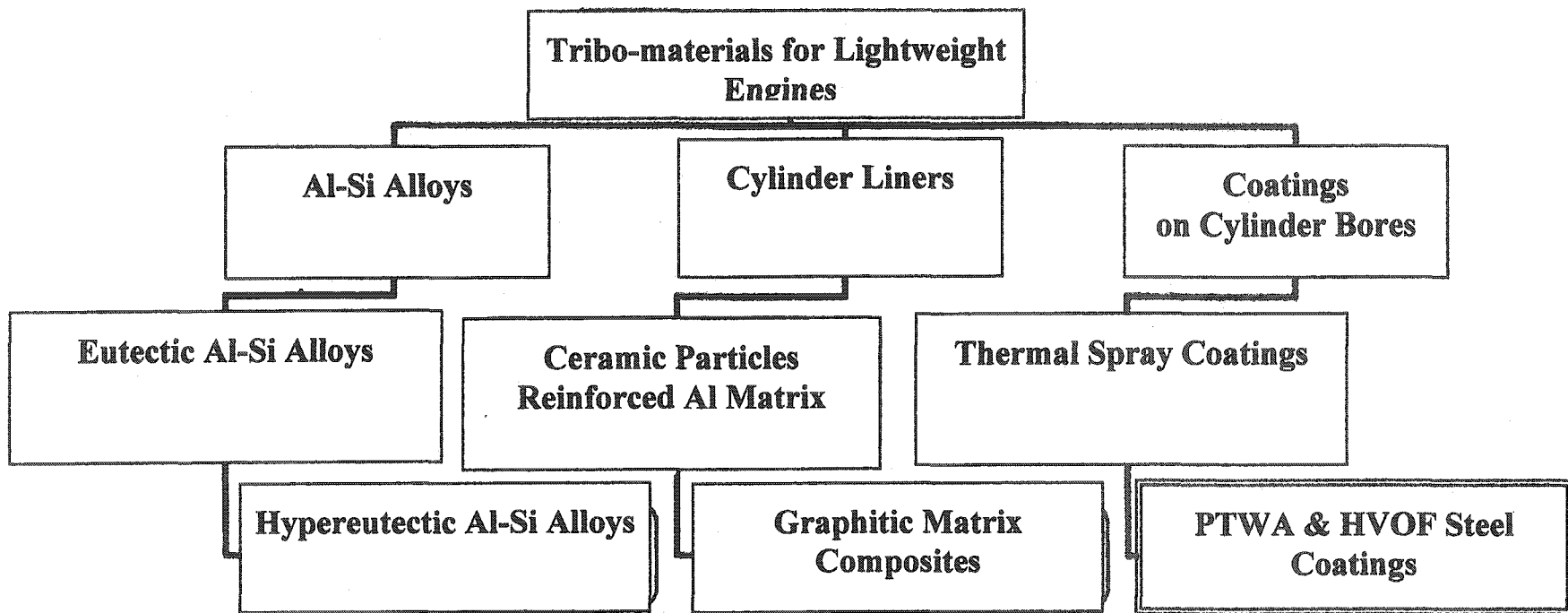


Fig. 2.1- Three groups of the lightweight materials , which are being developed as alternatives to the cast iron liners in cast aluminum engines.

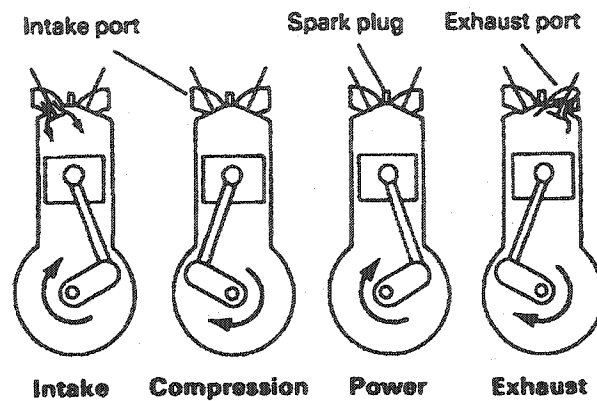


Fig. 2.2- Illustrates four strokes of internal combustion engines schematically: (1) the compression of air, (2) the raising of air temperature by the combustion of fuel, (3) the generation of energy from the heated air and the resultant expansion of pressure, and (4) exhaust of the gases.

CHAPTER III

MATERIALS AND EXPERIMENTAL METHODS

In this chapter the thermal spray deposition processes used for the production of the low carbon steel coatings are described. Two different thermal coating processes were used. These were the plasma transfer wire arc (PTWA) deposition, and the high velocity oxy-fuel (HVOF) deposition processes. Next, the sliding wear tests conducted using a pin-on-disc apparatus at different environments and loading conditions are described. The methods used in the determination of wear rates, and sliding induced contact temperatures are explained. Analytical methods that were employed to characterize microstructures, morphologies and compositions of the worn surfaces and the loose debris are also given. These methods include scanning electron microscopy (SEM) with energy dispersive spectroscopy (EDS), X-ray diffractometry (XRD) with Rietvelt refinement method, and optical surface profilometry. In the last part of the chapter experimental techniques used to examine the two worn (scuffed) engines that were coated with the thermal spray coatings are given.

3.1.1. COATING DEPOSITION PROCESSES

3.1.1. FABRICATION OF PLASMA TRANSFER WIRE ARC LOW CARBON STEEL COATINGS (PTWA 1020 COATINGS)

PTWA samples were deposited on 319 aluminum alloy substrates with the following composition in weight percent: 5.5-6.0 Si, 1 Fe, 3.0-4.0 Cu, 0.5 Mn, 0.1 Mg, 0.35 Ni, 1 Zn, 0.25 Ti, and the balance Al. The stock for the 319 Al substrates was cast

using a sand casting process in the General Motors Research and Development Foundry (Warren, Michigan) as 25.4 mm chill blocks (in order to have comparable dendrite size with that in the 319 aluminum alloy used in the engine cylinder). In the casting process nitrogen gas (N_2) was injected in order to degas molten aluminum. The aluminum blocks were cut in the form of square coupons with dimension 25mm \times 25mm \times 5mm, using a wire electric discharge machine (EDM).

The substrate surface was roughened to an average surface roughness of $R_a = 10 \pm 2$ μm , with an 80 grit sand blaster operating at 0.62 MPa (90 Psi) prior to the deposition. The purpose of this operation was to provide a mechanical interlock for the coating to adhere to the substrate.

The coatings were deposited using a commercial plasma transfer wire arc (PTWA) gun manufactured by Flame Spray Industries (New York). A photograph of the PTWA set up used to coat the inner surfaces of the cylinder bores is shown in Fig. 3.1. This set up is located at the General Motors Research and Development Centre, Warren, MI. In this work, five 319 Al coupons were fixed on a holder, which was then placed in the deposition chamber. The wire feed stock for the PTWA gun was mild steel with a nominal SAE 1020 composition. The wire was coated with copper to prevent oxidation. The gun was operated with a distance to the substrate of 45 mm. The plasma plume included molten iron droplets of 100-300 μm diameter, traveling at a nominal velocity of 100 m/s, which was measured using a thermal spray imaging system manufactured by Control Vision Company. The process parameters are given in Table 3.1. The coating was built up by translating the gun over the coupon surface multiple times to produce

coatings that were 250 ± 10 microns thick. These coatings were designated as PTWA EM-12K by General Motors. They are referred as PTWA 1020 in this thesis.

The surface roughness (R_a) of the as-deposited coatings was measured using a stylus type surface profilometer (Mitutoya MST-301). The average roughness of ten different samples was $18 \pm 2 \mu\text{m}$.

Wire Composition	Wire Diameter (mm)	Wire Feed Rate (kg/hr)	Plasma Gas	Spray Distance (mm)	Propellant
SAE 1020 Steel (0.2 % C)	1.5	3.2	65% Ar 35% H ₂	45	Air

Table 3.1- The plasma transfer wire arc (PTWA) processes parameters.

3.1.2. FABRICATION OF HIGH VELOCITY OXYGEN FUEL (HVOF) LOW CARBON STEEL COATINGS

HVOF process was used to produce two types of coatings. One of these was the coatings produced with the base SAE 1020 feed stock. The second type of HVOF coatings had 2.5 wt% Al added in the base SAE 1020 composition.

3.1.2.1. HVOF 1020 COATINGS

Samples for the substrates for HVOF 1020 type of coatings were taken from extruded cylinders that were made of 6061 Al alloy with the following composition in

weight percent 0.4-0.8 Si, 0.7 Fe, 0.15-0.40 Cu, 0.15 Mn, 0.18-1.2 Mg, 0.04-0.35 Cr, 0.25 Zn, 0.15 Ti, and the balance Al. Prior to thermal spraying using a high velocity oxy-fuel (HVOF) gun, the cylinder bores were cut with an electro-discharge machining process (EDM). The surfaces were then roughened using a high-pressure water jet. During the deposition process, the HVOF gun traveled along the length of the bore as it rotated inside the cylinder. The rotating gun on the surface of cylinder bores made a single pass to produce coatings with a thickness of $400 \pm 10 \mu\text{m}$. Methane was used as the fuel gas. The wire, with a nominal SAE 1020 composition, was used at a rate of 7.7 kg/hr in an oxidizing flame. The jet of material sprayed from the gun included molten Fe droplets with a nominal diameter of 25-100 μm , and a nominal velocity of 200 m/s. The HVOF process parameters are given in Table 3.2. These coatings were designated as HVOF EM-12K by General Motors. They are referred as HVOF 1020 coatings in this thesis.

Wire Composition	Wire Diameter (mm)	Wire Feed Rate (kg/hr)	Fuel Gas	Spray Distance (mm)	Propellant
SAE 1020 Steel (0.2 % C) & 1020+2.5%Al	3	7.7	Methane	45	Air

Table 3.2- The high velocity oxy-fuel (HVOF) processes parameters.

3.1.2.2. HVOF 1020-2.5% Al COATINGS

The deposition process of this type of coatings are the same as those of HVOF 1020 steel wire based coatings with the exception that the wire had a 2.5 wt% Al addition, which was introduced with the purpose of reducing the oxide content of the coating. These coatings were designated as HVOF HAR-4001 by General Motors. They are referred as HVOF 1020-2.5% Al coatings in this thesis.

The average surface roughness of the both types of the HVOF coatings (with and without Al) after deposition were $30 \pm 2 \mu\text{m}$.

3.2. LABORATORY WEAR TESTING PROCEDURES

3.2.1. DESCRIPTION OF THE PIN ON DISC TRIBOMETER

The wear tests were performed using a pin-on-disc sliding wear apparatus. Fig. 3.2.a shows the general view of the pin on disc set-up. This tribometer was designed and manufactured at the University of Windsor.

The apparatus comprised a variable speed rotating shaft arrangement to which a stainless steel sample holder was attached. A vertical loading arm, which was attached to the pin counterface at its bottom end, was lowered on to the rotating samples to produce a circular wear track of 16 mm average diameter. The load was applied using dead weight placed on a pan located on the upper end of the vertical loading arm. The pin contact geometry used was a flat-on-flat configuration. An enlarged view of the sample holder and the pin are shown in Fig. 3.2.b.

A special sample holder was designed to ensure that the contact surface of the test sample was parallel to the surface of the counterface pin. This was achieved by placing a self-adjusting sample holder where the samples were placed on a set of six small ball bearings and clamped in such a way that the top surface was always flush with the contact surface of the counterface.

A schematic drawing identifying the main parts of the set up is shown in Fig. 3.3. The test speed and the duration of the test were controlled by a PC driven motor. The control system consisted of a Lab-View control software (Version 5.0 Graphical Programming for Instrumentation software).

An enclosure around the machine equipped with a humidifier and dehumidifier system was used in order to run tests under controlled atmospheric conditions. Details of the environmentally controlled tests are given in Section 4.1.8.

3.2.2. SAMPLE PREPARATION FOR PIN ON DISC TESTS AND MEASUREMENT OF WEAR RATES

To eliminate the initial high wear rate normally caused by the coating roughness, and to ensure that the sample surfaces were flat, an automatic polishing machine was used to polish the wear test sample surfaces. As a result of polishing the average surface roughness was decreased to $0.38 \pm 0.08 \mu\text{m}$ with the exception of some small areas, where the coatings contained large amounts of porosity.

Wear tests were performed at sliding speeds between 0.2 and 2.5 m/s, and at constant loads between 5 and 75 N. The wear tests were normally run to a constant

sliding distance of 5×10^3 m. Prior to wear tests both the pin and the coated samples were ultrasonically cleaned in acetone, left for 24 hours under vacuum and weighed to ± 0.0001 g using an electronic balance. After each test the specimens were cleaned of loose debris and weighed to determine the amount of mass change during the test. Wear rates of both the coatings and the pins were obtained by dividing mass loss by the total sliding distance.

3.2.3. DESCRIPTION OF COUNTERFACE MATERIAL

The material for the counterface for the wear tests was AISI M2 type high-speed steel with the following composition in weight percent: 0.8 C, 4.0 Cr, 5.0 Mo, 6.0 W, 2.0 V, and the balance Fe. The dimensions of the pin were as follows: Diameter: 5.0 mm, length: 30 mm. The pins were cut by EDM, and the contact surfaces were then polished using 600 grid SiC paper. The roughness of the polished surfaces was 0.38 ± 0.08 μm , the same as that of the coating.

3.2.4. SLIDING CONTACT TEMPERATURE MEASUREMENTS

A 0.5 mm diameter K-type (Chromel-Alumel) ungrounded thermocouple probe was placed in a 0.6 mm diameter hole in the pin, which was drilled with EDM at about 200 μm from the pin contact surface. This was used to monitor the changes in bulk surface temperature (T_b) generated by frictional heating at the sliding interface as a function of sliding distance at various constant load and sliding speed levels. The Lab-view software was used to collect and store the temperature data.

3.2.5. MEASUREMENTS OF COEFFICIENT OF FRICTION

The tangential force generated during sliding contact was measured using a bending type load cell from Omega Instruments (max. load 25 lbs). The load cell was attached to the motor that rotates the sample through a shaft. The friction data was recorded continuously during the sliding tests via a software interface (Lab-View).

3.2.6. ENVIRONMENTALLY CONTROLLED WEAR TESTS

3.2.6.1. WEAR TESTS UNDER CONTROLLED HUMIDITY

A controlled environment chamber was built around the pin on disc tribometer. The dimensions of the chamber were 79 cm x 64 cm. The chamber was built of 0.5 cm thick plexiglass and equipped with a humidifier and a dehumidifier that were controlled with a humidity controller (Electro-Tech Systems). With this equipment the relative humidity in the chamber could be controlled from 0 to 99 percent. The controller measured and controlled the humidity level in the environmental chamber with an accuracy of $\pm 2\%$. The humidifier set up included an ultrasonic humidifier and 10 cm circular fan to circulate the chamber environment. The dehumidifier consisted of a vacuum-pressure pump and desiccator kit with calcium sulphate as drying medium.

3.2.6.2. WEAR TESTS UNDER ARGON ATMOSPHERE

The purpose of these experiments was to investigate the wear mechanisms that precluded oxidational wear. For this reason, a certain number of wear tests have been performed under an argon atmosphere. The environmental chamber around the pin-on-

disc tribometer was purged with compressed argon gas in order to eliminate oxidation during sliding.

3.2.7. MICROHARDNESS MEASUREMENTS

Microhardness tests were done on the cross-sections of the coatings as well as on the flat sections of the worn surfaces to measure the hardness of coating on a microscopic scale. A Vickers diamond indenter was impressed into the material using constant loads between 15 and 1000 gf. A Buehler Microhardness Tester was used to measure the hardness of the coatings and the worn surfaces. The indentations were made using a square-based pyramid indenter (Vickers hardness scale).

3.3. EXAMINATION OF SAMPLES WORN UNDER THE LABORATORY CONDITIONS

3.3.1. SCANNING ELECTRON MICROSCOPY

A scanning electron microscope (JEOL 5800 LV SEM) equipped with an energy dispersive spectroscope (EDS) was used to characterize the morphology of the plan view and cross sectional views of the worn surfaces, and to examine the wear debris particles. The cross-sectional samples for the SEM investigations were prepared as described in the next paragraph.

3.3.1.1. CROSS-SECTIONAL SEM METALLOGRAPHY

Worn samples for the SEM investigations were sectioned using a low-speed circular diamond saw. The sectioning was done as shown in Fig. 3.4 such that the metallographic cross-section to be examined was parallel to the sliding direction. The cutting was initiated at the free surface of the coating to reduce the possibility of separation from the substrate for metallographic preparation of the cross-sections. A fast curing epoxy resin mixed with a hardener was used as the mounting media. The surface of the mounted samples was ground with 180-grit SiC paper until the marks caused by the diamond saw were removed. The grinding operation was continued using 240, 400, 600, 1200 and 2500 grit SiC papers. To avoid oxidation of the steel coatings anhydrous ethanol was used as lubricant after the 400-grit stage of grinding. Samples were then polished on polishing cloths impregnated with 3.0, 1.0, 0.25 and 0.1 μm diamond paste. The samples were ultrasonically cleaned in methanol after each stage of polishing.

3.3.1.2. EXAMINATION OF LOOSE DEBRIS PARTICLES

A low accelerating voltage of 7-10 kV was used to examine the debris particles in the SEM. This was done in order to prevent charging of the debris particles that usually comprised of non-conductive oxides.

3.3.2. COMPOSITIONAL ANALYSES BY X-RAY DIFFRACTION METHOD

A Rigaku DMAX-1200X-ray diffraction (XRD) machine, equipped with Cu K α tube located at the University of Windsor, and a Siemens D-500 XRD machine equipped

with Cu K α tube located at the General Motors Research and Development Centre were used to characterize the composition of the wear debris particles. The quantitative phase analyses of the oxides formed were done using the Rietveld refinement technique. The Rietveld refinement method was used because in the conventional X-ray analysis method the iron oxide peaks were grossly overlapped. In principle, the Rietveld method provides an effective way to separate these overlapping XRD peaks, thereby allowing an accurate determination of the structure. In this method the expected XRD pattern, including overlapped peaks of various shapes, is calculated from a model involving the crystallite size and strain characteristics, absorption and various geometric features, and instrumental profiles. The calculated and observed patterns are then compared point by point and the parameters in the model are adjusted (by a computer program) to give the best fit, in a least-squares sense, of the calculated and observed patterns. In this way, quantitative phase analyses use of all of the information that can be extracted from an XRD pattern. Detailed information on the Rietveld method can be found in references [147-149].

3.3.3. WYKO AUTOMATED INTERFEROMETER

The surface morphologies of the wear tracks were quantified using an optical surface profilometer. For this purpose a WYKO surface profiler system (WYKO NT 8000 System) was used. This is a non-contact optical profiler that uses two technologies to measure a wide range of surface heights. The phase-shifting interferometry (PSI) mode allows measurement of smooth surfaces. In the PSI mode, the maximum height resolved between adjacent pixels is 160 nm. The vertical-scanning interferometry (VSI) mode

allows measurement of rough surfaces and steps. In the VSI mode, the greatest vertical distance is up to 500 μm . The basic interferometric principles are similar in both techniques and can be summarized as follows: Light reflected from a reference mirror combines with light reflected from a sample to produce interference fringes, the best-contrast fringe occurs at best focus. In the VSI mode, the white-light source is not filtered, and the system measures the degree of fringe modulation, or coherence, instead of the phase of the interference fringes. A beam splitter reflects half of the incident beam to the reference surface. The beams reflected from the sample and reference surface recombine at the beam splitter to form interference fringes. In this work, the VSI mode has been used to identify morphologies of the asperities on contacting surfaces, and the debris that is produced during sliding contact.

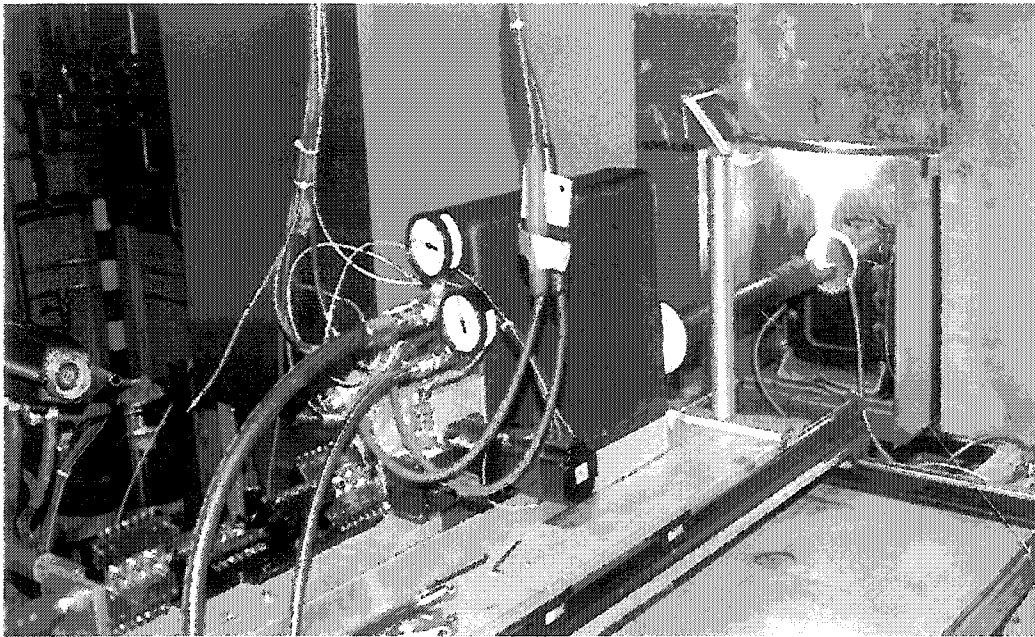


Fig. 3.1- The PTWA set up used to coat inner surfaces of the cylinder bores. This set up is located at the General Motors Research and Development Centre, Warren, MI.

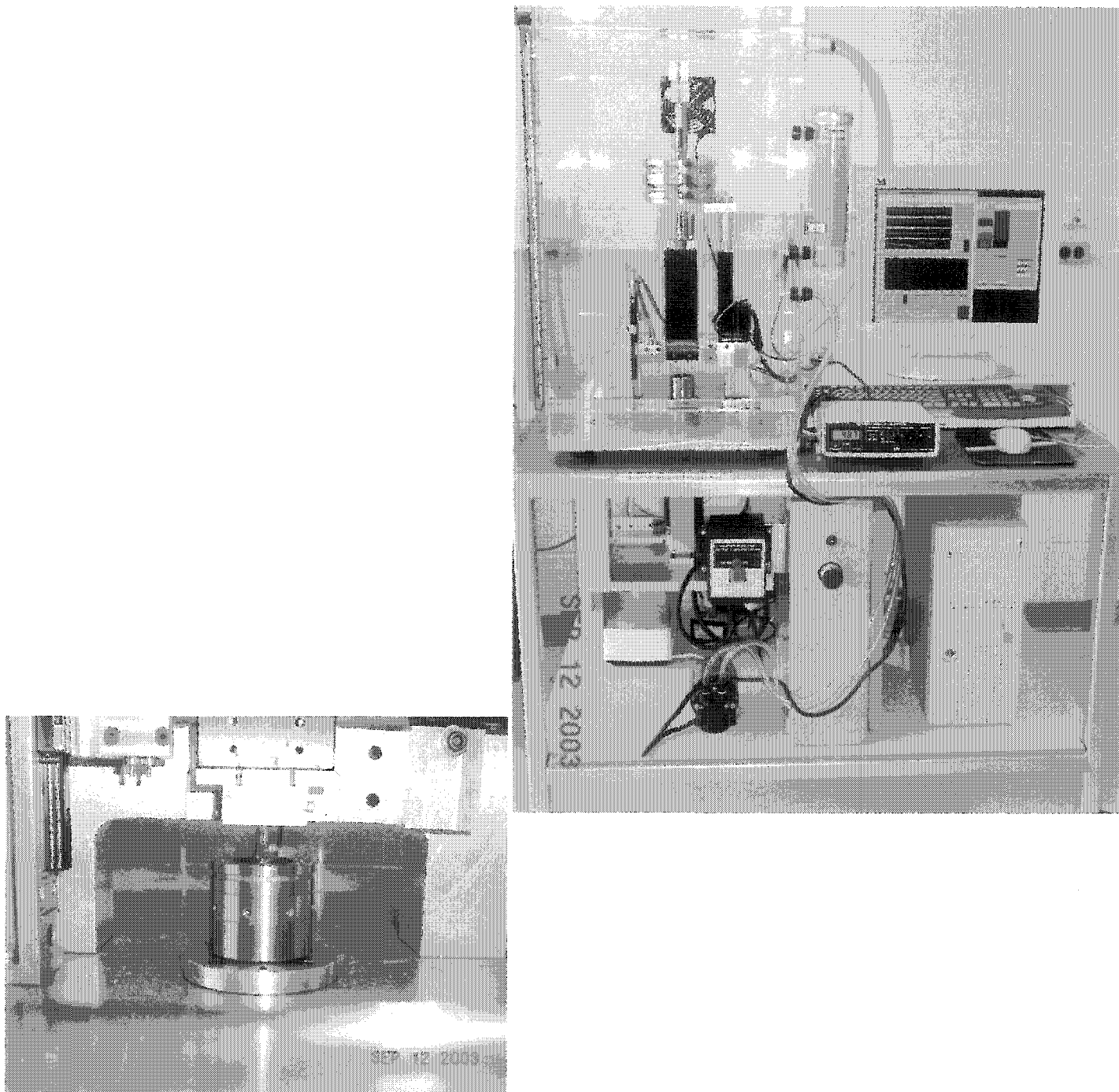


Fig. 3.2- Photograph showing a) The general view of the pin on disc tribometer. b) The sample holder and the pin.

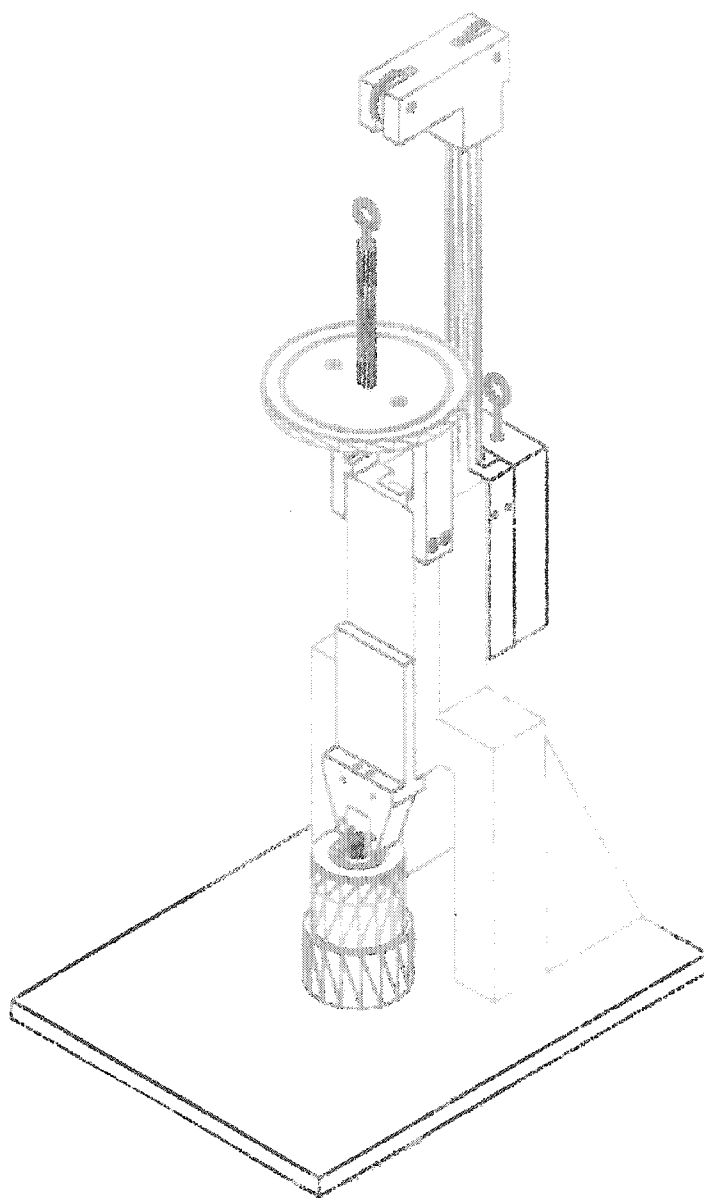


Fig. 3.3- Schematic drawing showing the main components of the pin-on-disc machine.

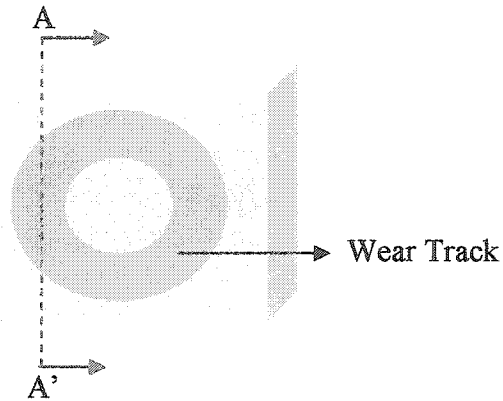


Fig. 3.4— This figure schematically shows the way that the worn sample was sectioned (AA'). This method provided a good way for the examination of the subsurface damage parallel to the sliding direction.

CHAPTER IV

RESULTS

COATING MICROSTRUCTURES, PIN-ON-DISC WEAR TESTS, AND CHARACTERIZATION OF WORN SURFACES

In this chapter, the results of the wear and friction tests performed on the PTWA 1020, HVOF 1020 and HVOF 1020-2.5% Al thermal spray coatings are presented. In addition, microstructural characteristics of the coatings that are used in the interpretation of the tribological data are described.

All three coatings had layered microstructures consisting of steel splats and oxide phases. The oxide phase was mainly in the form of thin veins (stringers) between the iron splats. Micropores that were formed during the thermal spraying process were also found to exist, mostly between the splats.

Wear tests were performed using a pin-on-disc type wear tester with a load range of 5-75 N and a sliding speed range of 0.2-2.5 m/s against tool steel pin. The majority of the tests were done in a dry air atmosphere. As will be shown later in this chapter, the wear rates of all the three types of coatings were high at low speeds and high loads. The wear rates of PTWA 1020 and HVOF 1020-2.5% Al coatings decreased by increasing the sliding speed. However, the HVOF 1020 coating showed a different behaviour; the coating showed high wear rates at high sliding speeds. The current chapter also includes the results of the microhardness tests done before and after the wear tests. The results of the wear tests done on the PTWA 1020 coatings in relative humidity levels between 10

and 99% are also presented. The worn surfaces were characterized and the compositional, as well as the morphological changes that took place during wear were presented following the results on the friction and wear measurements.

4.1. PLASMA TRANSFERRED WIRE ARC COATINGS (PTWA 1020)

4.1.1. MICROSTRUCTURE, COMPOSITION AND PROPERTIES

A typical SEM picture of the surface of the PTWA 1020 in the as-deposited condition is shown in Fig. 4.1. As shown in this secondary electron SEM image, the surface became rough after the thermal deposition process. The unmolten steel droplets can be seen on the surface as spherical protrusions, with an average diameter of 20-40 μm . There are also large and relatively featureless areas (mostly on the upper side of the figure), which correspond to the molten material. The micrograph also shows the existence of the micropores of about 10 μm in diameter in the microstructure. Micropores were formed when gas or air bubbles were trapped between the splats as they stacked up during the deposition process. The volume fraction and the size of the pores were analysed using an image analysis system and are presented in Table 4.1.

According to the WYKO optical profilometry measurements taken from the as-deposited condition of the coating surface, the average roughness (R_a) was $18 \pm 2 \mu\text{m}$.

Fig. 4.2 is a back-scattered SEM micrograph of the top surface of the same PTWA 1020 coating after polishing it to an average surface roughness, R_a of 0.1 μm . The circular features are the remnants of the unmolten droplets. The network of the thin oxide

Coating Thickness (μm)	250 ± 10
Coating Density (g/cm^3)	7.4 ± 0.1
Vickers Hardness of Coating (kg/mm^2)	310 ± 30
Volume Fraction of FeO	0.20 ± 0.02
Thickness of FeO Phase (μm)	0.2-5.0
Volume Fraction of Pores	0.05 ± 0.01
Diameter of Pores (μm)	3-18
Thickness of Steel Splats (μm)	10-20

Table 4.1- Microstructural characteristics of the PTWA 1020 coatings. Note that the volume fraction of constituents was computed using an image analysis system and Vickers hardness was measured using a load of 25 g.

vein structure that was formed between the steel splats can be seen clearly. The average width of the steel splats, as measured in the top view varies between 10 to 100 μm .

Fig. 4.3 shows the general cross-sectional view of the 319Al alloy that was used as the substrate on which the PTWA 1020 coating deposited. The interface of the coating and the substrate is rough ($R_a = 10 \pm 2 \mu\text{m}$) as a result of the sand blasting process described in Section 3.1.1. In this section, it was indicated that the surface roughening by sand blasting served to provide a mechanical adhesion and interlocking between the coating and the substrate. The thickness of the coating estimated from this figure is about $250 \pm 30 \mu\text{m}$.

Fig. 4.4.a is a back-scattered SEM micrograph of a polished cross-section of the PTWA 1020 coating (unetched). This micrograph shows the presence of two different phases in the microstructure. The energy dispersive spectroscopy (EDS) analysis of the light grey area shows the existence of only elemental Fe. The EDS spectrum of this area is shown in Fig. 4.4.b. The iron splats are separated by thin veins that are dark grey in colour. The EDS analysis from the veins shows the presence of Fe and O elements (Fig. 4.4.c). The X-ray diffraction spectrum of the coating indicates that the oxide corresponds to the peaks that belong to FeO type iron oxide. The diffraction pattern of the coating can be seen in Fig. 4.4.d, where α -Fe and FeO peaks are labelled. No other type of oxide could be detected.

The main microstructural properties of the PTWA 1020 coating, including the volume fraction FeO phase, the thicknesses of the oxide layers and iron splats, and the average pore diameter are listed in Table 4.1.

4.1.2. PIN-ON-DISC WEAR TEST RESULTS: WEAR RATES UNDER DRY ATMOSPHERE

The variation of wear rates of the PTWA 1020 coating as a function of sliding speed determined at several constant load levels of 5 N, 10 N, 25 N, 50 N and 75 N is shown in Fig. 4.5. As explained in Section 3.2.1., these tests were conducted using a pin-on-disc type wear machine under a dry air atmosphere with relative humidity, RH = 7-10%. The wear rates of the PTWA 1020 coatings were obtained by dividing mass loss after the wear test by the total sliding distance. Each point on the plots shown in Fig. 4.5 represents wear rate data for the coating worn at a given sliding speed and load. At 10 N

load and 0.5 m/s sliding speed, the coating wear rate was 5.80×10^{-6} g/m. The wear rates decreased to 1.50×10^{-6} g/m as the speed increased to 2.5 m/s. At 50 N load, for the tests performed at a low speed of 0.2 m/s, the measured wear rate was 30.52×10^{-6} g/m. At this load level, by increasing the sliding speed to 2.5 m/s, the wear rate decreased significantly to 7.52×10^{-6} g/m.

In summary, the wear rates of the PTWA 1020 decreased by increasing sliding speed. This was particularly evident at high loads of 50 N and 75 N. The decrease in the wear rate with speed indicates that the PTWA 1020 coatings were subjected to a transition at speeds approximately above 1.0 m/s. At sliding speeds more than 1.0 m/s, the wear behaviour of the coating was independent of the sliding speed, and remained almost constant at all the applied loads.

The measured weight loss was converted to volume using the density of the coating. The volumetric wear of the coating for different loads versus sliding speeds is presented in Fig. 4.6. As an example of typical volumetric wear rate values, for the tests performed at 50 N load and a sliding speed of 0.2 m/s, the measured wear rate was 4.12×10^{-3} mm³/m; by increasing the sliding speed to 2.5 m/s, the wear rate decreased to 1.02×10^{-3} mm³/m. The purpose of presenting the wear data in terms of volumetric wear was to compare the wear rates of the PTWA 1020 coatings with those of the two other coatings with different densities.

4.1.3. SEM OBSERVATIONS OF WORN SURFACES

4.1.3.1. SEM OBSERVATIONS OF THE SAMPLES TESTED AT LOW SPEEDS

The back-scattered SEM micrograph of the worn surface of the coating tested at 10 N load and 0.5 m/s sliding speed after 5000 m sliding distance is shown in Fig. 4.7.a. The SEM micrograph shows two different regions. The EDS analysis of the dark grey areas, which is shown in Fig. 4.7.b, indicates the formation of the oxygen rich patches during the sliding. The EDS analysis of the light grey area, which is given in Fig. 4.7.c, reveals the dominant presence of Fe. The light grey regions are identified as the iron splats. The micrograph shows that the top surfaces of the iron splats were subjected to plastic deformation and extruded in the direction parallel to the sliding direction. The surface also exhibits microscratches that have a typical width of a few micrometers. The oxide rich layers were formed within the microscratches on the contact area. These oxide rich layers covered about 20% of the total area of the worn surface. At this loading condition, the oxide rich patches on the contact surfaces had a powdery and porous appearance. The morphology of the oxide patches can be seen more clearly in Fig. 4.8, where they are tilted at an angle of 15° to the worn surface to emphasize the morphological details.

The wear debris generated at 10 N load and 0.5 m/s sliding speed was orange in colour to the naked eye. The secondary electron SEM image of the debris collected from the test performed under 10 N load and 0.5 m/s speed (Fig. 4.9) showed very fine particles agglomerated to form oxide aggregates of 2-4 µm thick. The XRD analyses of the debris indicated that Fe₂O₃ was the predominant constituent of the wear debris. Details on the X-ray diffraction analyses of the debris will be presented in Section 4.1.4.

Fig. 4.10.a is the back-scattered SEM micrograph of the worn surface of a sample tested at 75 N load and 0.5 m/s sliding speed. Once again, the micrograph shows two different areas that are light and dark grey in colour contrast. The EDS analyses from the light grey areas showed the presence of elemental Fe, indicating that they are steel splats. The top surfaces of the steel splats were flattened as a result of plastic deformation during wear, and extruded in the sliding direction. However, the mechanical damage was much more severe than those tested at 10 N load at the same low sliding speed. An important feature of the surface morphology is the presence of surface cracks mostly at the tip of the flattened steel splats. These cracks were formed as a result of the fracture of the edges of the severely deformed steel splats. The fractured edges of the steel splats are marked with the arrows on the micrograph in Fig. 4.10.a. The EDS of the dark grey regions indicated that the constituents in this area included iron and oxygen. About 30 % of the wear tracks were covered by the oxide rich films. Attempts were made to obtain the XRD spectra directly from selected areas on the wear tracks in this and other samples, but the oxide coverage was small, and the surface layers were too thin to resolve reliable information about the state of oxidation of these layers. However, the XRD spectra of the debris particles detached from the worn surfaces provided information about the oxides formed during sliding wear. This data is presented in Section 4.1.4. Fig. 4.10.b is a higher magnification micrograph, which shows the severe plastic deformation on the surface and fracture at the tip of the splats. The micrograph was taken from the worn surface of the coating tested at 50 N load and 0.2 m/s speed.

The wear debris collected under these conditions was magnetic, and dark brown in colour. The secondary electron SEM image from the debris gathered from the test

conducted at 50 N and 0.5 m/s is shown in Fig. 4.11. This figure illustrates plate-like fragments mixed with small powdery particles. The thickness of the plate-like debris was about 5-20 μm with an average width of 50- 200 μm . The XRD results of the wear debris showed the presence of ferrite, Fe_2O_3 , Fe_3O_4 , and FeO (see Section 4.1.4). It is important to emphasize that there was also a significant amount of metallic ferrite in the debris. The high magnification SEM image illustrating the morphology of the plate-like debris is shown in Fig. 4.11.b.

In summary, the surface of the coatings, which exhibited the highest wear, rates under test conditions of high loads (50 N and 75 N) and low speeds were characterized by relatively thin, oxide-rich films. However, the most important aspect of the worn surfaces was the presence of highly deformed steel splats with fractured tips.

4.1.3.2. SEM OBSERVATION OF THE SAMPLES TESTED AT HIGH SPEEDS

The back-scattered SEM micrograph of the sliding surface of the coating, worn at 50 N and 2.5 m/s is shown in Fig. 4.12. The EDS analyses showed the presence of Fe and O in the dark grey regions, and only the Fe peaks in the light grey areas. The micrograph shows evidence of deformation mostly in the form of surface grooving of both the oxide-rich layers and the iron splats. On the other hand, the steel splats although severely deformed, appeared to be much less susceptible to fracture compared to the coatings tested at the same load but at lower speeds (see Fig. 4.10). The worn surfaces of the samples tested at 50 N and 2.5 m/s were significantly different from the sliding surface of the coating tested at 50 N and 0.5 m/s, this was also the case in terms of the area fraction of the iron-oxide-rich layers on the worn surfaces. About 70% of the wear track of the

samples tested at high loads and high speeds were covered by relatively thick oxide rich layers, whose average thicknesses varied between 1-3 μm . In contrast, the oxide-rich layers on the high load and low speed samples were thinner (less than 1 μm) and discontinuous. The micrograph in Fig. 4.12 is selected in order to illustrate the deformation pattern, and to demonstrate that the area fraction of the oxide-rich layers was less than the average coverage. Fig. 4.13 is a back-scattered SEM image from worn surfaces of the samples tested at 50 N and 2.5 m/s that shows the section of the wear track that was almost totally covered by an oxide rich film. This micrograph also shows the spallation of the oxide film. A low-magnification SEM image that shows another example of the spallation of the oxide layers is given in Fig. 4.14. Therefore, formation and removal of the oxide layers, rather than the surface deformation and fracture, controls the wear rates under these loading conditions.

The wear debris collected under these conditions was magnetic and black in colour. The secondary electron SEM image from the debris gathered from the test performed at 75 N and 2.5 m/s is shown in Fig. 4.15. This figure illustrates plate-like iron oxide with a thickness of about 1-3 μm with an average width of 50-200 μm .

Samples tested at high velocities but low loads show some differences compared to those tested at high loads. For example, the percentage of the area covered by the oxide was smaller in comparison: Approximately, 50% of the worn surfaces of the samples tested at low loads and high speeds (e.g., tested at 10 N and 2.5 m/s) were covered by the oxide rich layers as shown in Fig. 4.16. These layers typically extended over the top of the steel splats, rather than being located in the grooves. Another difference was in the thickness of the layers, which was less than 1 μm in this region. On the other hand, the

SEM evidence for the steel splat fracture was very rare in this region as in the high load tests at the same as the high speed conditions. This could be seen by comparing Figs. 4.12 and 4.13 with Fig. 4.10.

4.1.4. X-RAY DIFFRACTION OF LOOSE DEBRIS PARTICLES

The XRD spectra of the loose wear debris obtained from samples tested at three different test conditions are shown in Figs. 4.17-4.19. Fig. 4.17 shows the XRD pattern of debris taken from samples tested at low loads and speeds, namely at 10 N and 0.5 m/s. Fig. 4.18 shows the XRD pattern for high load and low speed tests, i.e., at 50 N and 0.5 m/s. The high speed and high load XRD spectra is represented in Fig. 4.19 for samples tested at 50 N, 2 m/s. (Refer to Fig. 4.5 for the corresponding wear rates). XRD tests could not be done on the samples tested at high speeds and low loads because of the small amount of debris produced during wear under these condition. Although some oxide peaks overlapped, each oxide had a unique set of peaks that did not overlap with the others, making it possible to unequivocally identify each type of oxide in the debris.

Quantitative phase analyses of the oxides generated during wear at different testing conditions were done using the Rietveld analysis as described in Section 3.3.2. The results obtained from the Rietveld refinement of the spectra of Figs. 4.17-4.19 are summarized in Table 4.2. These samples exhibited different ranges of wear rates and were expected to follow different wear mechanisms. The XRD spectrum of the debris at 10 N load and 0.5 m/s speed, representing low load and low speed conditions, shows the peaks for hematite (Fe_2O_3) and a few small peaks of ferrite (Fig. 4.17). The quantitative phase analysis shown in Table 4.2 confirms that at low loading and speed conditions,

Fe_2O_3 was the predominant constituent (> 99.9 %) of the wear debris. As shown in Table 4.2, by increasing the load to 50 N at the same speed (0.5 m/s), the proportion of Fe_2O_3 in the debris was decreased. The XRD spectrum in Fig. 4.18 shows that at high load and low speed conditions, the debris consisted of a mixture of three types of iron oxides: Fe_2O_3 , Fe_3O_4 , and FeO . It is important to emphasize that there was also a significant amount of metallic ferrite in the debris, due to the fracture of the splat tips. Referring to Fig. 4.19 and Table 4.2, by increasing the sliding speed from 0.5 m/s to 2 m/s at a high load (50 N), the constituents of the debris remained the same, consisting of ferrite and three types of iron oxides, namely Fe_2O_3 , Fe_3O_4 , and FeO . However, the relative amounts of the oxide phases changed slightly. It was also noted that the percentage of ferrite in the debris was considerably smaller.

Phase	10N, 0.5m/s	50N, 0.5m/s	50N, 2 m/s
Ferrite (Fe)	0.02	15.38	6.70
Hematite (Fe_2O_3)	99.97	41.43	60.31
Magnetite (Fe_3O_4)	0.01	20.30	22.13
Wuestite (FeO)	0.00	22.89	10.85

Table 4.2- Quantitative XRD phase analysis of the debris (in weight fraction) at three different loading conditions.

4.1.5. SEM OBSERVATIONS OF THE CROSS-SECTION UNDER THE WORN SURFACE

The wear tracks of the PTWA 1020 samples that showed mechanical wear (deformation and splat tip fracture) at high loads and speeds were sectioned in order to observe the extent of subsurface damage. Figs. 4.19 and 4.20 are the back-scattered SEM micrographs of the cross-sections of the worn tracks of the PTWA 1020 coating tested at 50 N and 0.5 m/s where the highest wear rates were measured. Fig. 4.20 shows that the splats adjacent to the contact surfaces were deformed during wear and elongated in the sliding direction. Fig. 4.21 shows another area beneath the worn surface where steel splats adjacent to the worn surface delaminated along the FeO veins within the coating, causing the removal of entire individual splats as a whole. However, the removal of entire splats was not a commonly observed wear mechanism. Normally, only the tip of the severely deformed splats was fractured (Fig. 4.10). This mechanism will be discussed in detail in Section 5.1.1.

4.1.6. MEASUREMENTS OF TEMPERATURE AND COEFFICIENTS OF FRICTION

The contact surface temperature of the coating increased when both the sliding velocity and the applied load were increased. Tests were done to study the increase of the surface temperature at a constant load of (50 N), and the temperature was measured using a thermocouple embedded under the surface of the samples tested at different sliding velocities. The coefficients of friction were determined simultaneously. At any given loading condition, the surface temperature increased rapidly with the sliding distance at

the beginning of the test, and then reached a plateau. The temperatures reached a steady state after running to a certain sliding distance. This data is plotted in Fig. 4.22. The figure shows the variation of sliding induced temperatures increase and coefficients of friction with sliding speed, for samples tested at a constant load of 50 N. Another set of tests was performed at a constant sliding speed, and the load was changed systematically. Fig. 4.23 shows the variation of sliding induced temperature rises, and coefficients of friction (COF) with normal loads for samples tested at a constant speed of 2.5 m/s. In both cases, the coefficient of friction decreased as the load or the speed was increased. As shown in Figs. 4.22 and 4.23, the surface temperature increased significantly with the sliding speed (to 250°C at 2.5 m/s) and load (to 340°C at 75 N). This was attributed to an increase in the rate of surface oxidation. This was consistent with the SEM observations that the oxide rich layers on the wear tracks were thicker and more continuous when the test loads and speeds were high, hence reducing the COF. It should be noted that the temperatures reported in Figs. 4.22 and 4.23 were the average temperatures of a region of 100-200 μm above the contact surfaces. It is expected that the contact temperatures at the asperity tips (flash temperatures) could readily reach values approximately 3 times higher than those measured values.

4.1.7. HARDNESS OF WORN SURFACES

Fig. 4.24 shows the variations of the microhardness of the coating after wear testing with sliding speed at constant loads of 25 N, 50 N and 75 N. For samples where there was an oxide layer on the wear track, the hardness data were obtained from regions where the flattened top surfaces of the iron splats were exposed. An example of such an

area where a Vickers indentation was made at the surface of a non-oxidized part of the wear track is shown in Fig. 4.25. The hardness of the wear track was always higher compared to that of the unworn area of the coatings (310 kg/mm^2) under all conditions. For example, the average worn surface hardness of samples tested at 25 N and 0.2 m/s was about 400 kg/mm^2 . The increase of hardness after the wear test could be attributed to work hardening of the sliding surfaces as a result of severe plastic deformation of the steel splats at or near the contact surface. The effect of surface hardening was more pronounced at higher loads. For example, a surface hardness of 550 kg/mm^2 was measured at 75 N (0.5 m/s). In fact, the worn surface hardness increased as the test conditions became more severe.

For the tests conducted at high loads and velocities, the hardness of wear tracks increased to exceptionally high values of over 700 kg/mm^2 . At 75 N and 2.5 m/s, for example, the average hardness of the steel splats on the contact surfaces reached 800 kg/mm^2 . TEM analyses carried on the deformed subsurface of the sample tested at 75 N and 2.5 m/s will be presented in Section 5.3. to provide a more detailed understanding of the fundamentals of the surface hardening during the sliding.

4.1.8. WEAR RATES UNDER CONTROLLED HUMIDITY ATMOSPHERE

In the tests described so far, the humidity of the testing environment was kept low at 7-10% RH. Results of wear tests done at higher humidity levels are presented in this section. The variations of the wear rates of the PTWA 1020 coatings with the relative humidity (RH) are shown in Fig. 4.26. The coatings tested at 5 N and 0.1 m/s showed that at 30% RH, the wear rate dropped to zero. For humidity levels above 30%, the

samples gained weight during sliding (see the insert in Fig. 4.26 for the wear rates at 5 N and 0.1 m/s). The high humidity atmosphere could cause weight gain by either increasing the rate of oxidation, or hydrating the nascent surface oxide. The measured wear rate for the tests at 12% RH was 6×10^{-8} g/m. By increasing the relative humidity to 60%, the wear rate reached a negative value of 7×10^{-8} g/m.

Similarly, for the testing conditions of 10 N and 0.5 m/s, the wear rates decreased as the relative humidity increased. By increasing the relative humidity from 10 to 80%, the wear rates decreased from 5.8×10^{-6} to 0.98×10^{-6} g/m, but no weight gain occurred. On the other hand, when the tests were performed at the same sliding speed of 0.5 m/s, but a higher normal load of 50 N, the wear rates became significantly higher at all humidity levels. At %RH = 10, the wear rate was measured as 16×10^{-6} g/m. At relative humidity levels higher than 50%, the wear rates showed a small decrease up to %RH = 40, but then reached a maximum of 17×10^{-6} g/m at about %RH = 55. A steep decrease to 0.814×10^{-6} g/m at %RH = 90 occurred after this point.

For the tests at 50 N and 2 m/s, the wear rates first increased to a peak (12.4×10^{-6} g/m), after which, they showed a decline. The peak corresponded to a relative humidity level of 85% (Fig. 4.26). This rather complex dependence on the wear rates to the humidity has been rationalized by considering the effects of competing micromechanisms of wear that occurred as the humidity increased. The changes in the surface morphologies as determined by the SEM are described in the next section.

4.1.9. SEM OBSERVATIONS OF WORN SURFACES UNDER CONTROLLED HUMIDITY

Figs. 4.27 and 4.28 are the back-scattered SEM micrographs of the worn surfaces of the coatings tested at a load of 5 N and 0.1 m/s sliding speed, at low humidity (12% RH) and high humidity (80% RH) conditions respectively. The wear track of the sample tested at 80% RH (Fig. 4.28) was much smoother than that shown in Fig. 4.27 for 12% RH, which showed higher wear rates (see the insert in Fig. 4.26). EDS analyses identified the light grey areas as metallic, and the dark areas as oxygen-rich layers. At low humidity levels (Fig. 4.27), the oxide layer was uniformly distributed between the microscratches on the contact area. The metallic parts were subjected to plastic deformation and extruded in the sliding direction. The micrograph of the sample worn at high humidity levels (Fig. 4.28) showed a different behaviour. The metallic parts were polished to almost a mirror finish, so well that the oxide veins (FeO) between the splats can be clearly observed on the worn surfaces. At high humidity levels, the oxide that formed during wear was hydrated, and easily removed from the surface. This oxide was transported to and compacted in the surface pores and non-contact areas. At 10 N load and 0.5 m/s sliding speed, the worn coating morphologies were similar to those tested at 5 N and 0.1 m/s.

Figs. 4.29 and 4.30 show the worn surfaces of the coatings tested at 50 N load and 0.5 m/s sliding speed at a moderate humidity level of 50% (the highest wear rate among all the test conditions), and a high humidity level of 90% RH (the low wear rate). Fig. 4.29 shows two different morphologies of oxides on the worn surfaces. Using the EDS, the dark grey areas were identified as an oxide. The oxide decorated the depressions on

the surface and had a granular microstructure. The medium grey regions, which were surrounded by light grey areas were also identified as oxides. The light grey regions represent the steel splats. The steel splats were flattened as a result of plastic deformation during wear. This micrograph also shows that some of the splat fragments were forged on the contact surface by the counterface. In Section 5.1.1, it was reported that the fracture of the edges of the highly deformed steel splats was the primary reason that led to debris formation under dry air conditions. The same mechanical wear mechanism appeared to control wear at 50% RH (Fig. 4.29). At 90% RH, however, the metallic surfaces were smoother (Fig. 4.30), and there was less evidence for fracture and fragmentation compared to 50% RH.

In summary, at low humidity conditions, the splats adjacent to the sliding surfaces were deformed plastically, especially at high loads and low speeds conditions. Severe plastic deformation at the edges of the splats caused fracture and fragmentation of the splat tips. At high humidity conditions, the metallic parts of the contact areas were smoother, and exhibited less evidence for surface damage and fracture at high loads.

4.1.10. THE EFFECT OF HUMIDITY ON THE COEFFICIENT OF FRICTION

Figs. 4.31.a and b show the variation of the COF of the PTWA 1020 coatings with the sliding distance at different humidity levels for samples tested at 5 N - 0.1 m/s, and 50 N - 0.5 m/s. These plots show that the COF decreased at high RH for tests at both load levels. However, this effect was more pronounced at 50 N and 0.5 m/s and 50% RH (highest wear rate) where the average COF was 0.65 (Fig. 4.31.b). The COF decreased to 0.5 at 90% RH (lowest wear rate). It is also noted that the COF curve was smooth.

The change in the average COF as a function of humidity is shown in Fig. 4.32 for wear tests performed under the loading conditions of 50 N - 0.5 m/s. The data shows a monotonic decrease in the COF with increasing humidity.

4.1.11.RESULTS OF XRD ANALYSES

The XRD spectra of the wear debris of samples tested at 50 N and 0.5 m/s at two different relative humidity conditions of 50% and 90% are given in Fig. 4.33. Rietveld analyses were performed in order to analyze the relative amounts of four different components, namely, α -Fe, Fe_2O_3 , FeO, and Fe_3O_4 in the wear debris. As mentioned previously, it was difficult to differentiate between the various iron oxide phases because many X-ray intensity lines overlapped. However, the relatively strong α -Fe reflection at $2\theta = 44^\circ$ does not overlap with any oxide peaks, and consequently, the analysis resulted in a reliable estimate of the amount of non-oxidized iron in the debris. Fig. 4.34 shows how the metallic iron content in the debris varied as a function of the relative humidity of the wear environment for samples tested at 50 N and 0.5 m/s. The iron content of the debris first increased for RH values up to 50%, which corresponded to the highest wear rates, and then decreased for the tests done under higher humidity conditions. In this respect, there is a close correlation between the wear rates and the amount of metallic iron present in the debris. This was explained on the basis of a transition from mechanical wear that occurred by fracture of iron splat tip to a water activated chemical polishing wear which produced small amounts of metallic debris. These two wear mechanisms will be discussed in detail in Sections 5.1 and 5.4.

4.2. HIGH VELOCITY OXY-FUEL HVOF 1020 COATINGS

4.2.1. MICROSTRUCTURE, COMPOSITION AND PROPERTIES

Fig. 4.35.a is a back-scattered SEM micrograph of a polished cross-section of the HVOF 1020 coating. This micrograph shows the different constituents that existed in the microstructure. The energy dispersive spectroscopy (EDS) analysis of light grey regions seen in Fig. 4.35.a shows the existence of only elemental Fe (Fig. 4.35.b). The EDS analysis (Fig. 4.35.c) from the grey areas in Fig. 4.35.a shows the presence of Fe and O elements. The X-ray diffraction analyses of the coating exhibited the peaks that belonged to FeO type iron oxide and α -Fe. The diffraction pattern of the coating is presented in Fig. 4.35.d. The HVOF 1020 coatings had a composition similar to that of the PTWA 1020 for which the EDS and XRD results were reported in Section 4.1. However, the iron splats in the HVOF 1020 coatings were wavier, and in general thinner than those in the PTWA 1020.

It is important to note the considerable difference in the amount of FeO between the coatings. The amount of FeO in the PTWA 1020 coatings was estimated at 20% by volume using an image analysis system while the amount of FeO in HVOF 1020 was significantly higher, and was estimated at about 65%. Table 4.3 presents the important microstructural features and properties of the HVOF 1020 coatings.

4.2.2. PIN-ON-DISC WEAR TEST RESULTS UNDER DRY ATMOSPHERE

The variation of wear rates of the HVOF 1020 coating as a function of sliding speed at several load levels of 5 N, 10 N, 25 N, 50 N and 75 N is shown in Fig. 4.36. The wear

tests were conducted using a pin-on-disc type tribometer under a dry air atmosphere with relative humidity of 7-10%. The wear rates of the HVOF 1020 coatings were obtained by dividing mass loss after the test by the total sliding distance. The measured weight losses were converted to volumes using the density of the coating. For the tests performed at 25 N and 10 N, the wear rates increased monotonically as the sliding speed increased. At 10 N, the wear rate measured at a sliding speed of 0.2 m/s was $0.25 \times 10^{-3} \text{ mm}^3/\text{m}$. By increasing the sliding speed to 2 m/s, the wear rate increased to $0.76 \times 10^{-3} \text{ mm}^3/\text{m}$.

Coating Thickness (μm)	400 ± 10
Coating Density (g/cm^3)	7.1 ± 0.1
Vickers Hardness of Coating (kg/mm^2)	370 ± 25
Volume Fraction of FeO	0.65 ± 0.02
Thickness of FeO Phase (μm)	0.2-8.0
Volume Fraction of Pores	0.02 ± 0.01
Diameter of Pores (μm)	0.7- 5.0
Thickness of Steel Splats (μm)	1.5-7

Table 4.3- Microstructural characteristics of the HVOF 1020 coatings.

Similar wear behaviour, namely higher wear rates with increasing speed, was observed at a 25 N load. At high loads, the wear rates of the HVOF 1020 showed more sliding speed dependence. At 75 N, the wear rates at low speeds were very high, i.e., $7.6 \times 10^{-3} \text{ mm}^3/\text{m}$ at 0.2 m/s. The wear rates at this load decreased to a minimum at mid-range sliding speeds, i.e., $1.32 \times 10^{-3} \text{ mm}^3/\text{m}$ at 1 m/s, which was comparable to the wear rate of the PTWA 1020 measured under the same conditions in Fig. 4.6. However, contrary to the behaviour of PTWA 1020 in HVOF 1020 samples tested above 1m/s, the wear rates increased significantly with sliding speed, and reached $4.56 \times 10^{-3} \text{ mm}^3/\text{m}$ at 2 m/s. The wear rate of the HVOF 1020 coating at 75 N and 2 m/s loading condition was 74% higher than that of the PTWA 1020 coating at equal testing conditions.

4.2.3. SEM OBSERVATIONS OF WORN SURFACES

The secondary and back-scattered SEM images of the worn surface of the coating tested at 10 N load and 0.5 m/s sliding speed for a sliding distance of 5000 m are shown in Figs. 4.37.a and b. The microscratches are seen clearly in Fig 4.37.a. The secondary SEM image in Fig. 4.37.a exhibits the surface topography more clearly. The microscratches on the sliding surface of the coating extend parallel to each other with a typical width between 2 and 4 microns. The back-scattered image shows the existence of three different regions on the sliding surface. The EDS analyses of the medium and dark grey regions indicated the presence of the oxygen and iron. The medium grey areas had a morphology consisting of veins, with the composition of FeO, similar to the composition of the veins in the unworn samples. The dark grey regions were recognized as the oxygen rich patches. The SEM micrograph (Fig. 4.37.b) shows that iron oxides occupy regions

between the plastically deformed iron splats, and are inside the microscratches. The wear debris gathered was a non-magnetic powder that was dark orange in colour. The XRD analyses of the debris from this loading condition indicated that Fe_2O_3 was the predominant constituent.

The highest wear rates for the coating were observed at high loads and low sliding speeds. The back-scattered SEM micrograph of the worn surface of the coating tested at 75 N load and 0.5 m/s is shown in Fig. 4.38. The micrograph shows two different morphologies of oxides on the worn surfaces. Using the EDS, the dark grey areas were identified as oxygen rich regions (possibly mixed oxides). The oxide particles formed the granular microstructure seen on the upper part of this figure. The medium grey regions were also identified as oxides, which stayed on the surface and were surrounded by light grey regions identified as steel splats. The sliding surface of the coating was severely damaged, and in some parts the iron splats deformed and extruded in the sliding direction. Fig. 4.39 shows a back-scattered SEM image from the worn surface of the coating tested at the same loading conditions. In this figure, the splats on the contact surface appeared flattened as a result of plastic deformation during wear. The wear debris gathered under these conditions was magnetic and dark brown in colour. The quantitative XRD phase analysis of the debris of the coating tested at 75N load and 0.5 m/s shows the presence of ferrite, Fe_2O_3 , Fe_3O_4 , and FeO (Table 4.4). It is important to emphasize that there was a considerable amount of metallic ferrite in the debris. Similar observations were made on the PTWA 1020 coatings tested at the same loading conditions (Section 4.1.3.1.).

Fig. 4.40 shows the worn surface of the coating tested at high load (75 N) and high sliding speed (2 m/s) after 5000 m sliding distance. The micrograph shows a severely deformed and damaged surface associated with the cracks normal to the sliding direction. The existence of the cracks suggests that residual stresses of large magnitude existed in the oxide layers that covered the deformed surfaces. Fig. 4.41 shows a back-scattered SEM micrograph of the HVOF 1020 coating worn at 50 N load and 2.5 m/s. The micrograph was taken from a region on the wear track, which shows evidence for surface oxidation during sliding, and deformation mostly in the form of surface grooving of the iron splats. Fig. 4.42 exhibits the larger area of the worn surface. The micrograph shows that the worn surface has a high roughness along with scattered oxide patches. The sample tilted about 60 degrees in the direction of the horizontal axis to show the details of the surface roughness.

The observations summarized in the above paragraph indicated that the worn surfaces of the HVOF 1020 coatings tested at high loads and speeds were significantly different from the sliding surfaces of the PTWA 1020 coating tested at the same loading condition. The iron oxide rich layers generated on the contact surfaces of the HVOF 1020 samples were generally 3-10 μm thick. The oxide layers on the sliding surfaces were discontinuous and well apart. Fig. 4.43 shows that rich film as thick as 7 μm were formed on the sliding surface of the HVOF 1020 coating tested at 75 N and 2 m/s for a sliding distance of 5000 m. The micrograph was taken at a tilted angle of 60° to the worn surface to accentuate the morphological details. Fig. 4.44 is another micrograph, which shows again the formation of the thick oxide layer. This image shows cracking and the fragmentation of the oxide film. The secondary electron SEM image from the debris

gathered from the test done under 75 N and 2.5 m/s is shown in Fig. 4.45. This figure illustrates the plate-like iron oxide debris with a thickness of about 3-7 μm was detached from the oxide layers formed on the contact surface.

4.2.4. X-RAY DIFFRACTION OF LOOSE DEBRIS PARTICLES

The quantitative phase analyses obtained from Rietveld refinement of the XRD spectra of wear debris at high loads and low sliding speeds of HVOF 1020 are given in Table 4.4. The proportion of ferrite among the oxidized debris particles produced at these testing conditions was higher compared to other testing conditions. In HVOF 1020, 23% of the debris generated at 75 N, and 0.2 m/s consisted of ferrite. This was reduced to 6% on the surfaces of samples tested at 2.0 m/s, indicating that a transition from mechanical to oxidative wear mechanism occurred.

Phase	75N, 0.5m/s	75N, 2m/s	50N, 2m/s
Ferrite (Fe)	23	6	6
Hematite (Fe ₂ O ₃)	30	16	10
Magnetite (Fe ₃ O ₄)	20	36	36
Wuestite (FeO)	27	42	48

Table 4.4 - Quantitative XRD phase analysis of debris (weight percent) of the HVOF 1020 coatings tested at different loading conditions.

The other aspects of the wear of HVOF 1020 coatings, such as the frictional temperature increase are given in Section 5.2.2. where this data was analysed and compared with similar data from other coatings.

4.3. HIGH VELOCITY OXYGEN FUEL HVOF 1020-2.5% Al COATINGS

4.3.1. MICROSTRUCTURE, COMPOSITION AND PROPERTIES

The microstructure of the HVOF 1020-2.5% Al coatings (Fig. 4.46.a) exhibited similarities to the others and showed steel splats, and FeO layers between them. However, the addition of 2.5% Al caused two important changes. These were: i) The formation of an additional Fe, O, and Al rich phase (Fig. 4.46.b), and ii) the significant reduction of the FeO (60%) in the HVOF 1020 coatings to 15%. Therefore, the FeO amount in the HVOF 1020-2.5% Al was similar to that in the PTWA 1020. The diffraction pattern of the HVOF 1020-2.5% Al coating is presented in Fig. 4.46.d. The XRD spectrum in Fig. 4.46.d shows peaks that belong to ferrite. Unlike the EDS analyses, the XRD result from the coating did not show the presence of the Fe, O, and Al rich phase.

4.3.2. PIN-ON-DISC WEAR TEST RESULTS: WEAR RATES UNDER DRY ATMOSPHERE

Wear tests on the HVOF 1020-2.5%Al coatings have been performed at constant loads of 10, 50, and 75 N, and the wear rates are shown in Fig. 4.47. At 10 N, the wear rates of the HVOF 1020-2.5%Al were low and decreased slightly with the sliding speed.

Coating Thickness (μm)	400 ± 10
Coating Density (g/cm^3)	6.8 ± 0.1
Vickers Hardness of Coating (kg/mm^2)	290 ± 40
Volume Fraction of FeO	0.15 ± 0.02
Thickness of FeO Phase (μm)	0.2
Volume Fraction of Pores	0.01 ± 0.01
Diameter of Pores (μm)	0.7-1.5
Volume Fraction of (Fe, O, Al) Inclusion	0.06 ± 0.02
Thickness of Steel Splats (μm)	1.5 - 7

Table 4.5- Microstructural Characteristics of the HVOF 1020-2.5% Al Coatings.

It is important to note that at 75 N, the wear behaviour of HVOF 1020-2.5% Al was similar to that of the PTWA 1020 rather than HVOF 1020 in such a way that the wear rates of HVOF 1020-2.5% Al were high at low sliding speeds, but decreased when increasing the sliding speed. This can be seen from the results of the tests at 75 N for which increasing the sliding speed from 0.2 to 0.5 m/s caused a decrease in the wear rates of HVOF 1020-2.5% Al from $6.51 \times 10^{-3} \text{ mm}^3/\text{m}$ to $1.39 \times 10^{-3} \text{ mm}^3/\text{m}$. The wear rates of HVOF 1020-2.5% Al further decreased to $0.67 \times 10^{-3} \text{ mm}^3/\text{m}$ at 2 m/s, and as such were comparable to those of the PTWA 1020, but about 80% lower than those of the HVOF 1020 tested under the same conditions.

4.3.3. SEM OBSERVATIONS OF WORN SURFACES

The SEM investigations of the worn surfaces of the HVOF 1020-2.5% Al coatings indicated the existence of scratch paths in the sliding direction. Fig. 4.48 is a back-scattered SEM micrograph of the worn surface of the coating, which shows the scratches at low magnification. The micrograph was taken from the worn surface of the coating tested at 75 N and 2 m/s. The origin of the surface scratches can be attributed to the presence of (Fe, Al, O) rich inclusions on the surface. An example of these inclusions that lay on the contact surface is shown in Fig. 4.49. The inclusion is fractured and possibly acted as a third body particle causing formation of the scratch marks on the surface. Fig. 4.50 is a back-scattered SEM image that was taken from the worn surface of the coating tested at 75 N load and 0.2 m/s.

The EDS analyses showed the existence of the elemental Fe and O in the medium grey areas, and the presence of the Fe in the light grey regions of the micrograph. The figure shows the severe deformation and fracture of the iron splats on the sliding surface of the coatings. The micrograph also shows that the metallic fragments were flattened and forged on the sliding surface. Therefore, fracture of the tips of severely deformed splats was the main mechanism responsible for the high wear rates of the HVOF1020-2.5% Al coatings like the other two coatings (PTWA 1020 and HVOF 1020) at high loads and low sliding speeds.

The SEM investigations from the worn surface of the coating, which was tested at 75 N and 2 m/s showed the formation of the uniform iron oxide films on the sliding surfaces similar to those covered the surfaces of the PTWA 1020 tested at the same loading conditions. Fig. 4.50 shows the spallation of the oxide film on the sliding surface

of the coating. From this micrograph the thickness of the oxide film is estimated to be 1 μm . At this loading condition, the average thickness of the oxide layers formed on the sliding surface varied between 1 and 3 μm . In summary, the worn surfaces of the HVOF 1020-2.5% Al coating were covered with mixed iron oxides at high loads and velocities. The oxide layers were thin, and similar to those formed during the sliding wear of PTWA 1020 that showed similar low wear rates under these conditions.

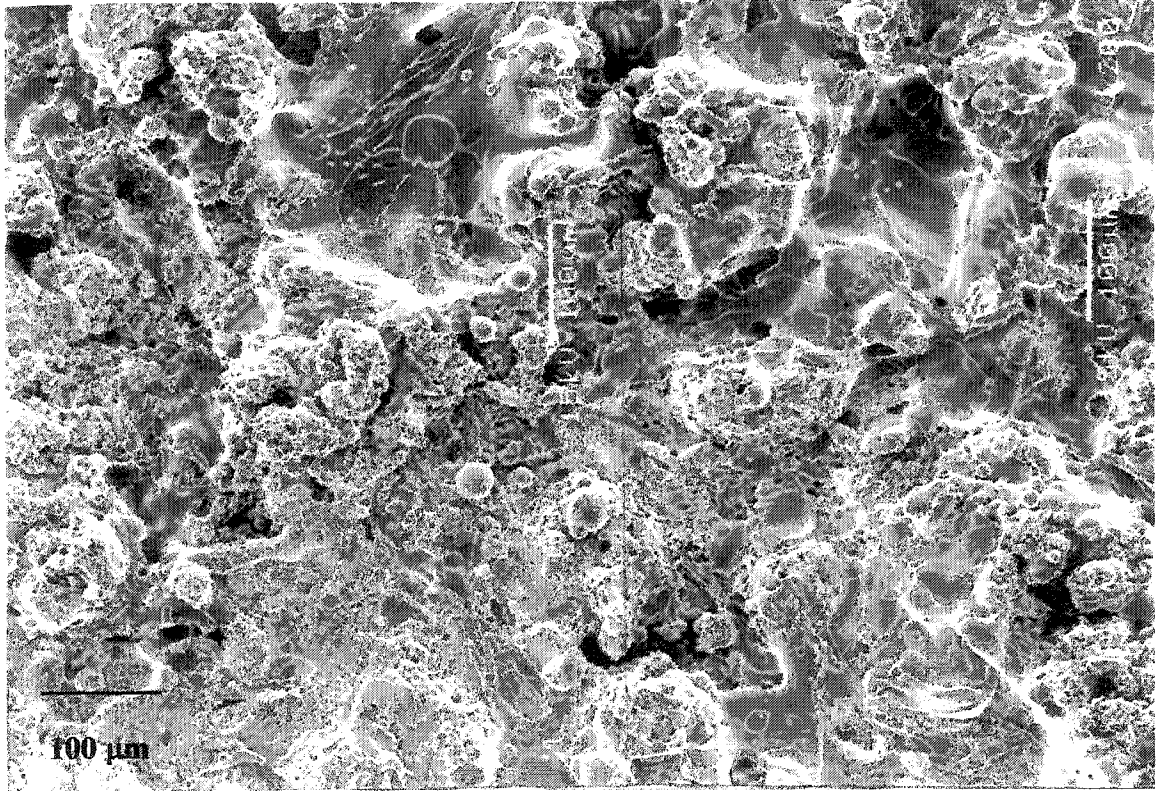


Fig. 4.1- A typical secondary electron SEM image of the surface of the PTWA 1020 coating in the as-deposited condition shows that the surface is very rough after the thermal deposition process.

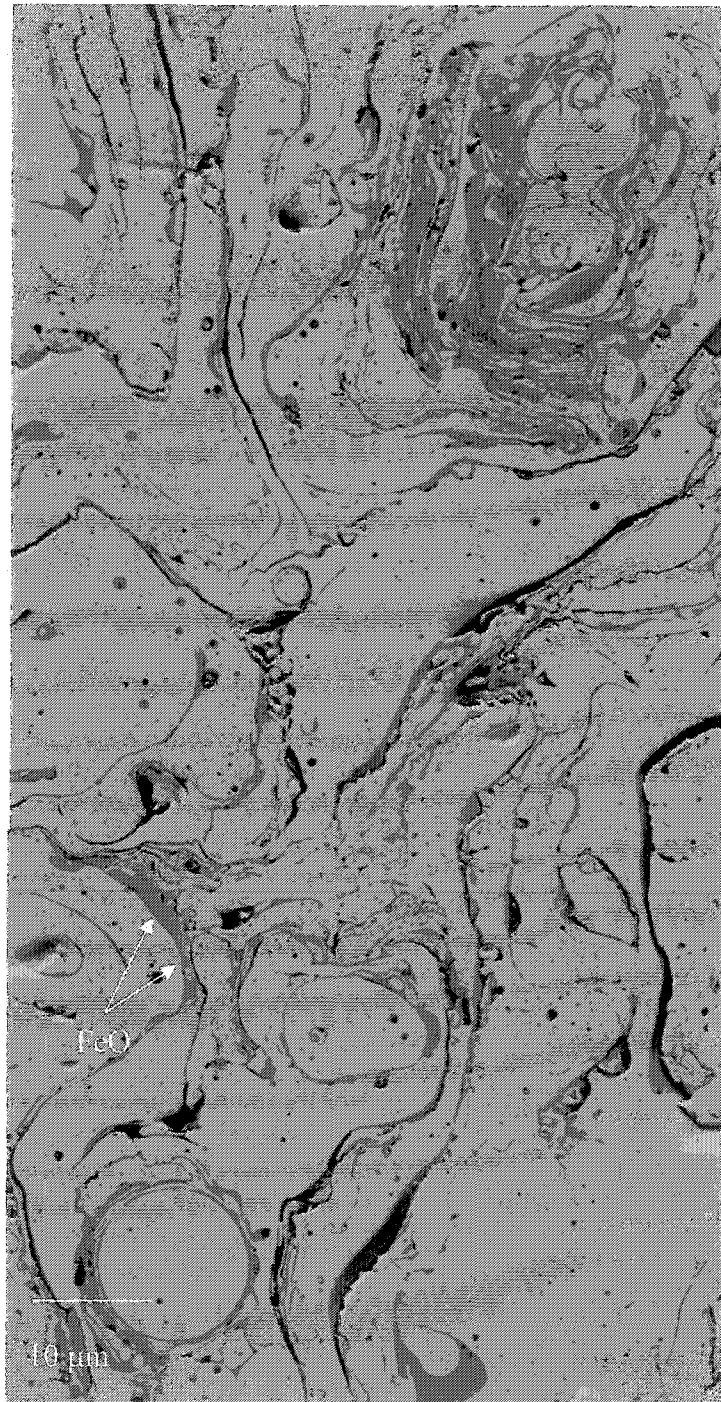


Fig. 4.2- A back-scattered SEM micrograph of the top surface of the PTWA 1020 coating after polishing to an average roughness (R_a) of 0.1 μm.

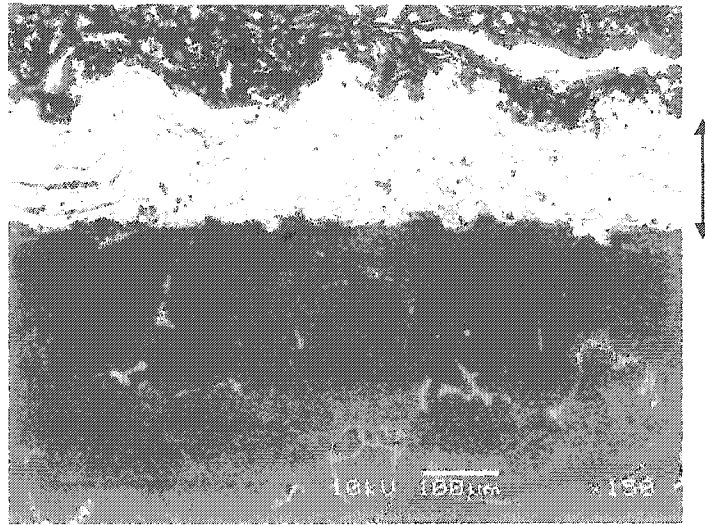
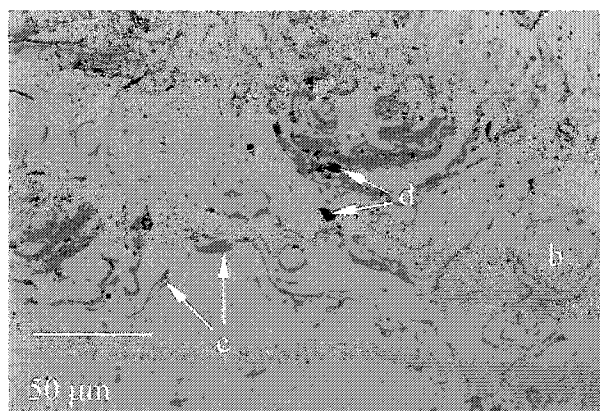
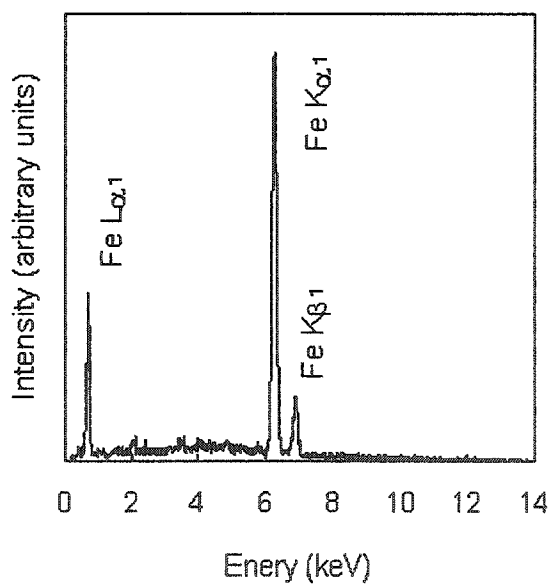


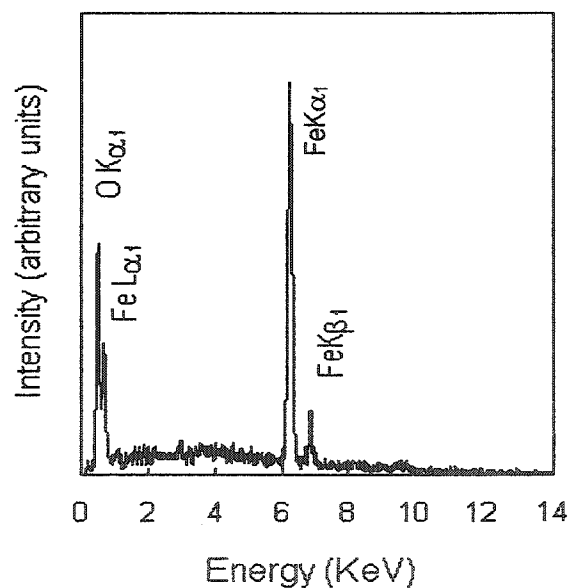
Fig. 4.3- The general cross-sectional view of the 319Al substrate coated with PTWA 1020 with as-deposited morphology.



(a)

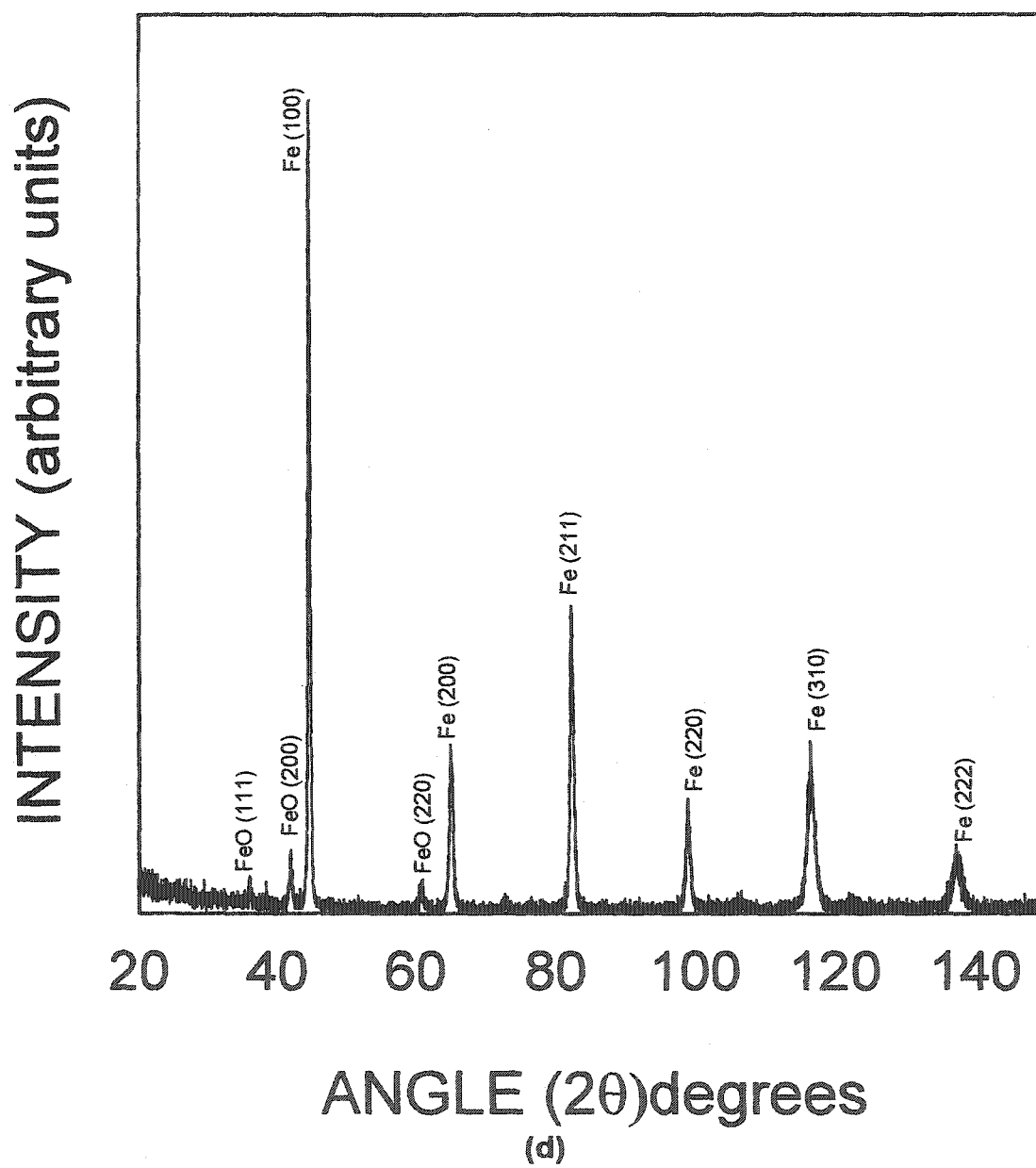


(b)



(c)

Fig. 4.4- The structure and chemistry of an unworn PTWA 1020 coating. (a) A back-scattered SEM image of a polished cross-section of the coating (unetched). Three distinct regions are evident in this photograph: The light areas labelled (b) in the image are iron as is shown in the EDS spectrum of Fig. 4.4 b; the dark grey regions labelled (c) are Fe and O as is shown in the EDS spectrum of Fig. 4.4 c; the round black regions are porosity (d). Fig. 4.4 d is the XRD spectrum of this sample showing the presence of iron and (FeO).



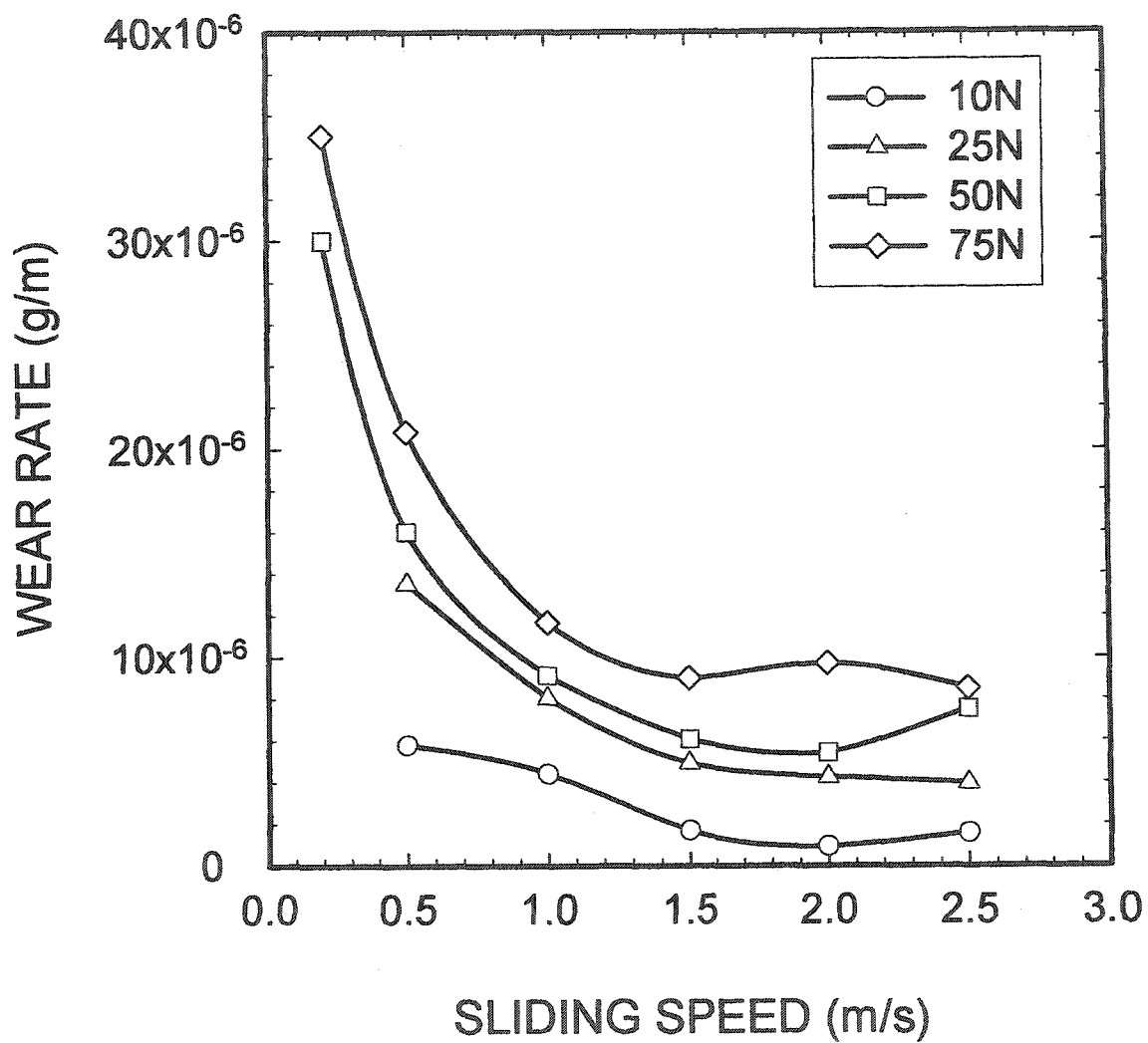


Fig. 4.5- The variation of the wear rates (g/m) of the PTWA 1020 thermal spray coatings plotted versus the sliding speed for four different normal loads. The trend is for decreased wear rates at increased speed.

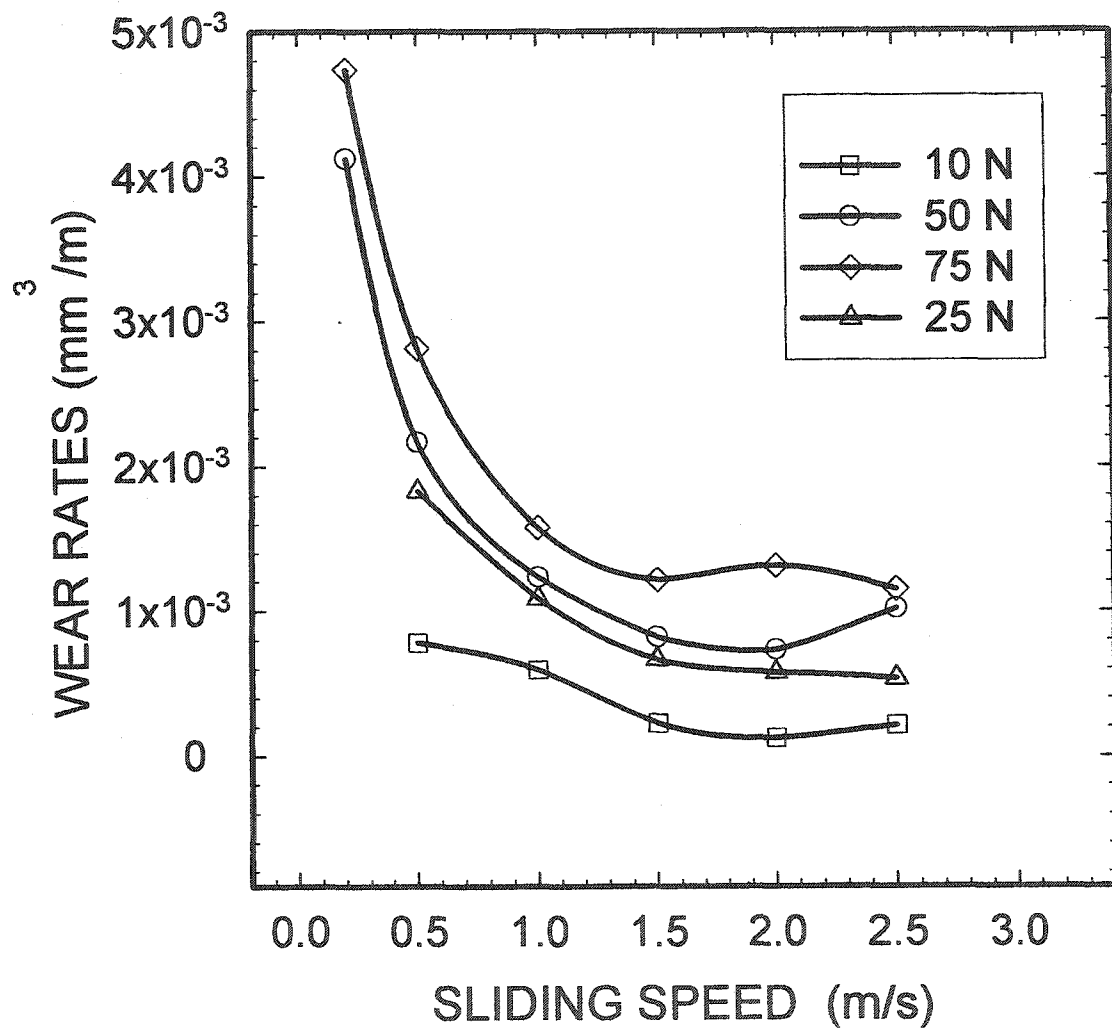
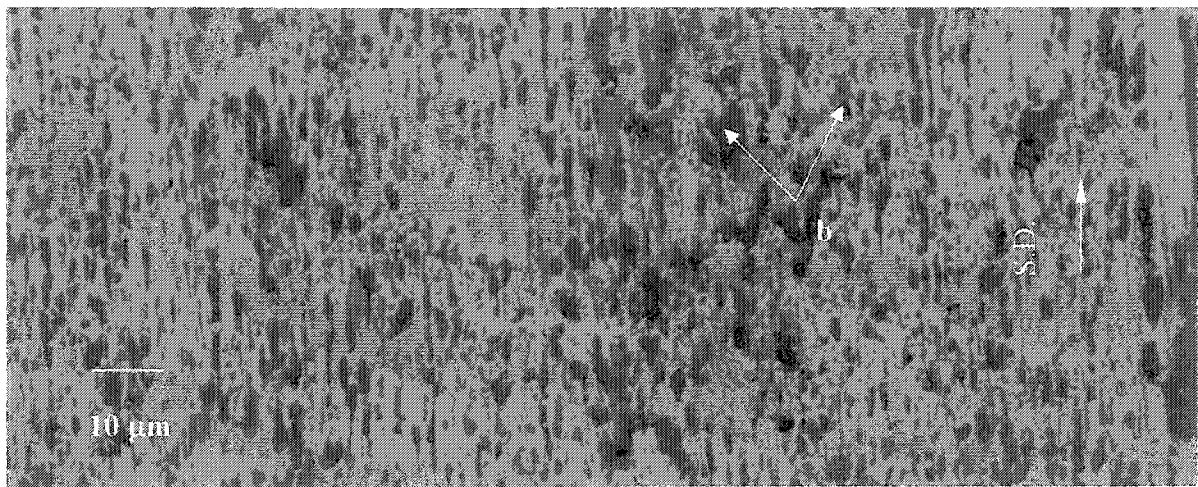
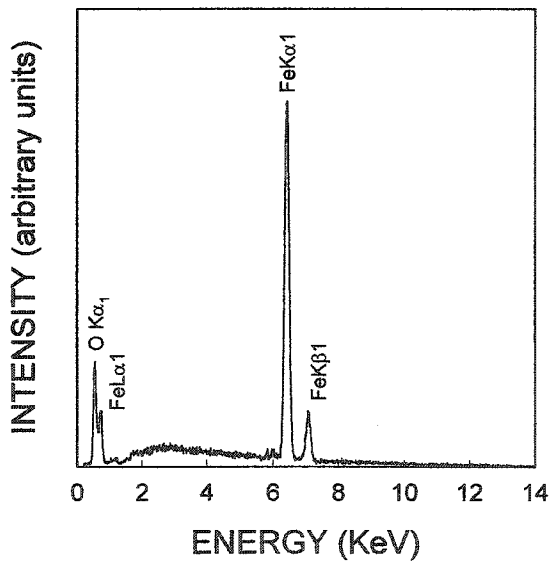


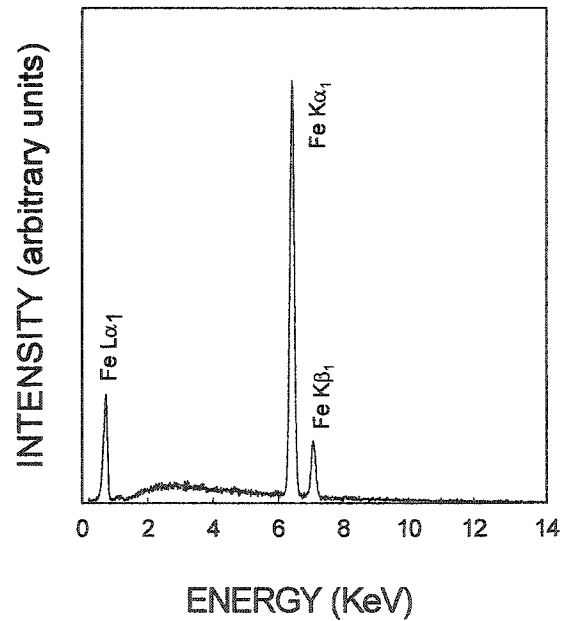
Fig. 4.6- The volumetric wear (mm^3/m) of the PTWA 1020 coatings at four different loads plotted against the sliding speeds.



(a)



(b)



(c)

Fig. 4.7- (a) Back-scattered SEM micrographs of the worn surfaces of the PTWA 1020 coating tested at 10 N load and 0.5 m/s sliding speed after 5000 m sliding distance. The SEM micrograph shows two different regions. EDS analysis of the dark grey areas marked as (b) on the SEM image are shown in Fig 4.7 (b). EDS analysis of the light grey area marked as (c) on the image are shown in Fig. 4.7 (c).

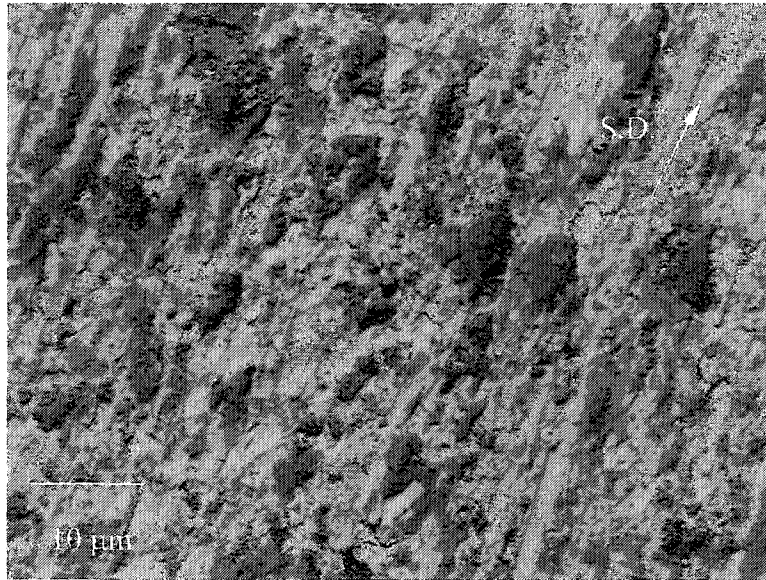


Fig. 4.8- A back-scattered SEM micrograph of the sliding surface of the PTWA 1020 sample worn at 10 N load and 0.5 m/s after 5000 m sliding distance. The micrograph is taken at a tilted angle of 15° to the worn surface to accentuate morphological details.

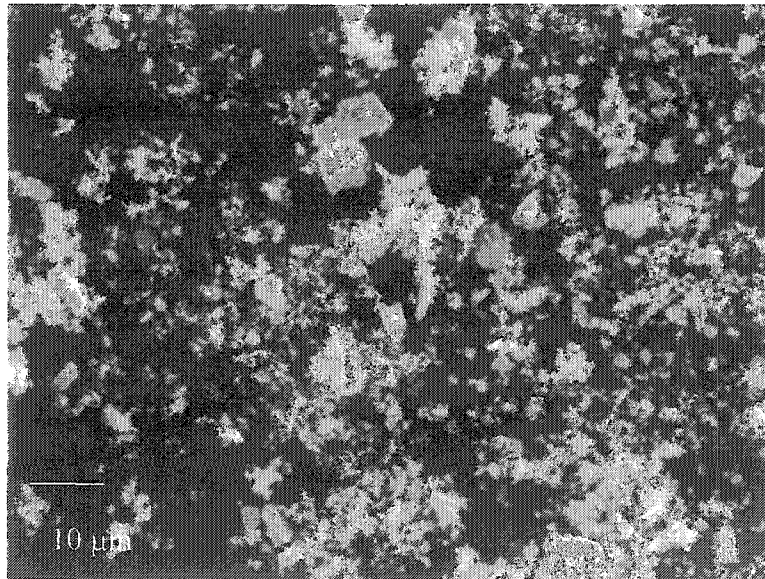


Fig. 4.9- A secondary SEM micrograph of the debris collected from the test performed under 10 N load, and 0.5 m/s showing that the fine particles agglomerated to form oxide aggregates of 2-4 μm.



Fig. 4.10- (a) A back-scattered SEM micrograph of a sample worn at 75 N load and 0.5 m/s. The dark grey regions were identified as the oxygen rich film with the aid of EDS. EDS analysis from the medium grey areas shows the presence of elemental Fe. The arrows on the micrograph show cracks on the deformed splats.

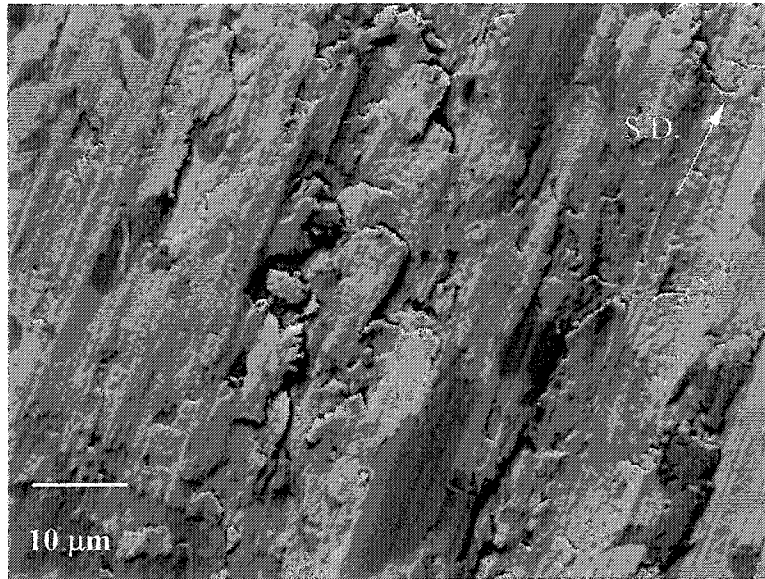
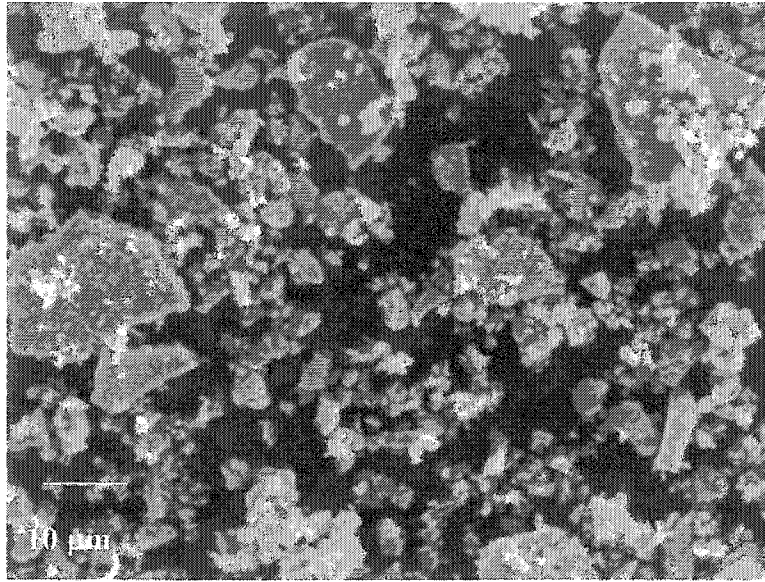
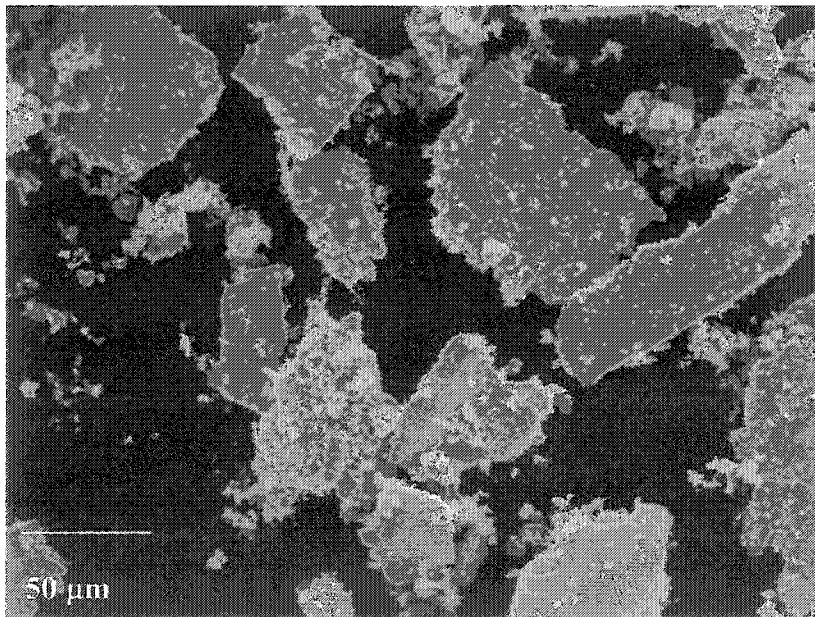


Fig. 4.10- (b) Another example of the deformation and fragmentation processes of the splats at the sliding surface of the PTWA 1020 coating at high loads (50 N) and low speed (0.5 m/s) testing conditions.



(a)



(b)

Fig. 4.11- (a) A secondary SEM micrograph shows the plate-like iron splat fragments mixed with powdery iron oxide particles. (b) A high magnification SEM image illustrates the morphology of plate-like debris from PTWA 1020 coatings tested at 75 N and 0.2 m/s.

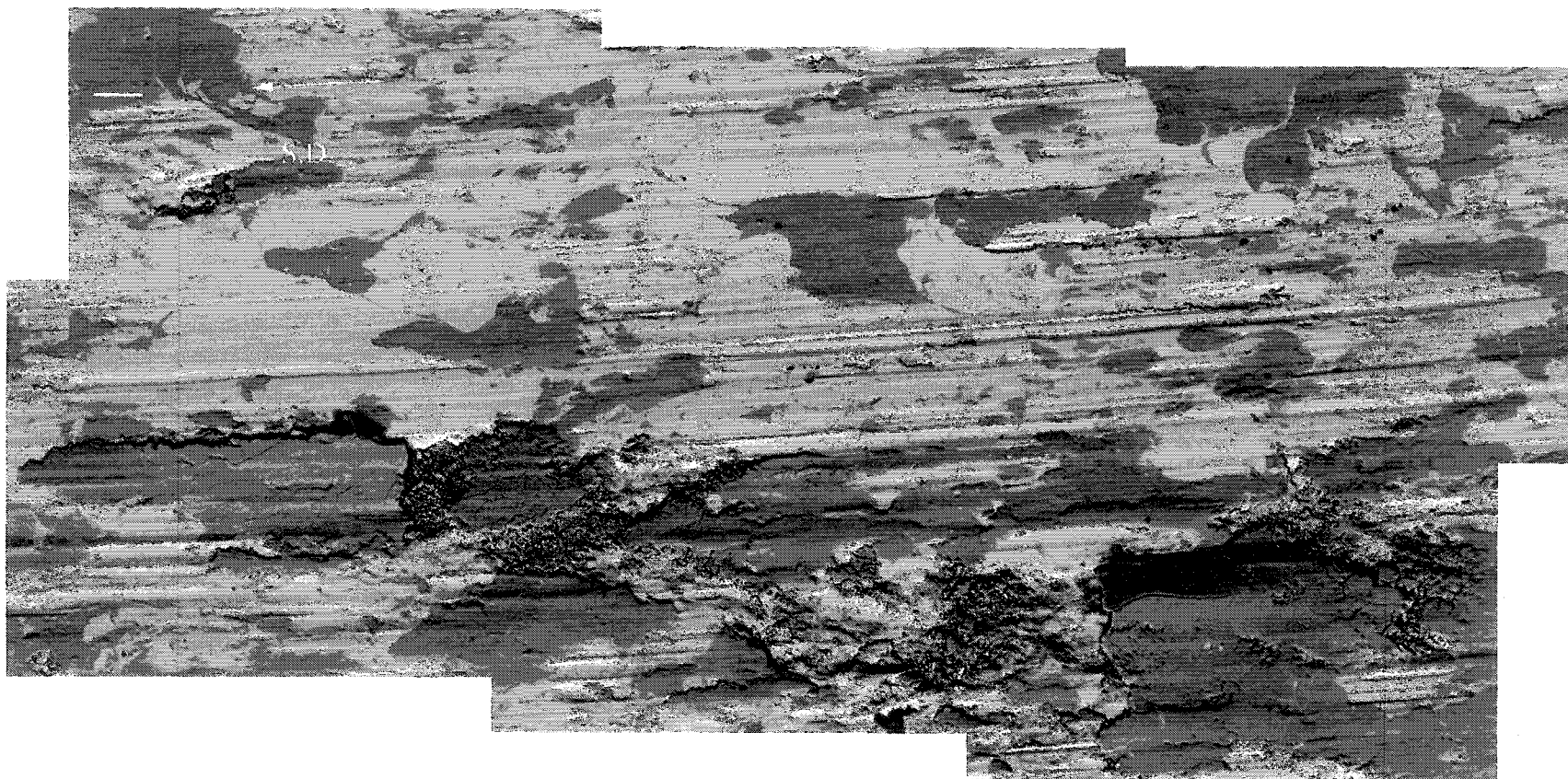


Fig. 4 12- A back-scattered SEM micrograph of a sample worn at 50 N load and 2.5 m/s. The micrograph is taken from a region, which shows evidence for deformation mostly in the form of surface grooving of both the oxide rich layers and the iron splats. (Note the micrograph was deliberately selected to illustrate the deformation pattern and that the area fraction of the oxide rich layers is less than the average coverage).

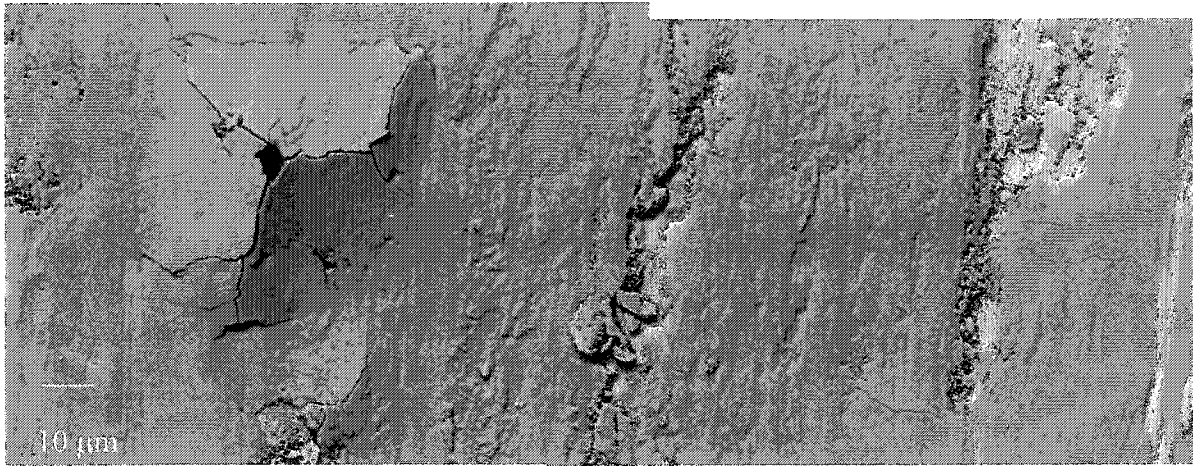


Fig. 4.1- A back-scattered SEM image of the worn surfaces of the PTWA 1020 coating tested at 50 N and 2.5 m/s shows the wear track was covered by an oxide rich film and the micrograph also shows the spallation of the oxide film.

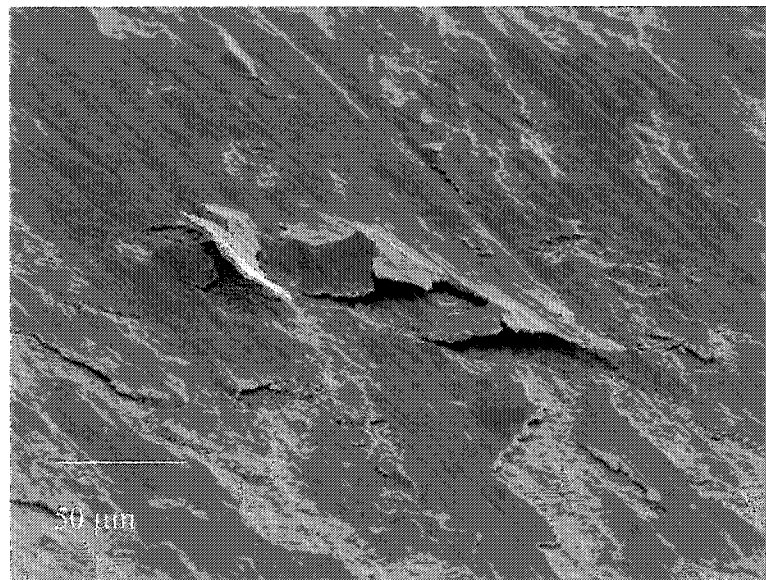


Fig. 4.14- Another example of the spallation of the oxide layers generated during the sliding of PTWA 1020 tested at 75 N and 2.5 m/s. The secondary SEM micrograph also shows the distribution of the oxide layers more accurately (70%).



Fig. 4.15- A secondary SEM micrograph of the debris from the test performed on PTWA 1020 at 75N load and 2.5 m/s that shows the plate like oxide particles.

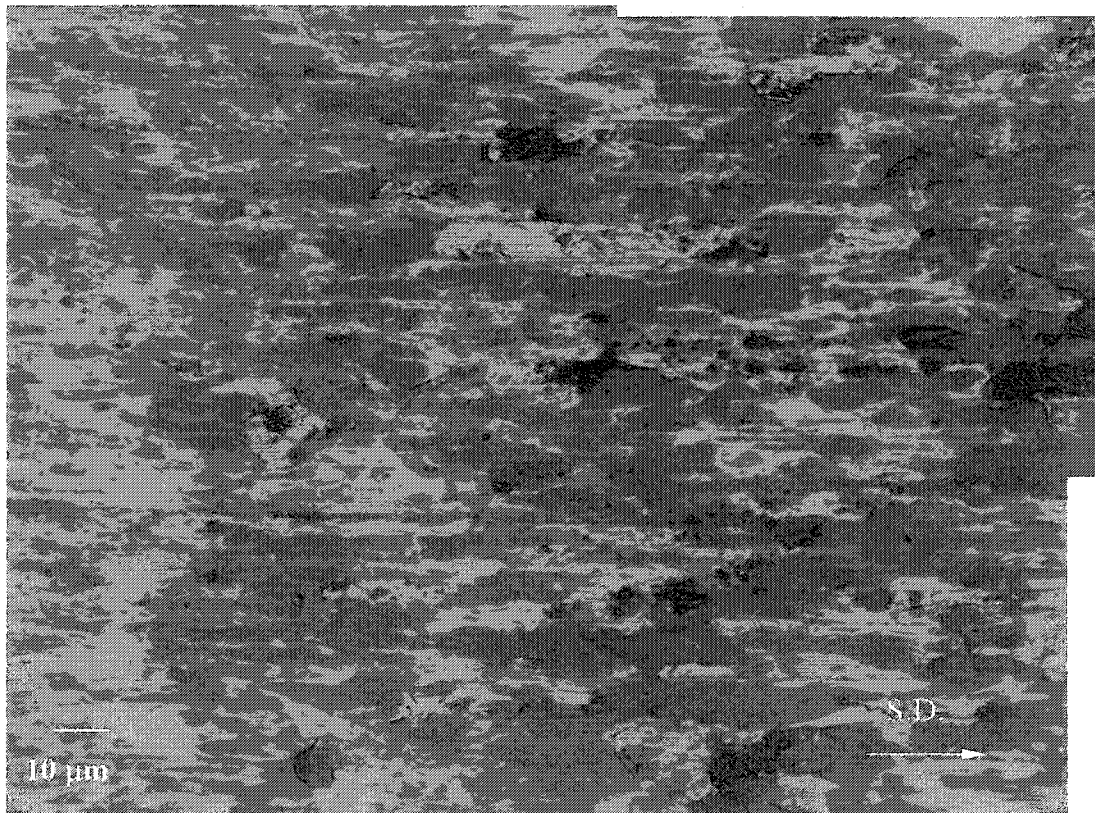


Fig. 4.16- A back-scattered SEM micrograph of a PTWA 1020 sample worn at 10 N load and 2.5 m/s. The dark grey extended regions are an iron oxide film that is smeared over the surface of the steel splats during sliding.

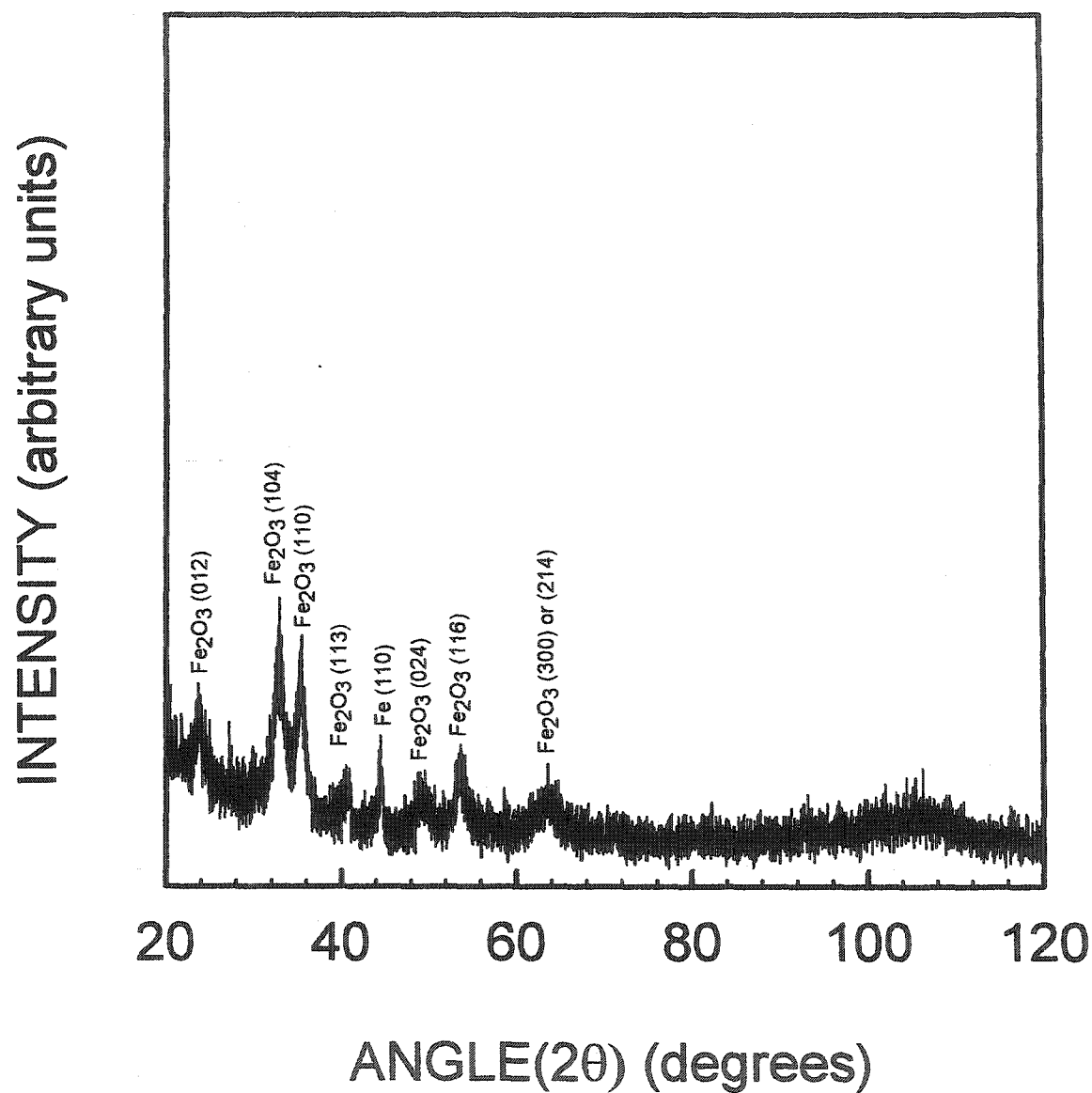


Fig. 4.17- The XRD spectra of the wear debris collected from PTWA 1020 at 10N (low load) and 0.5 m/s (low speed) shows the peaks for hematite (Fe_2O_3), and a few small peaks of ferrite.

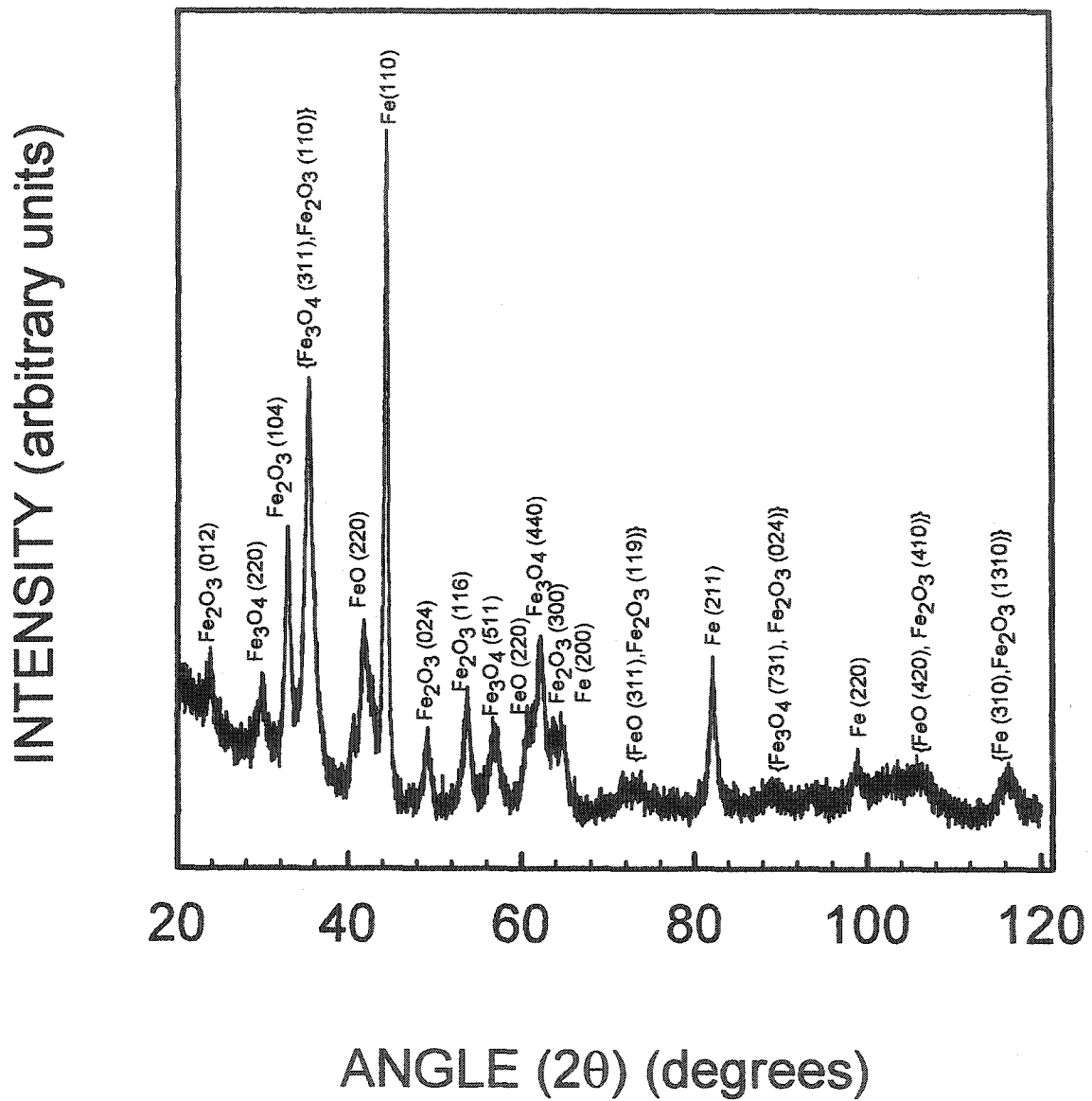


Fig. 4.18- The XRD spectra of the wear debris collected from PTWA 1020 at 50N (high load) and 0.5 m/s (low speed) shows the debris consisted of a mixture of three types of iron oxides: Fe_2O_3 , Fe_3O_4 , and FeO with a significant amount of metallic ferrite in the debris.

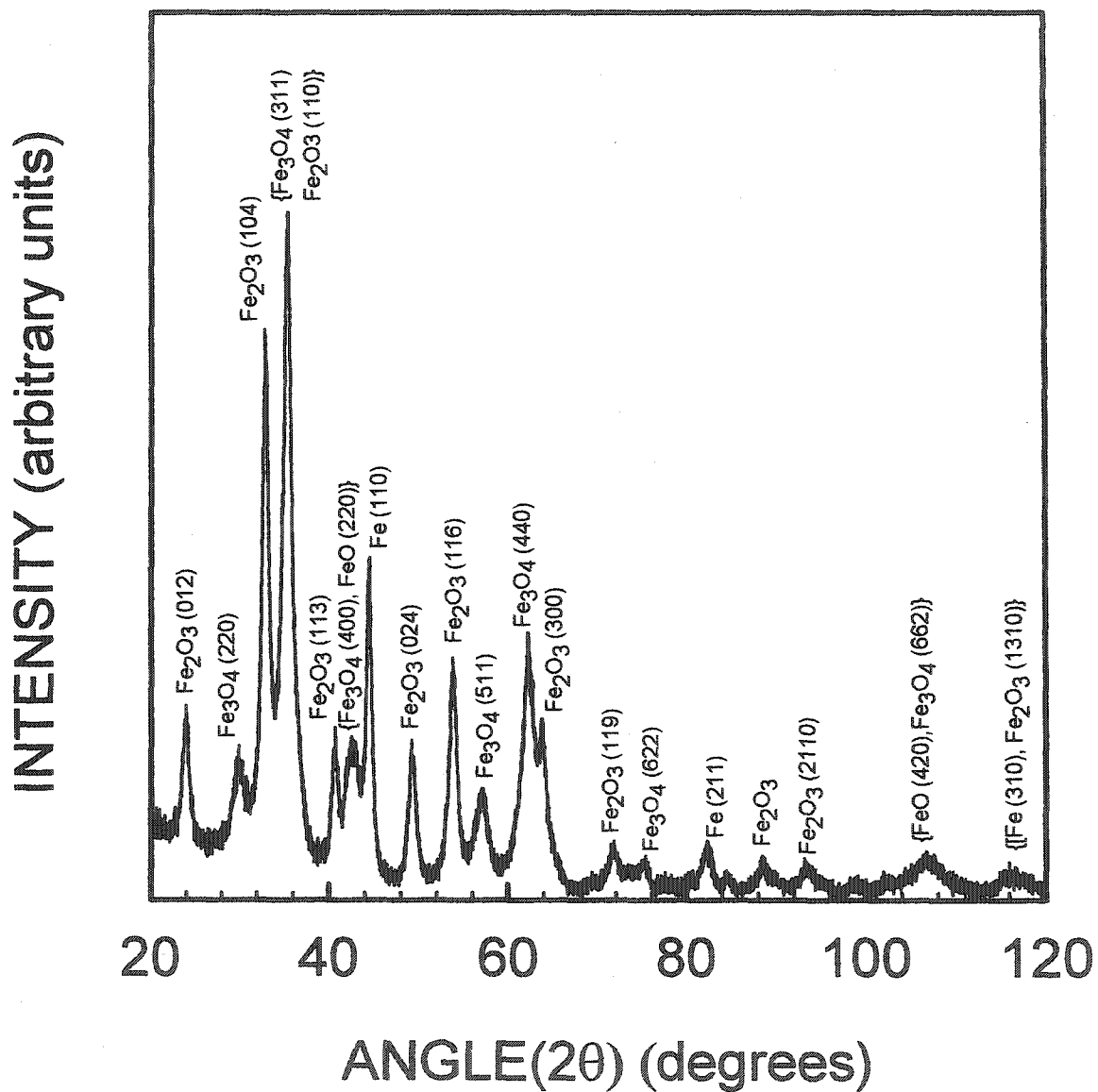


Fig. 4.19- The XRD spectra of the wear debris collected from PTWA 1020 at 50N (high load) and 2m/s (high speed) shows that the debris consists of ferrite, and three types of iron oxides, namely Fe_2O_3 , Fe_3O_4 , and FeO .

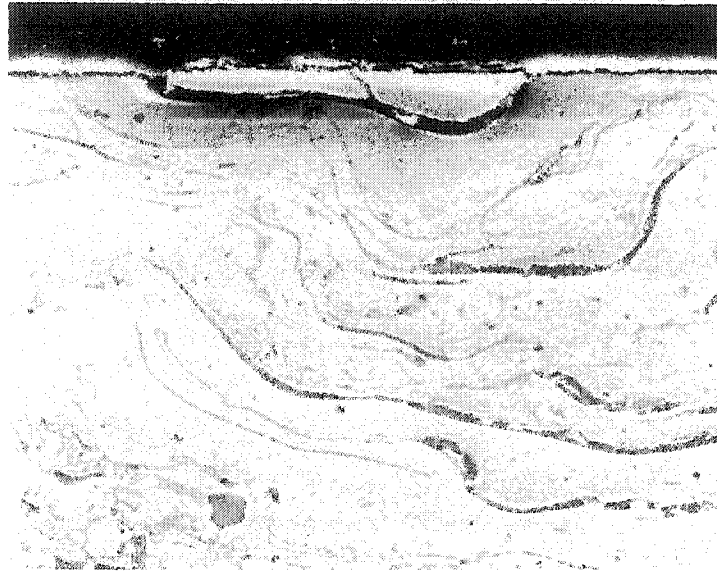


Fig. 4.20- A back-scattered SEM micrograph of the cross-section of the PTWA 1020 coating tested at 50 N and 0.5 m/s shows that the splat adjacent to the contact surfaces was deformed during wear and elongated in the sliding direction.

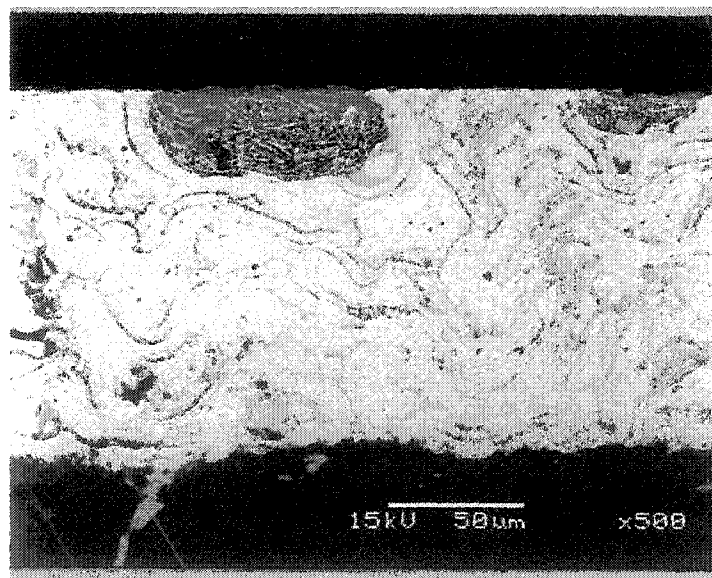


Fig. 4.21- The area beneath the worn surface of PTWA 1020 where the steel splats adjacent to the worn surface delaminated along the FeO veins within the coating causing removal of entire individual splats as a whole.

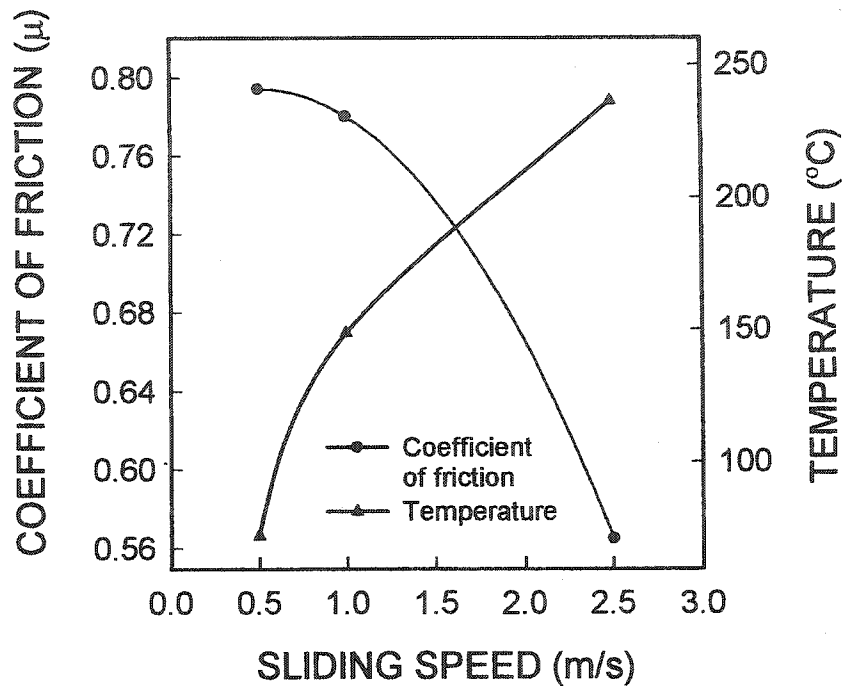


Fig. 4.22- The variation of the friction induced temperature rise of the pin, and the coefficient of friction with sliding speed for PTWA 1020 samples tested at a constant load of 50 N.

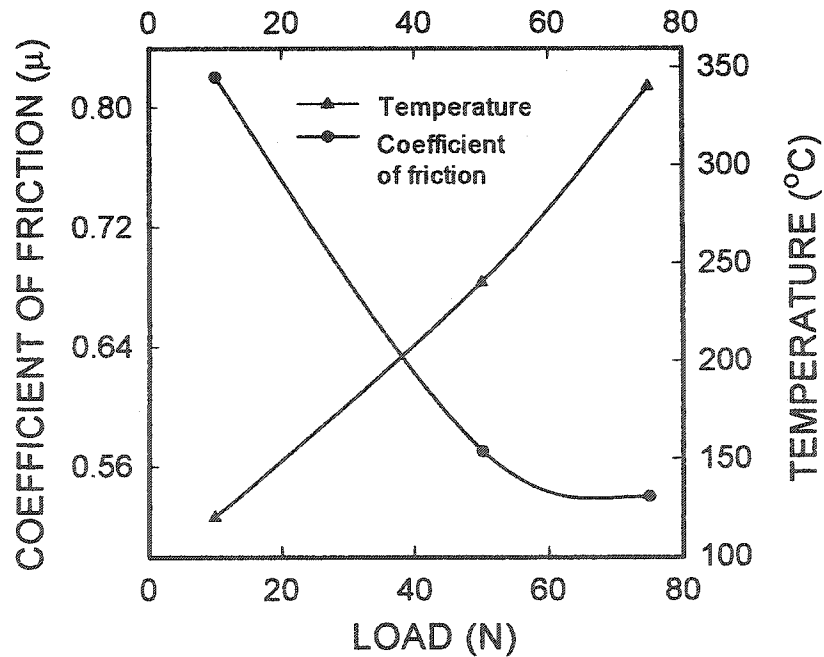


Fig. 4.23- The variation of the friction induced temperature rise of the pin, and the coefficient of friction with normal load for PTWA 1020 samples tested at a constant speed of 2.5 m/s.

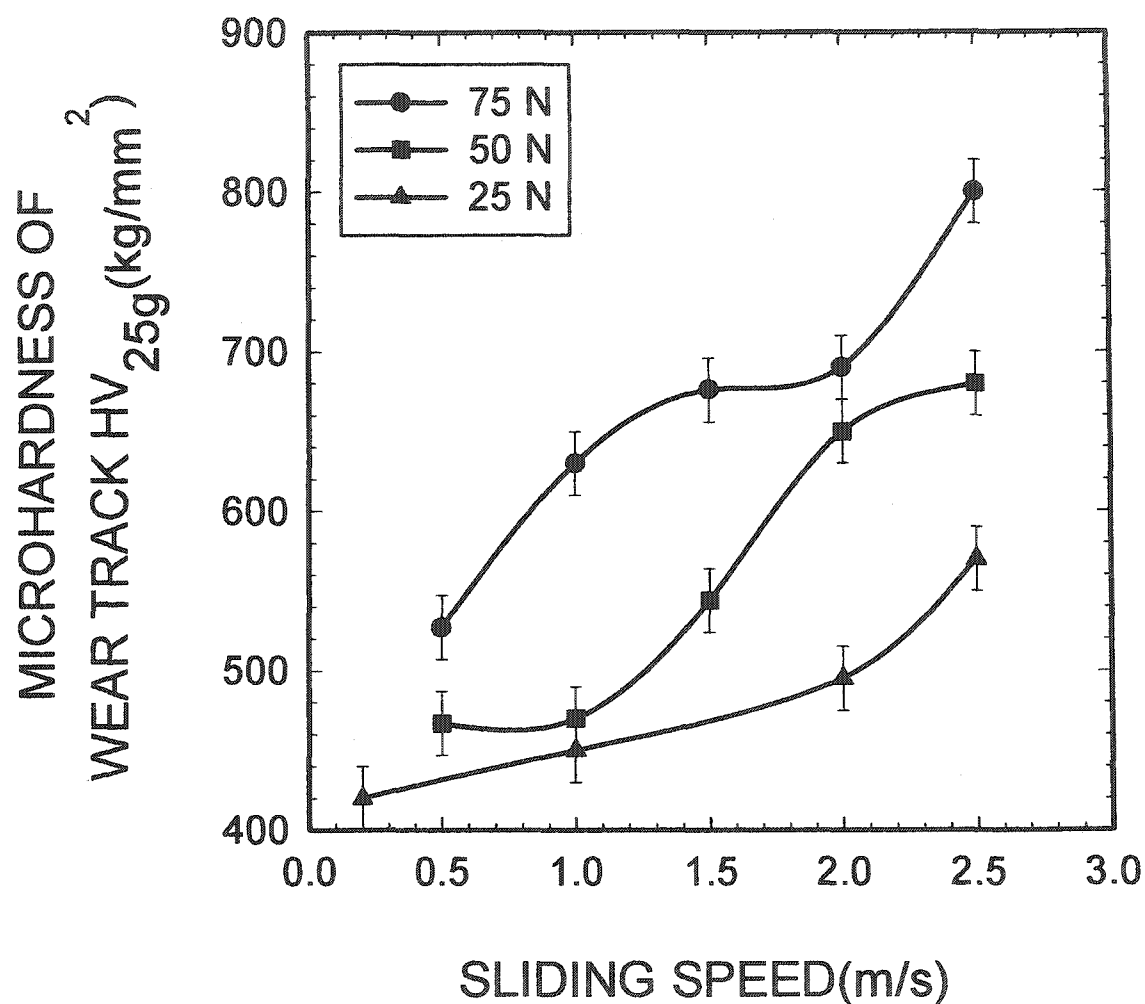
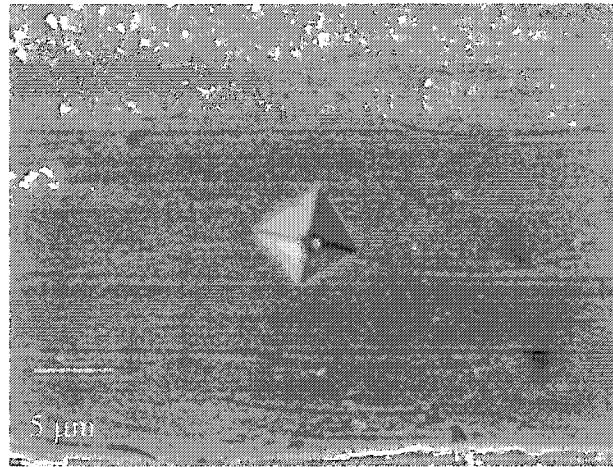
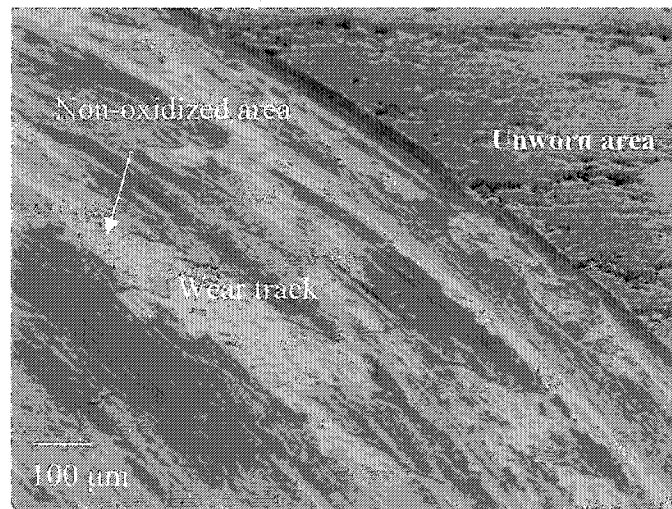


Fig. 4.24- The variation of hardness with sliding speed for high loads. The hardness measurements were taken from regions of the wear track where the PTWA 1020 coating was exposed through oxide deposit.



(a)



(b)

Fig. 4.25- (a) A Vickers indentation impression on the surface of a non-oxidized part of the wear track of the PTWA 1020 coating sample tested at 75 N and 2.5 m/s after 5000 m sliding distance, (b) the secondary SEM image from the coating tested at the same loading condition that shows the non-oxidized area on the wear track.

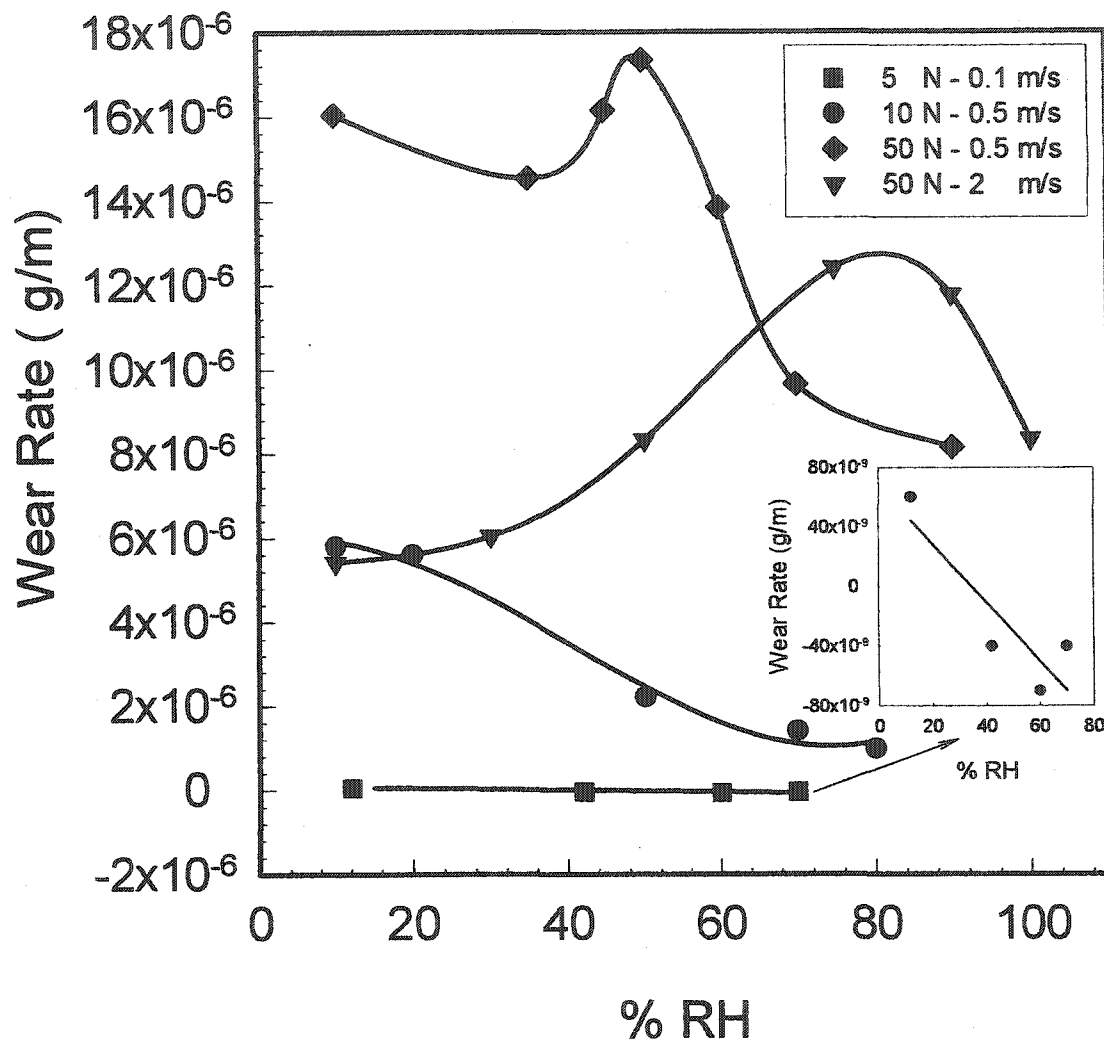


Fig. 4.26- Variation of wear rates of PTWA 1020 coatings with the relative humidity for four different testing conditions. The insert shows wear rates for tests at 5 N and 0.1 m/s at different humidity levels.

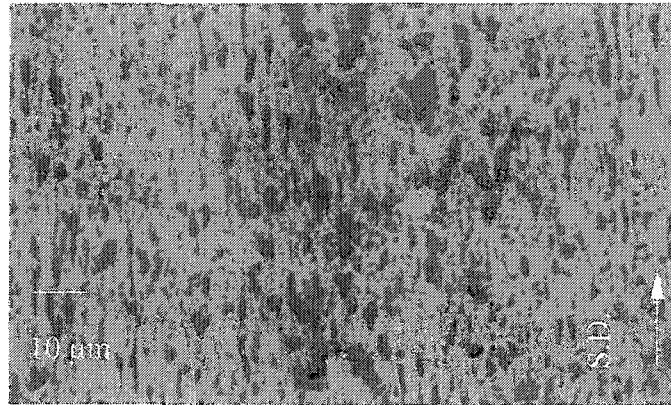


Fig. 4.27- A back-scattered SEM micrograph of a PTWA 1020 sample worn at 5 N load, 0.1 m/s sliding speed and 12% RH. The dark grey regions are thin oxide rich films, which are entrapped between the micro-scratches on the surface of the steel splats (medium grey regions).

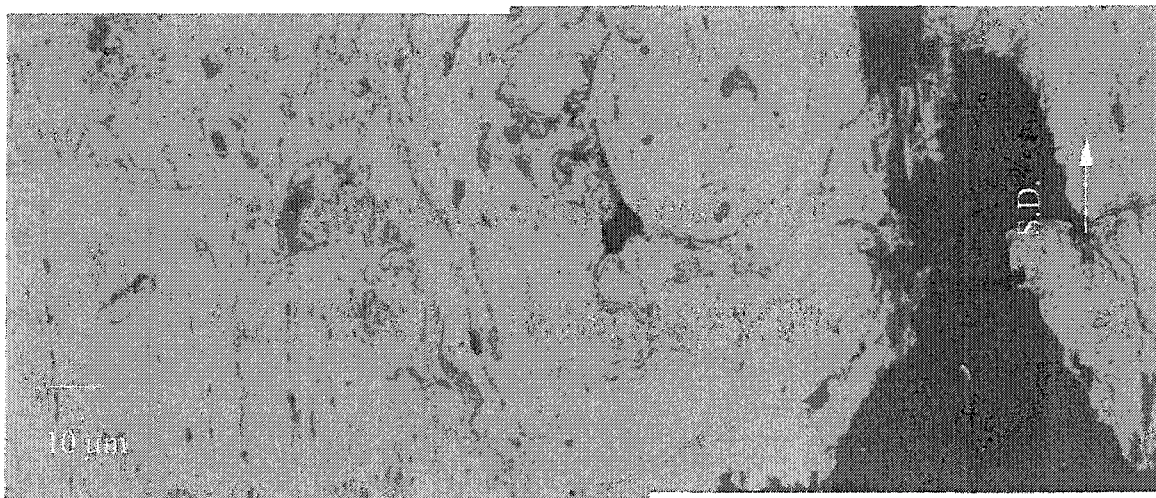


Fig. 4.28- A back-scattered SEM micrograph of a PTWA 1020 sample worn at 5 N load, 0.1 m/s sliding speed and 80% RH. The metallic parts are highly polished, and the oxide layers between the splats (dark grey veins) are noticeable. The porosity and the space between the contact areas are filled by the oxide layers, which were removed from the contact surfaces (dark grey regions).

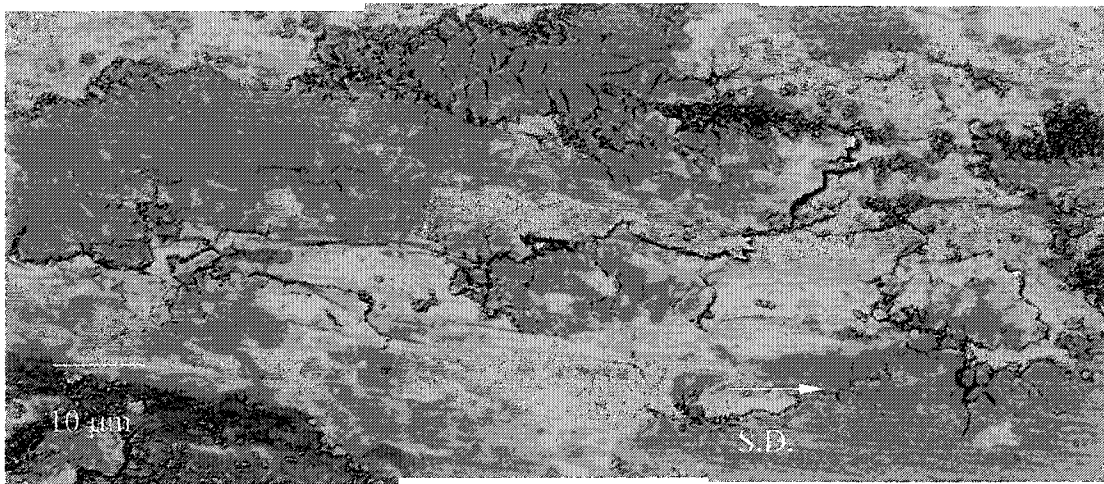


Fig. 4.29- A back-scattered SEM micrograph of a PTWA 1020 sample worn at 50 N load and 0.5 m/s and 50% relative humidity. The edges of the deformed steel splats show fracture and fragmentation.

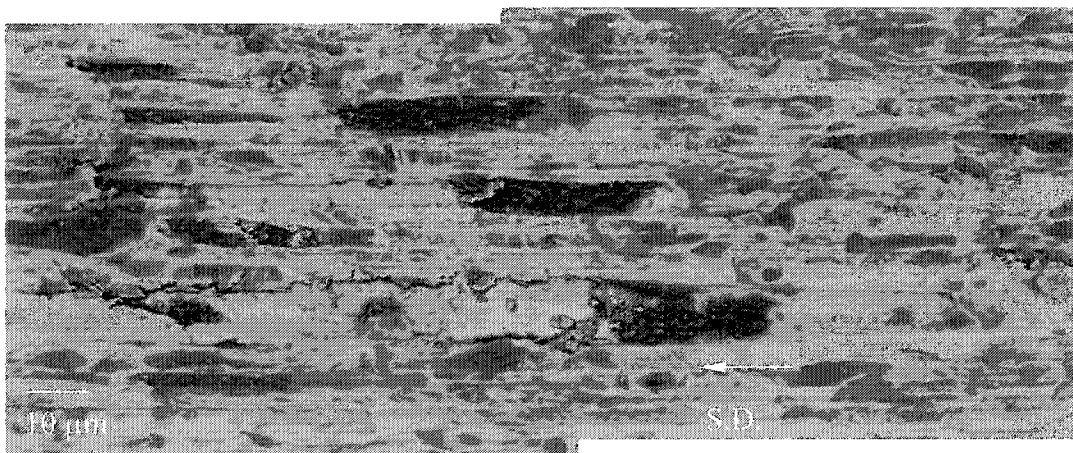


Fig. 4.30- A back-scattered SEM micrograph of a PTWA 1020 sample worn at 50 N load and 0.5 m/s and 90% relative humidity. The polishing wear mechanism is active at this relative humidity level, but there is still evidence of fracture.

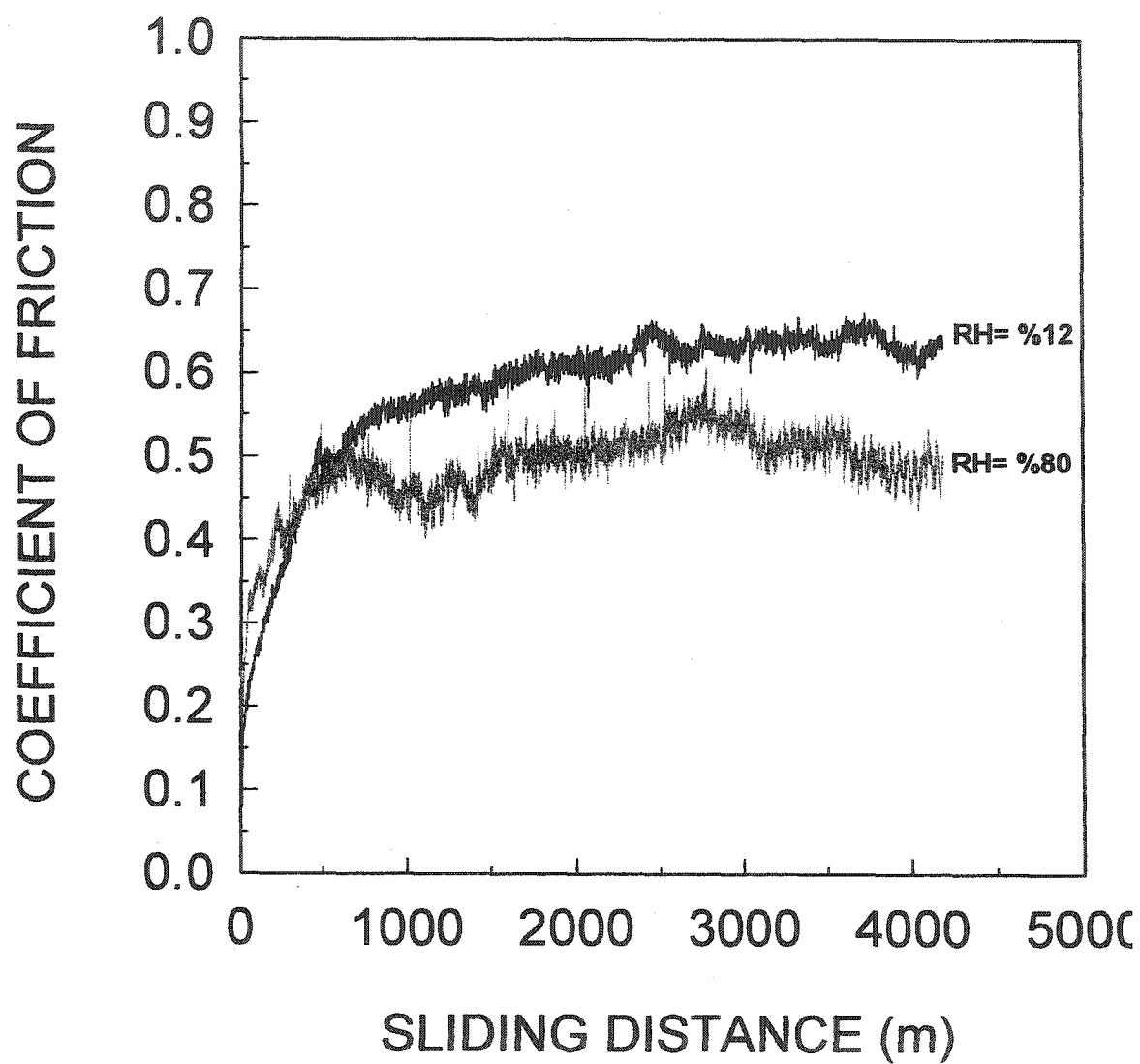


Fig. 4.31.a- A variation of the coefficient of friction with the sliding distance at different humidity levels for the PTWA 1020 coatings tested at 5 N - 0.1m/s.

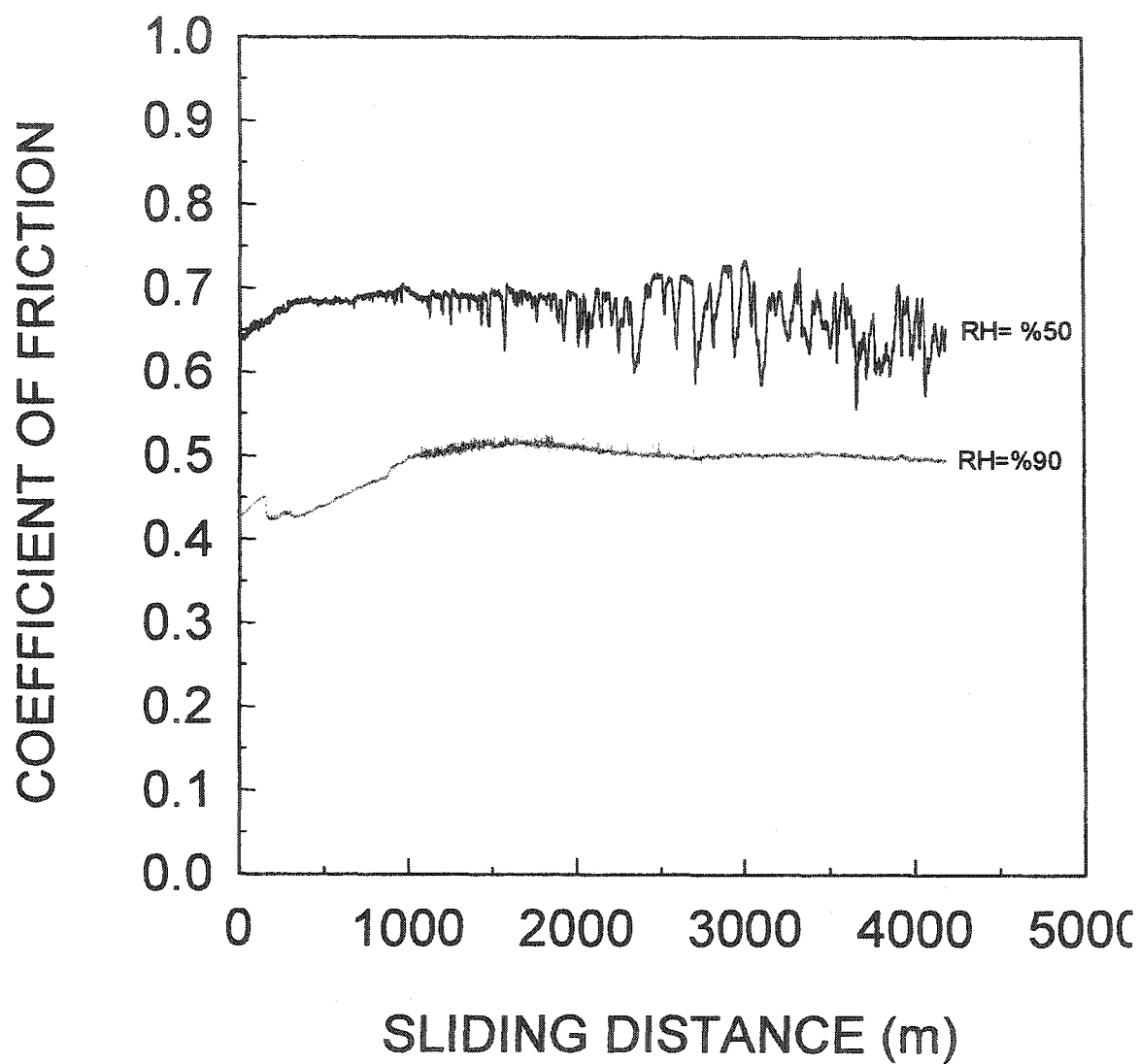


Fig. 4.31.b- Variation of the coefficient of friction with the sliding distance at different humidity levels for the PTWA 1020 coatings tested at 50 N - 0.5m/s.

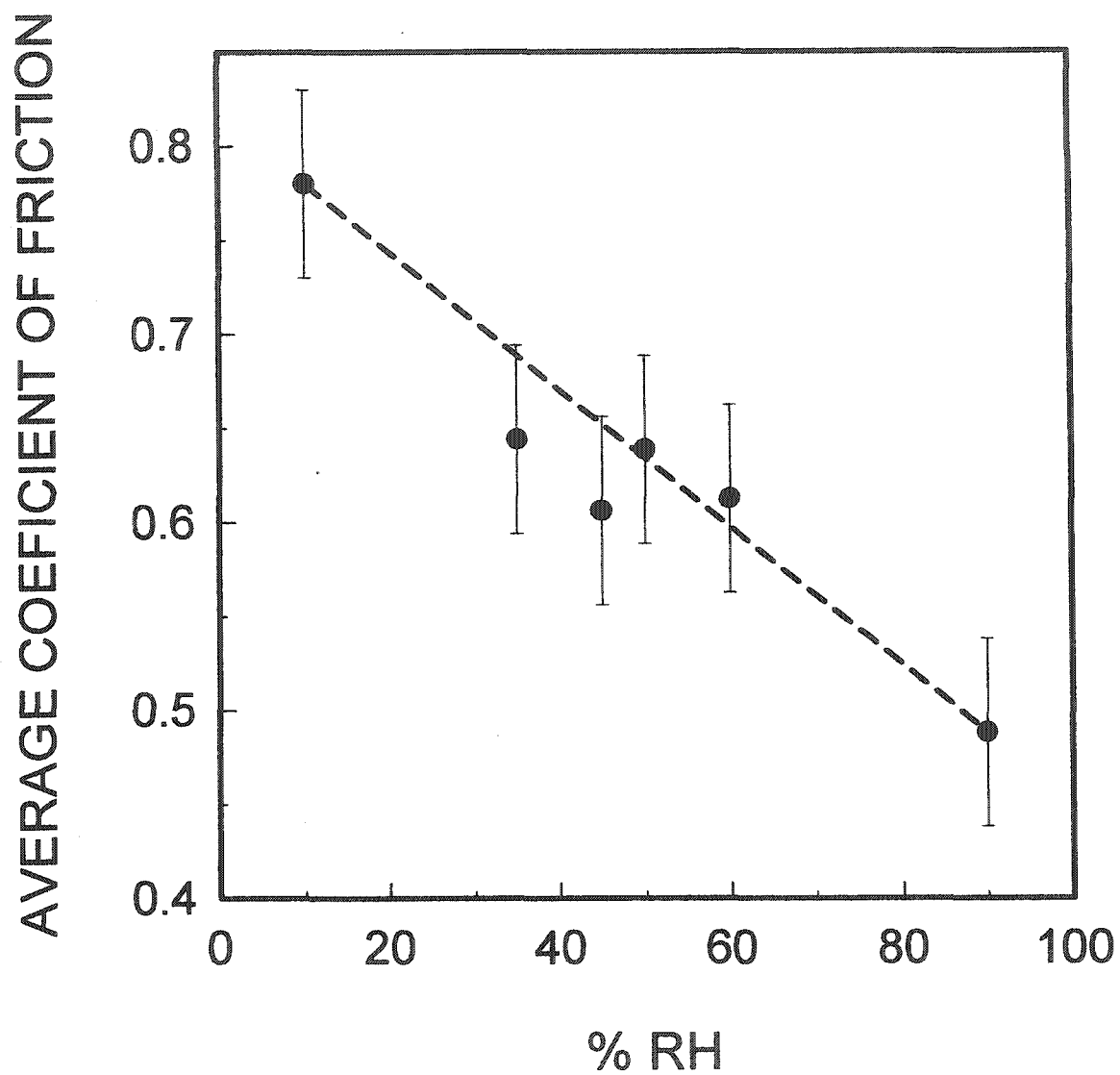


Fig. 4.32- The change in the average coefficient of friction of PTWA 1020 coatings for the wear tests performed under 50 N, 0.5 m/s loading condition as a function of humidity.

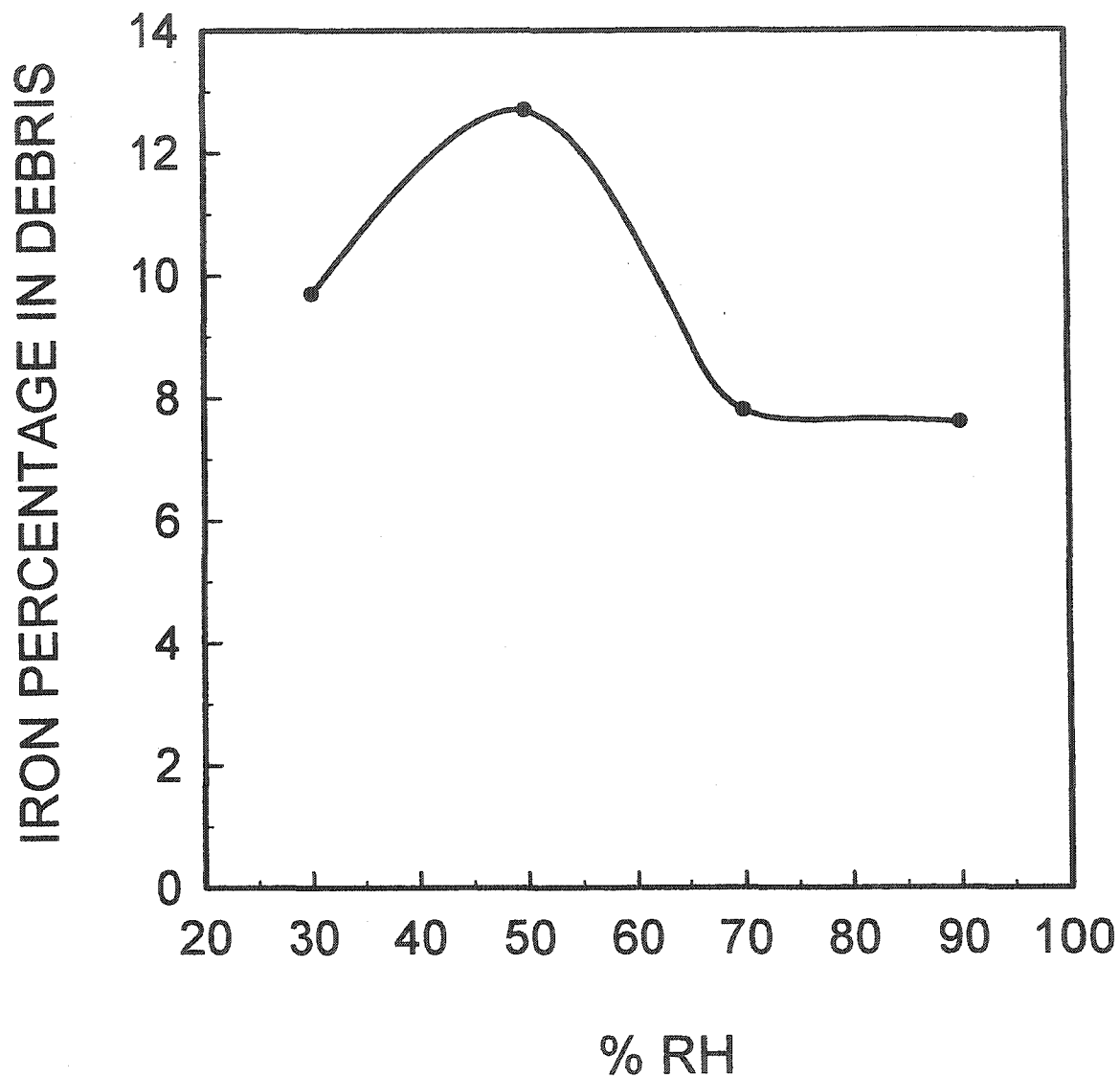
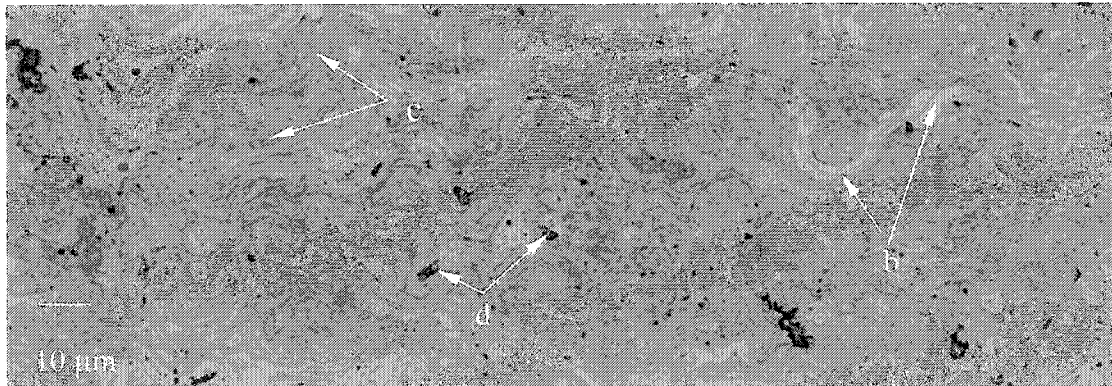
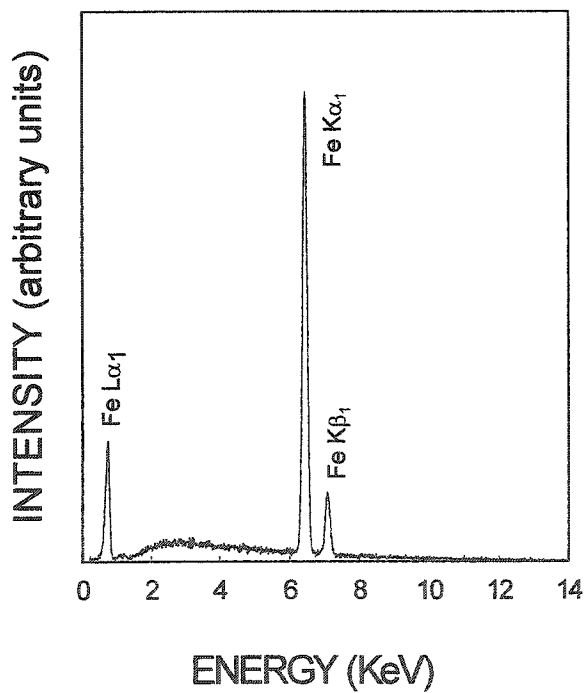


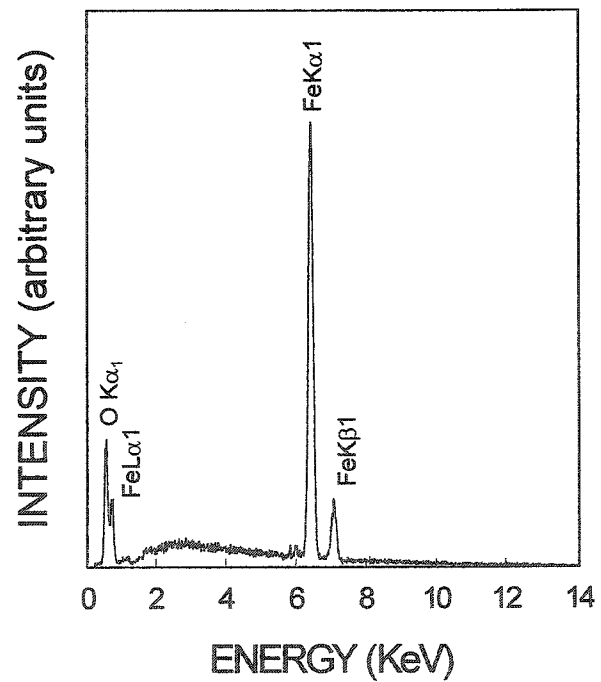
Fig. 4.34- The fraction of the elemental iron content of debris of PTWA 1020 obtained from wear tests performed at 50 N and 0.5 m/s as a function of the relative humidity of the wear environment. The quantitative phase analysis was obtained from the Rietveld analyses with an accuracy of $\pm 0.5\%$. The iron content follows a similar trend as the wear rate.



(a)

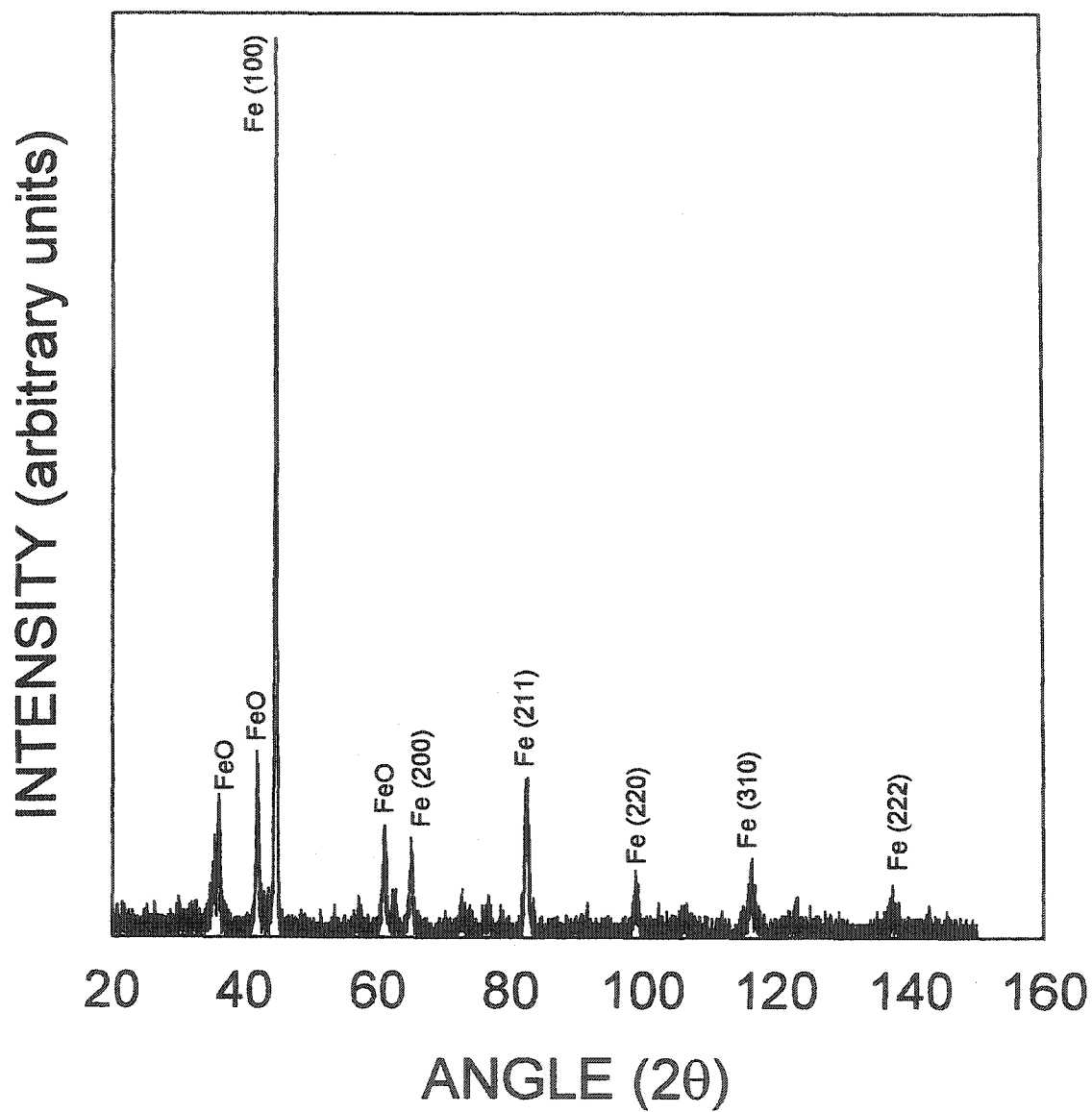


(b)



(c)

Fig. 4.35- Microstructure and composition of HVOF 1020 coatings: (a) is a back-scattered SEM micrograph showing the cross-sectional microstructure. The light areas labelled (b) in the micrograph are the steel splats, (see the EDS spectrum of (b)); the dark grey regions labelled (c) consist of Fe and O as shown in the EDS spectrum of (c); the black regions labelled (d) are the pores.



(d)

Fig. 4.35.d- XRD spectrum of HVOF 1020 confirming the presence of iron and (FeO).

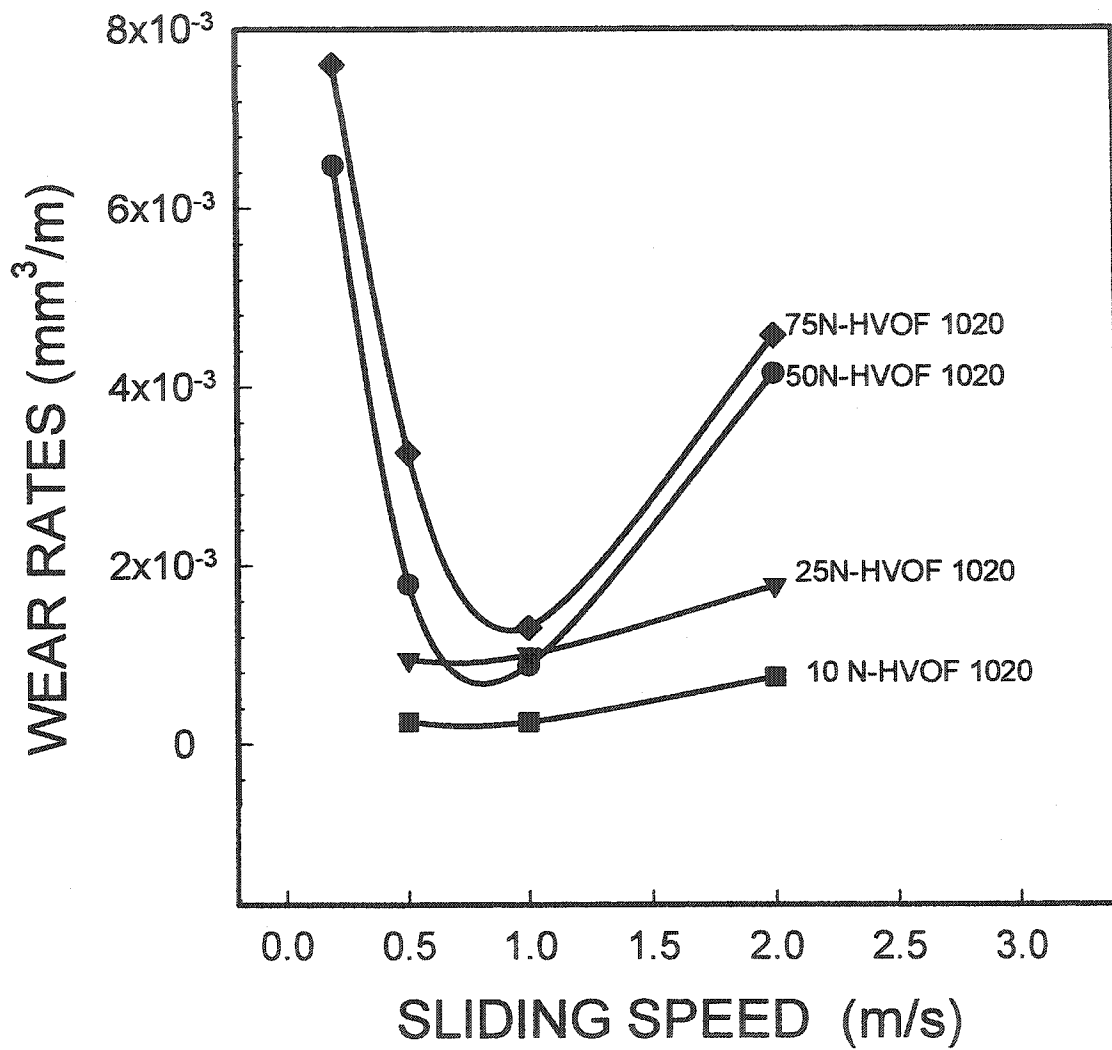
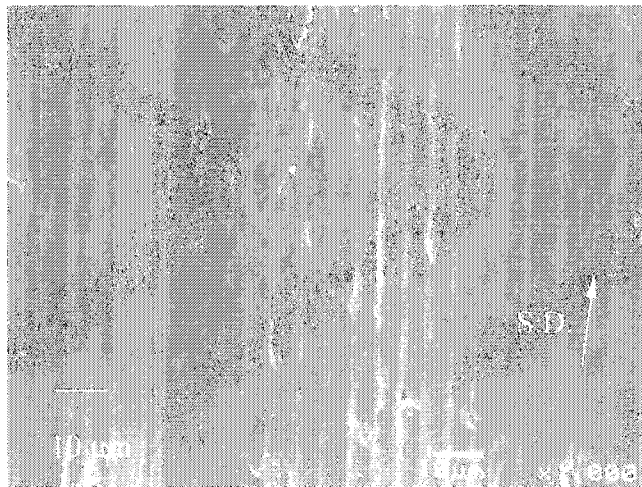
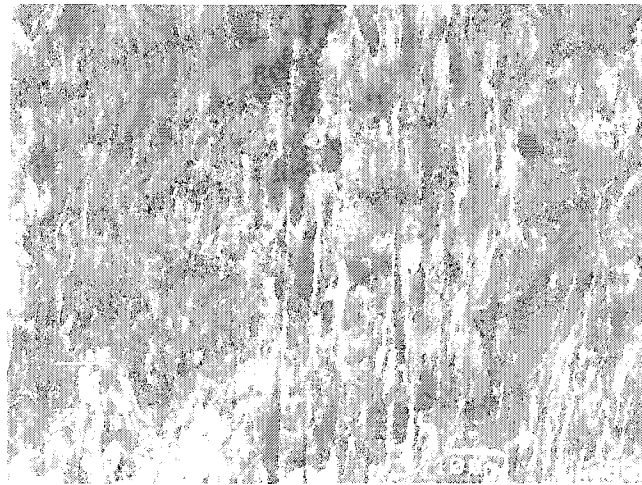


Fig. 4.36- Variation of wear rates (mm^3/m) of the HVOF 1020 coatings is plotted as a function of sliding speed at several load levels of 5 N, 10 N, 25 N, 50 N and 75 N.



(a)



(b)

Fig. 4.37– (a) Secondary and (b) back-scattered SEM images of the worn surface of the HVOF 1020 coating tested at 10 N load and 0.5 m/s sliding speed after 5000 m sliding distance.

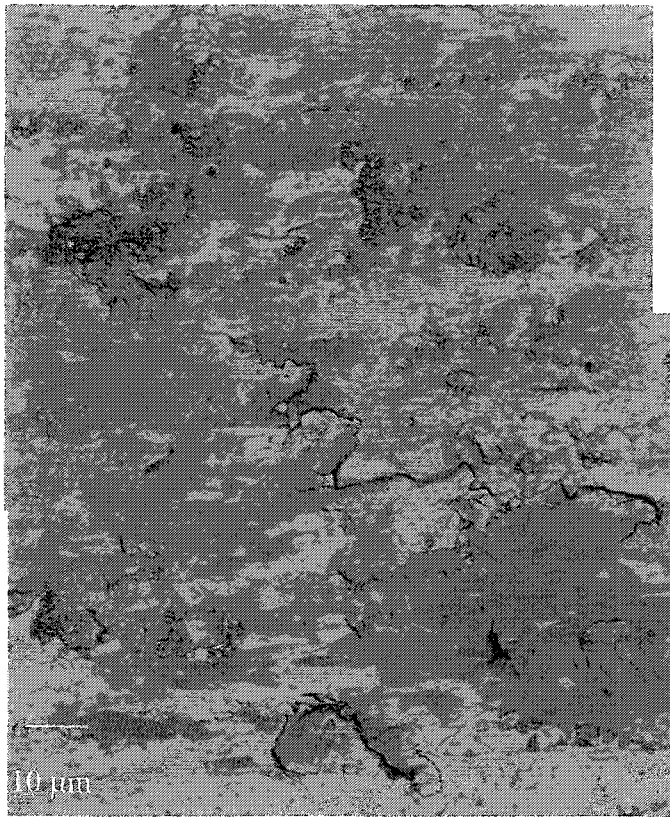


Fig. 4.38- A back-scattered SEM micrograph of the worn surface of the HVOF 1020 coating tested at 75 N load and 0.5 m/s shows severe plastic deformation on the sliding surfaces.

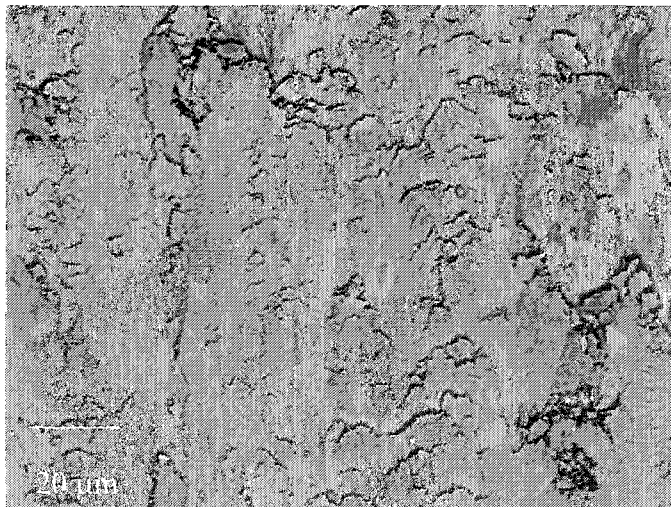


Fig. 4.39- A back-scattered SEM micrograph of the worn surface of the HVOF 1020 coating tested at 75 N load and 0.5 m/s shows severe deformation and fracture at the tip of the splats on the contact surface.

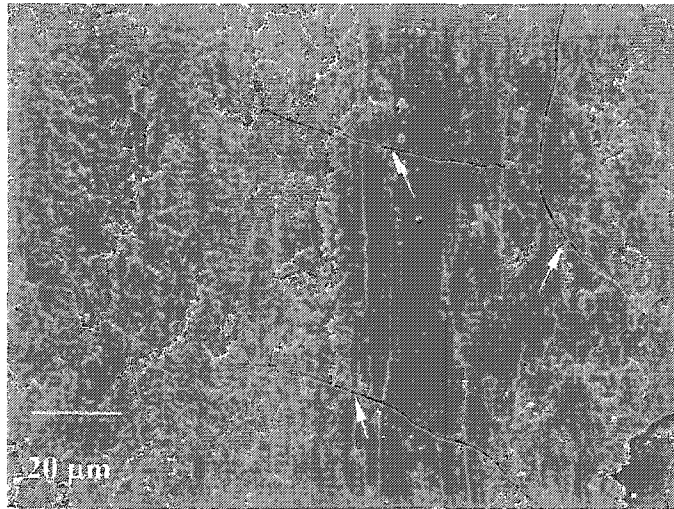


Fig. 4.40- A secondary SEM micrograph of the worn surface of the e HVOF 1020 coating tested at high load (75 N) and high sliding speed (2 m/s) after 5000 m sliding distance that shows a severely deformed and damaged surface associated with the cracks (marked with arrows) normal to the sliding direction.

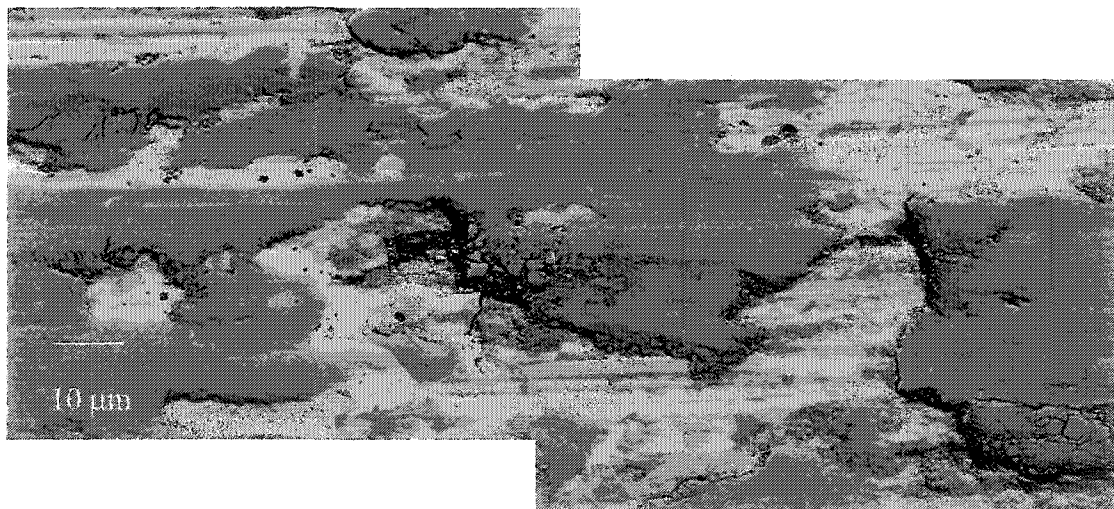


Fig. 4.41- A back-scattered SEM micrograph of the HVOF 1020 coating tested at 50 N load and 2 m/s. The micrograph was taken from a region on the wear track, which shows evidence for surface oxidation during sliding.

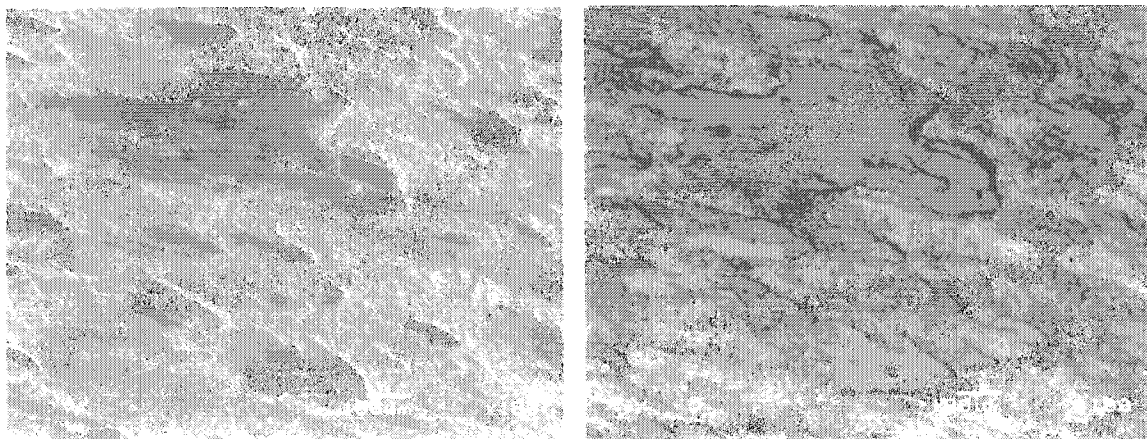


Fig. 4.42- A low magnification back-scattered SEM image from the worn surface (on a tilted angle 60°) of the HVOF 1020 coatings tested at 50 N and 2 m/s shows that the worn surface has a high roughness along with scattered oxide patches.

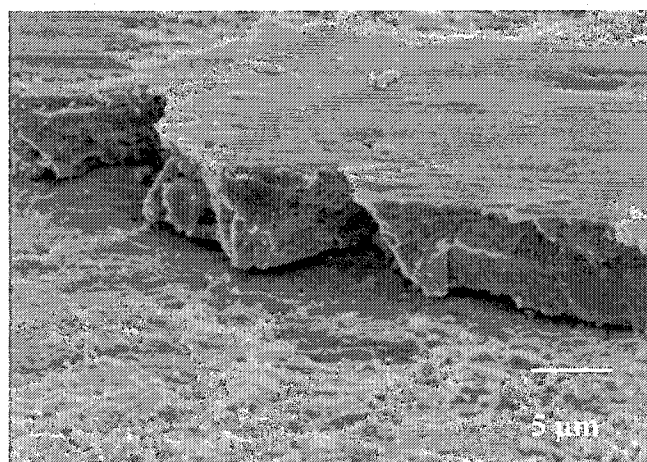


Fig. 4.43- A secondary SEM image of the HVOF 1020 that shows the 7 μm thick oxide rich films that formed on the sliding surface of the coating tested at 75 N and 2 m/s after 5000 m sliding distance.

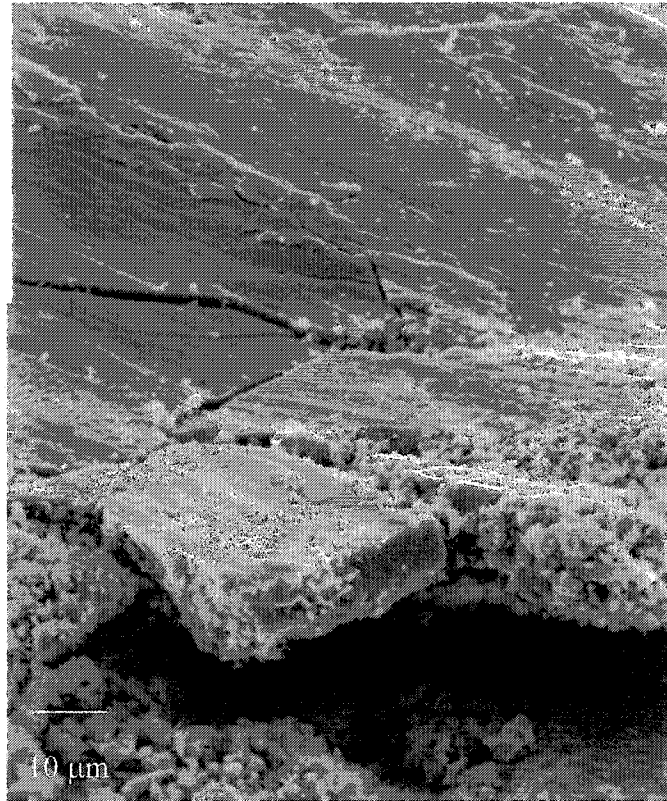


Fig. 4.44- Another example of the formation of the thick oxide layers of the HVOF 1020 during sliding at high loading conditions. The figure also shows cracking in the oxide film.

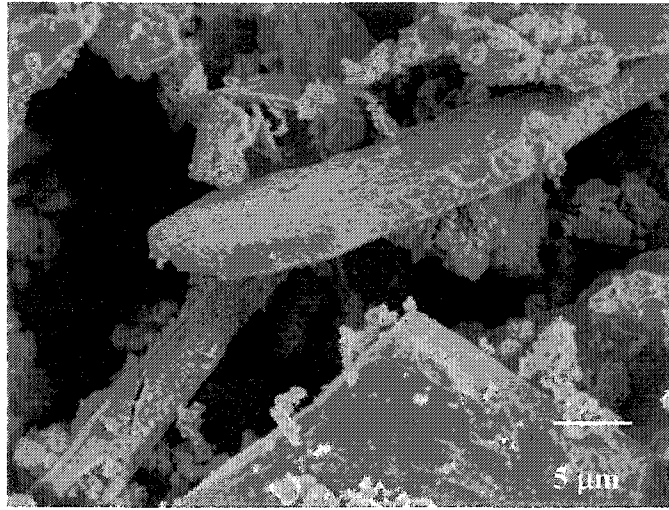
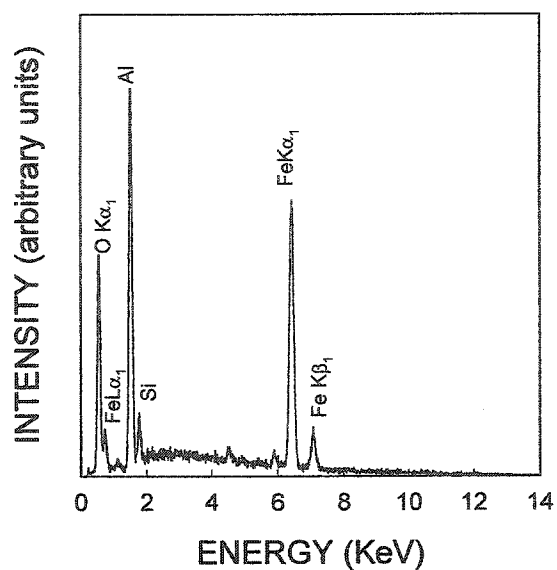
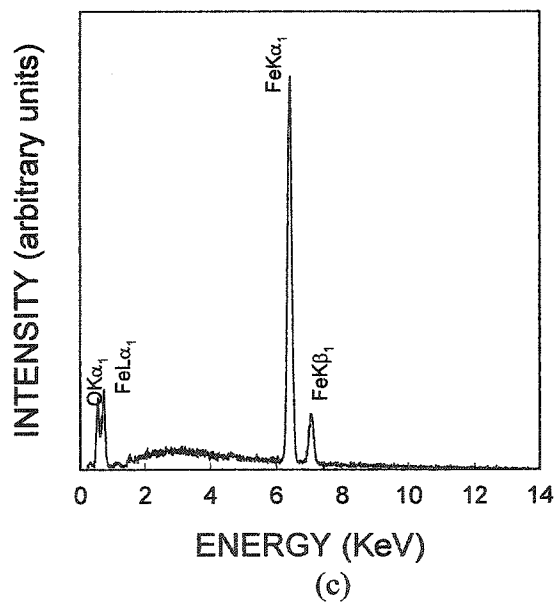
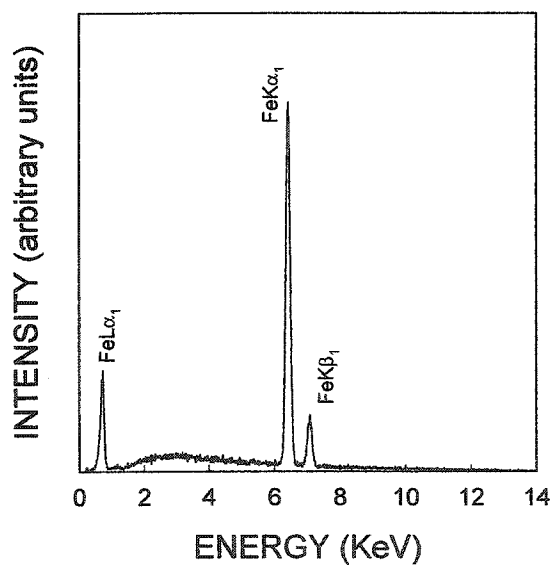
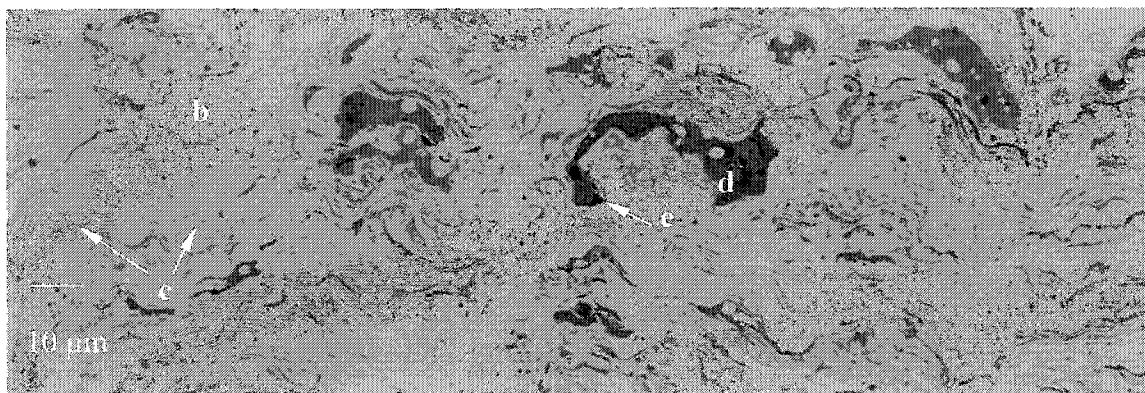
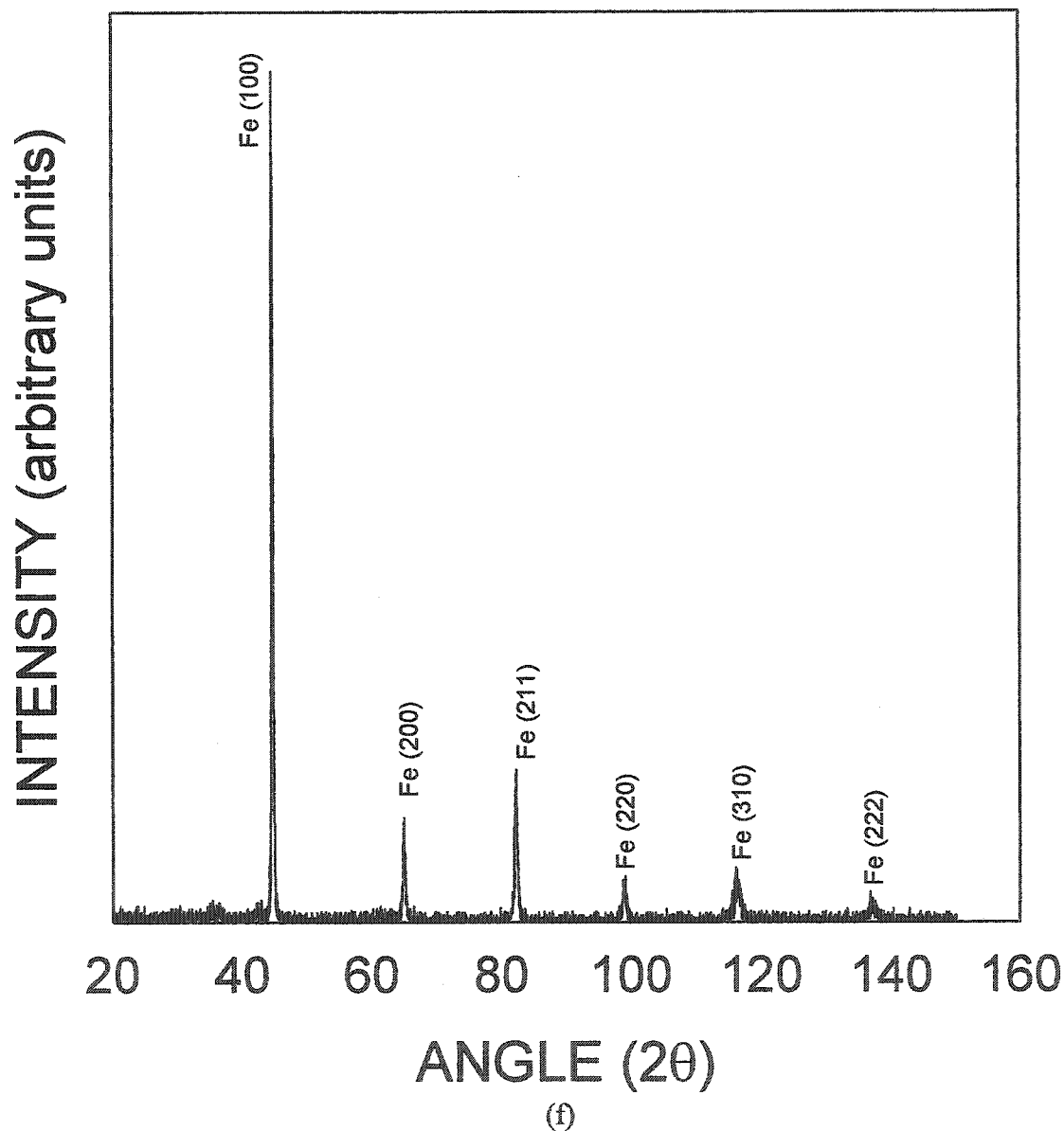


Fig. 4.45— A secondary electron SEM image from the debris gathered from the HVOF 1020 tested under 75 N and 2.5 m/s shows the plate-like iron oxide debris.





(f)
Fig. 4.46- Microstructure and composition of HVOF 1020-2.5% Al coatings: Fig. 4.46.a is a back-scattered SEM micrograph showing the cross-sectional microstructure. The light areas labelled (b) the steel splats (see EDS spectrum of Fig. 4.46.b); the medium grey regions labelled (c) are the iron oxide veins that consists of Fe and O as shown in the EDS spectrum of Fig. 4.46.c; the dark grey regions labelled (d) are inclusions consisting of Al, Fe and O as shown in the EDS spectrum of Fig. 4.46.d; the black regions labelled (e) are the pores. Fig. 4.46 f is the XRD spectrum of this coating.

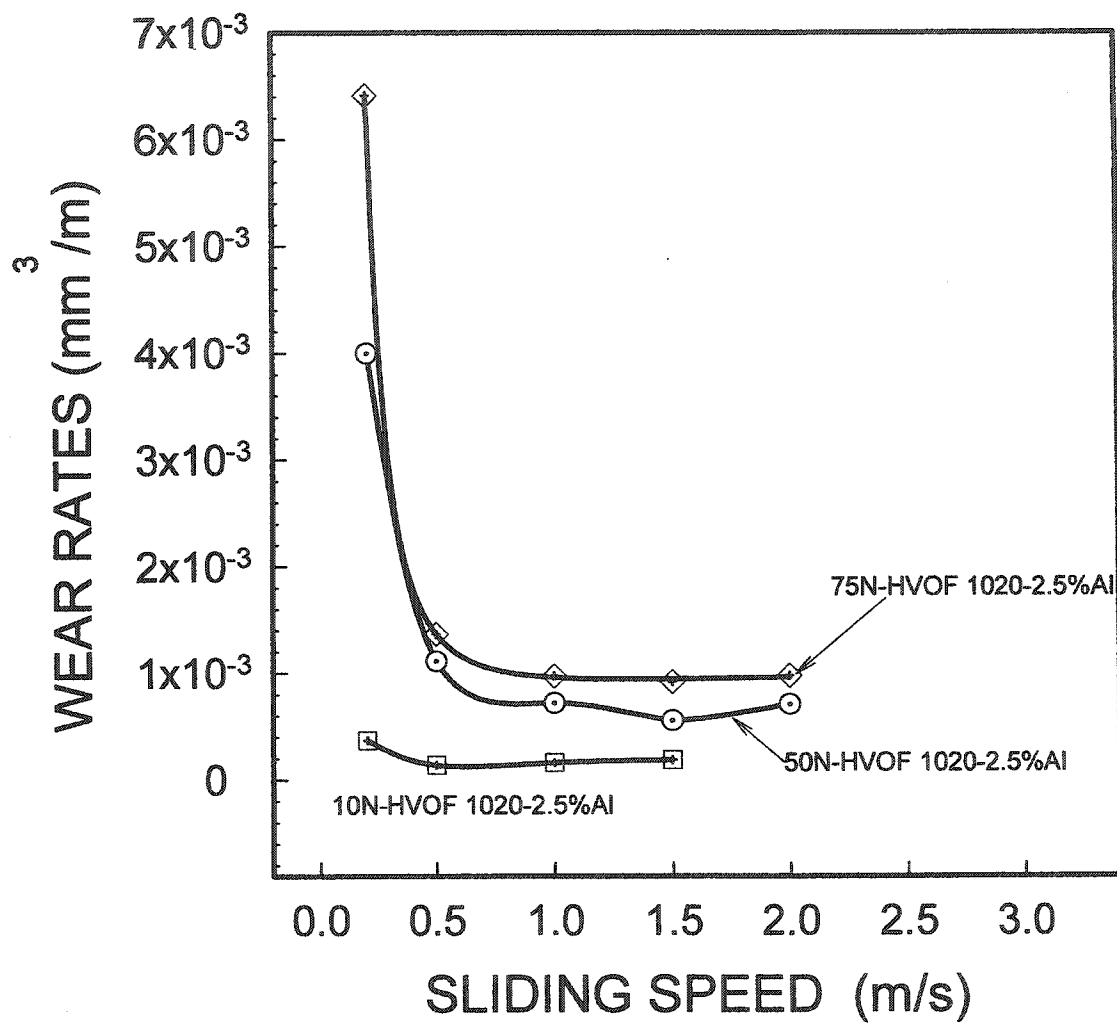


Fig. 4.47- The variation of the wear rates (mm³/m) of the HVOF 1020-2.5% Al coatings is plotted as a function of sliding speed at load levels of 5 N, 10 N, 25 N, 50 N and 75 N.

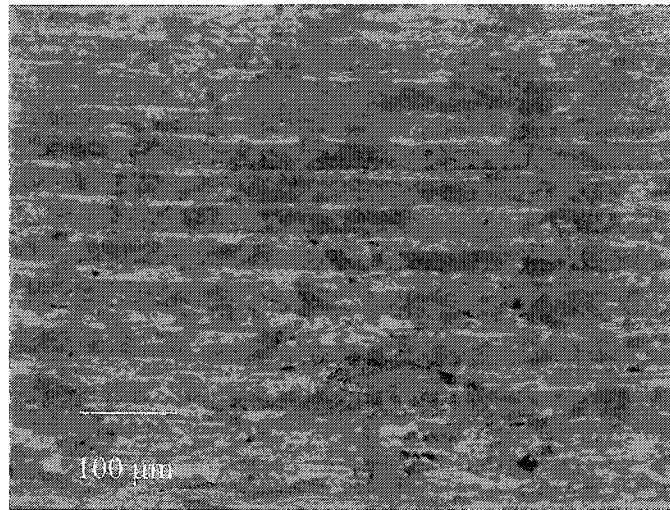


Fig. 4.48- A back-scattered SEM micrograph was taken from the worn surface of the HVOF 1020-2.5% Al coating tested at 75 N and 2 m/s, which shows the scratches at low magnification.

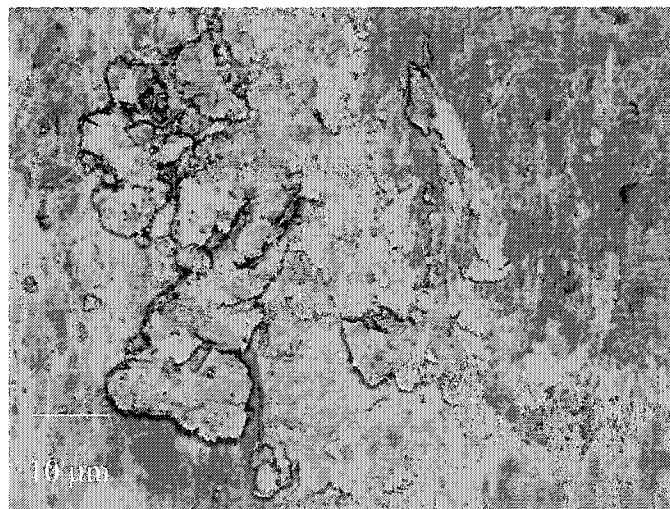


Fig. 4.49- A back-scattered SEM image that was taken from the worn surface of the HVOF 1020-2.5% Al coating tested at 75 N load and 0.2 m/s that shows that the metallic fragments were flattened and forged on the sliding surface.

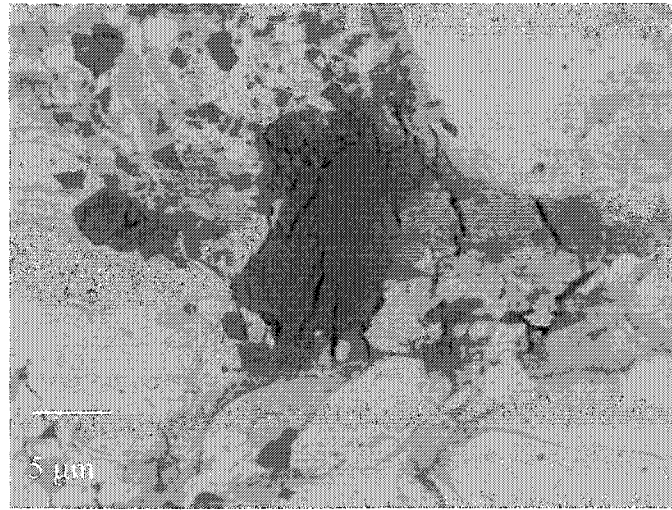


Fig. 4.50- A back-scattered SEM micrograph shows the fracture of the inclusions into the small particles which can act as abrasive and scratch the sliding surfaces of HVOF 1020-2.5% Al.

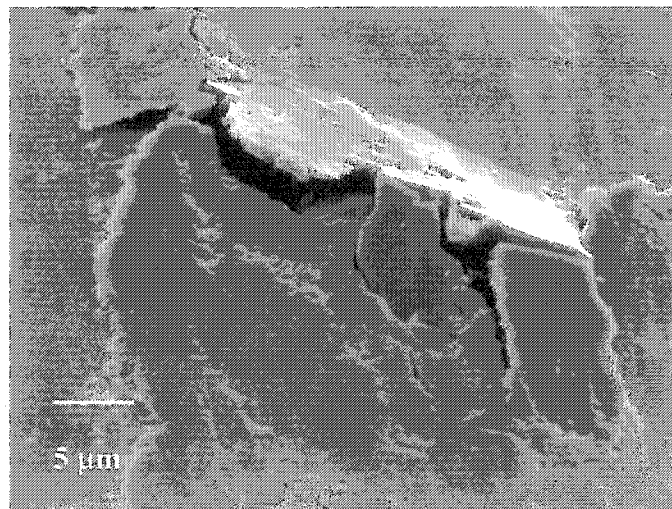


Fig. 4.51- A secondary SEM micrograph (on a 60° angle) showing the morphologies of the worn surface of HVOF 1020-2.5% Al coatings tested at 75 N load and 2 m/s sliding speed. Iron oxide layers on the worn surface are about 1 μm thick.

CHAPTER V

DISCUSSION OF THE RESULTS:

WEAR MECHANISMS AND WEAR MAPS

The results presented in Chapter IV are discussed in this chapter. The current chapter is organized as follows:

- 1) The micromechanisms that control the wear rates in the thermal spray coatings are discussed. These mechanisms are divided into several groups. They are: a) Mechanical wear (by severe plastic deformation and splat tip fracture, and splat delamination through oxide veins), b) Oxidational wear, c) Polishing wear, and d) Surface hardening. The first two of these mechanisms, namely mechanical wear and the oxidational wear were the most important mechanisms that operated under dry air. Polishing wear occurred under high humidity conditions. Significant surface hardening occurred during sliding wear at high loads and speeds.
- 2) The role of the coating microstructure and the production process of the thermal spray coatings on wear are discussed by comparing the wear tests results of the PTWA 1020 and the HVOF 1020 coatings. The discussion includes analysis of the friction induced temperature increase for both coatings. The surface temperatures generated at different loads and velocities are summarized in the form of temperature maps.
- 3) Wear rates and wear mechanisms that operate in thermal spray coatings, are summarized in the form of wear maps constructed for each of the coatings. The

wear maps show the wear rates as a function of applied load and speed. These maps could now be considered as practical guidelines for tribological applications of coatings under the actual service conditions.

- 4) The use of wear maps in material selection is illustrated by comparing the wear maps of the coatings among themselves and with that of aluminum.

Wear mechanisms that are common to all three coatings are illustrated using PTWA 1020 coatings as an example. The wear rates of the PTWA 1020 coatings at constant load decreased as the sliding speed increased to 1.0-1.5 m/s, at higher speeds the wear rates were almost constant as shown in Fig. 4.7 of Section 4.1.2. This behaviour became more obvious at high loads such as 50 N and 75 N, where the wear rates were higher initially, and decreased faster than those at lower loads. From Fig. 4.7, four wear regimes can be identified amongst the testing conditions. They are defined as low speeds ≤ 1 m/s, high speeds ≥ 1 m/s, low loads ≤ 20 N, and high loads ≥ 20 N. These regimes were defined according to the differences in the wear rates as well as in the chemical compositions and/or microstructures of the worn surfaces and the debris, and will be considered separately below. The characteristic features of the worn surfaces and debris are summarized in Table 5.1.a and b.

Low Loads $\leq 20\text{N}$

	Low Sliding Velocity $\leq 1\text{m/s}$	High Sliding Velocity $\geq 1\text{m/s}$
<u>Worn Surfaces</u>	Porous oxide rich patches, mostly located between deformed splats. Area percentage $\approx 20\%$.	Oxide rich layers extend on iron splats. Area percentage = 50%. No significant splat fracture.
<u>Wear Debris</u>	Dark orange non-magnetic powder.	Dark brown magnetic powder.
	Sub-micron particles of iron oxide.	Very small amount of sub-micron particles of iron oxide.
	Fe_2O_3 (99%) and Fe (XRD analysis).	Insufficient amount of debris generated for XRD analysis.
<u>Wear Mechanisms</u>	Heavy surface oxidation to Fe_2O_3 .	Formation of mixed iron oxides covering most of the coating surface. (lowest wear rates)

Table 5.1.a- Summary of metallographic observations of worn PTWA 1020 coatings at low loads $\leq 20\text{ N}$.

High Loads ($\geq 20\text{N}$)

	Low Sliding Velocity $\leq 1\text{m/s}$	High Sliding Velocity $\geq 1\text{m/s}$
<u>Worn Surfaces</u>	Extensive fracture of steel splat tips. ~ 25% of contact surface covered by oxide rich layer, with average thickness $< 1\mu\text{m}$. Average hardness = 450-550 (kg/mm^2).	Thick oxide rich layers (1-3 μm thick), covering ~ 70% of contact surfaces. Severe steel splat deformation but no significant fracture. Average hardness = 550-800 (kg/mm^2).
<u>Wear Debris</u>	Dark brown magnetic powder. Mainly deformed plate-like metallic iron fragments mixed with iron oxide particles. Fe_2O_3 , FeO, Fe_3O_4 & Fe (XRD analysis).	Black magnetic powder Thick iron oxide plates, occasionally containing iron fragments. Fe_2O_3 , FeO, Fe_3O_4 & Fe (lower Fe concentration compared to low velocity). (XRD analysis).
<u>Wear Mechanisms</u>	Fracture and fragmentation of steel splats at the contact surface (primary mechanism). (Highest wear rates)	Formation of a thick, protective iron oxide films reducing coefficient of friction. Hardening of steel splats during sliding.

Table 5.1.b- Summary of metallographic observations on worn PTWA 1020 coatings at high loads $\geq 20\text{ N}$.

5.1. MECHANICAL WEAR

5.1.1. SEVERE PLASTIC DEFORMATION AND SPLAT TIP FRACTURE

The highest coating wear rates were measured in the tests performed under the conditions of high loads and low speeds (Fig. 4.7). This was the case for all the three coatings tested. SEM and XRD results of the wear debris showed the presence of plate-like iron fragments mixed with small particles of iron oxide. The XRD spectrum of the wear debris of a PTWA 1020 sample tested at these loading conditions showed the presence of metallic ferrite, Fe_2O_3 , Fe_3O_4 , and FeO (Table 4.2). It is important to note that under these conditions, the percentage of ferrite in the debris in the three coatings was relatively high. Therefore, the wear mechanism at high loads and low velocities must account for the presence of the metallic ferrite particles in the wear debris (Table 5.1.b).

The typical type of damage that could be observed from the SEM images of the worn surface of the coatings tested at high loads and low velocities was the fracture of the iron splats. Iron fragments were formed and detached from the surfaces as a result of fracture of the splats that were subjected to severe plastic deformation. In particular, the tips of the splats on the contact surfaces were severely deformed and fractured.

Damage accumulation events resulting in the splat tip fracture is shown schematically in Fig. 5.1. At the first stages of sliding (Fig. 5.1.a), iron splats adjacent to the contact surfaces start to deform and elongate in the direction of sliding. These splats have nominally 0.2% C, and hence have high ductility that can accommodate large surface strains imposed during sliding. At the subsequent stage, as the sliding continues, more deformation is induced especially at the tips of splats, which become progressively work hardened (Fig. 5.1.b) as they elongate parallel to the direction of the imposed strain.

Finally, the exhaustion of ductility of the material at the splat tips causes fracture and fragmentation as shown in Fig. 5.1.c. Examples of fractured splat tips can be seen in Fig. 4.11. Occasionally, repeated fracture and fragmentation of splats progresses to a degree where the entire splat is lost. Porosity or surface defects makes this mechanism worse. Steel splats adjacent to surface depressions can plastically deform and elongate into these regions more easily than in dense smooth regions that are self-supporting.

5.1.2. SPLAT DELAMINATION THROUGH THE OXIDE VEINS

Another wear mechanism that operates in the coatings is the delamination or removal of entire splats. Oxide layers between splats are considered as the weakest link in many spray deposited coatings [6]. In order to observe the fracture behaviour of the coatings during bending, PTWA 1020 coated 319 Al alloy samples were subjected to three point bending tests. Rectangular samples 10 mm wide, 25 mm in length, and 1 mm thick were tested using a specially constructed miniature three point bending jig. Round pins (4 mm in diameter) were put in contact with the lower face of the aluminum substrate (away from the coating) as shown in Fig. 5.2. The load was increased in regular steps of about 20 N to a maximum of 160 N. The cross-sectional morphology of the coating tested at 160 N is shown in Fig. 5.3. It is seen that a large crack perpendicular to the contact surface propagated through the coating into the substrate. The path of the crack was more torturous in the coating, but relatively straight in the 319 Al substrate. A high magnification micrograph of the fractured PTWA 1020 is given in Fig. 5.4. It was observed that the path of the crack followed the oxide veins, and splats along the crack

path were delaminated. This observation has proven that the oxide veins are the weakest link in the coatings.

In previous publications [e.g., see 7], high wear rates were generally associated with the formation and propagation of subsurface cracks within the oxide veins in the thermal spray deposited coatings, resulting in the removal of entire steel splats during the sliding process. The splat orientation and surface waviness were suggested to have an influence on the delamination mechanism. Delamination was shown to be easier when the splats were parallel to the coating surface, and more difficult when they were wavy and not parallel to the interface

Splat delamination was observed in the coatings tested in this work. An example is shown in Fig. 5.5. However, this was not a dominant wear mechanism for the thermal spray coatings. The severe surface delamination leading to the localized fracture (Fig. 5.2) of the splat tips was by far the most common type of mechanical wear mechanism.

5.2. OXIDATIONAL WEAR

The observations of the worn surfaces of PTWA 1020 coatings showed that for most loading conditions, surface oxidation created a chemically altered layer that played a critical role in controlling the wear rates.

At high speeds and low loads, the wear rates had the lowest values compared to the other regimes. The SEM investigations of the worn surface of the coatings tested under these conditions showed a deposit of an oxygen rich film on the sliding surfaces. This layer extended over the top of the steel splats. The measured pin temperature for the

sample tested at 10 N and 2.5 m/s was 110°C, which indicated that surface oxidation was likely to occur. The oxide layers were almost continuous acting as the protective layers.

The wear rates of the coatings at high loads and high speeds were about 50% lower than those measured at similar loads, but using low sliding speeds. The temperature measurement results presented in Section 4.1.6. showed that surface temperatures reached higher values. The high surface temperatures reduced wear rates by producing a uniform oxide layer on the sliding surface of the coatings that suppressed the splat tip fracture mechanism. An investigation of the plotted pin temperatures (Figs. 4.23 and 4.24) showed that the sliding induced temperature rise was influenced more by the sliding speed than the load. The maximum bulk temperature rise occurred on the samples tested at 75N and 2.5 m/s, where the increase was about 390°C. SEM investigations from the worn surface of the coating tested at this loading condition showed that the splat tip fracture mechanism that was responsible for the high wear rates at low load and velocity conditions was not as significant when the sliding speed was high. About 70% of the wear track of the coating tested at high loads and speeds were covered with a uniform oxygen rich film whose thickness varied between 1-3 μm (Fig. 4.15). The results on the variation of the coefficients of friction as a function of the sliding speed showed that by increasing the speeds from 0.5 to 2.5m/s at 50 N load, the coefficient of friction decreased from 0.78 to 0.56, which is consistent with the formation of oxide rich films and less metal to metal contact. The XRD spectrum of the wear debris gathered from the test carried out on the coating that was tested at these loading conditions showed the presence of Fe_2O_3 , Fe_3O_4 , and FeO type iron oxides. The quantitative phase analysis showed the relative amount of ferrite at high velocity was significantly lower.

Therefore, the oxide layers that were composed of mixed oxides appeared to reduce the wear rates by protecting the surfaces from mechanical wear. Wear occurred by the spallation of oxide layers (Fig 4.15). In PTWA 1020 coatings, these layers reached a thickness of 1-3 μm before they became detached from the surface.

5.2.1. COMPARISON OF WEAR RATES DUE TO OXIDATIONAL WEAR IN PTWA 1020 AND HVOF 1020 COATINGS

As shown in Fig 4.6, the wear rates of the PTWA 1020 coatings, and the HVOF 1020-2.5% Al coatings (Fig. 4.48) decreased by increasing the sliding speed, at sliding speeds greater than 1 m/s. In contrast, the wear rates of the HVOF 1020 coatings increased by increasing the speed (Fig 4.37), and were significantly higher than those of the PTWA 1020 and HVOF 1020-2.5% Al coatings in this speed range, especially when tested at high loads. According to Tables 4.2 and 4.4, when the sliding speed increased from 0.5 m/s to 2 m/s at a high load (e.g., 50 N), the constituents of the debris remained the same for all three coatings. They consisted of iron and three types of iron oxides, (Table 5.1) although the relative amounts of the oxide phases increased at the expense of native iron in the debris. The iron oxide rich layers generated on the contact surfaces of HVOF 1020 samples were thicker compared to PTWA 1020, and HVOF 1020-2.5% Al. The worn surface of the HVOF 1020 coatings tested at 75 N and 2 m/s is shown in Fig. 4.44. At this loading condition, the average thickness of oxide layers formed on the sliding surface of PTWA 1020 (Fig. 4.15) and HVOF 1020-2.5% Al (Fig. 4.51) varied between 1 and 3 μm . However, the high wear rates of HVOF 1020 observed under similar loading conditions were associated with the formation of a much thicker oxide

rich films, about 7 μm , as shown in Figs. 4.44 and 4.45. The oxide layers on the HVOF 1020 was discontinuous, and the worn surfaces were rough compared to the worn surfaces of the two other coatings. Therefore, severe oxidation and spallation of the thick oxide layers were responsible for the high wear rates of HVOF 1020 at high loads and speeds.

5.2.2 THE ROLE OF SURFACE TEMPERATURE ON OXIDATIONAL WEAR

The contact surface temperatures in HVOF 1020 reached higher values compared to other coatings tested under the same sliding conditions because of the higher initial inherent oxide (FeO) content in this coating (Table 4.2). Because of the lower thermal conductivity of the oxide compared to the iron splats, when tested under the same loading conditions, the surface friction increased the contact temperature of the HVOF 1020 coating to higher temperatures than the coatings with lower oxide contents. In this section, an analysis of friction induced contact temperature increase will be given as a function of the initial oxide content of the thermal spray coatings.

The surface temperature increase (ΔT) due to the sliding contact can be calculated using the following equation [11]:

$$\Delta T = \frac{\mu F v}{A_n} \left[\frac{k_p}{l_p} + \frac{k_d}{l_d} \right]^{-1} \quad (5.1)$$

where F and v are the applied load and sliding speed, and μ is the coefficient of friction. A_n is the nominal contact area, l_p and l_d are the linear heat diffusion lengths for the pin

and the disk. k_p is the thermal conductivity of the pin, and k_d is the thermal conductivity of the disk (which consists of the plasma spray coating and 319Al alloy substrate).

In the present experiments, the pin is an AISI M2 type tool steel, so that $k_p = 45$ J/msK [150]. At any instant of the sliding process, the nominal contact area A_n can be considered equal to the cross-sectional area of the pin ($A_n = 5 \times 10^{-6} \text{ m}^2$). l_p is the physical length of the pin ($l_p = 2.5 \times 10^{-2} \text{ m}$), and l_d is the total thickness of the coating and the substrate ($l_d \cong 5 \times 10^{-3} \text{ m}$).

The thermal spray coatings can be considered as composite materials with a two-phase mixture. The thermal conductivity of such material is a function of the volume fraction of each phase. The thermal conductivity of the thermal spray coatings k_c can be estimated using the following equation assuming that the coating is a series of plates of iron oxide, and iron normal to the direction of heat flow [151].

$$k_c = \left(\frac{V_{\text{FeO}}}{k_{\text{FeO}}} + \frac{(1 - V_{\text{FeO}})}{k_{\text{steel}}} \right)^{-1} \quad (5.2)$$

where k_{FeO} is the thermal conductivity of FeO taken as 3.2 J/msK [11], and $k_{\text{steel}} = 65$ J/msK is the thermal conductivity of the 1020 steel [150].

Table 4.1, shows that for the PTWA 1020, the volume fraction of FeO, V_{FeO} is 0.20 (± 0.02). The volume fraction of HVOF 1020 is 0.65 (± 0.02). Accordingly, using equation 5.2, the thermal conductivities of the PTWA 1020 and HVOF 1020 coatings are calculated as 13.4 J/msK and 4.8 J/msK respectively.

The coated substrate assembly can be considered as a simple series made up of two different materials with two different thermal resistances. The total thermal

resistance of the disk R_d is simply the sum of the coating thermal resistance $R_c = \frac{l_c}{AK_c}$,

and the thermal resistance of the substrate $R_s = \frac{l_s}{AK_s}$ so that $R_d = R_c + R_s$, and thus

$$\frac{l_d}{AK_d} = \frac{l_c}{AK_c} + \frac{l_s}{AK_s} \quad (5.3)$$

where l_s is the thickness of the substrate, and K_s is the thermal conductivity of the Al alloy substrate $K_s=160$ J/msK [152]. Equation 5.3 can then be rearranged in the following form

$$k_d = \frac{k_s k_c}{\left[\frac{l_s}{l_d} \right] k_c + \left[\frac{l_c}{l_d} \right] k_s} \quad (5.4)$$

The thermal conductivity of the disk, k_d , can be calculated using the k_c values obtained from equation 5.2, and ignoring the effect of surface oxidation.

Equation 5.4 shows that the thermal conductivity of the 319Al alloy samples coated with the PTWA 1020 is 103.0 J/msK. On the other hand, the thermal conductivity of the samples coated with the HVOF 1020 is 65.2 J/msK. This analysis assumes identical microstructures. The difference in K between the thermal conductivity of HVOF and PTWA is probably even greater due to splat size.

In order to calculate the temperature increase ΔT in equation 5.1, the values of the coefficients of friction are needed. The average values of coefficients of friction of the PTWA 1020 samples measured during the wear tests at 75 N were 0.54 (0.5 m/s), 0.48

(1.0 m/s), and 0.51 (2.0 m/s). The coefficients of friction of HVOF 1020 at 75 N were 0.47 (0.5 m/s), 0.45 (1.0 m/s), and 0.46 (2.0 m/s) (Table 5.2). Accordingly, the friction induced temperature increases in the samples coated with PTWA 1020 and HVOF 1020 were calculated at 75 N as a function of sliding speed. The results are shown in Fig. 5.6.

	0.5 m/s	1.0 m/s	2.0 m/s
<u>PTWA 1020</u>	0.54	0.48	0.51
<u>HVOF 1020</u>	0.47	0.45	0.46

Table 5.2- The coefficients of friction of the PTWA 1020 and HVOF 1020 coatings measured at 75 N at different velocities.

A comparison of the surface temperature increase curves for the two coatings shown in Fig. 5.6. This indicates that at any testing velocity the contact surface temperature of the HVOF 1020 reached a higher value than the temperature that was reached on the contact surface of PTWA 1020. More specifically, under the conditions where oxidation controlled wear took place, the temperatures on the contact surfaces of HVOF 1020 were about 50 K higher than the PTWA 1020. For example, at 75 N and 2.0 m/s, the temperature increase on the contact surface of the HVOF 1020 coatings reached 230°C. The surface contact temperature of the PTWA 1020 under the same loading conditions was calculated as 180°C. Therefore, it is expected that thicker oxide layers should form on the surfaces of the HVOF 1020 coatings. This is in agreement with the

observations that the mixed oxides generated on the surfaces of HVOF 1020 samples are 2 to 3 times thicker compared to those generated on the surfaces of the PTWA 1020 coatings. The worn surfaces of PTWA 1020 were covered with thinner oxides layers (1-3 μm). The spallation of thinner oxide layers was responsible for the lower wear rates in PTWA 1020.

It should be noted that the temperature analysis presented above is for the average surface contact temperature, and the flash temperatures (local temperatures at the tip of asperities) are higher. In summary, the temperature analysis shows that for thermal spray coatings that incorporated a large amount of inherent oxide, higher surface temperatures are reached during sliding wear. If the sliding conditions are such that an oxidational wear mechanism becomes operative, the coatings with lower oxide content, such as PTWA 1020, exhibit lower wear rates. This is an important conclusion since it clearly implies that the wear mechanisms in the plasma thermal spray coatings are closely related to the microstructures of the coatings. The coatings that had approximately three times higher FeO content (HVOF 1020) exhibited higher wear rates (2-3 times) in the oxidative wear regime. Another important conclusion is that the surface oxide production process plays a significant role in controlling the wear rates. The HVOF coatings that were produced from the same wire stock of 1020 steel as the PTWA 1020 coatings showed higher wear rates because during the HVOF process larger amounts of oxides were introduced in the microstructure. Therefore, control of the FeO content of the coating is of significant technological importance. This was proven by the examination of the wear rates of the HVOF 1020-2.5%Al coatings that exhibited the same wear rates as the PTWA 1020, because they had the same low FeO content.

5.3. SURFACE HARDENING DURING WEAR

An important observation that was reported in Section 4.1.7. was the increase in the hardness of the sliding surfaces of the PTWA 1020 during the course of the sliding wear process. The hardness increase was especially high at high loads and speeds. For example, during tests at 50 N and a sliding speed of 2.5 m/s, the surface hardness increased to 650 kg/mm² from the initial hardness of 310 kg/mm² of the unworn surface. The hardness increase was even more dramatic during the tests done at 75 N, and a sliding speed of 2.5 m/s where surface hardness values of 800 kg/mm² were measured as depicted in Fig. 4.25. This increase in hardness cannot be attributed to the formation of the surface oxides, because the indentations were taken from the regions on the wear tracks that were not covered by the oxide layers. The measured hardness thus reflect, changes that occurred in the microstructure of the iron splats.

In order to investigate the microstructural changes that took place during wear, the longitudinal cross-sections (parallel to the sliding direction) of the PTWA 1020 coatings tested at 50 N and 75 N at 2.5 m/s were examined by TEM ¹. As mentioned above, samples tested at both these loads showed considerable hardening on the wear tracks after the sliding wear test. The cross-sectional TEM micrograph (Fig. 5.7) shows that the hardened subsurface microstructures consisted of three different regions. In the region close to the contact surface, namely about 0-400 nm below the contact surface, grains had an ultrafine structure with an equiaxed grain morphology (Region I). The grain size in this region can be estimated to be about 200-300 nm. The substructure that formed at the depths of about 400-1500 nm below the contact surfaces consisted of deformation

⁽¹⁾ TEM studies were preformed at Sheffield University using a FEI Technai 20 TEM operated at an accelerating voltage of 200kV.

bands (Region II). These bands were elongated in the sliding direction (marked by the arrow on the top surface). The width of the elongated structures was about 250 nm. Their length appeared to reach several micrometers. The region marked as Region III shows the undeformed bulk structure, which usually extends at depths below 2 μm .

The existence of the ultrafine grains adjacent to the sliding surfaces suggested that a large strain gradient existed under the worn surfaces of the coatings. The strain increased significantly towards the surface, and caused grain refinement in the material.

As indicated above, the original hardness of 310 kg/mm^2 of the unworn surface increased to 800 kg/mm^2 during wear that caused the development of the microstructure shown in Fig 5.7. Using the Hall-Petch equation [153], an approach was to rationalize the relationship between the hardness increase and the structural refinement. Expressing the Hall-Petch equation in terms of the hardness gives

$$H = H_0 + \frac{m}{\sqrt{d}} \quad (5.5)$$

where H_0 is the hardness of the coating without contributions from grain boundaries (intrinsic hardness), and H is the hardness of the worn surface. The grain size is d , and m is the Hall-Petch coefficient, which is usually attributed to the resistance of the grain boundaries to the passage of dislocations. The average ferrite grain size in the undeformed splats is 1.0 μm . As shown in Fig. 5.7, as a result of surface deformation, the original grain size has been reduced to 50nm in the layers adjacent to the contact surfaces worn in the sample in the sample at 75 N. Therefore, from equation 5.5.

$$\frac{H_i - H_0}{H_{75} - H_0} = \frac{d_i^{-0.5}}{d_{75}^{-0.5}} \quad (5.6)$$

where H_0 is 167.8 kg/mm^2 . Using the initial hardness value of undeformed surface of 310 kg/mm^2 and 800 kg/mm^2 of the sample surface tested at 75 N , the ratio of both sides of this equation is 0.21 . Therefore, the strengthening due to plastic deformation during wear is scaled according to the reduction in the grain size in agreement with the prediction of the Hall-Petch equation.

5. 4. POLISHING WEAR

The wear mechanisms that were discussed so far in Sections 5.1-5.3. operate essentially under dry air conditions. In this section, a wear mechanism that was found to operate in the thermal spray coatings tested under high humidity conditions is discussed.

In Sections 4.1.8.- 4.1.10., it was shown that complex relations existed between the humidity levels in the test atmosphere and the coating wear rates. An important observation was that the reduction in the wear rates and coefficients of friction, and polishing of the surface under the counterface contact as the humidity was increased. The typical worn surface of the coating tested under $80\% \text{ RH}$, (Fig. 4.29) had a highly polished contact area with compacted (hydrated) oxide that filled the exposed pores, and the depressions between the contacts points. The appearance of the worn surface was strikingly similar to the surface of the coating that was carefully polished using metallographic methods. The comparison of the SEM micrograph of the top surface of the coating worn under $80\% \text{ RH}$ revealed the surface details equally well. Individual iron splats, inter-splat oxides, and pores can be clearly distinguished on the worn surface (Fig. 4.29). This observation led to the conclusion that a polishing type wear mechanism operated on the surfaces of the coatings tested at high humidity levels.

An interpretation of the polishing wear mechanism in PTWA 1020 coatings is shown schematically in Fig. 5.8. In the first stage, a hydrated iron oxide layer was formed across the entire surface (Fig. 5.8.a). Then the counterface mechanically removed the peaks of the oxide layer. The detached hydrated iron oxide particles were compacted, and became entrapped in the spaces between the actual contact areas (Fig. 5.8.b). The process progressed by repetition to a degree where the crests of surface asperities were removed, and the surface became levelled (Fig. 5.8.c). This mechanism is expected to be active whenever there is a balance between chemical and mechanical wear. In many ways, this mechanism is similar to that proposed in [154] for ceramics.

Tests done under the same loading conditions that gave rise to polishing wear, but in the absence of the high atmospheric humidity resulted in mechanical wear. Splat deformation and fracture dominated the surface degradation, and as a result, the wear rates were high. The coefficient of friction decreased at high humidity levels, and the amount of metallic debris, indicative of high wear rates, was also considerably reduced. All this evidence indicates the beneficial effect of humidity in reducing the wear rates of the thermal spray coatings.

5.5. WEAR MECHANISM MAPS FOR THE THERMAL SPRAY COATINGS

The micromechanisms of wear that control the wear rates under a specific set of experimental conditions are summarized in the form of wear maps. The wear maps are constructed for each of the three coatings tested as discussed in the following sections.

5.5.1. WEAR MAP FOR PTWA 1020

Wear rates of the PTWA coatings for tests in the 5 N-75 N load, and 0.25 m/s-2.5 m/s sliding speed ranges under dry air atmosphere (RH=10%) are presented in the form of a map on load versus sliding speed axes (Fig. 5.9). The wear rates are given numerically at different sliding velocities and loads combinations in units of 10^{-6} g/m. The wear rates were high at low sliding velocities, but decreased when the sliding velocity increased. The map shows four main regimes. The wear regimes are classified on the basis of differences in wear rates, worn surface (Fig. 5.9.a-d) and debris morphologies, and compositions.

Regime I

Regime I occurs at low sliding velocities and loads i.e., below approximately 1 m/s and 20 N. In this regime, the oxide rich layer was uniformly distributed between the micro-scratches on the contact area. The metallic parts were subjected to plastic deformation, and extruded in the sliding direction (Fig. 5.9.a). The XRD spectrum of the debris at 10 N load and 0.5 m/s velocity, representing regime I, showed the peaks for hematite (Fe_2O_3), and a few small peaks of ferrite. The quantitative phase analysis confirmed that at low loading and velocity conditions, Fe_2O_3 was the predominant constituent (> 99%) of the wear debris. Therefore, the main wear mechanism in Regime I was surface oxidation to Fe_2O_3 .

Regime II

Regime II is the region of high wear rates at loads above approximately 20N, and sliding speeds lower than 1 m/s. An important aspect of wear in this regime is the fracture

of the edges of the highly deformed steel splats (Fig. 5.9.b). It is important to emphasize that there was also a significant amount of metallic ferrite in the debris. The iron fragments were the result of the fracture of splat tips. Steel splats adjacent to contact surfaces were deformed and became elongated in the sliding direction. At subsequent stages, more deformation was induced, especially at the elongated tips of splats. Exhaustion of ductility of the material at the splat tip caused their fracture and fragmentation. Occasionally, repeated fracture and fragmentation of splats progressed to a degree where the entire splat was lost. This regime is marked as Regime II, splat fracture (mechanical wear) on the wear map (Fig. 5.9).

Regime III

Regime III exists at sliding speeds above those in regime II, and at the same loads. In this regime, the wear rates were about 50% lower than those measured in regime II. About 70% of the wear tracks of the high load and high velocity samples were covered by relatively thick oxide rich layers, whose average thicknesses varied between 1-3 μm . The worn surface appeared to be much less susceptible to splat fracture (Fig. 5.9.c). The friction results showed that by increasing the velocity, the coefficient of friction decreased, which is also consistent with the formation of oxide rich films. In this regime, especially at high loading conditions, the hardness of wear tracks increased to exceptionally high values of over 800 kg/mm^2 . Therefore, the wear rates were reduced in regime III as a result of two mechanisms; i) the production of thick oxide rich layers that reduced the coefficient of friction, and probably suppressed the splat tip fracture mechanism, and ii) surface hardening during wear that was possibly due to local strain hardening.

Regime IV

At sliding speeds above 1 m/s and loads below approximately 20 N, the wear rates were the lowest compared to those in the other regimes. The oxide coverage was more significant than at low load and low velocity conditions, and extended over the top of the steel splats (Fig. 5.9.d). The favourable factors, including the formation of an almost continuous oxide rich films, hardening of the coating during wear, and lack of any significant iron splat fracture are among the possible reasons why the wear rates are the lowest under these conditions.

5.5.2. WEAR MAP FOR HVOF 1020

The wear map for the HVOF 1020 coatings plotted on load versus sliding speed axes is presented in Fig. 5.10. The wear map shows wear rates and mechanisms for HVOF 1020 coatings in dry sliding against tool steel pin material using the pin-on-disc geometry, at room temperature in air (RH=10%). The wear rates are given numerically (units of 10^{-6} g/m) at different sliding speeds and loads combinations in a similar way as they are presented in the wear map for PTWA 1020.

It can be seen that the wear map for the HVOF 1020 coatings is similar to the wear map of the PTWA 1020 coatings (Fig. 5.9). However, the map for this coating consists of five regimes. Four of these regimes exhibited wear mechanisms that were identical to those in PTWA 1020. The oxidative wear regime in Fig. 5.10 (regime I) during which the Fe_2O_3 type oxides are formed on the contact surfaces is located at the lowest loads and speeds end of the wear map. The quantitative XRD phase analysis

confirmed that at low loading and velocity conditions, Fe_2O_3 was the predominant constituent (> 99%) of the wear debris. Another common wear regime is labelled as the splat fracture and oxidation regime (regime II). This regime occurs at higher loads but at speeds lower than 1 m/s, which coincides exactly with the loading conditions under which mechanical wear takes place in the PTWA 1020 coatings. The wear rates decrease in regime III, where a uniform and protective oxide film forms. The whole wear track in this regime was covered by a uniform and protective oxide. Regime IV, where mixed oxides are generated, can be regarded as an extension of this regime, but this regime shows similarities with the same regime (regime IV) on the wear map of the PTWA 1020. In both coatings, in this regime the wear rate was controlled by mixed oxidation to Fe_2O_3 and Fe_3O_4 . Fig. 5.10 indicates that the wear map for HVOF 1020 coatings shows an additional wear regime, which is marked on the wear map as the regime V. At sliding speeds above 1.5 m/s and loads above approximately 25 N, the wear rates increased as the sliding speed increases. In this regime, the contact surface was severely deformed and damaged due to crack formation normal to the sliding direction. The oxide layers on the HVOF 1020 were discontinuous, and the worn surface was rough compared to the worn surfaces of the two other coatings. Therefore, severe oxidation and spallation of the much thicker oxide layers were responsible for the high wear rates of HVOF 1020 at high loads and speeds. Fig. 5.10.b shows a back-scattered SEM micrograph from this regime (at 50 N load and 2.5 m/s). It shows evidence for oxide formation on the contact surfaces of HVOF 1020 samples during sliding. At this loading condition, the average thicknesses of oxide layers formed on the sliding surfaces of the HVOF 1020 reached 7 μm , as shown in Fig. 5.10.c. The topographical features of the thick oxide layers formed in this regime on

the surfaces of HVOF 1020 can be appreciated better from the Wyko optical surface profilometer scans presented in Fig. 5.11.a. The surface profile in this figure is from the sample tested at 75 N and 2 m/s. The oxide topography shown is typical of regime V and exhibits a very rough surface. The average roughness of the surface is $R_a = 2.61 \mu\text{m}$ but spots that are as high as $34 \mu\text{m}$, (due to the remnants of spalled oxide layers) can also be observed. As mentioned before this regime was not observed during sliding wear of PTWA 1020 samples. A representative Wyko image that was taken from a PTWA sample tested at 75 N and 2m/s is given in Fig. 5.11.b for comparison. It is clear that the average surface roughness of this sample ($R_a = 1.25 \mu\text{m}$) is lower and the oxide film is continuous. This continuous oxide layer acted as a protective coating as a result in regime III in the PTWA 1020 samples (Fig. 5.9) the wear rates are three times lower than those measured in Regime V in the HVOF coatings despite the fact that both regimes extend in approximately the same load and velocity conditions on the respective wear maps.

5.5.3. WEAR MAP FOR HVOF 1020-2.5% Al

The wear map for HVOF-2.5% Al under a dry air atmosphere (RH=10%) is presented in Fig. 5.12 on load versus sliding speed axes in a similar way as the previous two wear maps. The wear map for the HVOF-2.5% Al coatings consists of five regimes. The map for this coating is similar to the wear map of the PTWA 1020 coatings (Fig. 5.9), it exhibits the same mechanical wear mechanism (regime II) by splat tip fracture during which the wear rates are high; as well as the oxidation wear regime at high speeds, where a decrease in the wear rates are observed (regime III). Other oxidative wear regimes cover similar load and speed conditions that were found in the wear maps of PTWA 1020

(Fig. 5.9) and HVOF 1020 (Fig. 5.10) coatings. It is observed that the wear map of HVOF 1020 (Fig. 5.10) exhibits the mechanical wear regime (regime II) that corresponds to the same loading conditions as in that of HVOF 1020-2.5% Al. The major difference between the wear maps of these two HVOF coatings is that without the Al addition the wear rates at high loads and speeds are high, as depicted by regime V in the wear map of HVOF 1020. This high wear rate regime does not exist in the wear map of HVOF 1020 - 2.5% Al. Therefore, the comparison of the wear maps shed light on the beneficial effect of the addition of Al in the HVOF coatings under certain conditions. It is also seen that a new regime, namely regime IV, which is identified as abrasive wear appears in the wear map of HVOF 1020-2.5% Al. As will be discussed below this is due to the abrasive action of the hard Al rich inclusions that exist in the microstructure of this coating (Fig. 4.49). A more comprehensive discussion of the wear mechanisms in each regime operating in HVOF 1020-2.5% Al is given in the paragraphs below.

In Regime I surface oxidation to Fe_2O_3 was the main wear mechanism for lowest load and speeds conditions. Regime II has the highest wear rates as a result of mechanical wear in the form of severe plastic deformation and fragmentation at the tip of the splats, this regime was shown in the previous wear maps (Figs. 5.9 and 5.10).

Regime III takes place at sliding speeds greater than 1 m/s. In this regime, the wear rates of the HVOF 1020-2.5% Al decrease with increasing the sliding speed. The wear rates of HVOF 1020-2.5% Al at this regime are comparable to those of the PTWA 1020, but significantly lower than those of the HVOF 1020. The average thickness of oxide layers formed on the sliding surfaces of HVOF 1020-2.5% Al (Fig. 5.12) at high loading condition varies between 1 and 3 μm similar to regime III in the PTWA wear

map. In this regime formation of a uniform oxide film on the sliding surface and surface hardening were the mechanisms that control the wear rates.

The thickness of the surface oxide layer is related to the initial oxide (FeO) content of the coating, as discussed in Section 5.2.1. The addition of Al during the production of the HVOF coatings reduced the oxide content from 60% to 15%, to a level similar to that in PTWA 1020 coatings. Consequently the sliding induced surface temperature increase in the HVOF 1020-2.5% Al coatings did not increase as much as in the HVOF 1020, resulting in lesser amount of surface oxidation and hence lower wear rates. For this reason regime V (severe oxidative wear regime) of the HVOF 1020 map does not exist in the wear map of HVOF 1020-2.5% Al. This is clearly an advantage of this type of HVOF coating over the HVOF 1020 coatings that do not contain Al. Based on the information arising on the wear map, it can be suggested that the production method of the thermal spray coatings can be modified for better wear resistance. The composition of PTWA 1020 coatings that have a low FeO content in their microstructures could be modified by the addition of 2.5% Al to further reduce the initial oxide content of the coating. This may be potentially useful method to control oxidative wear in the thermal spray coatings.

Fig. 5.12 shows that the wear map for HVOF 1020-2.5% Al coatings shows an additional wear regime, which is marked on the wear map as the Regime VI. This regime does not exist on the other maps. Regime V is located at loads between 20 N and 50 N and sliding speeds above 1m/s. Abrasive wear due to existence of the hard inclusions in the coatings was significant in this regime. Fig. 5.12.d shows a typical microstructure of the sliding surface of the coating. The micrograph shows less oxide coverage compared

to those of PTWA 1020 coatings tested at the same loading conditions. This is due to the abrasive action of the hard inclusions that exist in the microstructure of this coating only (see Fig. 4.51). The Al rich oxides fracture and leave scratch marks on the surface. This can be regarded as a disadvantage of the coatings that contain hard inclusions. The hard inclusions can be abrasive to the counterfaces, such as piston rings. The wear mechanisms that operate in actual engines will be discussed in Chapter VI.

5.6. TEMPERATURE MAPS FOR THE THERMAL SPRAY COATINGS

The friction induced surface temperature plays an important role in controlling the wear mechanisms of the coatings. The surface temperature increase is particularly important in understanding the oxidative wear mechanisms. As stated in Section 5.2.1., the differences between the thicknesses of the oxide films generated on the contact surfaces are directly related to the surface temperature increases. Therefore, it is useful to present the surface temperature information in the form of temperature maps on load and speed axes similar to the wear mechanism maps. A method to calculate the surface temperatures as a function of the oxide content of the coatings was given in Section 5.2.1. Using this method surface temperature maps for PTWA 1020 and HVOF 1020 coatings were constructed. The temperature maps for PTWA 1020 and HVOF 1020 are presented in Figs. 5.13 and 5.14 respectively. In constructing these maps an additional step was taken in such a way that the boundaries that delineate transitions from one wear mechanism to another are plotted on the same axes. By superimposing the temperature maps over the wear mechanism maps it becomes possible to compare the temperature isotherms that correspond to each wear regime. For example Fig. 5.14 reveals that in

HVOF 1020 the onset of severe oxidation regime corresponds to a frictional temperature increase of 110 °C.

5.7. COMPARISON OF THE WEAR MAP OF ALUMINUM 356 WITH PTWA 1020 COATINGS

Since the thermal spray coatings are being developed to improve the wear resistance of cast aluminum alloys. The wear maps can be used as guidelines to assess the degree of protection the coatings provide to the aluminum alloys. A simplified version of the wear map of PTWA 1020 is superimposed on the wear map of the cast A356 alloy. This composite wear map is shown in Fig. 5.15. The map indicates that at low sliding velocities and loads, corresponding to mechanical wear of the PTWA 1020 coatings, the wear resistance of 356 Al is better than that of the coating. Therefore, the use of the PTWA 1020 under these conditions does not provide wear resistance. On the other hand, 356 Al shows a mild to severe wear transition at high loads and speeds [116] and consequently the wear rates increase dramatically. This corresponds to the oxidative wear regime in the PTWA 1020 coatings where the wear rates are relatively low. Consequently, the wear resistance of the PTWA 1020 coatings in this region is considerably better than the aluminum substrate and it is useful to protect aluminum surfaces with the PTWA 1020 coatings (Fig. 5.15). This example illustrates the benefits of the wear mapping approach on the selection and design of the protective coatings.

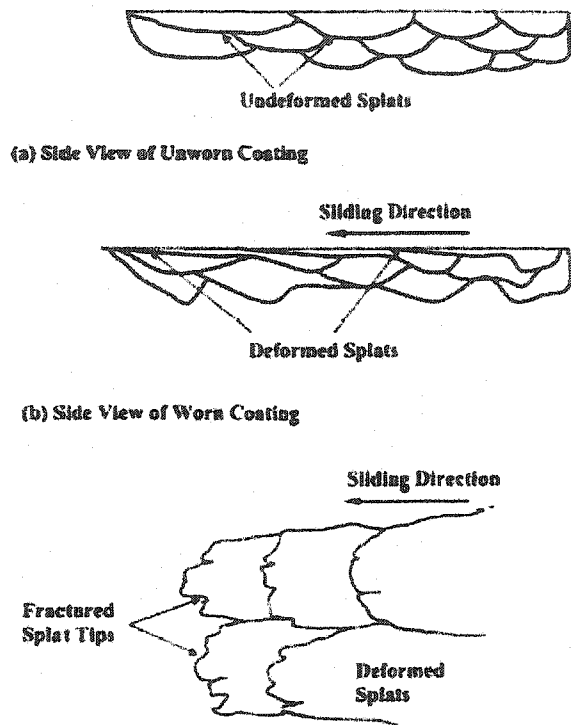


Fig. 5.1-A schematic diagram illustrating the mechanism for deformation and fracture of steel splats. a) shows a cross-section of the unworn surface. b) shows a cross-section of plastically deformed splats elongated along the sliding direction. c) is a surface view showing fracture at the edges of the splats.

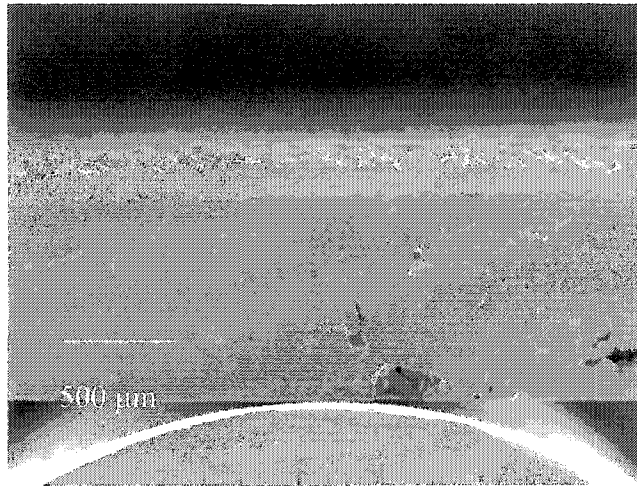


Fig. 5.2- Rectangular PTWA 1020 sample of 10 mm wide and 25 mm in length with 1 mm in thickness were tested using a miniature three point bending jig. 4 mm diameter round pins were put in contact with the lower face of the aluminum substrate.

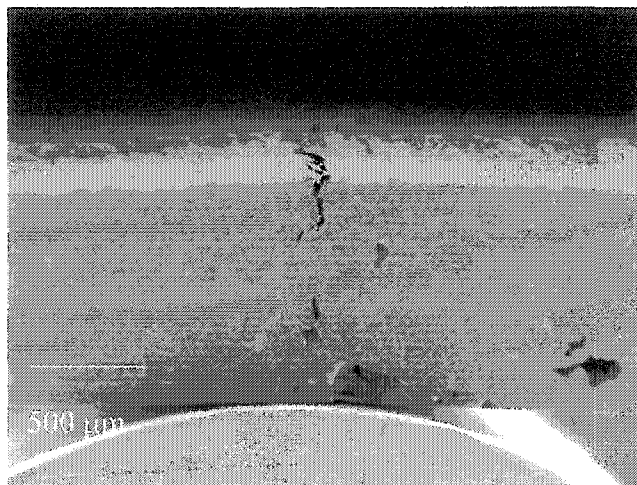


Fig. 5.3- The cross section of the PTWA 1020 coating after the three point bending test at the maximum load of 160 N shows a large perpendicular crack to the surface propagated through the coating into the substrate.

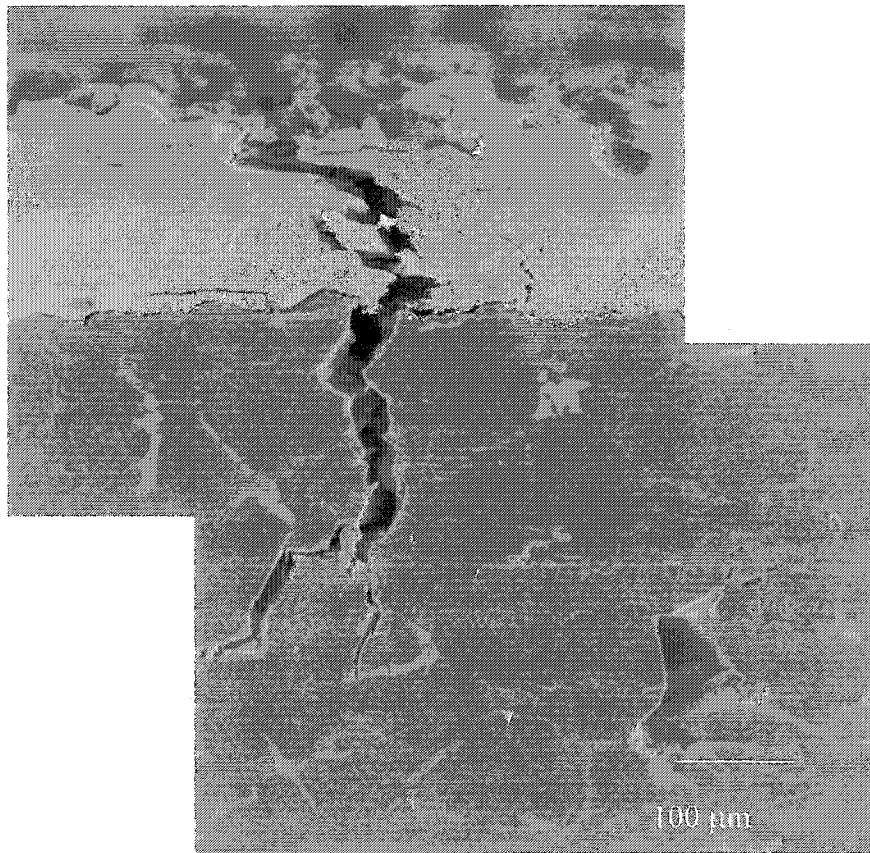


Fig. 5.4- A high magnification micrograph of the cross section of the PTWA 1020 presented in Fig. 5.3.

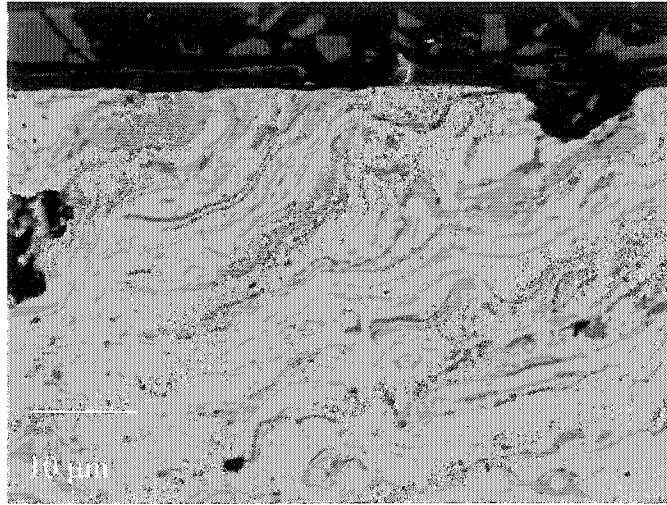


Fig. 5.5- A back-scattered SEM micrograph from the cross section of the worn surface of HVOF 1020-2.5% Al shows the cracks propagated through the oxide veins and caused delamination of an entire iron splat adjacent to the contact surface. The same type of delamination wear was also observed in PTWA 1020. But the occurrence of this wear mechanism is rare.

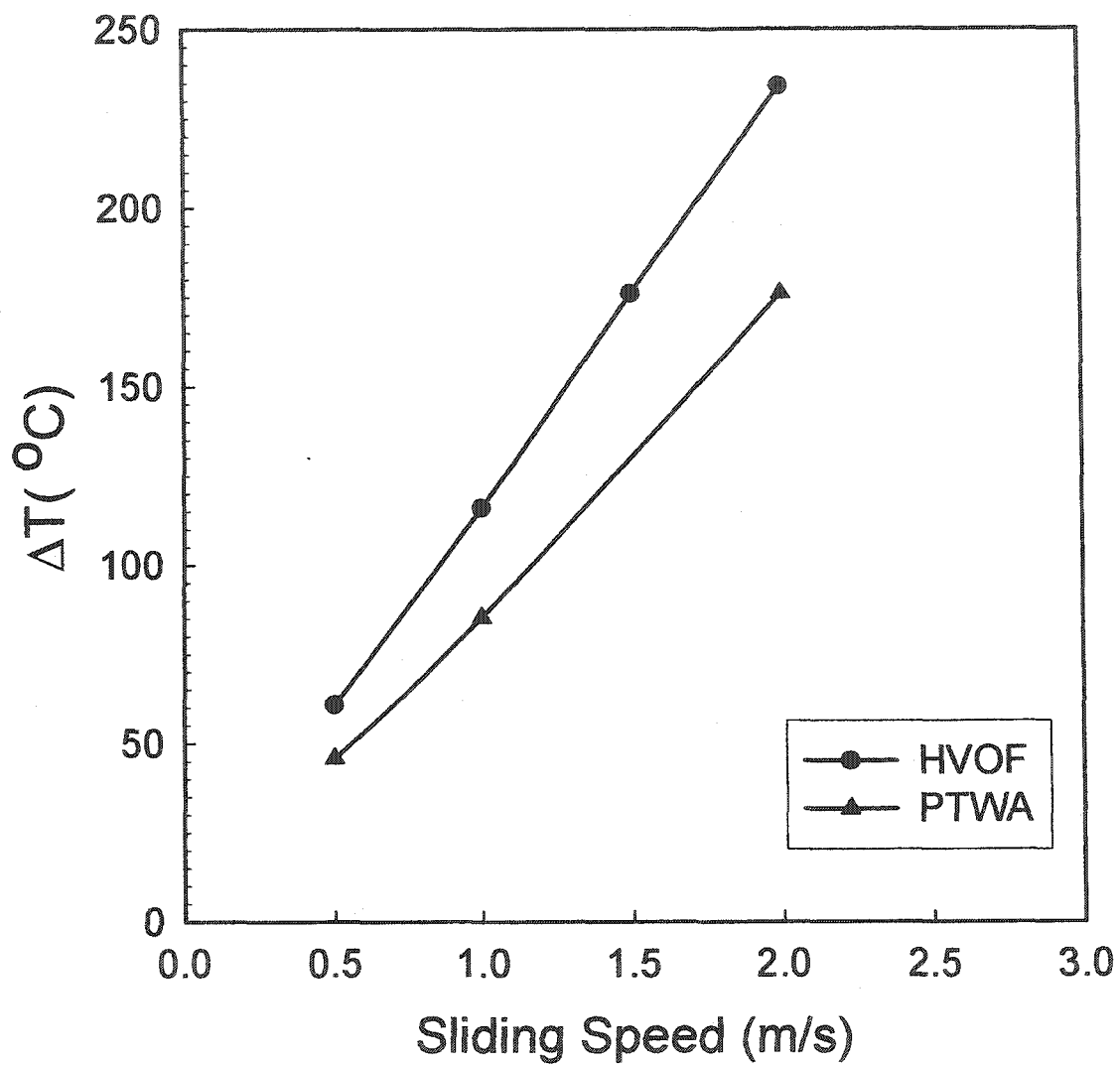


Fig. 5.6- Comparison of friction induced surface temperatures for PTWA 1020 and HVOF 1020 at different sliding speeds at 75 N load.

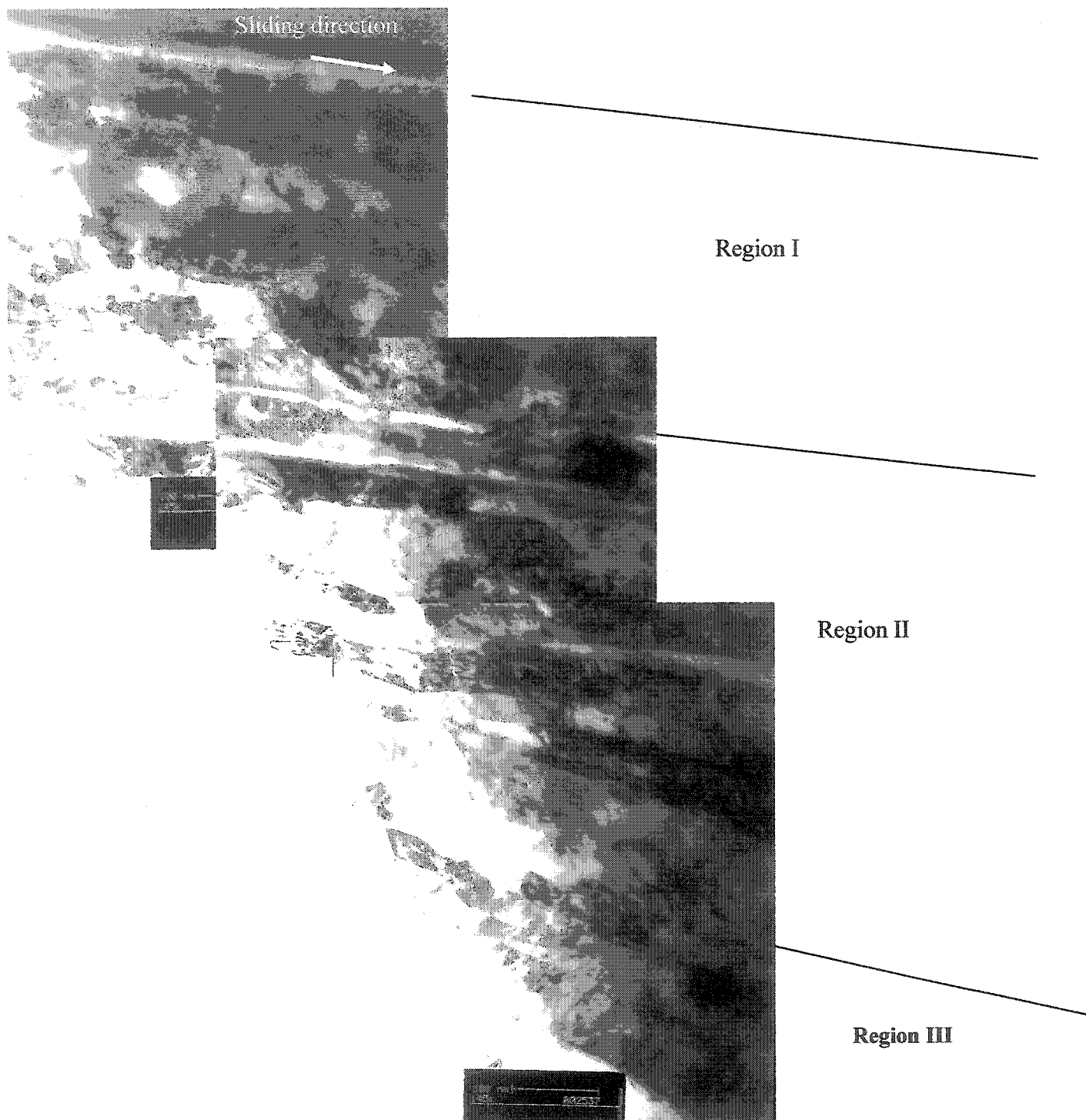


Fig. 5.7- TEM metallographic investigations on the longitudinal sections of the PTWA 1020 sample tested at 75 N and 2.5 m/s which showed surface hardening after wear. The microstructure is divided into three distinguished layers: 1) on the contact surface where the grain size is about 50 nm, and 2) adjacent to the layer where there is a substructure consisting of an elongated sub-grain and 3) undeformed coating.

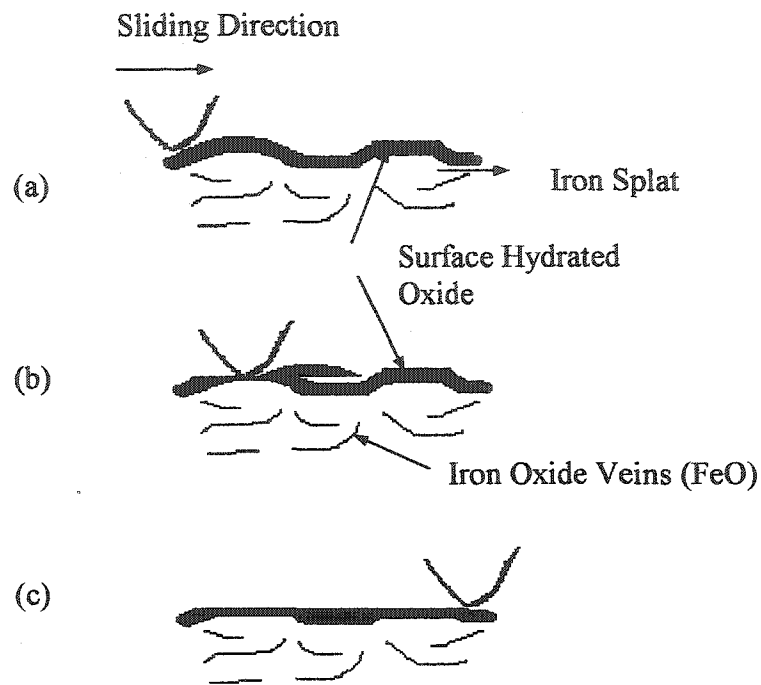


Fig. 5.8- Schematic diagrams illustrating a mechanism for polishing wear by chemical and mechanical mechanisms. **a)** a cross-section of the coating and the formation of the oxide film at high humidity. **b)** the detached hydrated iron oxide by counterface becomes entrapped in the spaces between the actual contact areas. **c)** The crests of asperities are removed and the surface becomes flat.

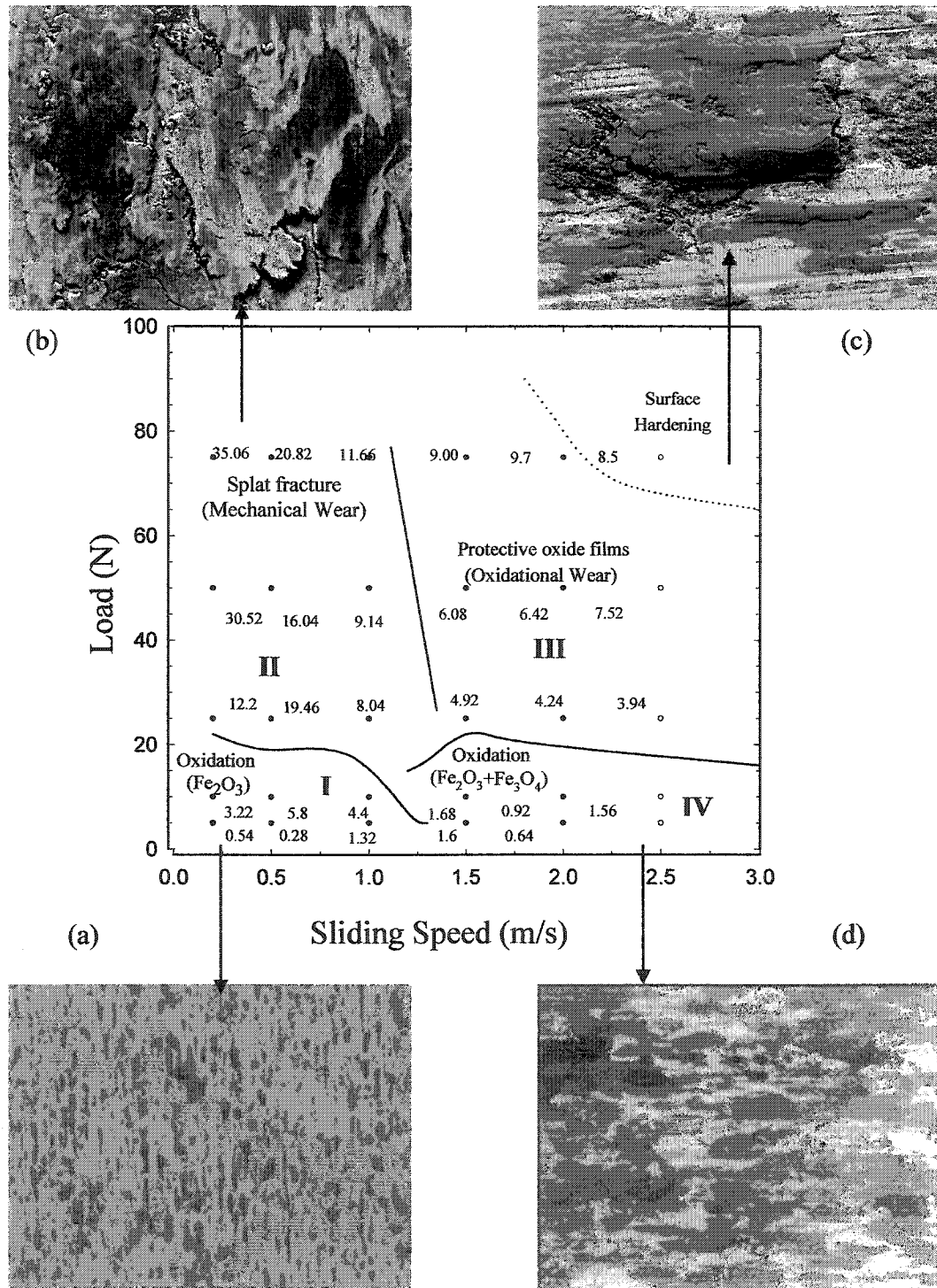


Fig. 5.9- Wear map showing wear rates and mechanisms for PTWA 1020 thermal spray coatings in dry sliding against tool steel pin material. The coatings wear rates have units of 10^{-6} g/m. Experiments were conducted using the pin-on-disc geometry, at room temperature in air (RH=10%). (a-d) Typical SEM micrographs (backscattered electron (BSE)) of worn surface morphologies from Regimes I-IV.

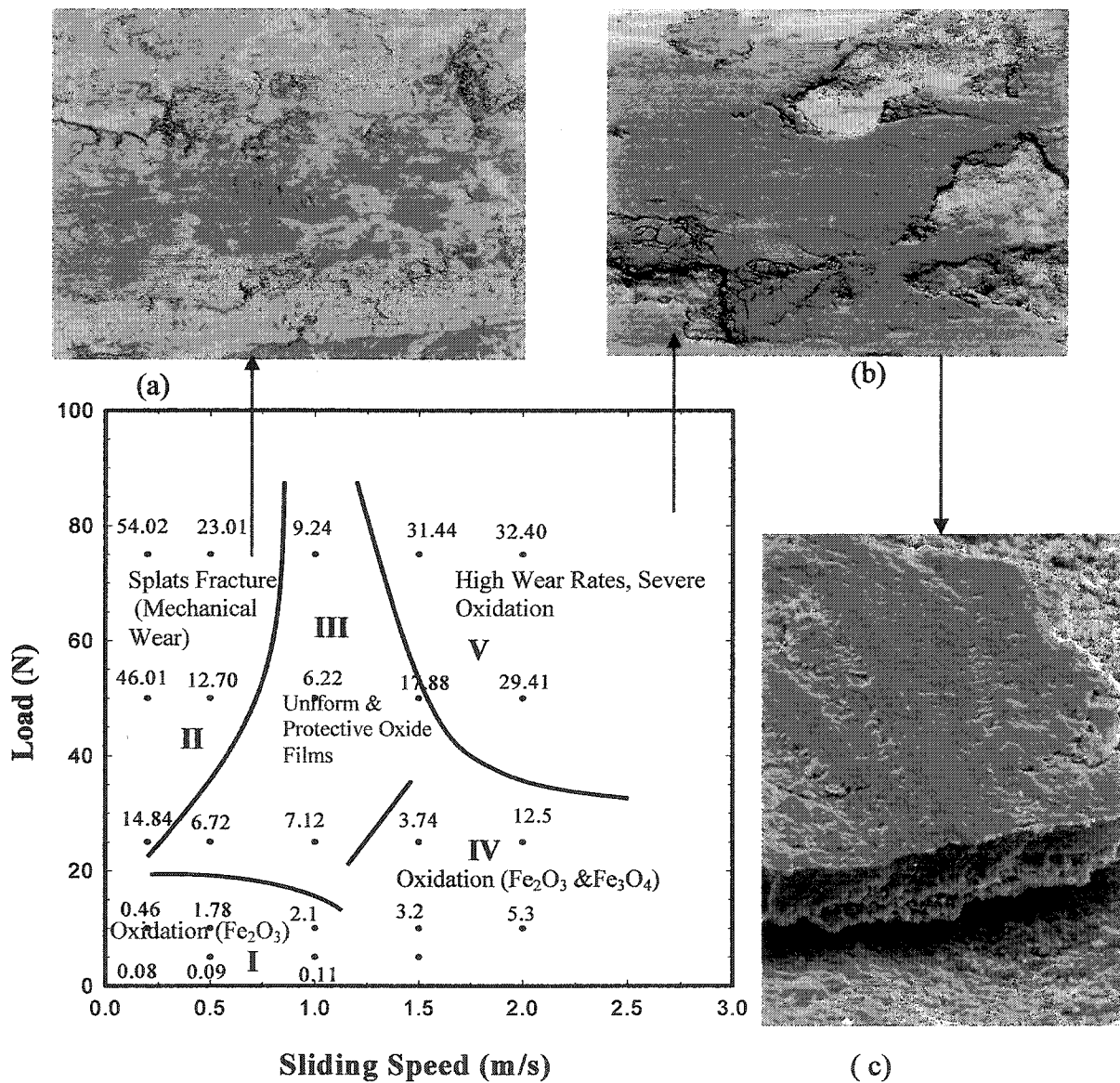
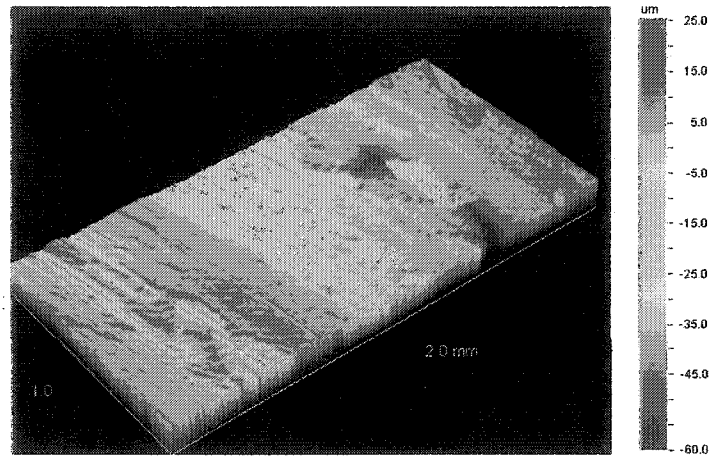
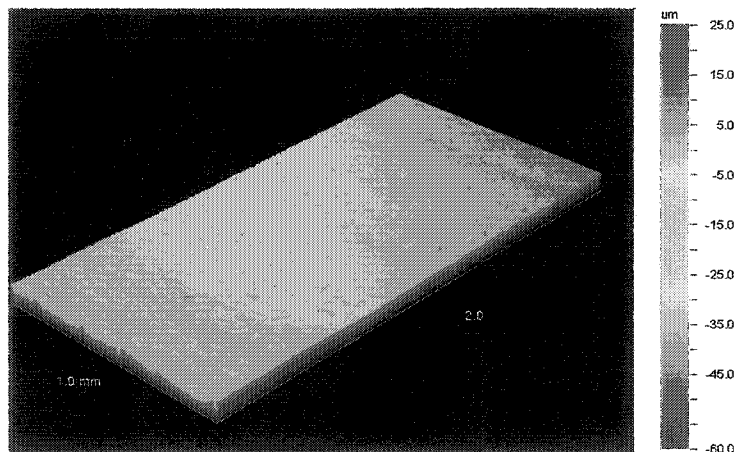


Fig. 5.10- Wear map showing wear rates and mechanisms for HVOF 1020 thermal spray coatings in dry sliding against tool steel pin material. The coatings wear rates have units of 10^{-6} g/m. Experiments were conducted using the pin-on-disc geometry, at room temperature in air (RH=10%). (a-c) Typical SEM micrographs of worn surface morphologies.



(a)



(b)

Fig. 5.11- (a) Wyko optical surface profilometer image from the worn surface of the HVOF 1020 coating tested at 75 N and 2 m/s shows the topographical features of the thick and rough oxide layers formed during sliding, (b) Wyko image from the worn surface of the PTWA 1020 coating tested at same loading condition shows uniform and protective oxide film on the sliding surface.

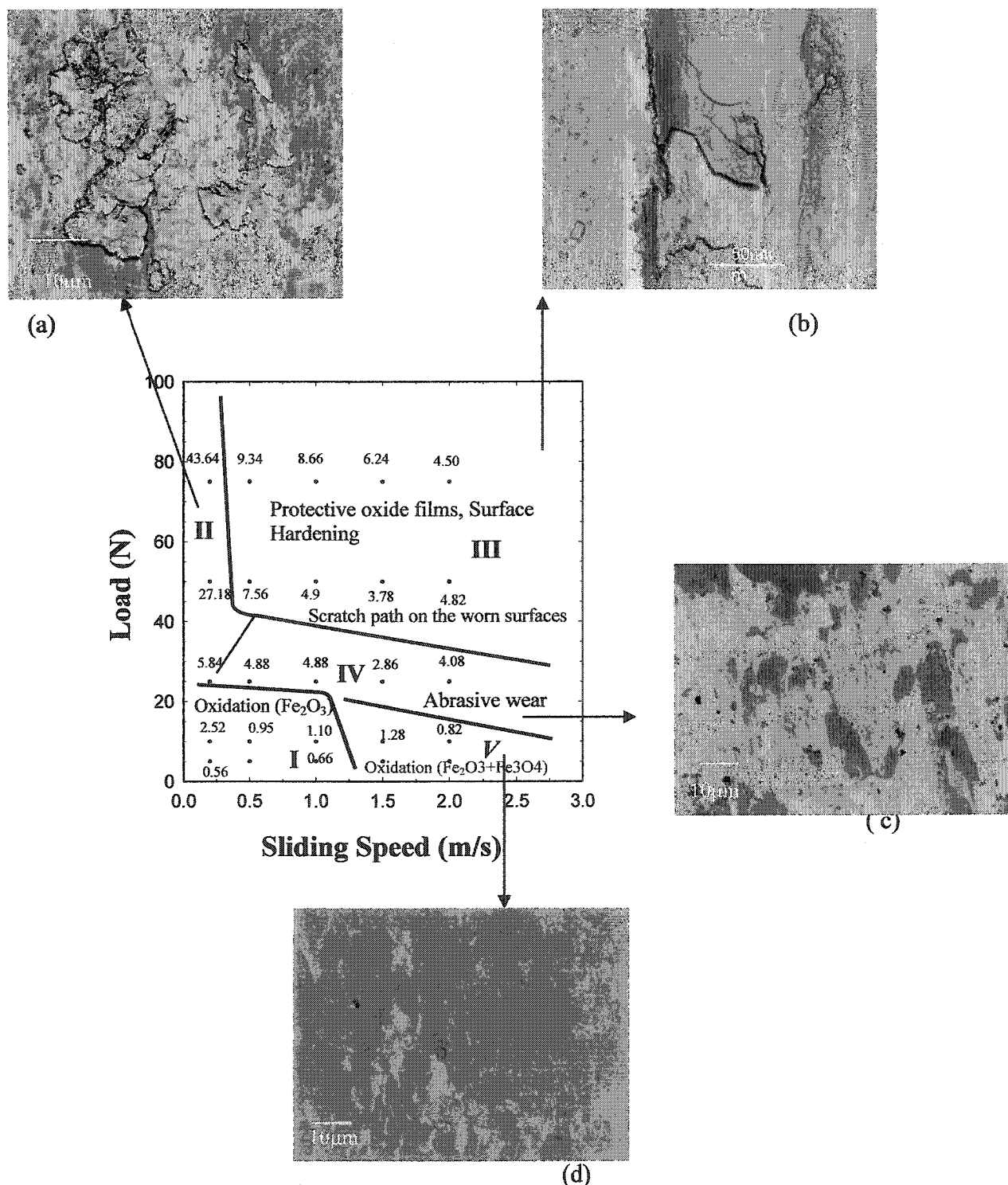


Fig. 5.12- Wear map showing wear rates and mechanisms for HVOF 1020-2.5% Al thermal spray coatings in dry sliding against tool steel pin material. The coatings wear rates have units of 10^{-6} g/m. Experiments were conducted using the pin-on-disc geometry, at room temperature in air (RH=10%). (a-d) Typical SEM micrographs of worn surface morphologies.

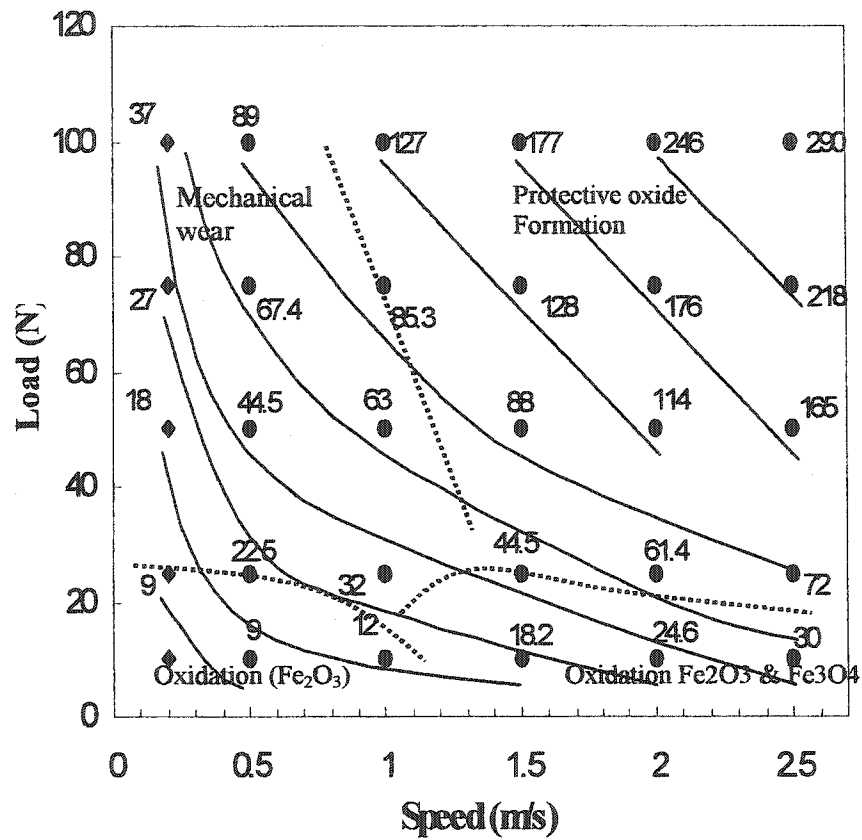


Fig. 5.13- The surface (bulk) temperature map for the PTWA 1020 constructed on load vs. speed axes. The temperature map shows the temperature increase (in °C) on the sliding surface during the sliding at various combinations of load and velocity. The wear regimes are superimposed on the temperature map.

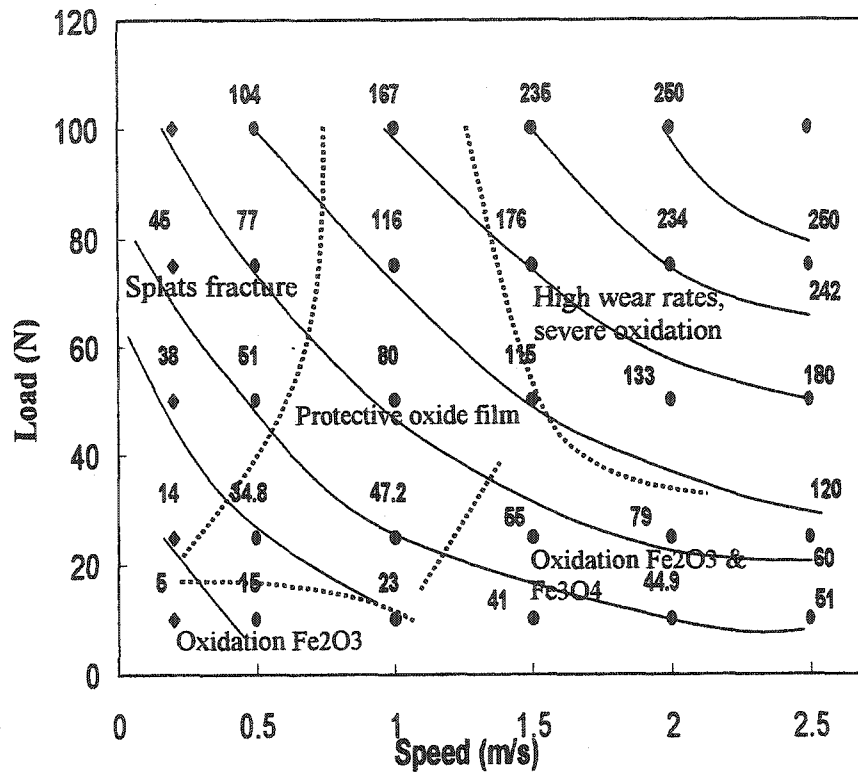


Fig. 5.14- The surface (bulk) temperature map for the HVOF 1020 constructed on load vs. speed axes. The temperature map shows the temperature increase (in °C) on the sliding at the various combinations of load and speed. The wear regimes are superimposed on the temperature map.

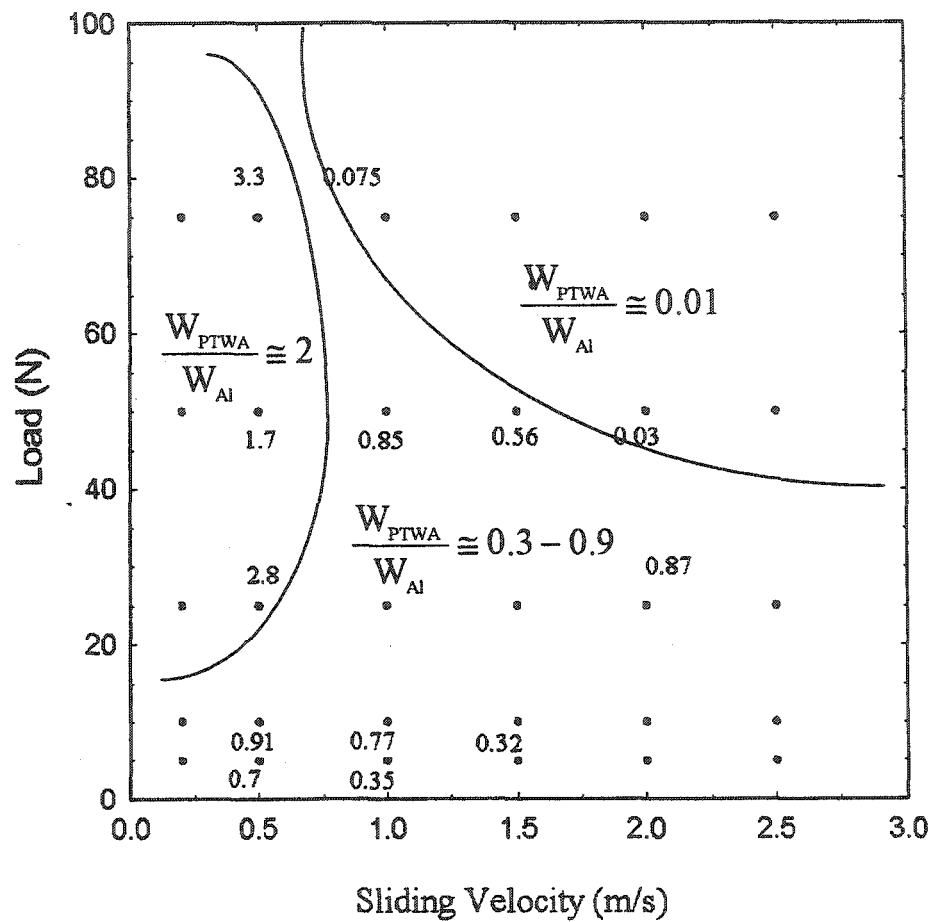


Fig. 5.15- The comparative wear map of the PTWA 1020 coatings and the 356 Al alloy showing the degree of protection provided by the coatings to the aluminum surfaces. The numbers on the map are the ratios of the wear rates of PTWA 1020 to the wear rates of 356 Al alloys at the same loading conditions.

CHAPTER VI

ENGINEERING APPLICATIONS: INVESTIGATION OF SCUFFED ENGINES WITH THERMAL SPRAY COATINGS

The objectives of this chapter are to:

- 1) Investigate the micromechanisms responsible for scuffing damage in actual engines, namely (a) a Corvette engine block with bores coated with High Velocity Oxy-fuel (HVOF) 1020-2.5% Al low carbon steel thermal spray coating; and (b) a Saturn engine block with bores coated with the same type of coating.
- 2) Establish the correlation between the wear mechanisms observed in the scuffed engines and those on the wear map for HVOF 1020-2.5% Al coatings that were presented in Chapter V.
- 3) Design a pin-on-disc test to simulate the micromechanisms responsible for cold scuffing in engines.

6.1 MATERIALS AND TESTING METHODS

6.1.1. SCUFFED THERMAL SPRAY COATED ALUMINUM ENGINES

Microscopic investigations were performed on actual engines that had failed with scuffing type of damage under different conditions. These engines were:

- 1) A standard LS1 Corvette engine block (5.7 litre V8, 350 horsepower). The Corvette engine failed under racetrack conditions.
- 2) A standard Saturn engine (2.2 litre inline 4 cylinder, 140 horse power). The Saturn engine failed during dynamometer cold scuffing tests.

The engine blocks were cast from 319-Al alloy. The deposition process of the actual engine bores is shown schematically in Fig. 6.1. The bores were cut to a rough size, and prepared for thermal spraying by a water jet machining process [155]. During the water jet machining process, water was forced through nozzles of 0.005 inches at speeds up to 3000 feet/second. The spray disc was rotated at a speed of 500- 1500 rpm and the surface was roughened at a water pressure of 55,000 psi. The average depth of the water eroded peaks ranged between 10- 75 μm [155]. The process cleaned and roughened the surface, providing a good mechanical interlock adhesion for the coating. The blocks were subsequently coated with a High Velocity Oxygen Fuel gun using a wire with a nominal 1020-steel composition with the addition of 2.5 wt.% Al as feedstock (HVOF 1020-2.5% Al). During the deposition of the coating, the gun traveled along the length of the bore as it rotated inside the cylinder. The last step of this process was honing the rough surfaces of the thermal spray coatings. In this step, sufficient excess coating was applied so that about 30 % of the coating layer was removed subsequently.

The chemical composition and the microstructure of the coating were described in Chapter IV. The bores were single-pass diamond-reamed (microsized) from the as-

sprayed condition and then peak honed, also with a diamond abrasive, producing a 30° crosshatch angle with a surface finish of 0.6 μm R_a .

A detailed description of the properties of the Corvette engine is given in Table 6.1. The pistons were originally tin-plated. The top ring was made of nitrided stainless steel with a symmetric barrel face and positive ovality. The second ring was the standard production cast iron ring, but modified with a burnished lower edge radius, while the oil ring used a reduced tension (4 lbs.) expander. Some properties of the Saturn engine studied are given in Table 6.2.

Corvette LS1 Engine Block	
Type	5.665 litre V-8
Horsepower	345 @ 5600 rpm
Torque (lb-ft)	350 @ 4400 rpm
Max. Engine Speed	6000 rpm
Bore/Stroke	99.00/92.00mm
Engine Materials	
Block	A-319 cast aluminum
Cylinder Head	A-319 cast aluminum

Table 6.1 Properties of the LS1 engine

Saturn Engine Block	
Type	2.2 liters 4 cylinder in line
Horsepower	137
Torque (lb-ft)	147
Max. Engine Speed	5400 rpm
Bore/Stroke	92.00mm.
Engine Materials	
Block	A 319 cast aluminum
Cylinder Head	A 319 cast aluminum

Table 6.2- Properties of the Saturn engine.

6.1.2. RACE TRACK PROCEDURES OF THE CORVETTE ENGINE

The Corvette engine was first installed in a prototype Z06 vehicle that was prepared for race track testing in order to compare oil consumption with a bogie that was established for a production Z06 at the Grattan Race Track in Grattan, MI. Following successful completion of the evaluation, the engine was installed in a Michigan State University sponsored ASA race car for demonstration purpose in the 2001 ASA season where a total of 4 races were run. After the MSU team finished its race activities, the engine was removed from the ASA car. The scuffed parts were obtained from this engine.

6.1.3. COLD SCUFF ENGINE TESTING PROCEDURES ON THE SATURN ENGINE

The cold scuffing tests were performed on a Saturn engine in an environmental chamber in which the temperature was less than -20 °C. The engine was turned on and

off about 50 times. After that, the engine was left running until the temperature of the oil reached 65 °C.

6.1.4. METALLOGRAPHIC SAMPLE PREPARATION FROM THE SCUFFED ENGINES

One bore with the most visible damage from each engine was cut into four stripes with consideration given to major, minor, front, and back faces. Fig. 6.2 shows the sectioned faces of the Corvette engine. 1.5 x 1.5 cm coupons were cut from the front, major, and minor sections at a distance of 45 mm from the deck face, and also from 5 mm below the deck face on the major section using a low-speed circular diamond saw. Each of these samples was then cut in half, providing two sections to be used later for plan and cross-sectional view microscopy parallel to the sliding direction. The cutting was initiated at the free surface of the coating to reduce the possibility of separation from the substrate. Hexane solution was used to remove the residual engine oil from the sliding surface of the coupons. The parts were ultrasonically cleaned in methanol and washed with ethanol prior to the WYKO and SEM investigations. The parts were mounted in Buehler Diallyl Phthalate Blue compound for the cross-sectional microscopy. The surface of the mounted sample was ground with 180 grit silicon paper until the marks caused by the diamond saw were removed. The grinding operation was continued using 240, 400, 600, 1200 and 2500 grit SiC papers. Samples were then polished on polishing cloths impregnated with 3, 1, 0.25 and 0.1 μm diamond paste respectively. The samples were ultrasonically cleaned in methanol after each stage of polishing.

The most damaged part of the top ring was selected by visual inspection. 2 cm sections were cut from the ring using a diamond saw. These samples were used for plan view and cross-sectional microscopy of the sliding surface. Additionally, a segment of the second ring was prepared in a similar way for cross-sectional imaging. Mounting, grinding and polishing were the same as for the bore sections. Coupons were also cut from the major and minor faces of the piston skirt, and mounted and polished in a similar way.

In order to study the scuffing mechanisms in the Saturn engine, the microscopic investigation has been carried on the major thrust face of the scuffed bore. One-inch (2.54 cm) diameter coupons were cut from the major face of the engine bore at a distance of 45 mm from the deck face (top surface of the bore). These samples were then cut in half, providing two sections to be used later for plan and cross-sectional view microscopy parallel to the sliding direction. The cutting was initiated at the free surface of the coating to reduce the possibility of separation from the substrate. Hexane was used as a solvent to remove the residual engine oil from the sliding surface of the coupons. The same metallographic preparation sequence was used for these samples as previously described for the Corvette engine bores.

TEM investigations were performed on the major face of the scuffed Corvette engine. TEM samples were taken along both the longitudinal and the transverse directions of the engine. Strips were cut from the damaged area of the major face of the engine with the length of 2.3 mm and width of 1.1 mm using a diamond low speed saw. The samples were further glued together with worn surfaces towards each other using epoxy. They were then mounted into copper tube with inner diameter of 2.3 mm. The

surfaces with the scuffing damage were located in the centre of the tube. Disks were sectioned from the tubes with a thickness of 0.7 mm and hand polished down to 100 μm . The centres of the samples were then mechanically dimpled using a dimple grinder to a minimum thickness of 30 μm . The dimpled disks were then argon-ion-beam milled at room temperature using an ion polishing system until the final perforation.

6.1.5. PIN-ON-DISC WEAR TESTS UNDER ARGON ATMOSPHERE

Careful experiments were made to determine the laboratory test conditions under which the scuffing micromechanisms that occurred in the engines could be simulated. There are a number of advantages using a tribometer (e.g. pin-on-disc) in a laboratory in order to simulate scuffing. They include:

- 1) Pin-on-disc tests enable precise control of test load and duration.
- 2) It is possible to continuously monitor the coefficient of friction, so that the onset of scuffing may be determined.
- 3) Tests can be stopped at the onset of scuffing for metallographic investigation.

Engine tests are time consuming and expensive to set up and run. Therefore, if the conditions under which scuffing occurs in a given material can be simulated using pin-on-disc tests, an efficient and cost effective way of improving wear, and scuffing resistance materials can be obtained.

The problem of studying a damage accumulation events leading to scuffing is much more complicated in an engine bore than the controlled laboratory tests. The

temperature and atmosphere that the contacting surfaces are exposed to are not constant in an engine. The loading is more complicated and variable, because neither the sliding velocities nor the normal loads are fixed, as in pin-on-disc bench tests. The bore wall experiences loading from the gas pressure, which may be corrosive from the piston ring(s) and from the piston skirt. It must also be recognized that the interaction of the cylinder bore wall with engine oil is a critical parameter in determining the thickness of the lubricant film. There are many other effects that influence the thickness of the lubricant oil film between the bore wall and the rings or piston. These include the amount of oil available to the contact, ring tensions, surface finish, pressure, temperature, oil properties, etc. Consequently, the thickness of the lubricant in the contact is unknown, neither its quality and physical properties. Furthermore, the onset of scuffing is usually not immediately apparent in a running engine. The damage observed then becomes the combined result of the initial scuffing and any subsequent wear due to fracture, seizure, 3-body wear from loose hard particles, etc. The main points can be summarized as follows:

- 1) The temperature and atmosphere of the contact surfaces in an engine bore are not constant.
- 2) Loading is complicated since the loads and speeds are not constant as they are in pin-on-disc tests.
- 3) The bore wall experiences loading from the piston rings, the piston skirt, and from gas pressure which may be corrosive.

The pin-on-disc wear tests in this work were conducted on HVOF 1020-2.5% Al samples under an argon atmosphere to avoid oxidation of the contact surfaces of the

coatings. The tests were performed under a boundary-lubricated conditions. An all purpose oil was used as a lubricant to eliminate the formation of chemical components (e.g. zinc dialkyldithio phosphate (ZDDP)) on the sliding surfaces. Tests were run to 15,000 m. The wear samples were in the form of 25mm x 25mm x 5mm square 319 Al alloy coupons coated with HVOF 1020-2.5% Al, which was the same as the coatings in the scuffed engines.

Engine grade cast iron samples (ASTM A30 grey cast iron) were tested for comparison of their scuffing resistance. The A30 grey cast iron has a pearlitic matrix with graphite flakes of 45 μm in average length, and a distance of approximately 9 μm between them. The properties of this material are as follows: Vickers hardness at 25 g 251 ± 10 (kg/mm^2), density 7.3 ± 0.3 (g/cm^3), tensile strength 238 ± 6 (MPa) [80].

The surfaces of all the samples (HVOF 1020-2.5% Al coatings and cast iron) tested under the argon atmosphere were polished to a roughness of $R_a = 0.10 \pm 0.05$ μm prior to the wear tests. The tests were performed under a high load of 100 N to produce high shear stresses and to deform the surfaces, and a low speed of 0.2 m/s to minimize the contact temperature increase during deformation. The pin was an AISI type M2 high speed tool steel with a diameter of 5 mm. The worn coatings were sectioned both normal and parallel to the sliding direction with a diamond saw to produce samples for cross-sectional microscopy in both directions. The same metallographic preparation sequence was used for these samples as previously described for the preparation of engine bores (Section 6.1.4).

6.2. RESULTS

6.2.1. SCUFFED CORVETTE ENGINE BORES

6.2.1.1. OPTICAL SURFACE PROFILOMETER MORPHOLOGY

Visual inspection showed that the scuffing damage depended strongly on the position around the bore. As seen in Fig. 6.2, the damage was the greatest on the major thrust face. The damage was also visible on the minor thrust face, but not as severe as the damage on the major face. In contrast, the front and back of the cylinders had no visible damage. The WYKO surface profiler system (WYKO NT 8000 system) was used to measure the surface roughness of the faces of the scuffed bores. The vertical-scanning interferometry (VSI) mode was used because it was more suitable to investigate rough surfaces and steps generated during scuffing. The system was able to sweep a wide surface area by using the stitching option. Because the samples were cut from the actual cylinder bores, cylinder and tilt correction, were applied. Low pass filtering was chosen to eliminate noise. The initial visual observations were confirmed by the WYKO optical profilometry data from the front, major, and minor faces, and these are shown in Figs. 6.3, 6.4, and 6.5 (a and b) respectively. The important features seen on these images are explained in the following paragraph.

Fig. 6.3 is a 3D WYKO image from the front face of the bore, which shows the 30° crosshatch hone marks very clearly with no evidence of scuff marks. An analysis of the profilometry data found the average surface roughness, R_a , to be 0.6 μm , which is consistent with the original surface preparation. The back of the bore was found to have a similar profile. The surface morphologies of these faces differ significantly from the minor thrust face (Fig. 6.4) where evidence of the hone marks was almost completely

removed, and wear scars parallel to the direction of piston travel are apparent. The average roughness of this surface has increased slightly to $R_a = 0.7 \mu\text{m}$. Fig. 6.5.a is a typical 3D WYKO image from the scuffed area on the major thrust face, which demonstrates the severity wear associated with deep scratches. The hone marks are completely removed, and the scars from the scuffing are very deep, resulting in a surface R_a of $3.6 \mu\text{m}$. Fig. 6.5.b is the 2D WYKO image of the major face, which shows Y (perpendicular to the direction of surface scratches) and X (parallel to surface scratches) profiles. The important information arising from this figure is that the depth of the scratches can be as large as $15\text{-}20 \mu\text{m}$. This is shown in the Y profile where $R_v = 17.27 \mu\text{m}$ was obtained. The R_v is defined as the depth of the lowest point of a valley on the surface. The main observations can be summarized as follows:

- 1) The scuffing damage depended strongly on the position around the bore.
- 2) The scuff marks were parallel to the direction of piston movement.
- 3) The crosshatch hone marks were removed on the major and minor faces, and scuff marks were visible on both faces.
- 4) The scuffing damage was much more significant on the major face.

6.2.1.2. SEM OBSERVATIONS OF THE MAJOR FACE OF SCUFFED CORVETTE ENGINE BORES

SEM and EDS analyses were performed on the surfaces and cross-sections of the major, minor, front, and back faces of the scuffed cylinder bores. Fig. 6.6 shows a plan

view secondary electron SEM image taken from the surface of the major face of the bore at 45 mm below the deck face of the engine (middle part of the bore). This area of the bore was subjected to the sliding contact motion of both the piston skirt and the piston rings. The magnification of this image is 400 times the WYKO images presented in Fig. 6.5.b. There is no evidence of hone marks at this magnification, and the deep longitudinal scratches with widths of 500 μm are apparent. There are cracks on the sliding surfaces perpendicular to the sliding direction. The large areas that have a rough appearance are the regions where subsurface cracks have propagated to the surface, and a part of the coating delaminated and induced high surface roughness. It is also important to note that the surface is free of oxide, indicating that the scuffing of the engine on the coating did not exhibit the oxidative wear mechanisms observed in laboratory tests done in air.

Cross-sectional micrographs taken from the area on the major thrust face (middle part of the bore) with different magnifications are shown in Figs. 6.7.a and b. The sample was prepared according to the metallographic preparation method explained in Section 5.1.3. The micrograph shows that a subsurface crack extended to the free surface, and it also shows the presence of a mechanically mixed tribolayer at the sliding surface. The high magnification micrograph in Fig. 6.7.b shows the features of the severely deformed region more clearly. At this magnification, the mechanically mixed layer appears to be less than 5 μm thick, usually with a sharp boundary with the underlying material. The layer appears to be compact and exhibits a fine oxide particle morphology that is different from the ones found in the underlying bulk. There is no oxide vein or chunky inclusion structure; rather the oxide appears to have been fractured into small spherical particles of

0.5-1.00 μm in size. (TEM investigations showed that the particles were actually reduced to nanometric size, as will be discussed in Section 6.3.2.). The micrograph shows that subsurface cracks propagated along the oxide veins at the Fe /FeO interfaces, which have a low local fracture toughness of only 0.5 MPa ($\text{m}^{1/2}$) [6]. The cracks eventually reached the free surface and caused the formation of the fractured areas seen in Fig. 6.6.

Fig. 6.8 is another SEM image of the tribolayer that was formed on the major face. The micrograph shows oxide veins and the iron splats that are aligned in a direction parallel to the direction of the plastic deformation. The significance of this figure is that it indicates that the deformation is unidirectional, because all the visible microstructural elements were aligned in the same direction, namely from the right to the left of the figure. This implies that the direction of the shear stress that was generated during the sliding contact of the rings and/or the piston was significantly higher in one direction. This is discussed in detail in Section 6.3.2 by taking into consideration the magnitudes of the thrust forces in the combustion cycles. Oxide inclusions in the tribolayers were aligned in the direction of the strain gradient as shown in Fig. 6.8.

Fig. 6.9 is another micrograph taken from the same region revealing in more detail the mechanism for the cracking in the inclusions. Using the energy dispersive spectroscopy (EDS) capability of the electron microscope, the large medium grey particles were identified as iron, aluminum and oxygen containing constituents. These particles had a stoichiometric composition of FeAlO_3 (according to selected area diffraction patterns of TEM, see Section 6.3.2.). The micrograph in Fig. 6.9 shows cracking in these particles. Several of the particles show cracks that are localized within the particles; others show cracks that extend between adjacent particles, and some to the

free surface. These observations imply that the FeAlO_3 inclusions in the HVOF 1020 2.5% Al coatings played a detrimental role and caused degradation of the coating surfaces deposited inside the Corvette engine bores.

Fig. 6.10 is a secondary electron SEM image of the longitudinal cross section from the major face of the Corvette engine that shows how the surface layers were detached from the scuffed HVOF 1020 2.5% Al coatings. It shows that highly deformed tribolayers were delaminated at some parts of the coating, and produced plate like loose debris of about 100 μm width. A large crack propagating parallel to the sliding direction near the bottom of the tribolayer, i.e., 10-20 μm below the contact surface is also clearly seen. Fracture of the part of tribolayer to the right of the figure appears to be imminent. The fractured section shown in this cross section corresponds well to the fractured sections observed on the scuffed surfaces shown in Fig. 6.6.

Therefore, it can be concluded that the main mechanism causing material loss during scuffing is the detachment of the tribolayers from the surface.

6.2.1.3. SEM OBSERVATIONS OF THE MINOR FACE OF SCUFFED CORVETTE ENGINE BORES

The damage on the minor side of the engine bore was not as severe as the damage on the major face. Therefore, only a brief discussion of the SEM observations is presented here. Fig. 6.11 is a cross-sectional secondary SEM image taken from 45 mm below the deck face of the minor face. The micrograph shows deformation of the tips of the iron splats on the contact surface. It also shows delamination of the part of the splats as a result of crack propagation along the oxide veins/iron splat interface and total

separation of some splats. The microstructure however, is considerably different from the one found for the equivalent position on the major face. There is no evidence of a mechanically mixed layer or of any flow parallel to the shear loading direction. There is also no evidence for fracture of the oxide inclusions. Therefore, the damage on the minor face was mainly due to the fracture of the deformed splat tips, and the removal of some splats adjacent to the contact surface.

In summary, the current metallographic observations revealed the following important features of the scuffing mechanisms:

- 1) The cross-sectional microstructures of the major and the minor faces are considerably different from each other, with the major face exhibiting more severe scuffing damage.
- 2) The mechanically mixed tribolayers were formed only on the major face, which consisted of a matrix of deformed iron with fine particles of inclusions dispersed in it.
- 3) Plastic deformation beneath the mechanically mixed layer on the major face exhibited a unidirectional pattern, which was due to the application of high loads during the power stroke of the combustion cycle.
- 4) The delamination of the tribolayers was the primary source of material removal during scuffing. This process was facilitated by crack formation at the FeAlO_3 inclusions as well as fracture along the FeO veins between the iron splats.

6.2.1.3. SEM OBSERVATIONS OF THE PISTON SKIRT

Figs. 6.12 a and b are photographs taken from two sides of the piston skirt in contact with the major and minor faces of the cylinder bore. Just as the bore was more damaged on the major thrust face than on the minor face, the piston skirt also had more damage on the side in contact with the major face. The piston skirts originally had tin plating. This plating is known to reduce scuffing during break in. The plating is thin and wears away rapidly on the high points during the first few hours of operation. The back-scattered SEM images from the side of the piston in contact with the major side of the bore are shown in **Figs. 6.13 a and b**. The micrographs show surface damage in two different magnifications. In **Fig. 6.13 a**, cracks perpendicular to the sliding direction are clearly visible. The light grey areas in the image are identified as iron by the EDS. The iron particles were transferred from the HVOF 1020-2.5%Al coating on the cylinder bores. **Fig. 6.13b** shows higher resolution microscopy of the transferred iron particles. There was no evidence of tin-plating on the damaged regions of the piston in contact with the major face.

The main observations on the piston skirt can be summarized as follows:

- 1) The piston skirt had more damage on the side in contact with the major face, and less damage on the side in contact with the minor side.
- 2) SEM observation of the major side shows materials transferred (presence of iron) from the bore coating.

6.2.1.4. SEM OBSERVATIONS OF THE TOP PISTON RING

Visual inspection of the top piston ring showed that some parts of the ring were severely damaged, and the damage was not uniform around the ring. A segment of the top ring that was prepared from the undamaged area for cross sectional microscopy imaging is shown in Fig. 6.14. The cross sectional micrograph shows the microstructure of the ring. Fig. 6.15 is a back-scattered SEM micrograph of the mid section of the damaged area of the contact surface of the ring. The image shows that the contact surface of the ring was cracked along a direction perpendicular to the sliding direction with scratches parallel to the sliding direction. There is also evidence of material transfer (dark region) to the surface of the ring. The EDS analysis of the dark coloured area in Fig. 6.15 showed that this area consists of Al, Fe, O, and Cr. Possible sources of the Al are i) the transfer of aluminum directly from the Al containing inclusions detached from the surface of the coating or ii) the Al is transferred from the other parts of the engine, most likely from the piston skirt. Fig. 6.16 consists of secondary and back-scattered SEM micrographs taken from the edges of the severely damaged area. The edge of the ring in the damaged area was fractured in chips. The released particles could have contributed to the surface damage and deformation by scratching the coating surfaces. The longitudinal scratches seen on the sliding surface in Fig. 6.6 may be due to the action of the particles fractured from the ring.

In summary, the metallographic observations of the piston top ring underline the following points:

- 1) The damage on the ring was asymmetric.

- 2) The edges of the ring were chipped in the most severely damaged areas. This may have contributed to the damage of the coating surfaces on the bore surfaces.

6.2.2. SEM OBSERVATIONS OF THE SCUFFED SATURN ENGINE BLOCK

Extensive SEM investigations have been performed on the major face of the bore 45 mm below the deck face (middle part of the bore) of a Saturn engine that failed during a cold scuff test. Fig. 6.17 shows a typical microstructure of the scuffed area. The micrograph shows a three-layered microstructure. The first layer was the undeformed bulk structure. Near the contact surface, the microstructure was very fine and severely deformed. It consisted of finely fractured oxide inclusions aligned in the power stroke direction. Mechanically mixed tribolayers existed on the top. The micrograph shows that the tribolayers were almost completely detached from the sliding surface. Therefore, the material removal mechanism during scuffing was similar in both the Corvette and Saturn engines.

Fig. 6.18 shows that a subsurface crack extended parallel to the contact surface at a depth of 5 μm below the contact surfaces. Similar to the coating in the scuffed Corvette engine, the propagation of subsurface cracks appeared to have caused the delamination of tribolayers.

The deformation patterns of the highly deformed coating layers beneath the tribolayers in both engines were similar. This can be seen when the features shown in Fig. 6.18 are compared with those in Fig. 6.8. Fig. 6.18 reveals that at a depth of 10-15

μm , the oxide veins have assumed a preferred symmetry along lines running from the lower left area to the upper right area of the image. This indicates that the direction of the damage was unidirectional, and that it was dictated by the direction of the power stroke.

It is clear from Fig. 6.19 that AlFeO_3 inclusions acted as crack initiators. They were the nucleation sites for more extensive cracks that propagated beneath the tribolayers. This is another common aspect of scuffing damage in the HVOF 1020-2.5% Al coatings taken from the two engines.

In conclusion, the SEM investigations of the scuffed Saturn engine showed considerably similar microstructures to those found at the same locations in the Corvette engine. The mechanisms of scuffing of the HVOF 1020-2.5% Al coatings in both engines were the same.

6.2.3. SEM OBSERVATIONS OF HVOF 1020-2.5% Al COATINGS AFTER PIN-ON-DISC WEAR TESTS

HVOF 1020-2.5% Al coatings were tested at 100 N load, and 0.2 m/s speed for 15,000 m sliding distance under Ar atmosphere and boundary lubricated conditions in order to simulate scuffing under the laboratory conditions (see Section 6.1.5.). The worn samples were examined under the SEM to observe the similarities between the microstructures of the coatings scuffed under the laboratory conditions, and those taken from the scuffed engines. SEM cross sections prepared parallel to the sliding direction of the samples subjected to pin-on-disc wear tests are shown in Figs. 6.20 and 6.21. Fig. 6.20 is a back-scattered image, and shows the presence of a highly deformed layer at the

sliding contact of the coating. This layer was generally discontinuous with a thickness of less than 4 μm . The layer had a microstructure consisting of small oxide particles that were distributed in the severely deformed iron matrix. This morphology of finely distributed oxide particles was different from the large inclusions and the oxide veins seen in the underlying bulk material. The micrograph also shows cracking of inclusions, which were identified as FeAlO_3 with the aid of a TEM. Similar microstructure was observed in the scuffed engines bores, as reported in Section 6.2.2. It is also important to note the presence of a long crack extending parallel to the contact surface at the bottom of the tribolayer. Similar to the coatings taken from the scuffed engines, this type of crack formation led to a surface fracture during the pin-on-disc tests.

Fig. 6.21 shows extensive damage to the inclusions. The fractured particles became connected to form longer cracks that typically propagate through the tribolayer to the surface. Fig. 6.22 shows that the highly deformed tribolayer fractured, this led to the formation of loose debris during pin-on-disc tests.

In summary, the pin-on-disc tests that were performed on the thermal sprayed coatings of HVOF 1020-2.5% Al under Ar atmosphere and boundary lubricated condition were successful in reproducing the microstructures that closely matched with those generated in the scuffed engine bores coated with the same coating. This microstructural link suggests that the pin-on-disc tests can be used to simulate engine scuffing provided that the appropriate conditions are used.

6.2.4. SEM OBSERVATIONS OF CAST IRON AFTER PIN-ON-DISC WEAR TESTS

Cast iron engines subjected to the same cold scuff tests did not scuff where as the HVOF 1020-2.5% Al coatings showed extensive surface damage. Cast iron samples were subjected to pin-on-disc tests under the same conditions as the HVOF 1020-2.5% Al coatings for comparison. The SEM investigations from the longitudinal cross-section of the worn cast iron showed that unlike the HVOF 1020-2.5% Al, no severe subsurface damage occurred in cast iron. There was no evidence of the formation of the deformed layer in the material below the worn surface nor of the tribolayers on the contact surface (Fig. 6.23). The only type of damage that could be observed was the occasional fracture of a fragment of iron that was sandwiched between graphite flakes that were adjacent to the contact surface and the steel pin of the tribometer (Fig. 6.24). In this mechanism the fragment of iron was separated from the bulk by the graphite flake and removed when the flake delaminated. The detached fragments were typically 10-20 μm in size. This mechanism has been reported previously [80] and it is known to correspond to the typical mild wear mechanism in cast iron.

As noted previously, the pin-on-disc tests on the HVOF 1020-2.5% Al were done under argon atmosphere using a load of 100 N. Cast iron samples did not show evidence for scuffing under these conditions. In order to observe the scuffing phenomena in the cast iron, a higher load, namely 150 N, was applied. The sample tested at 150 N exhibited damage due to scuffing on the contact surface. The cross sectional SEM investigations of the sample parallel to the sliding direction showed deformed graphite flakes that elongated parallel to the sliding direction. Several of these graphite flakes that were

elongated in the sliding direction are marked in Fig. 6.25. A layer of material on the contact surface is seen just before it became detached. This layer was 150-200 μm in length. Fig. 6.26 is a higher magnification micrograph of a section near the contact surface, and shows the extent of damage and fracture of the material adjacent to the contact surface. It is clear from the length of the graphite particle extended parallel to the contact surface that the strains in this region were very large (probably greater than 5). The iron layers at these strains were fractured and fragmented into smaller pieces. This mechanism shows similarities to the scuffing mechanism in the HVOF 1020-2.5% Al coatings where the surfaces were also very severely deformed.

In summary, the fracture and fragmentation of brittle constituents in grey cast iron led to the formation of the tribolayers that were subsequently delaminated and detached from the surface. This is similar to the same scuffing mechanism observed in HVOF 1020-2.5% Al coatings.

6.3. ANALYSIS OF ENGINE SCUFFING MECHANISMS

Results of the investigations presented in Section 6.2. shed light on certain important aspects of scuffing in the engines. The microscopic events leading to scuffing on the major thrust surface of the bores namely, extensive subsurface deformation, tribolayer formation, and fracture of the surface layers have been characterized using surface profilometry and SEM. In the next section an analysis of the mechanical events that took place during the engine cycles (Section 6.3.1.) is given to provide a better understanding as to why the major surface of the bore is subjected to scuffing TEM analyses of the deformed subsurface layers taken from the scuffed Corvette engine are

presented in Section 6.3.2. to provide a more detailed understanding of the fundamental physical mechanisms leading to scuffing of the thermal spray coated engines.

6.3.1. CONSIDERATION OF FORCES DURING THE ENGINE CYCLES

The damage on the bores of the scuffed engines was localized on the major and minor thrust faces. A comparison of the major and minor thrust face damage showed that both faces experienced enough surface damage to remove the hone marks, and to exceed the threshold for scuffing. This was visually determined at the end of cold scuffing tests with the observation of scratch marks on the surface. However, the damage was significantly more severe on the major face. The major and minor thrust faces of the bore carry larger piston skirt loads than the front and back portions of the bore. Figs. 6.27.a and b are the free body diagrams of the forces that act during combustion and compression strokes. During the combustion stroke, the crankshaft position changes between 0° and 180° angles. The connecting rod forces the piston skirt to make contact with the major thrust face during this event. Fig. 6.27.a shows the free body diagram of a piston during a power stroke at the crank angle of 30° after top dead centre (TDC) position. The x component of the force exerted by the connecting rod drives the piston against the major thrust face. This is seen from Fig. 6.27.a where the piston skirt is in contact with the major thrust face, while there is no contact at the minor thrust face. The position of the rings is also asymmetric in the contact. The crankshaft position varies between 180° - 360° during the compression stroke. Fig. 6.27.b shows the free body diagram of a piston during the compression stroke at the same position. At this cycle, the

x component of the force applied by the connecting rod drives the piston against the minor thrust face.

Variation of the cylinder pressure against the crank angle during each of the four major engine cycles namely, intake, compression, expansion, and exhaust is shown in **Fig. 6.28**. It is important to note that the gas pressure during combustion and compression are not equal, and the peak gas pressure during combustion is greater than throughout the compression stroke. This explains why more severe damage exists on the surface of the major thrust face, which is consistent with the metallographic results presented in Section 6.2. **Fig. 6.28** also illustrates an important point. Although the total motion of the piston against the major face can be seen as a reciprocating motion in fact because the force applied to the cylinder bore is much higher in the combustion cycle the scuffing is due to the unidirectional sliding motion. This point will be discussed in more detail in Section 6.3.3.

The differences between the major and minor faces initially seen in the WYKO and optical micrographs from the scuffed bores were subsequently confirmed by the SEM images. The microstructure that was observed in the micrographs from the major thrust face was different from the minor face. There was clear evidence of a mechanically deformed tribolayer on the major face. A typical microstructure of the major face of the scuffed engines also exhibited the deformed layer beneath the tribolayer that indicated a region characterized by a pattern of oxide veins elongated towards an orientation in one direction parallel to the surface, which again was indicative of a unidirectional deformation pattern.

The extensive subsurface plastic deformation consisted of iron matrix and fractured oxide particles. Because the deformation microstructure of the subsurface layers and the microstructure of the tribolayers were very different from the original matrix structure additional characterization studies were done on these layers by TEM. They are discussed in Section 6.3.2.

6.3.2. TRANSMISSION ELECTRON MICROSCOPY (TEM) FROM THE MAJOR FACE OF THE CORVETTE ENGINE BORES

TEM investigations on a longitudinal (parallel to the sliding direction) section of the major face of the scuffed Corvette engine confirmed that a graded microstructure was formed as a function of depth in the scuffed HVOF 1020-2.5% Al coating. The substructure formed at depths of about 0.4-0.6 μm below the contact surfaces, and consisted of elongated sub-grains of 0.2-0.3 μm in width, and about 0.1 μm in thickness. These sub-grains were elongated in the direction of sliding. The elongated grain structure can be seen in the TEM micrograph in Fig. 6.29, which is a section parallel to the scuffed surface. It should be noted that a similar structure of elongated grains was formed under the contact surfaces of the samples subjected to pin-on-disc tests carried out in air at 75 N, 2.5 m/s (Section 5.1.4.). The elongated grain structure of the subsurface material obtained from the TEM micrograph of the scuffed coating is schematically shown in Fig. 6.30.

In the region closer to the contact surface, namely 0-0.3 μm below the contact surface, the grain size was remarkably smaller and it was difficult to distinguish the

individual grains. The high magnification TEM micrograph (Fig. 6.31) taken from the material layers immediately below to the contact surface, namely about 0.2 μm below the surface, is shown in Fig. 6.29. This figure reveals the nano-size grain structure more clearly. The nano-size grains are no longer elongated but assumed equiaxed morphology. As shown in Fig. 6.29, the Fe grain size in this region was 20 nm, and the equiaxed grains were mixed with AlFeO_3 particles that were reduced to almost the same size as the Fe grains. The presence of AlFeO_3 is confirmed by the SAED pattern shown in the insert of Fig. 6.29. The features of the layers adjacent to the contact surfaces, namely the fragmented oxide particles and the nano-sized Fe grains, are schematically shown in Fig. 6.30.

It is suggested that the nanostructured grains were formed by the subdivision of the elongated grains into smaller sizes as the strain increased towards the surface, and by the increase in the misorientation angle between them. It is well known that these two processes cause grain refinement as the strain in the material increases [156]. This is consistent with increasing strain gradients towards the contact surfaces in the scuffed coatings. Typically, strains in excess of 3-4 are needed to refine the grain size to the nanoscale range, i.e. less than 50 nm [157]. Therefore, the mechanically mixed layers should have formed under the influence of such high strains.

In summary, TEM results in conjunction with the SEM investigations indicated the formation of the tribolayer on the sliding surface of the scuffed major face and a severely deformed layer below the tribolayer.

6.3.3. CORRESPONDENCE BETWEEN THE MECHANISMS IN THE SCUFFED ENGINE AND THE WEAR MAP FOR HVOF 1020-2.5% Al

It is instructive to compare the microstructural information obtained from the investigation of the scuffed engine bores with the wear micromechanisms presented in the wear map of the HVOF 1020-2.5% Al. The wear map for the HVOF 1020-2.5% Al coatings is presented in Section 5.2.3., and shows the wear mechanisms in this coating at low relative humidity (10% RH) levels on load vs. sliding speed axes. The wear map of the HVOF 1020-2.5% Al (Fig. 5.12) distinguishes between five different wear regimes. It was found that in most areas on the wear map, surface oxidation created a chemically altered layer that played the critical role in controlling the wear rates. It was at high loads and low speeds that the mechanical wear was a dominant wear mechanism. Although some surface oxidation also occurred at this loading condition, the oxide layer was too thin to eliminate the mechanical contact between the sliding surfaces. The highest coating wear rates were measured in tests performed under these conditions. Fracture of splats that were subjected to severe plastic deformation was the principal wear mechanism for the coating under this testing condition. The scuffing mechanism that occurred on the minor face of the Corvette and Saturn engines was similar to the mechanical wear by splat tip deformation, and fracture observed on the wear mechanism map of the HVOF 1020-2.5% Al coatings.

The scuffing damage inflicted on the major faces of the engine bores was much more severe than the mechanical damage identified on the wear map. The wear map was constructed using pin-on-disc tests that were run in air, and as mentioned before, was influenced by the surface oxidation. It is conceivable that the oxides reduced the friction

coefficient hence the shear forces transmitted to the contact surfaces in the mechanical wear regime of the HVOF 1020-2.5% Al coatings. Consequently, mechanically mixed tribolayers that were the typical features of the scuffed sub-surfaces of the coatings on the engines were not observed on the wear map of the HVOF 1020-2.5% Al coatings because the maps were constructed for sliding in air.

The arguments presented above imply that, if a correlation is to be established between the microstructures generated during engine scuffing and those in the pin-on-disc tests, the role of the environment must be taken into account. The gases surrounding the surfaces within a running engine differ significantly from the ambient air. The bore surfaces are periodically exposed to a combustion mix that can be partially reduced. When the engine is appropriately lubricated, the oil film protects the bore wall from excessive shear forces, and can provide a diffusion barrier to oxygen slowing surface oxidation. In addition, sulphur in ZDDP is known to react with the surface and reduce oxygen absorption. The oil has a double role of reducing both the shear stress by reducing the coefficient of friction, and the rate of oxidation. This is the reason why the pin-on-disc tests that were used to replicate the engine scuffing were conducted in an Argon atmosphere. Furthermore, it is useful to introduce lubricants to the surface during these tests. The similarities between the microstructures of the scuffed engines and those of the pin-on-disc tests that were done under the argon atmosphere, and boundary lubricated conditions (see Section 6.1.5) justified the choice of the selection of these conditions.

On the other hand, as discussed in Section 6.3.1. that the motion of the piston against the bore surface is reciprocal; the bore walls are not symmetrically loaded. Because the loading is substantially heavier during the combustion stroke than the

exhaust stroke, the damage is unidirectional on the major face. Therefore, it is appropriate to use unidirectional pin-on-disc tests to simulate the scuffing engine damage. Contrary to general belief, unidirectional tests provide a closer simulation of the engine scuffing than reciprocating tests. This is proven with the close match of the microstructures generated in the experiments described in Sections 6.2.1. and 6.2.3.

To replicate comparable shear loads in the pin-on-disc tests, it was necessary to apply a high normal load to the surface of the coating. This load was found by iterative process, starting from a load of 10 N, and increasing to 100 N, where microstructures exhibited similar features as those found in the scuffed HVOF 1020-2.5% Al coated engines. As noted in Section 6.2.4., cast iron samples is scuffing during the cold scuff tests. Cast iron samples did not exhibit scuffing damage when they were subjected to pin-on-disc tests at 100 N, but they showed scuffing at the higher load of 150 N.

The methodology that was used to develop the laboratory scale pin-on-disc type scuffing tests for the coatings is summarized in Table 6.3.

In the future, it may be possible to further develop these tests as an economical and effective way to determine the onset of engine scuffing under laboratory conditions. An understanding of the mechanism of scuffing in these coatings using laboratory tests will help to optimize their compositions, microstructures, and their fabrication process. Therefore, laboratory scale scuffing tests are expected to provide an efficient way to design scuff resistant coatings for automotive engine applications.

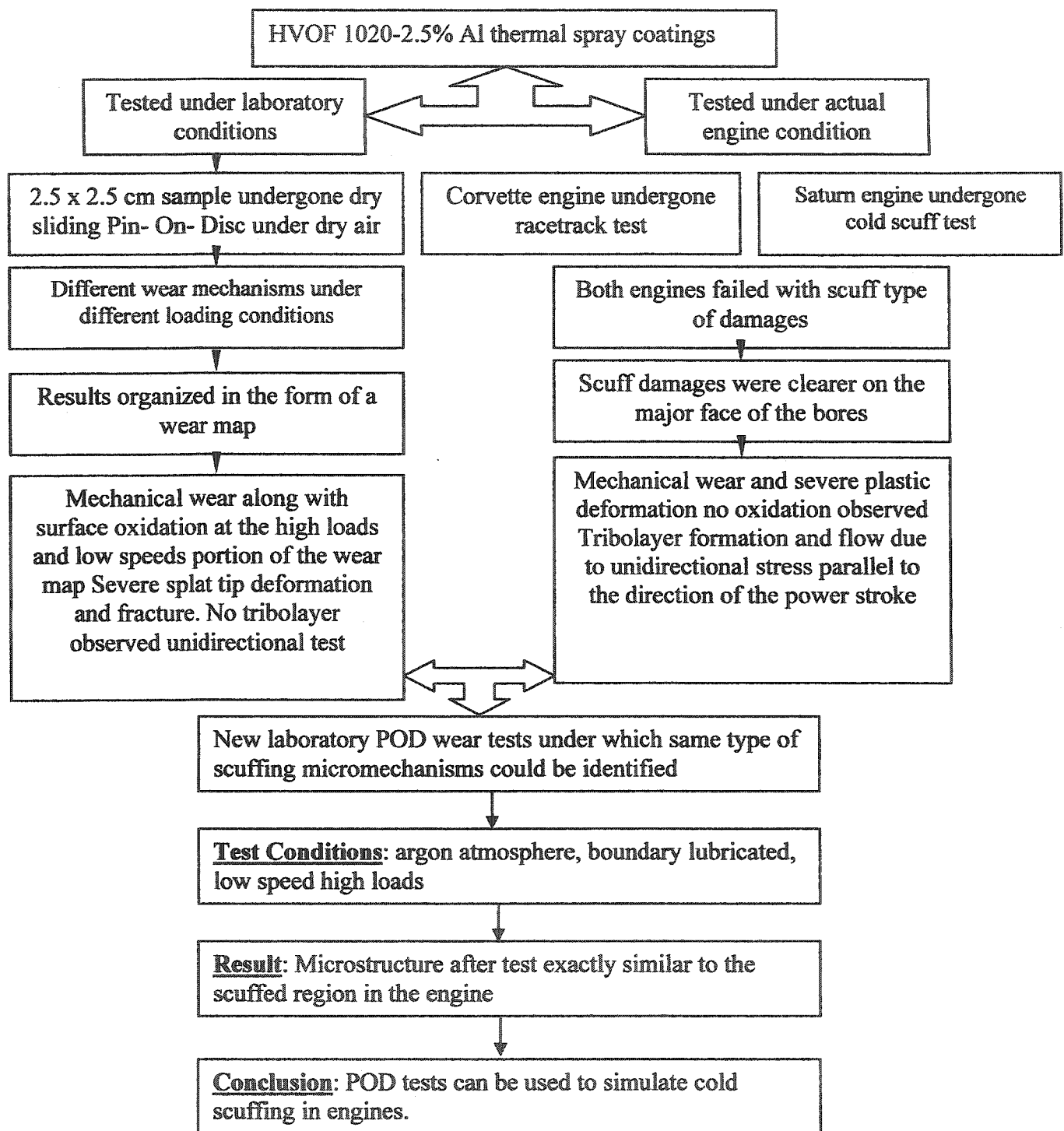


Table 6.3- Methodology used to develop new laboratory test in order to determine the scuff resistance of the materials.

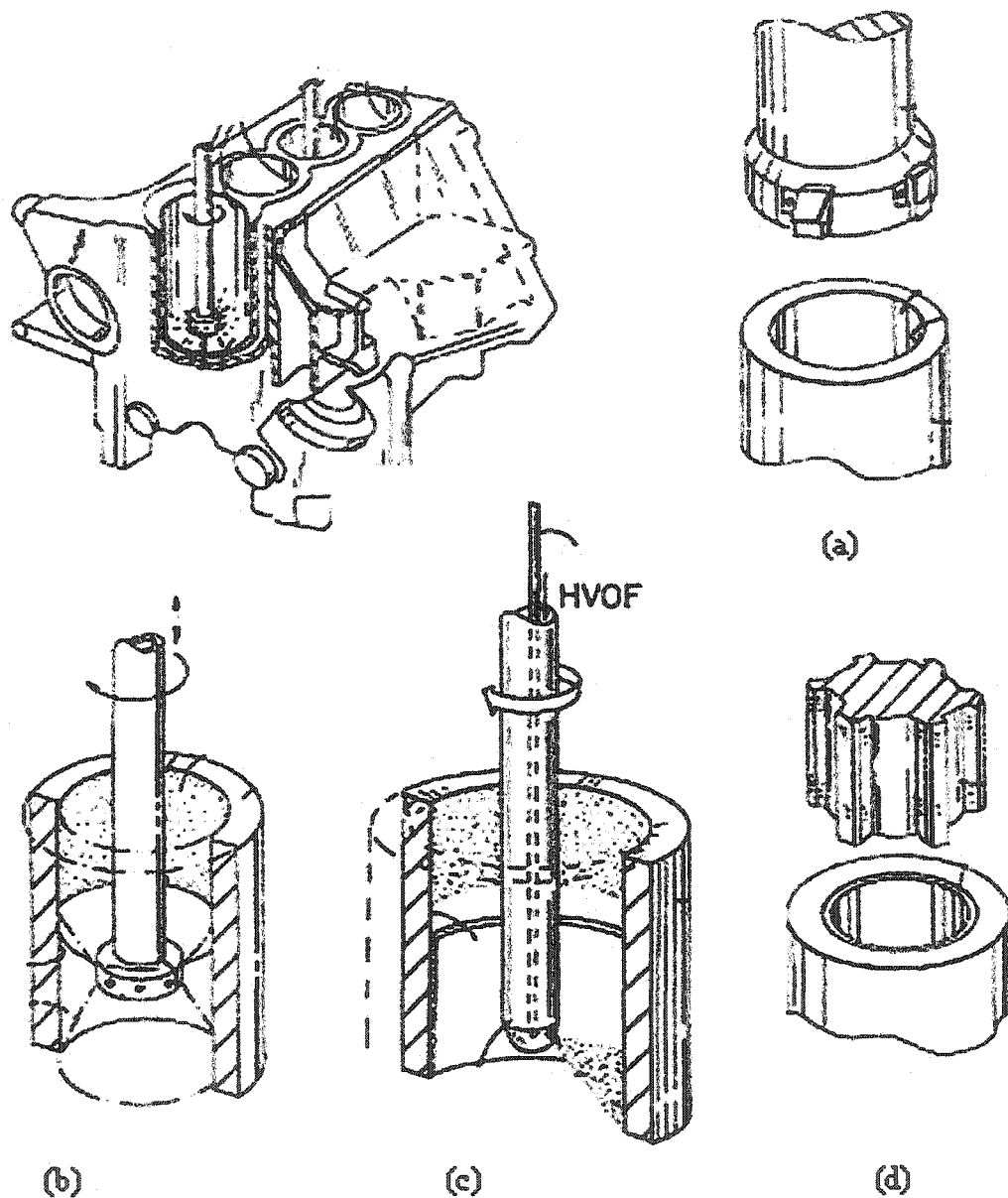
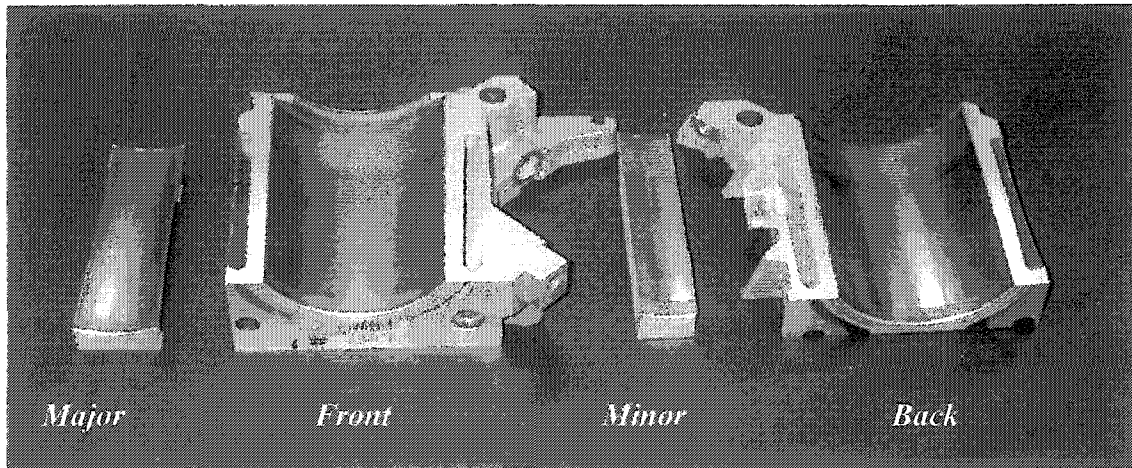
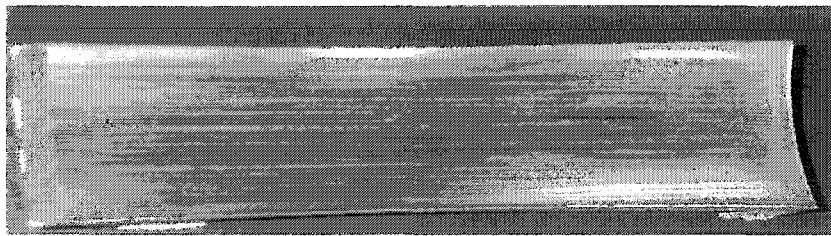


Fig. 6.1- Schematic of the thermal spray deposition process inside a cylindrical sample (a) illustrates the boring of the cast cylinder wall; (b) shows the water jet cleaning/surface roughening treatment of the cylinder wall; (c) illustrates the application of the thermal spray coating to the cylinder wall and (d) shows the honing of the cylinder wall to the finished dimension.



(a)



(b)

Fig. 6.2- a) Photographs of the sectioned bore coated with HVOF 1020-2.5% Al; b) severe scuffing of the major thrust surface of the bore.

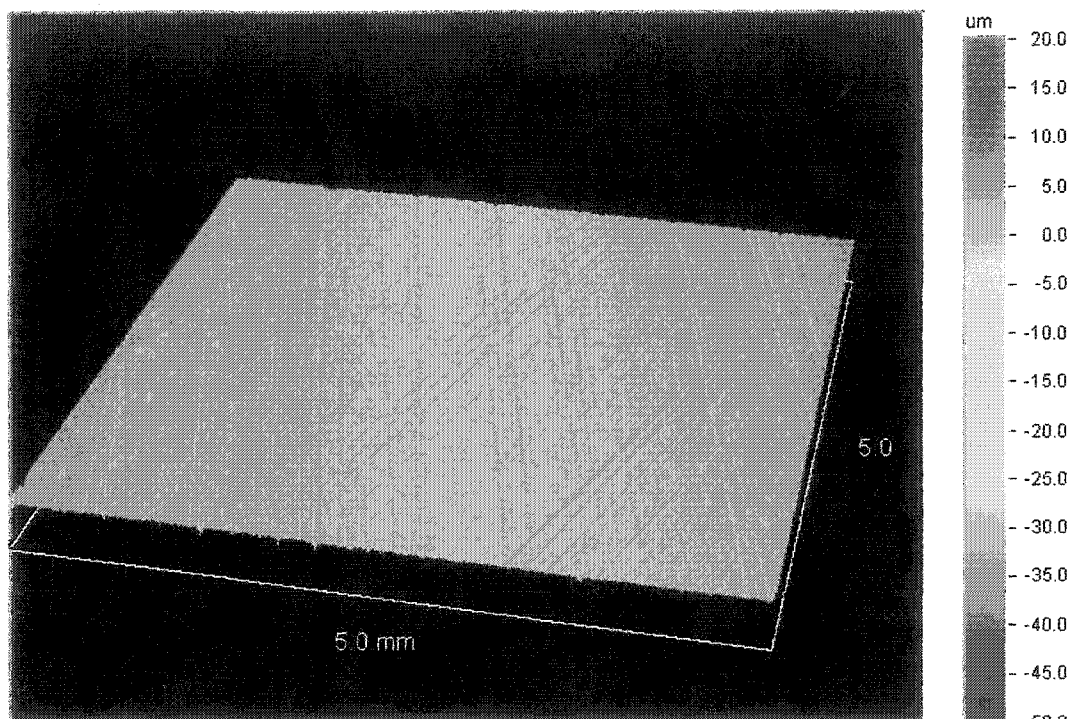


Fig. 6.3- Surface profilometry image from the front face of the scuffed Corvette engine, which shows the crosshatch hone marks on the surface of the HVOF 1020-2.5% Al coating.

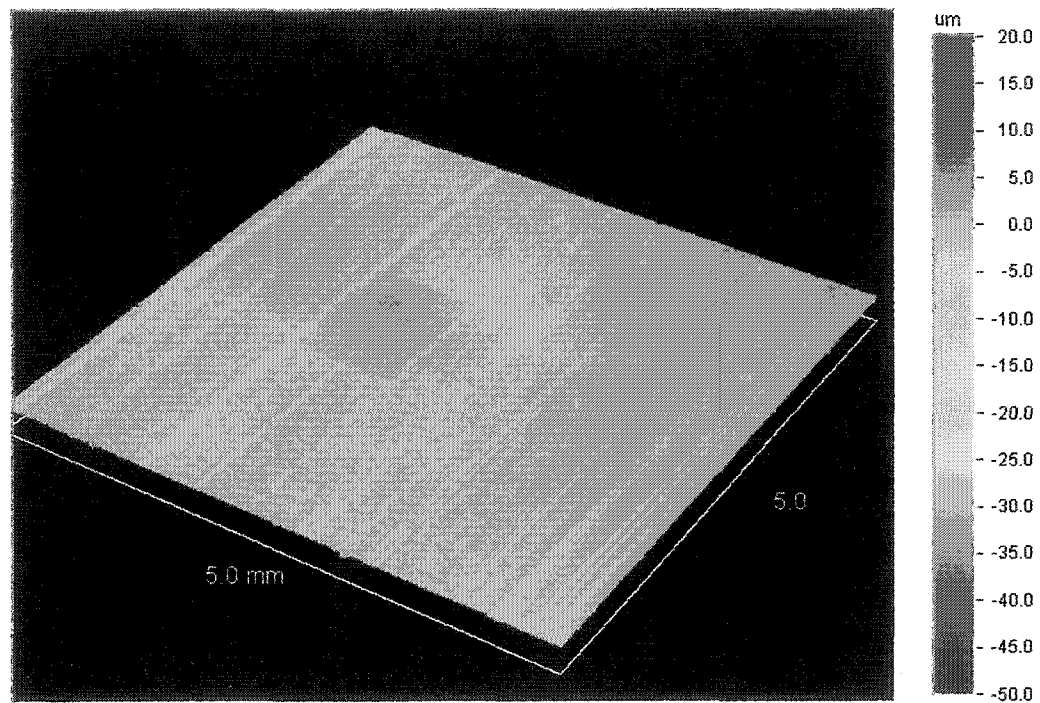


Fig. 6.4- Surface profilometry image from the minor face of the scuffed corvette engine, which shows that the hone marks are completely removed. Scratches and wear scars appeared on the surface of the HVOF 1020-2.5% Al coating.

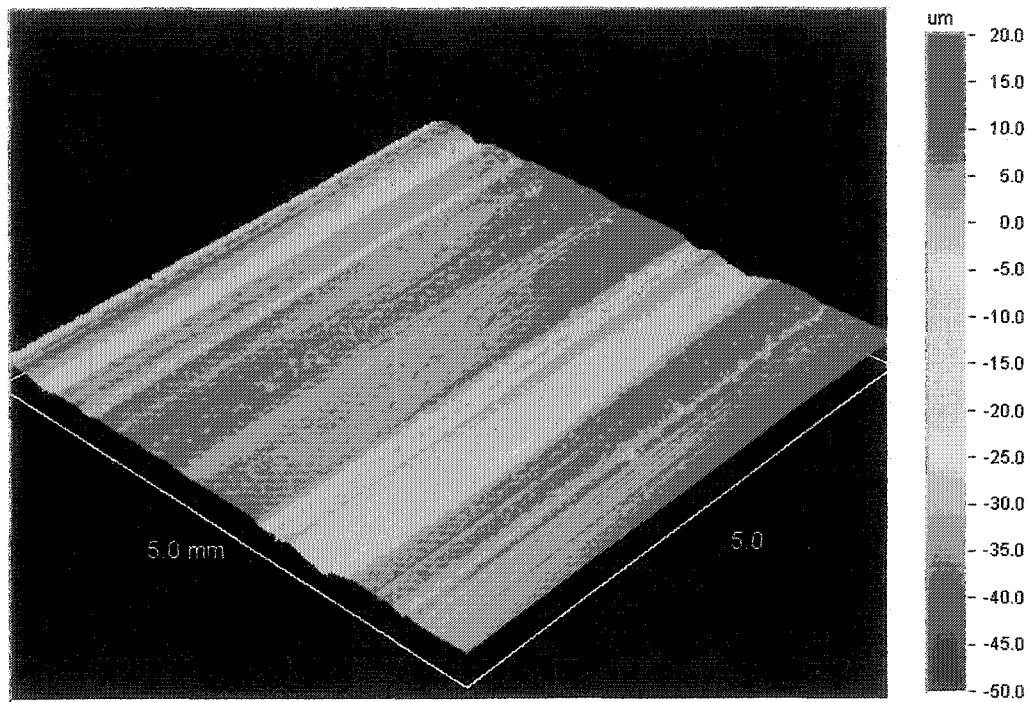


Fig. 6.5.a- Surface profilometry image from the major face of the scuffed Corvette engine. The rough surfaces associated with deep scratches and deep wear scars are clearly seen.

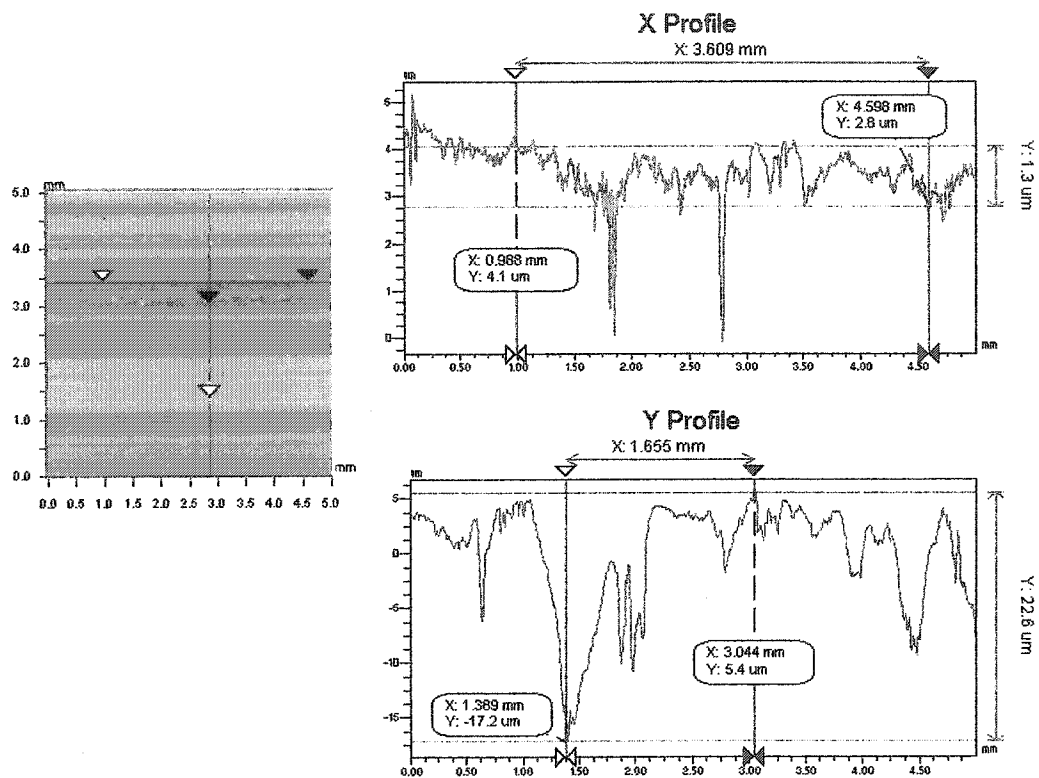


Fig. 6.5.b- Plan view WYKO image of the major face, along with Y and X profiles of selected points as marked on the image.

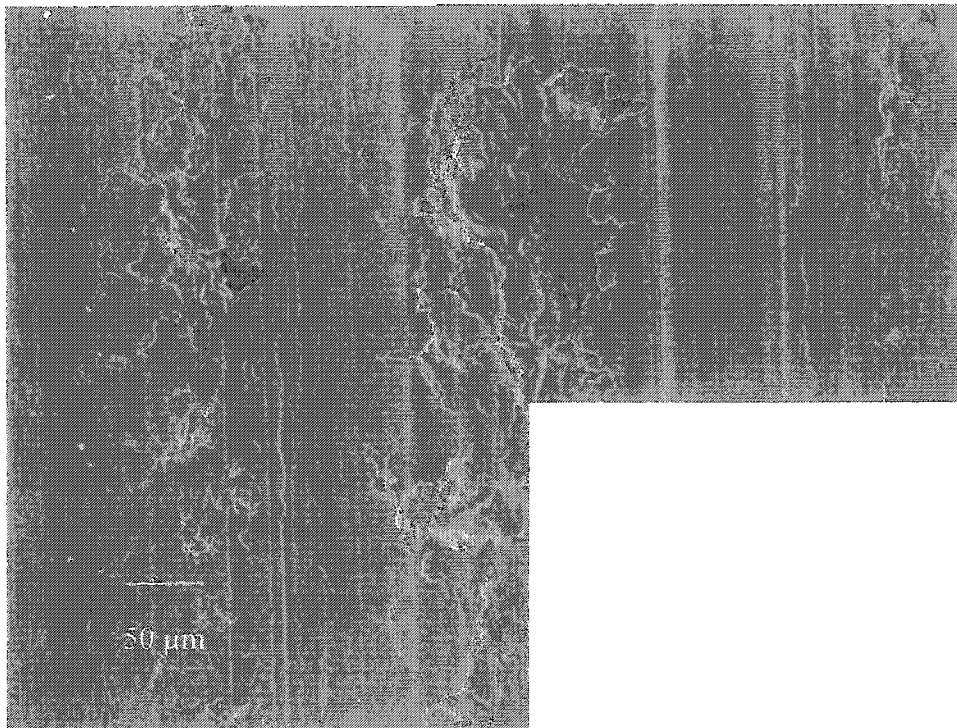
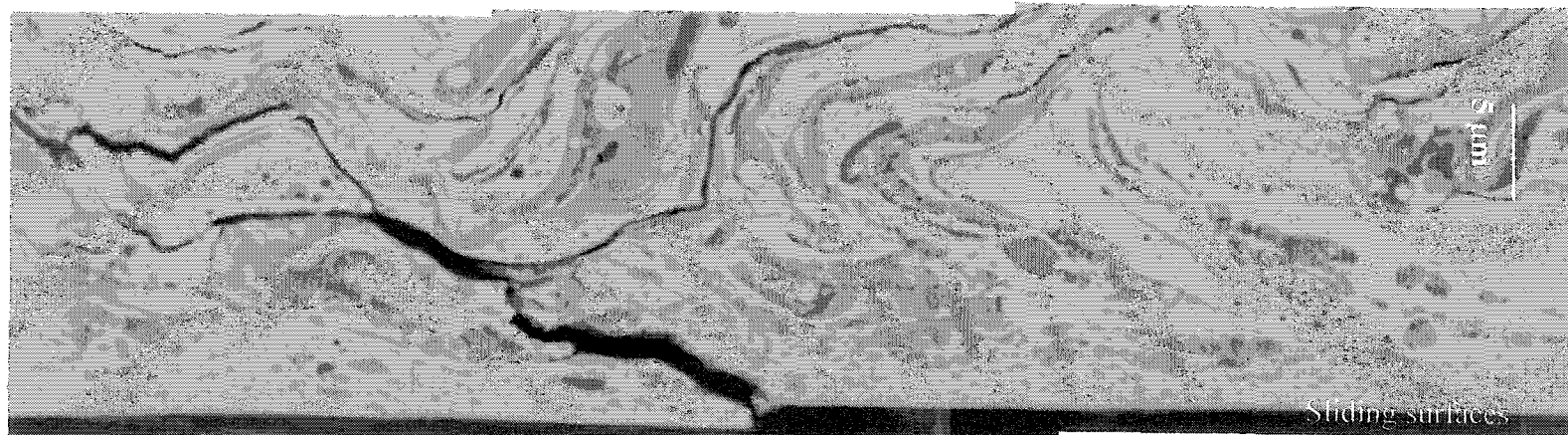


Fig. 6.6- Plan view secondary electron SEM image taken from the surface of the major face of the middle part of the scuffed Corvette engine bore.



(a)



(b)

Fig. 6-7.a- Cross-sectional micrograph taken from the same area on the major thrust face (middle part of the bore), the micrograph shows 2-5 μm tribolayer thick on the sliding surface and extensive sub-surface cracking. Fig. 7b High magnification of the back-scattered SEM image of the damaged surface region (area inside the rectangle) in Fig. 7a shows a mechanically mixed tribolayer, evidence of plastic deformation and flow beneath the tribolayer more clear.

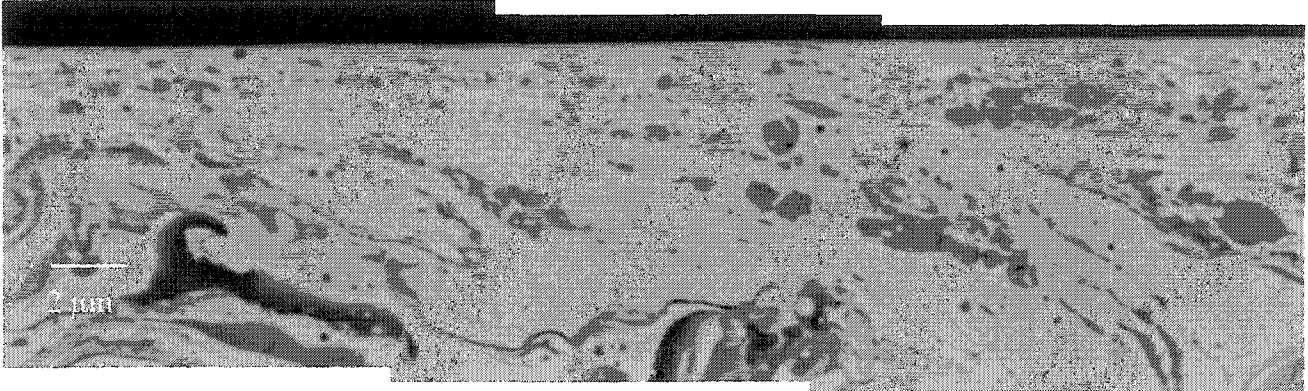


Fig. 6.8- Secondary SEM micrograph taken from the major face of the Corvette engine shows that the shear stress from sliding of the rings or piston induced subsurface plastic deformation and a net flow of the relatively soft matrix. This shear stress also fractured the oxide particles in the tribolayer, reducing their size and dispersing them in the matrix.

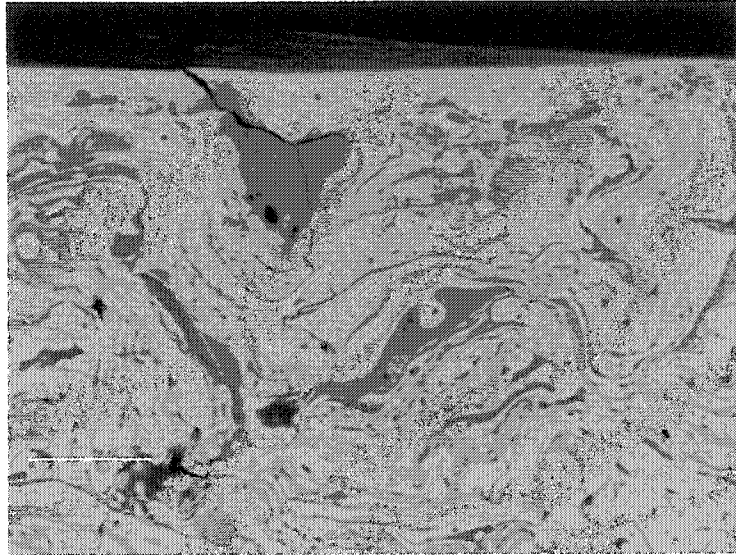


Fig. 6.9- Back-scattered SEM image from the major face of the Corvette engine bore that shows cracking in the particles identified rich in Fe, Al and O using EDS analyses.

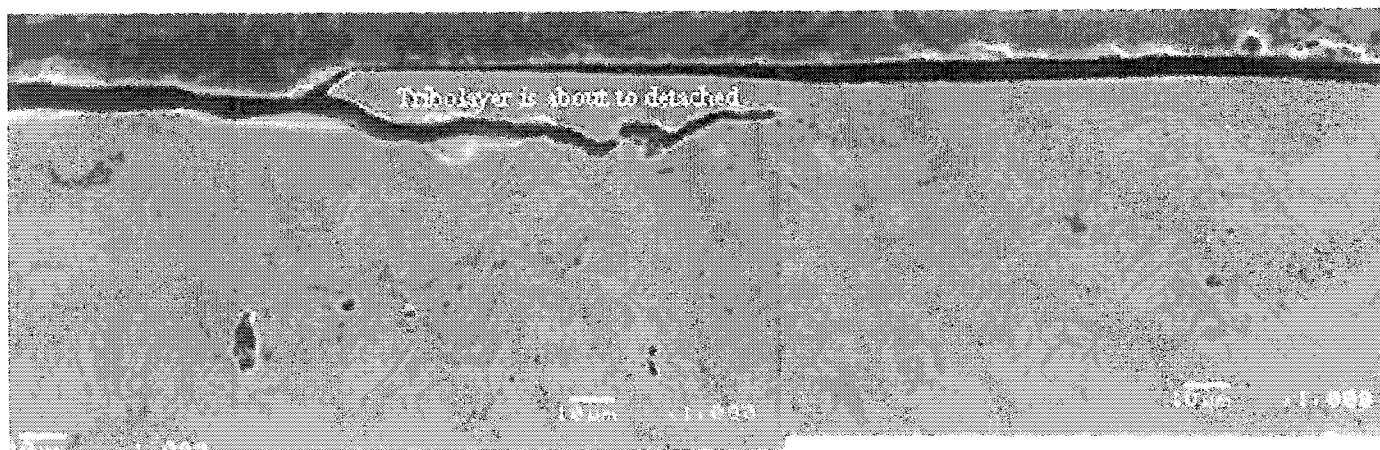


Fig. 6.10- Secondary electron SEM image of the longitudinal cross section from the major face of the Corvette engine shows how the surface layers were detached from sliding surfaces.

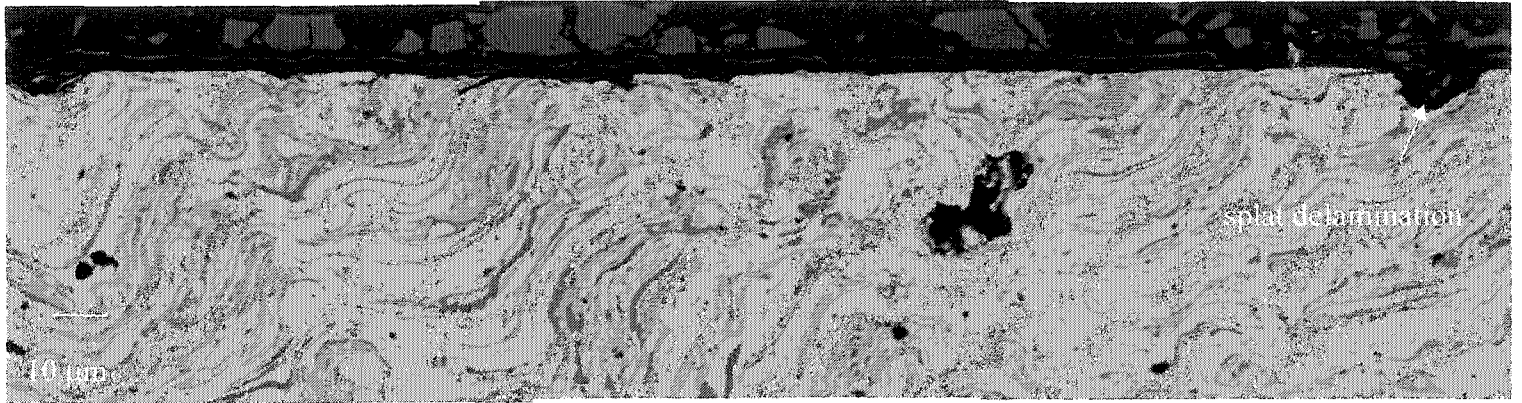
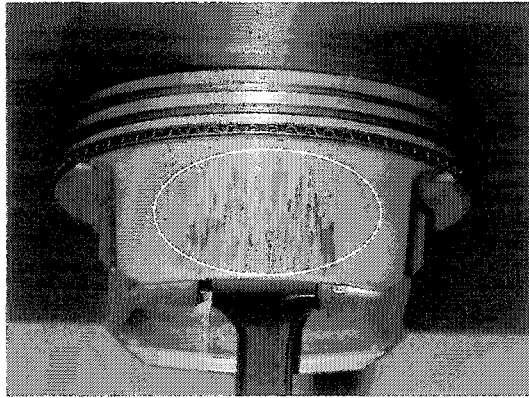
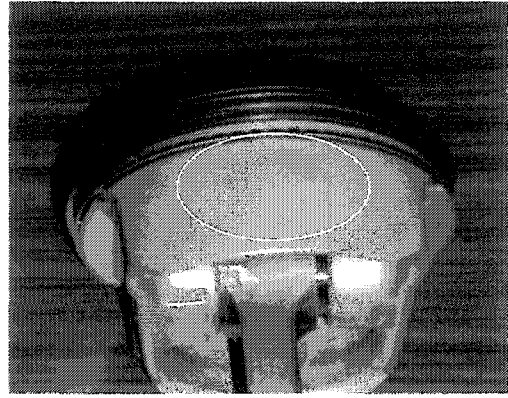


Fig. 6.11- Cross-sectional secondary SEM image taken from the minor face 45 mm below the deck face shows the surface damages in the form of splat delamination. There is no evidence of the tribolayer.



(a)



(b)

Figs. 6.12- Photographs taken from two sides of the piston skirt in contact with (a) the major and (b) minor faces of the cylinder bore.

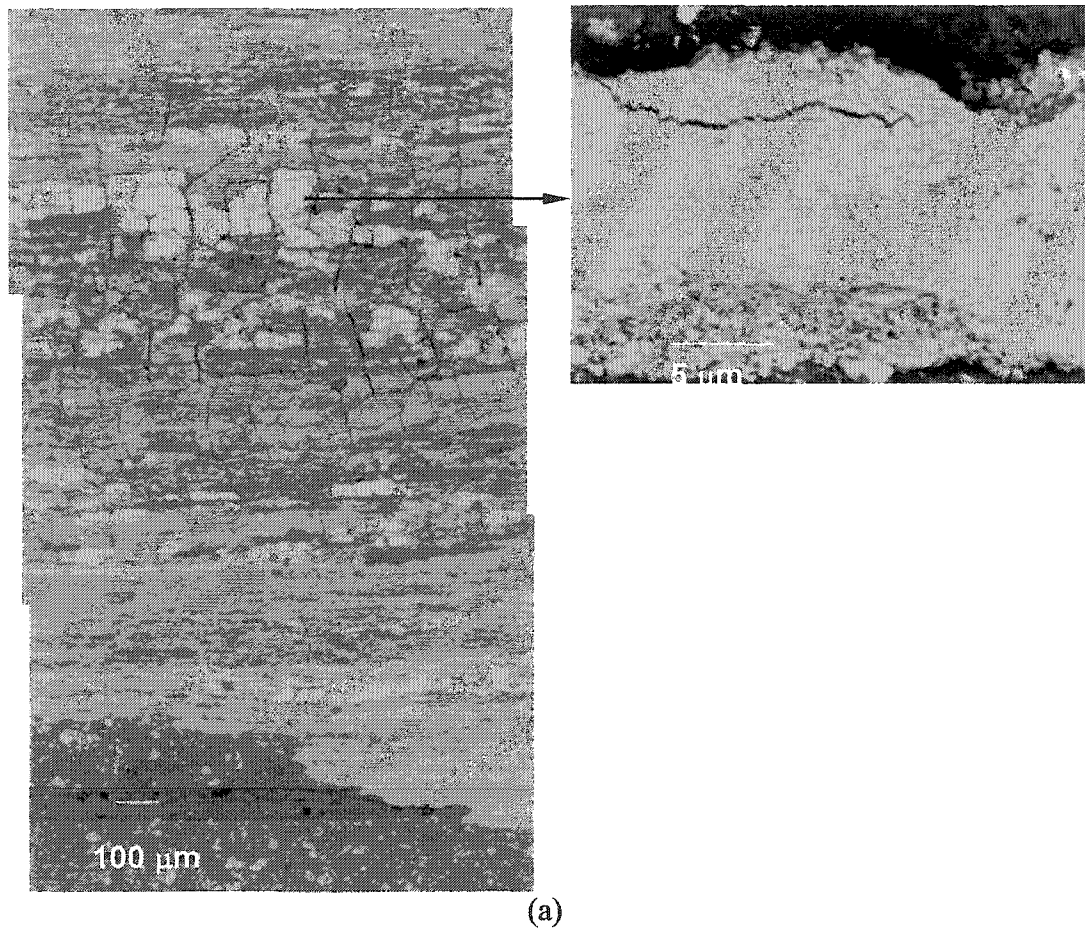


Fig. 6.13- (a) Back-scattered electron SEM image taken from the side of the piston skirt in contact with the major face of the bore with the greatest damage; (b) High magnification micrograph that shows iron patches (light grey area) transferred from the HVOF 1020-2.5% Al coating on the cylinder bores.

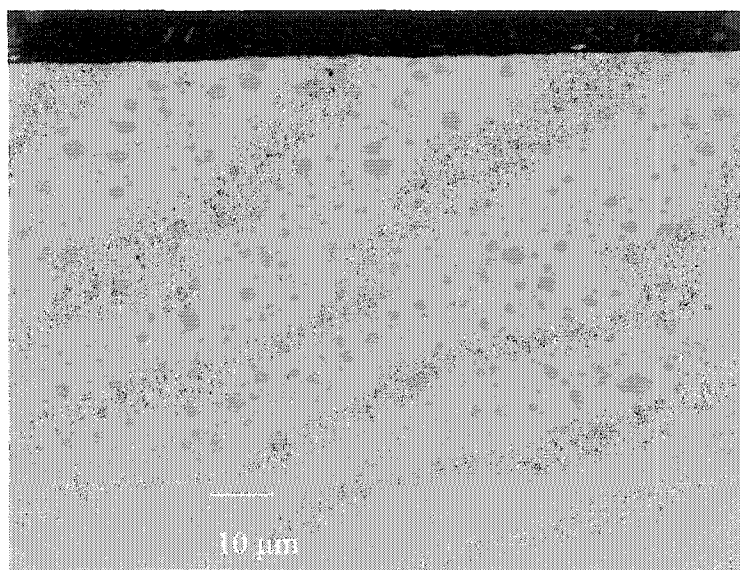


Fig. 6.14- Cross-sectional micrograph of the nitrated stainless steel top ring.

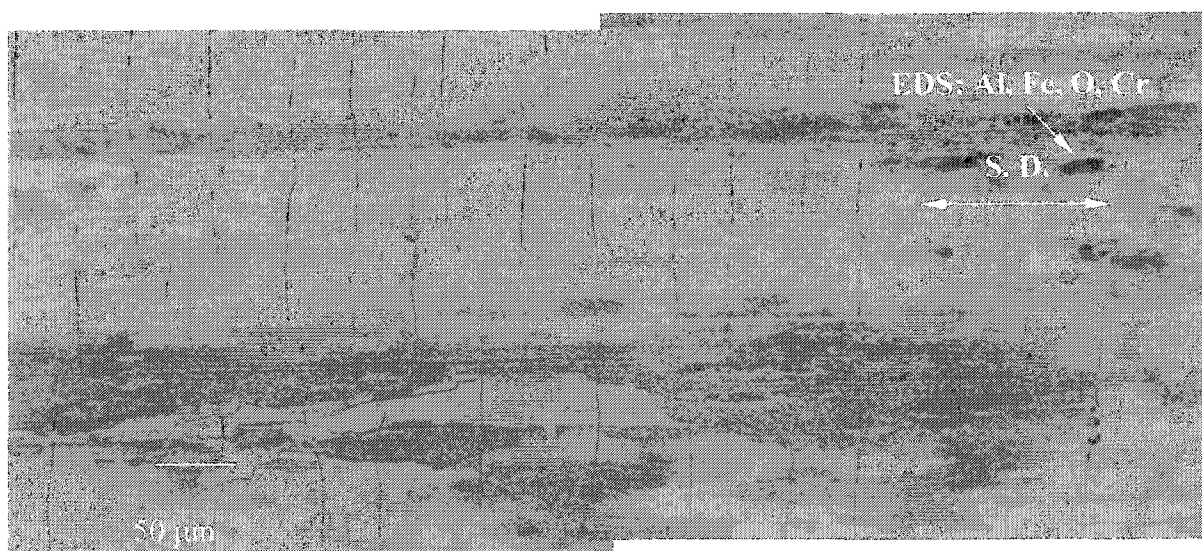


Fig. 6.15- Back-scattered SEM micrograph of the centre of the damaged area of the ring shows that the surface is cracked along a direction perpendicular to the sliding direction with scratches parallel to the sliding direction. There is also evidence of material transfer (dark region) to the surface of the ring.

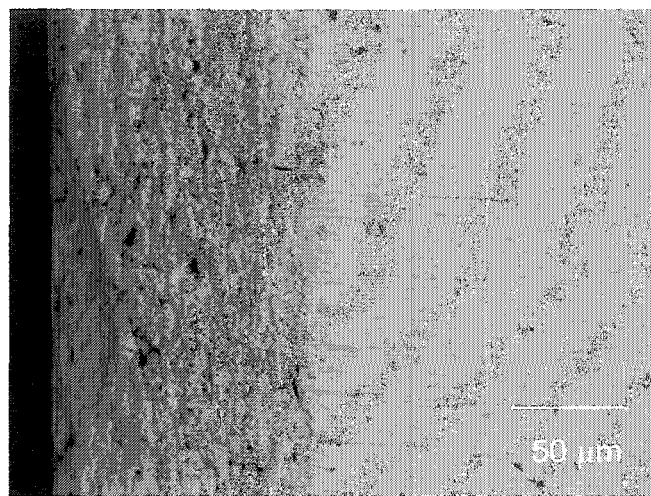
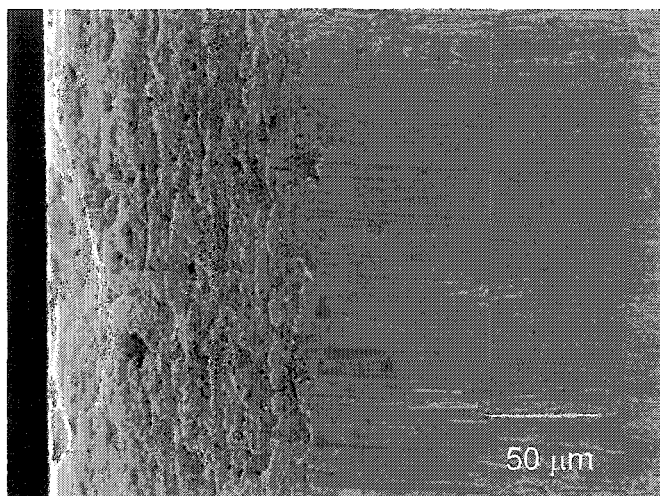


Fig. 6.16- Secondary and back-scattered SEM micrographs taken from the edges of the severely damaged part of the top ring shows that chipping has been occurred at this area.

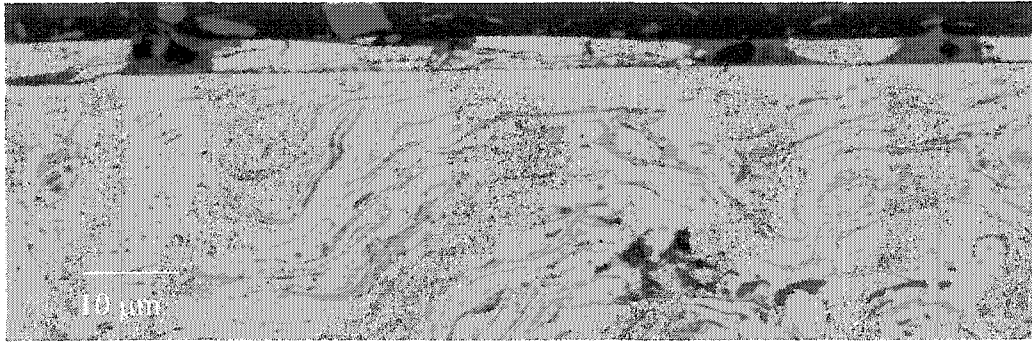


Fig. 6.17- Back-scattered SEM micrograph from the cross section of the major side of the scuffed Saturn engine bore shows the tribolayer were almost completely detached from the sliding surface.

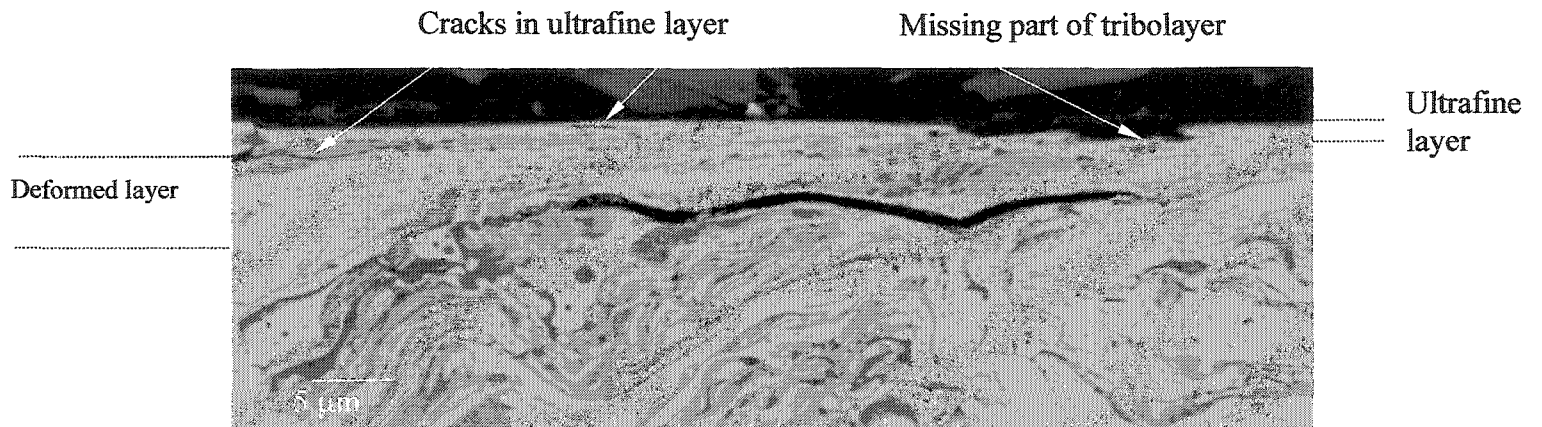


Fig. 6.18- Back-scattered SEM micrograph from the cross section of the major side of the scuffed Saturn engine bore that shows subsurface cracks parallel to the surface.

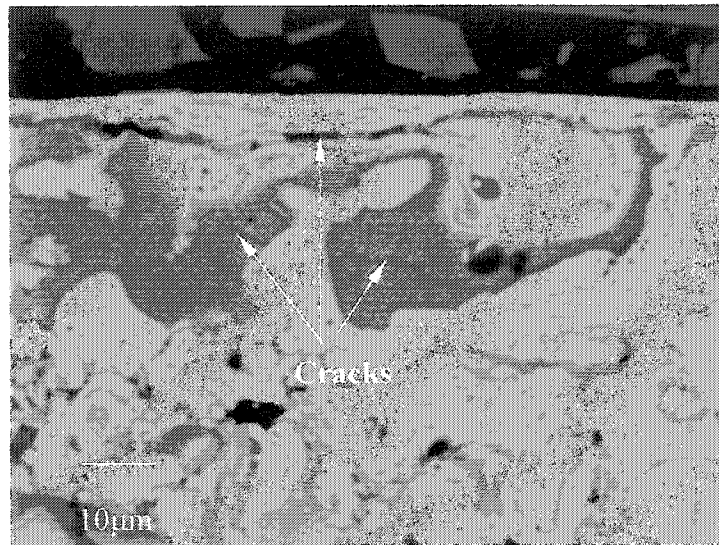


Fig. 6.19- Back scattered SEM micrograph from the major side of the scuffed Saturn engine that shows cracking of the inclusions and also the crack in the deformed layer extending parallel to the contact surface.

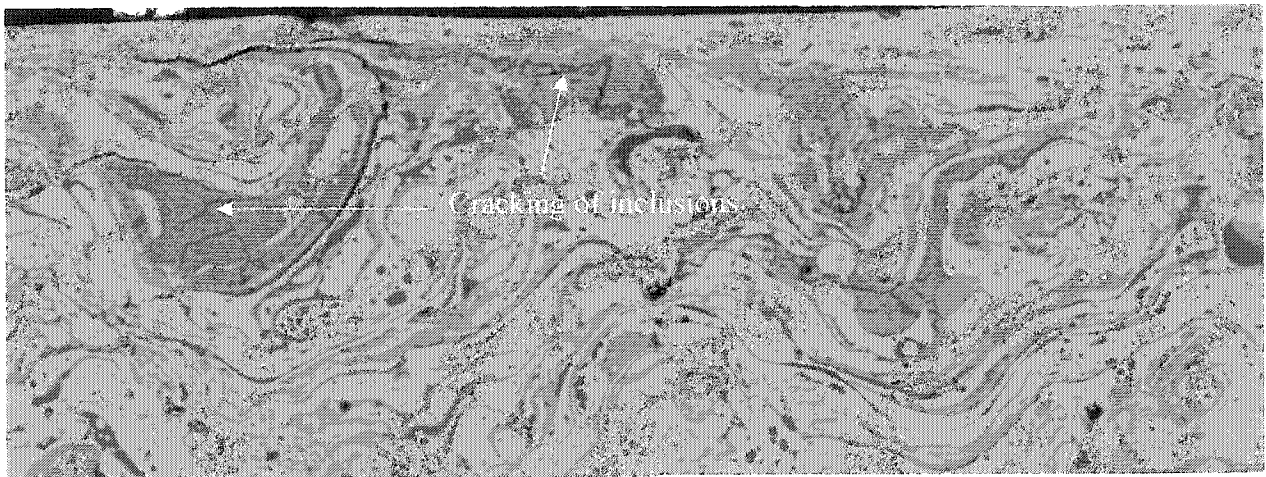


Fig. 6.20- Back scattered SEM image from the cross section of HVOF 1020-2.5% Al tested at 100 N load and 0.2 m/s speed under Ar atmosphere and boundary lubricated condition to 15,000 m using pin-on-disc tribometer that shows formation of deformed layer and cracks in the inclusions.

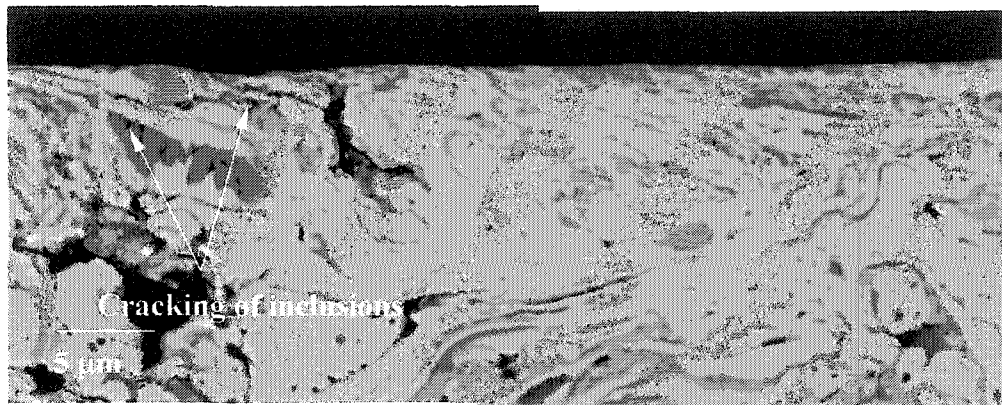


Fig. 6.21- Back-scattered SEM image from the cross section of HVOF 1020-2.5% Al tested at 100 N load and 0.2 m/s speed under Ar atmosphere and boundary lubricated condition to 15,000 m using pin-on-disc tribometer that shows extensive cracks in the inclusions and subsurface cracks which reached the surface.

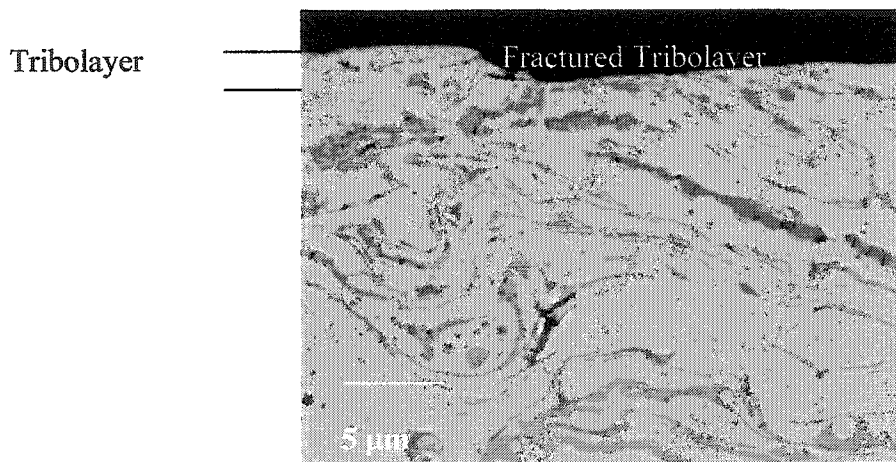


Fig. 6.22- Back-scattered SEM image from the cross section of HVOF 1020-2.5% Al tested at 100 N load and 0.2 m/s speed under Ar atmosphere and boundary lubricated condition to 15,000 m using pin-on-disc tribometer that shows the highly deformed tribolayer fractured and this has led to the formation of loose debris during sliding.

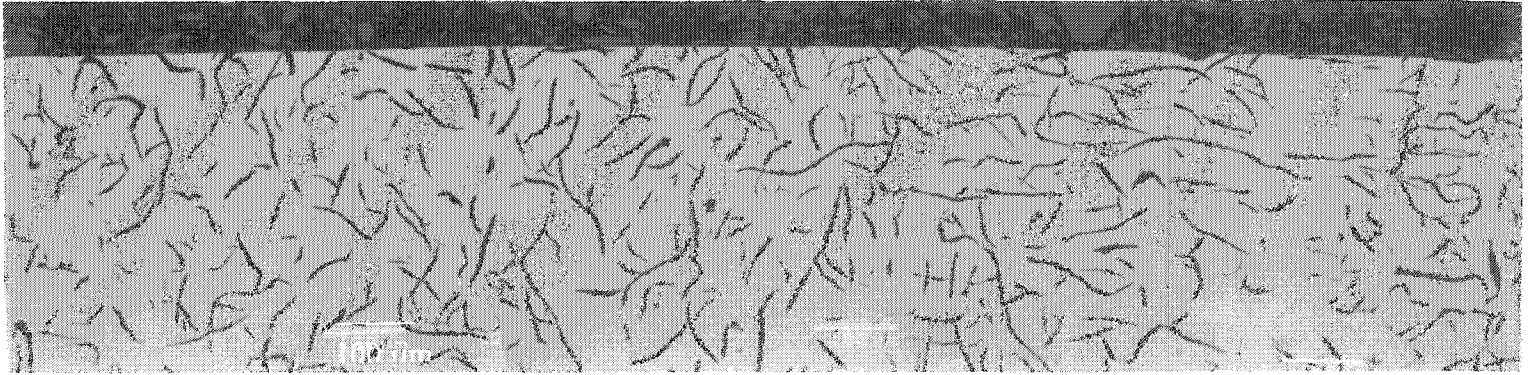


Fig. 6.23- Back-scattered SEM image from the cross section of cast iron tested at 100 N load and 0.2 m/s speed under Ar atmosphere and boundary lubricated condition to 15,000 m using pin-on-disc tribometer that shows no visible damage and deformed layer at the contact surface.

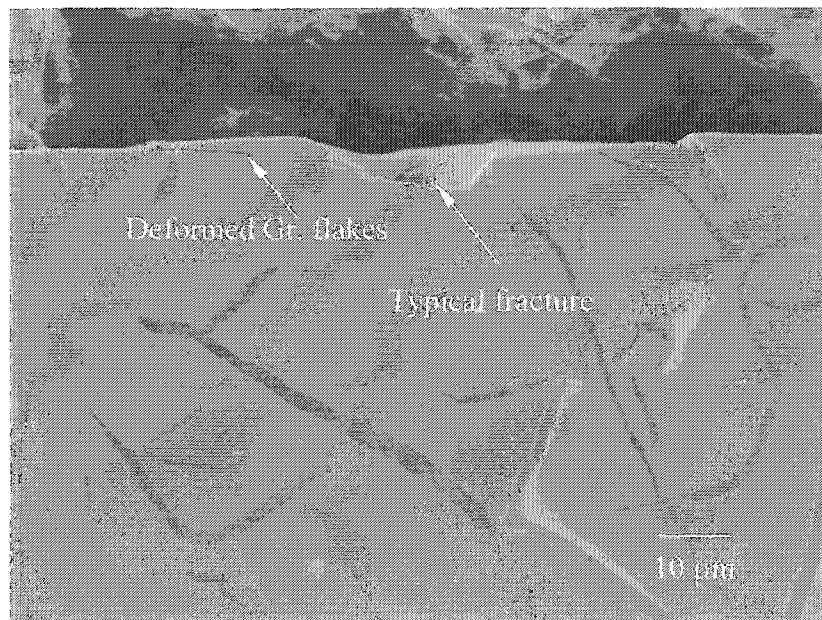


Fig. 6.24- Back scattered SEM image from the cross section of cast iron tested at 100 N load and 0.2 m/s speed under Ar atmosphere and boundary lubricated condition to 15,000 m using pin-on-disc tribometer that shows the typical type of damage.

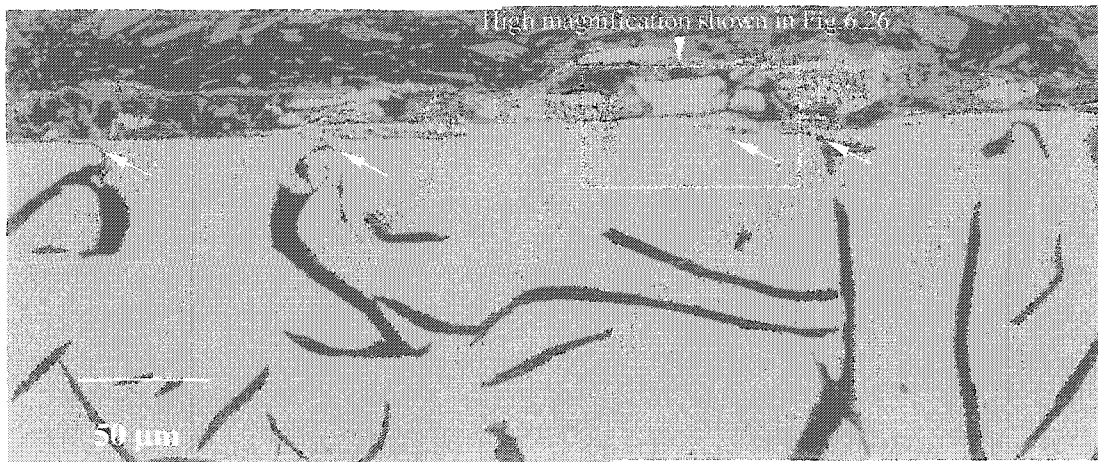


Fig. 6.25- Back-scattered electron image from the cross section of cast iron tested at 150 N load and 0.2 m/s speed under Ar atmosphere and boundary lubricated condition using pin-on-disc tribometer that shows elongated graphite flakes (marked on the micrograph).

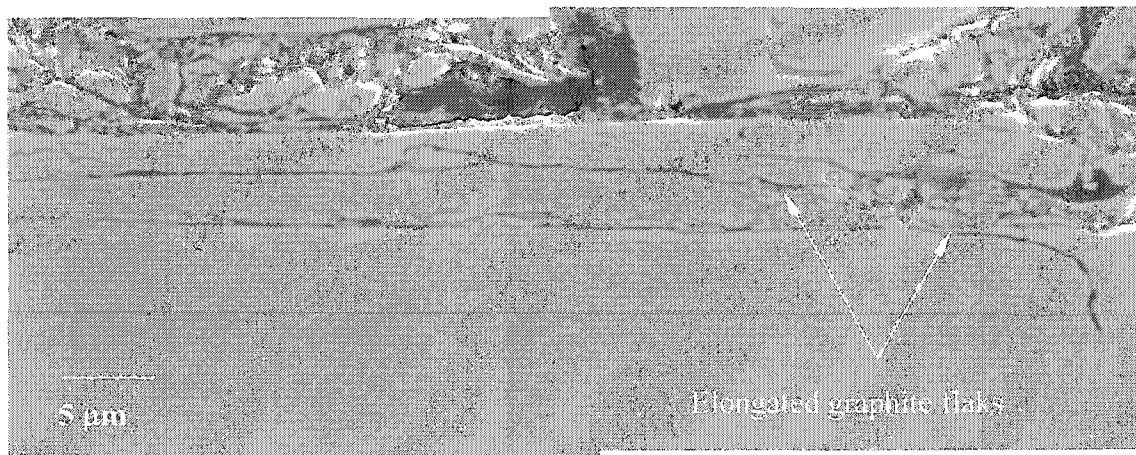


Fig. 6.26- High magnification of the back-scattered SEM image of the damaged surface region (area inside the rectangle in Fig. 6.25) shows elongated graphite flakes in detail. Extensive fracture of the iron near the contact surface is evident.

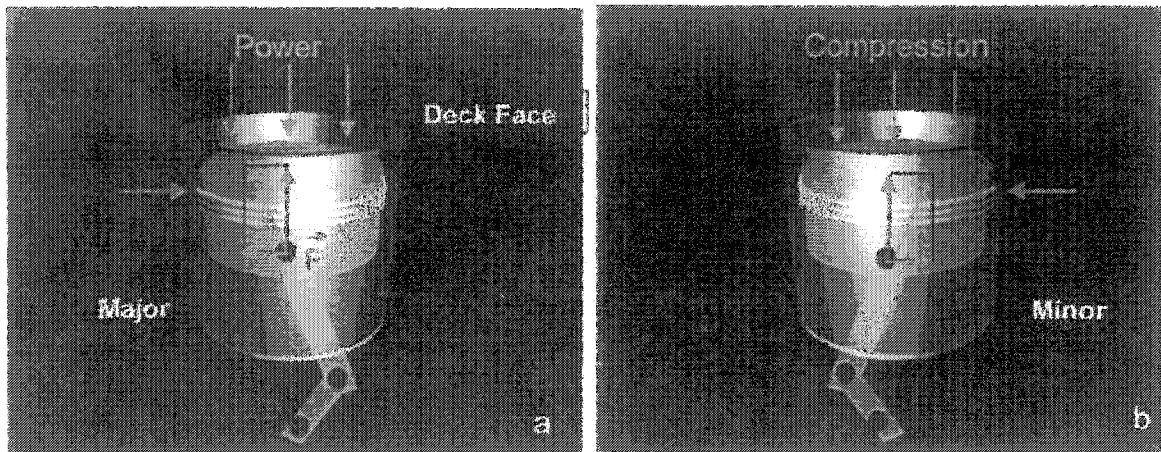


Fig. 6.27- (a) A free body diagram showing the forces during a combustion stroke, (b) A free body diagram during a compression stroke.

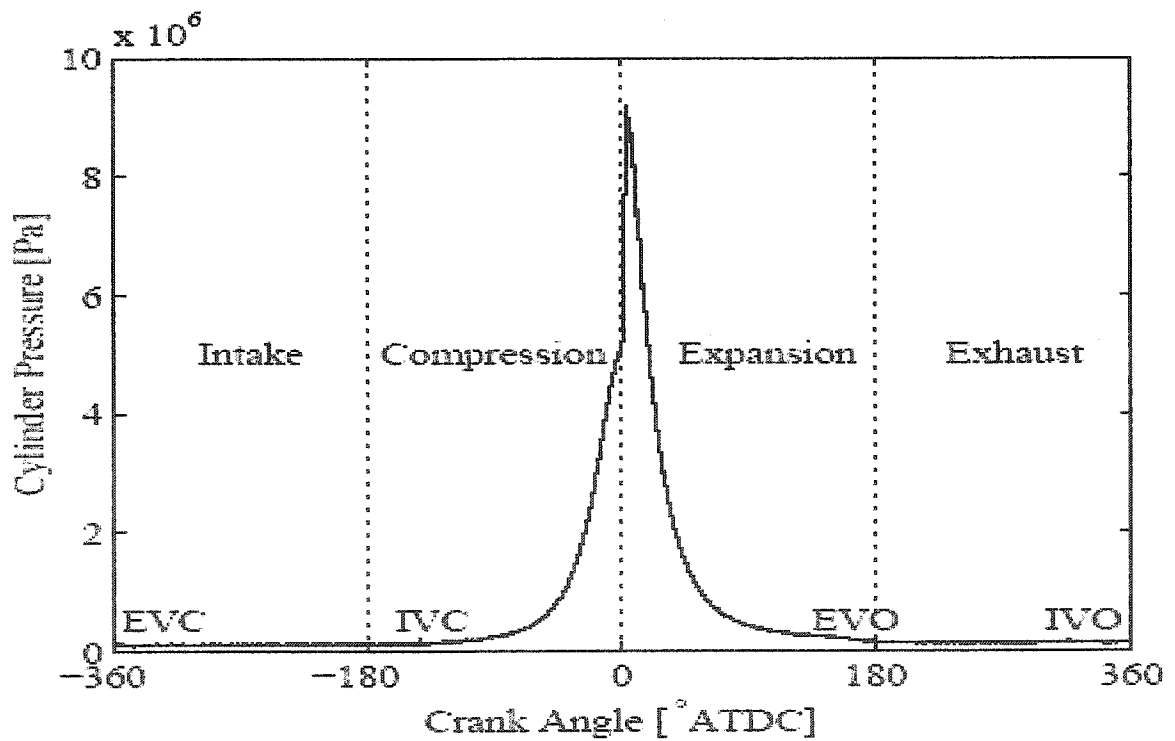


Fig. 6.28- Major engine cycle events. EVC = Exhaust valve closing, IVC = Intake valve closing, EVO = Exhaust valve opening, and IVO = Intake valve opening.

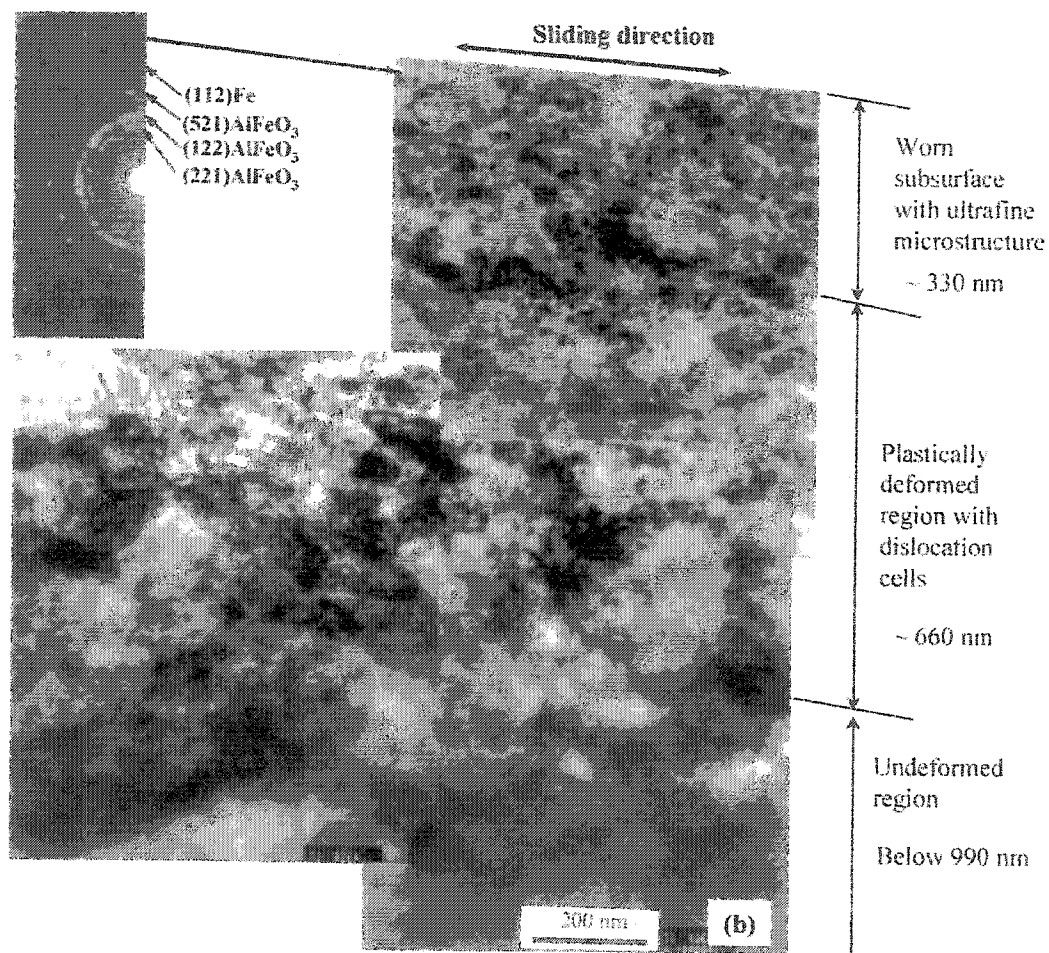


Fig. 6.29- TEM metallographic investigations on the longitudinal sections of the major face of the scuffed Corvette engine along with the corresponding selected area electron diffraction (SAED) pattern from the ultrafine region.

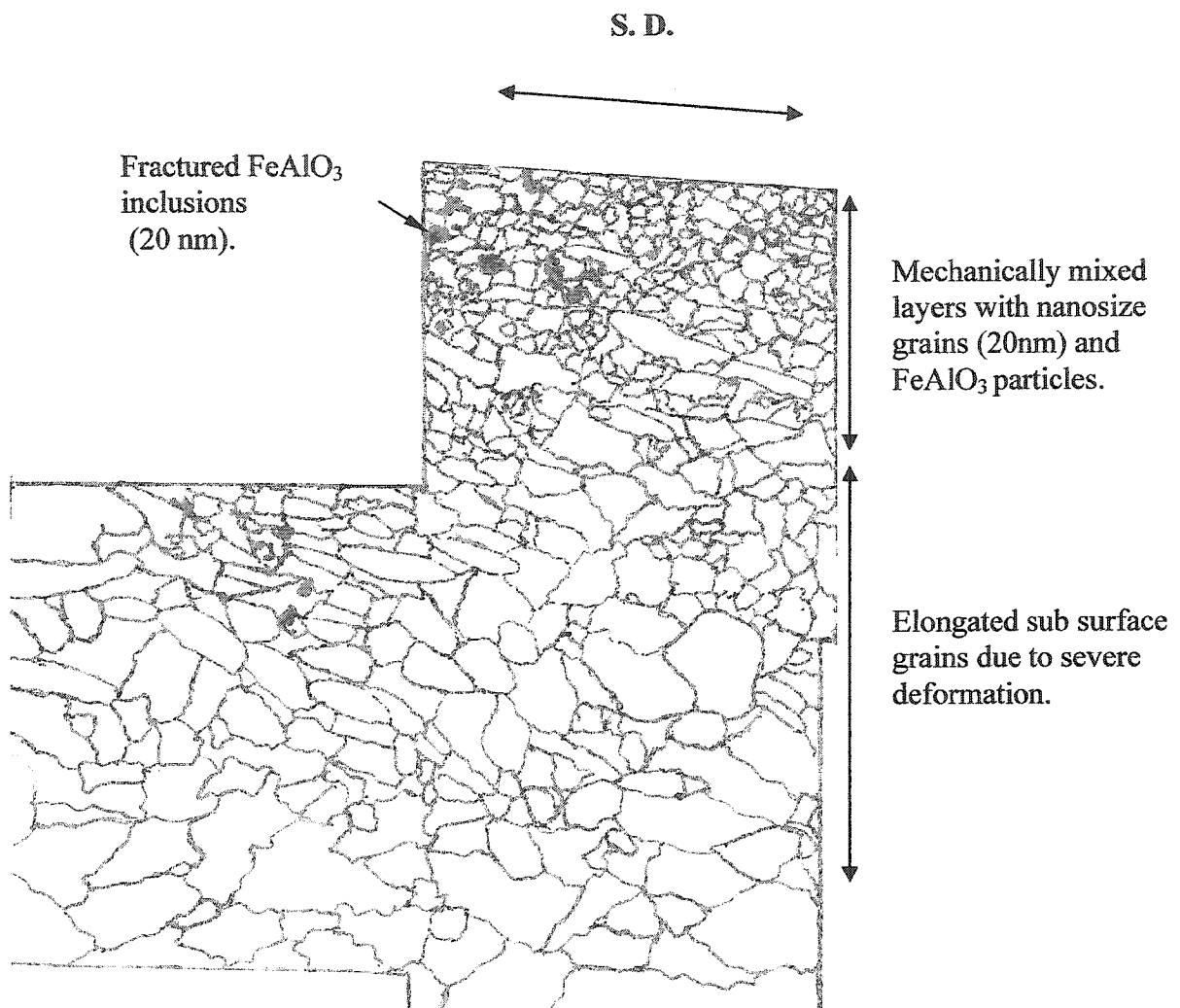


Fig. 6.30- Schematic diagram showing the microstructure of the longitudinal sections of the major face of the scuffed Corvette engine. The microstructure is divided into two separated layers of a mechanically mixed layer with nanosize grains of Fe and FeAlO_3 particles and a highly deformed layer with elongated grains due to severe plastic deformation.

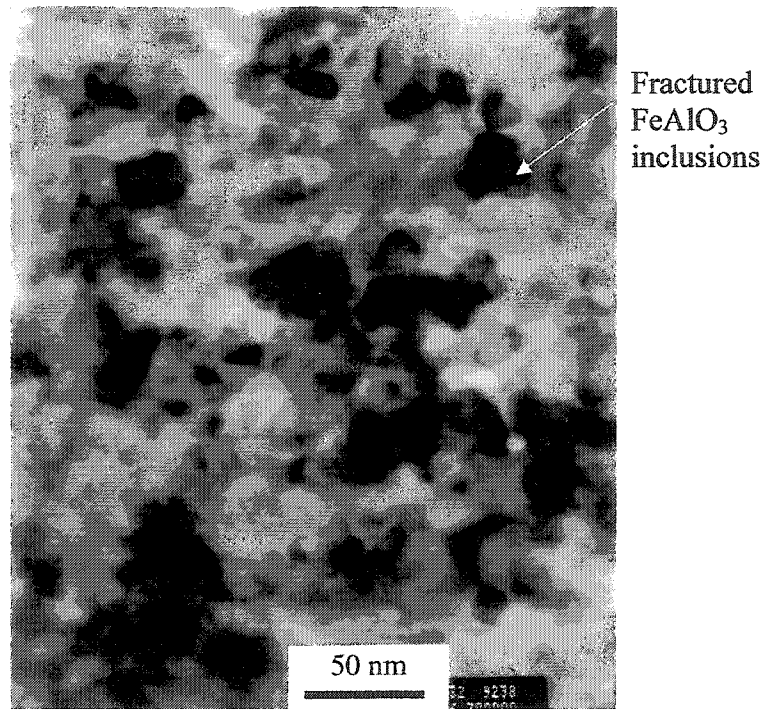


Fig. 6 31- High magnification TEM micrograph from the material layers immediately below to the contact surface, namely about 0.2 μm below the surface of the scuffed Corvette engine shows nano-size grain structure with an equiaxed morphology.

CHAPTER VII

SUMMARY AND CONCLUSIONS

- 1) The wear behaviour of low carbon steel thermal spray coatings, which were deposited using plasma transfer wire arc (PTWA), and high velocity oxy-fuel (HVOF) processes on cast 319 Al alloy were investigated. It was observed that the micromechanisms of the wear that control wear rates under dry sliding conditions could be classified in two main groups: a) mechanical wear, which involved by severe plastic deformation and splat tip fracture and splat delamination through the oxide veins; b) oxidational wear that took place by the formation of various iron oxides whose compositions and thicknesses depended on the loading conditions. A third type of wear namely, chemical polishing wear occurred in tests performed under high humidity conditions.
- 2) The wear mechanisms and the wear rates of the all three types of thermal spray coatings, which consisted of PTWA 1020, HVOF 1020, and HVOF 1020-2.5% Al were summarized in the form of wear maps that were constructed separately for each coating. In the wear map for the PTWA 1020 coatings four main regimes were identified as follows:
 - i) At low load and velocity conditions, surface oxidation by formation of Fe_2O_3 was the main wear mechanism.
 - ii) At low velocity and high load conditions the high wear rates that were observed were associated with severe deformation of the steel splat tips and eventually splat fracture and fragmentation. In addition tribological

layers consisting of a mixture of Fe_2O_3 , FeO , and Fe_3O_4 were formed on the contact surfaces.

- iii) At high loads and velocities the wear rates decreased. Evidence was found for two different wear mechanisms that accounted for the relatively low wear rates. The first mechanism was the formation of a continuous protective oxide layers on the wear track. The second mechanism was the hardening of the coating surfaces during sliding contact.
 - iv) The wear rates were the lowest at high velocity and low load conditions where there was no evidence for the splat tip fracture mechanism and the surfaces were covered with oxide rich tribolayers.
- 3) Comparison of the wear maps of all three coatings led to the following conclusions:
- i) The wear rates of all the coatings were high at low sliding speeds due to the fracture of heavily deformed iron splat tips at the contact surfaces.
 - ii) The wear rates of PTWA 1020 decreased with the sliding speed. However the wear rates of HVOF 1020 increased significantly until the sliding speed after passing through a minimum.
 - iii) Wear rates of HVOF 1020-2.5% Al were lower than those of HVOF 1020 at all conditions tested. An improvement in the wear resistance of HVOF 1020 was observed as a result of addition of 2.5% Al in the wire feed stock used to produce the coating.
- 4) In order to study the role that the production method played on the wear behaviour of the thermal spray coatings, sliding wear behaviour of the iron based

PTWA 1020 and HVOF 1020 thermal spray coatings were compared. It was found that the HVOF coatings despite the fact that they were produced from the same wires stock as the PTWA 1020 coatings contained 65 % by volume FeO as opposed to 20% by volume FeO in PTWA 1020. The wear rates of HVOF 1020 coatings were significantly higher than those of the PTWA 1020 coatings at high loading conditions and their surfaces were severely oxidized. This was attributed to the higher oxide content of HVOF 1020 coatings. It was concluded that the wear rates were sensitive to the production process and hence to the composition of the coatings.

- 5) In order to explain the differences in the oxidative wear behaviour of PTWA 1020 and HVOF 1020 coatings, friction induced surface temperatures for both coatings were compared at different loading conditions. A model was constructed to estimate the contact surface temperature. It was shown that under high loading conditions where oxidation induced wear rates were high in HVOF 1020, the temperatures on the contact surfaces were also high (about 100°C higher compared to PTWA 1020. The PTWA 1020 samples whose surfaces were covered with thinner oxide layers showed lower wear rates. Therefore the sliding surface of the coating with the higher initial iron oxide content reached higher temperature.6) The effect of the test atmosphere on the wear rates of the coatings was studied by performing sliding wear experiments under various relative humidity levels. The results of the wear tests under relative humidity levels ranging between 10% and 99% showed that the wear rates of the PTWA 1020 coatings were a strong function of the testing environment. At high humidity

conditions the wear rates and the coefficient of friction decreased. The decrease in wear rates coincided with higher relative humidity levels at high loads and sliding velocities. SEM investigations have shown that:

- i) At low humidity conditions, the splats deformed plastically, especially at high load and low velocity loading conditions. Severe plastic deformation at the edges of splats caused fracture and fragmentation.
 - ii) At high humidity conditions, the metallic parts of contact areas were smoother and exhibited less evidence for surface damage and fracture at high loads. At low loads, high humidity caused polishing of the worn surfaces to a mirror like finish. It was suggested that the lower wear rates at high humidity atmosphere were due to the effect of a tribo-chemical wear mechanism.
- 7) The micromechanisms responsible for scuffing damage in actual combustion engines were investigated. For this purpose a Corvette engine block with bores coated with HVOF 1020-2.5% Al low carbon steel thermal spray coating, and a Saturn engine block with bores coated with the same type of coating were subjected to detailed metallographic investigations. Microscopic observations on these two engine blocks that exhibited scuffing type wear damage showed that the damage on the bores depended strongly on the position around the bore and the scuffing damage was much more pronounced on the major faces. SEM observations have revealed the following important aspects of scuffing damage in the engines:

- i) The mechanically mixed tribolayers were observed on the major face. These tribolayers were composed of a matrix of deformed iron with fine particles of inclusions. The tribolayers had a nanocrystalline structure.
- ii) Plastic deformation beneath the mechanically mixed layer on the major face exhibited the unidirectional pattern. This was due to the high loads applied during the power stroke of combustion cycle.

The delamination of the tribolayers was the principal source of material removal during scuffing. This process was facilitated by crack formation at the FeAlO_3 inclusions that were presented in HVOF 1020-2.5% Al coatings as well as at FeO veins between the iron splats.

- 8) A correlation was established between the wear mechanisms observed in the scuffed engines and those deposited on the wear map for the HVOF 1020-2.5% Al coatings. The close correlations between the wear microstructures generated in HVOF 1020-2.5% Al coatings in the scuffed engines and those tested under Ar atmosphere and boundary lubricated conditions using the pin-on-disc tribometer suggested that the unidirectional pin-on-disc tests can be used to study the micromechanism of the scuffing in the actual engines.

LIST OF REFERENCES:

- [1] L. Byrnes, and M. Kramer, in Proceedings of 7th National Thermal Conference, C. C. Berndt, and S. Sampath, (eds.) ASM Int. Materials Park, OH, USA, 1994, 39-42.
- [2] E. Morf, "A method producing bodies and coatings of glass and other substances" US patent no 28001, 1912.
- [3] P. J. Meyer, and D. Hawley, in Thermal Spray Coatings: Properties, Processes and Applications, T. F. Bernecki, (ed.), ASM Int., Materials Park, OH, USA, 1991, 29-38.
- [4] A. Ferslon, in Thermal Spray Science and Technology, C. C. Berndt, and S. Sampath, (eds.) ASM Int. Materials Park, OH, USA, 1995, 57-63.
- [5] D. W. Parker, and G. L. Kutner, Advanced Materials and Processes, 1991, 68-72.
- [6] A. Rabiei, D. R. Mumm, J. W. Hutchinson, R. Schweinfest, M. Ruhle and A. G. Evans, Materials Science and Engineering A, 269, 1999, 152-165.
- [7] S. E. Hartfield-Wunsch and S. C. Tung, in Thermal Spray Industrial Applications, C. C. Berndt and S. Sampath (eds.), Materials Park, OH, ASM International, 1994, 19-32.
- [8] N.C. Welsh, The Dry Wear of Steels, Phil. Trans. R. Soc. London Ser. A257, 1965, 31- 50.
- [9] N. C. Welsh, Journal of Applied Physics, 28, 9, 1957, 960-968.

- [10] J. F. Archard, *Wear*, 2, 1952, 438-449.
- [11] S.C. Lim and M. F. Ashby, *Acta Metallurgica*, 35, 1987, 1-24.
- [12] ASTM Standard G40, *Standard Terminology Relating to Wear and Erosion*, American Society for Testing and Materials, Metals Park, OH, 1999.
- [13] K. Zum Gahr, *Microstructure and Wear of Materials*, Tribology Series, 10, Elsevier, 1987.
- [14] Masounave, J., "Abrasive Wear: Cost and Cause, Laboratory Tests" Presented in the ASM-IMRI Seminar "Abrasive Wear: A Struggle" held in NRC, Boucherville, Quebec, March 1986.
- [15] J. T. Burwell and C.D. Strang, On the Empirical Law of Adhesive Wear, *J. Appl. Phys.*, 23, 1952, 18-28.
- [16] J. T. Burwell, Survey of Possible Wear Mechanisms, *Wear*, 1, 1957-58, 119-141.
- [17] T. S. Eyre, Wear Resistance of Metals, in *Treatise on Materials Science and Technology*, D. Scott (ed.), 13, 1979, 363-441.
- [18] J. F. Archard, Wear Theory and Mechanisms, in *Wear Control Handbook*, M. B. Peterson and W. O. Winer (ed.), ASME, 1980, 35-80.
- [19] M. B. Peterson, Classification of Wear Processes, in *Wear Control Handbook*, M. B. Peterson and W. O. Winer ed., ASME, 1980, 9-16.
- [20] S. L. Rice, A Review of Wear Mechanisms and Related Topics, in *Fundamentals of Tribology*, N. P. Suh and N. Saka (eds), MIT Press, 1980, 469-476.

- [21] N .P .Suh, Wear Mechanisms: An Assessment of the State of Knowledge, in Fundamentals of Tribology, N. P. Suh and N. Saka (eds.), MIT Press, 1980, 443-453.
- [22] S. Jahanmir, in Fundamentals of Tribology, N. P. Suh and N. Saka (eds.), MIT Press, 1980, 455-467.
- [23] T. F. J. Quinn, The Classifications, Laws, Mechanisms and Theories of Wear, in Fundamentals of Tribology, N. P. Sub and N. Saka (eds.), MIT Press, 1980, 477-492.
- [24] D. Godfrey, Diagnosis of Wear Mechanisms, in Wear Control Handbook, M. B. Peterson and W. O. Winer (eds.), ASME, 1980, 283-312.
- [25] C. S. Yust, Tribology and Wear, Inter. Met. Rev., 30, 1985, 141-154.
- [26] I. M. Hutchings, Tribology-Friction and Wear of Engineering Materials, Kent, U.K., 1992.
- [27] E. Rabinowicz, Friction and Wear of Materials, John Wiley & Sons, Inc., New York, 1965.
- [28] Glossary of Terms and Definitions in the Field of Friction, Lubrication and Wear (Tribology), Research Group on Wear of Engineering Materials, Organization for Economic Cooperation and Development (OECD), Paris, 1968.
- [29] J. F. Archard and W. Hirst, Proc. Roy. Soc., A236, 1956, 397-410.
- [30] E. F. Finkin, Materials in Engineering Applications, 1, 1979, 154-161.
- [31] R. F. J. Quinn, Tribology International, 16, 1983, 257-271.

- [32] R. F. J. Quinn, *Tribology International*, 16, 1983, 305-315.
- [33] F. P. Bowden and D. Tabor, *The Friction and Lubrication of Solids*, Clarendon, Oxford, 1958.
- [34] T. S. Eyre, *An Introduction to Wear-Wear Characteristics of Metals*, in *Source Book on Wear Control Technology*, D.A. Rigney and W. A. Glaeser (eds.), ASM, Metals Park, OH, 1978, 1-10.
- [35] K. Kato, *Wear*, 136, 1990, 117-128.
- [36] T. Yamamoto, M. Olsson and s. Hogmark, *Wear*, 174, 1994, 21-31.
- [37] A. T. Alpas and J. Zhang, *Metallurgical Transactions*, 25A, 5, 1994, 969-983.
- [38] N. P. Suh, *Tribo-physics*, Prentice-Hall Inc., 1986.
- [39] A. D. Hearle and K. L. Johnson, *Journal of the Mechanics and Physics of Solids*, 33, 1985, 61-81.
- [40] Y. Kimura, *The role of Fatigue in Sliding Wear*, in *Fundamentals of Tribology*, N. P. Suh and N. Saka (eds.), MIT Press, 1980, 187-221.
- [41] R. A. Smith, *Interfaces of Wear and Fatigue*, in *Fundamentals of Tribology*, N. P. Suh and N. Saka (eds.), MIT Press, 1980, 477-492.
- [42] I. V. Kragelsky, *Friction and Wear*, Butterworths, London, 1965.
- [43] J. H. Dautzenberg and J. H. Zaat, *Wear*, 23, 1973, 9-19.
- [44] A. W. Ruff, L. K. Ives and W. A. Glaeser, *Characterization of Wear Surfaces and Wear Debris*, in *Fundamentals of Friction and Wear of Materials*, D.A. Rigney (ed.), ASM, 1981, 235-289.

- [45] F. E. Kennedy, J. Lubric. Technol. (Trans. ASME), 104, 4, 1982, 582-588.
- [46] F. E. Kennedy, Journal of Applied Mechanics (Transactions of the ASME), 51, 3, 1984, 687-689.
- [47] F. E. Kennedy, L. A. Hartman, K. E. Hauck and V. A. Surprenant, in Wear of Materials, K. C. Ludema (ed.), ASME, Metals Park OH, 1985, 273-279.
- [48] K. Kato, T. Kayaba and Y. Ono, in Wear of Materials, K. C. Ludema (ed.), ASME, Metals Park OH, 1985, 463-470.
- [49] W.A. Glaeser, in Wear of Materials, K. C. Ludema (ed.), ASME, Metals Park OH, 1985, 155-162.
- [50] T. Kjer, in Wear of Materials, K. C. Ludema (ed.), ASME, Metals Park OH, 1987, 191-198.
- [51] S. L. Rice, H. Nowotny and S.F. Wayne, A Survey of the Development of Subsurface Zones in the Wear of Materials, Key Engineering Materials, 33, 1989, 77-100.
- [52] P. Heilmann, W. A. T. Clark and D. A. Rigney, Acta Metallurgica, 31, 1983, 1293-1305.
- [53] P. Heilmann and D. A. Rigney, Wear, 72, 1981, 195-217.
- [54] D. A. Rigney, L. H. Chen and M. G. S. Naylor, Wear, 100, 1984, 195-219.
- [55] N. Ohmae, T. Tsukizoe and F. Akiyama, Philosophical Magazine, 40A, 1979, 803-810.

- [56] N. Ohmae, In Fundamentals of Tribology; Cambridge, MIT Press, N. Saka and N. P. Suh (eds.), 1980, 201-222.
- [57] A. W. Ruff, L. K. Ives and W. A. Glaeser, in Fundamental of Friction and Wear of Materials, D. A. Rigney (ed.), ASM (1981), 235-289.
- [58] K. Kato, T. Kayaba and Y. Ono, in Wear of Materials, K.C. Ludema (ed), The American Society of Mechanical Engineer, 1985, 463-470.
- [59] P. Heilmann, J. Don, T. C. Sun, W. A. Glaeser and D.A. Rigney, Wear, 91, 1983, 171-190.
- [60] A. R. Riahi 'Characterization of Tribological Behaviour of Graphitic Aluminum Matrix Composites, Grey Cast Iron and Aluminum Silicon Alloys', Ph.D. Dissertation, University of Windsor, 2002
- [61] D. A. Rigney, Sliding Wear of Metals, Ann. Rev. Mater. Sci. , 18, 1988, 141-163.
- [62] L. H. Chen and D. A. Rigney, in Wear of Materials, K. C. Ludema (ed.), ASME, 1985, 437-446.
- [63] D. A. Rigney and J. P. Hirth, Wear, 53, 1970, 345-379.
- [64] A. R. Rosenfield, Wear, 61, 1977, 1-16.
- [65] X. Y. Li and K. N. Tandon, Wear, 245, 2000, 148-161.
- [66] P. Heilmann, I. Don, T. C. Sun, W. A. Glaeser and D. A. Rigney, in Sliding Wear and Transfer, Wear of Materials, K. C. Ludema (ed), ASME Metals Park OH, 1983, 414-425.
- [67] M. Cocks, J. Appl. Phys., 33, 1962, 2152-2161.

- [68] M. Antler, *Wear*, 7, 1964, 181-203.
- [69] J. Zhang and A. T. Alpas, *Acta Mater.*, 45, 1997, 513- 528.
- [70] J. F. Archard, *J. of Applied Physics*, 24, 8, 1953, 981-988.
- [71] H. C. Meng and K. C. Ludema, *Wear*, 181-183, 1995, 443-457.
- [72] K. C. Ludema, in *ASM Handbook, Friction, Lubrication, and Wear Technology*, ASM International, 18, 1992, 236-241.
- [73] R. Atoniou, and C. Subramanian, *Scr. Metall.* 22, 6, 1988, 809-814.
- [74] M. F. Ashby, J. Abulawi and H. S. Kong, *STLE Tribology Tran.*, 34, 1991, 577-587.
- [75] D. Z. Wang, H. X. Peng, J. Liu, and C. K. Yao, *Wear*, 184, 1995, 187-192.
- [76] Y. Liu, R. Asthana and P. K. Rohatgi, *J. Materials Sci.*, 26, 1991, 99-102.
- [77] P. K. Rohatgi; Y. Liu and R. Asthana, in *Tribology of Composite Materials*, P. K. Rohatgi, P. I. Blau, C. S. Yust, (eds.), ASM International, Materials Park, OH, 1991, 69-80.
- [78] H. Kato, T. S. Eyre, and B. Ralph, *Acta Metall. Mater.*, 42, 5, 1994, 1703-1713.
- [79] S. Wilson and A. T. Alpas, *Wear*, 212, 1997, 41-49.
- [80] A. R. Riahi and A. T. Alpas, *Wear*, 255, 1, 2003, 401-409
- [81] F. E. Kennedy, L. A. Hartman, K. E. Hauck and V. A. Supenant, in *Wear of Materials*, K. C. Ludema (ed.) ASME, 1985, 273-279.
- [82] J. F. Archard and R. A. Rowntree, *Wear*, 128, 1988, 1-17.

- [83] P. K. Rohatgi, Y. Liu and S. Ray, Friction, Lubrication and Wear Tech., ASM Handbook, ASM, Materials Park, Ohio, 18, 1992, 801-811.
- [84] J. C. Jaeger, Moving Sources of Heat and the Temperature at Sliding Contacts, Proc. Roy. Soc. 56, 1942, 203-224.
- [85] T. F. J. Quinn, ASLE Transactions 10, 1967, 158-168.
- [86] T. F. J. Quinn, BRIT. J. Appl. Phys., Vol. 13, 1962, 33-37.
- [87] D. E. Davies, U. R. Evans, and Agar, J. N, Proc. Roy. Soc. A, 1954, 225-443.
- [88] J. Moreau and J. C. R. Bardolle, Proceeding of Acad. Sci. Paris, 1955, 240-524.
- [89] A. Muan and E. F. Osborn, Phase Equilibria Among Oxides in Steelmaking, Addison Wesley, Reading MA, 1965, 27.
- [90] J. Molgaard, Wear, 40, 1976, 277-291.
- [91] T. S. Eyre, Wear of Aluminum Alloys, Stevens, Microstructural Science, in Vander Voort, McCall (eds.), 8, 1980, 142-151.
- [92] J. K. Lancaster, Tribol. Int. 23 (6), 1990, 371-389.
- [93] H. Goto and D. H. Buckley, National Aeronautics and Space Administration (NASA) Technical paper 2403, Lewis Research Centre Cleveland, Ohio, 1984, 1-9.
- [94] H. K. Oh, K. H. Yeon and H. Y. Kim, J. Mater. Proc. Technol. 95, 1999, 10-16.
- [95] C. Papaphilippou, M. Vardavoulias and M. Jeandin, Wear 177, 1994, 151-157.
- [96] D. J. Barnes and J. E. Wilson, Wear, 45, 1977, 161-176.

- [97] R. Shivanath, P. K. Scugupta, and T. S. Eyre, in: International Conference on Wear of Materials, W. Gleaser, K. Ludema, S. Rhee (eds.), ASME, 1977, 186-192.
- [98] A. J. Clegg and A. A. Das, *Wear*, 1977, 333-339.
- [99] A. D. Sarkar and J. Clark, *Wear*, 31, 1975, 331-339.
- [100] B. N. Pramila Bai, S. K. Biswas, and N. N. Kumtckar, *Wear*, 87, 1983, 237-249.
- [101] K. M. Jasim, *Wear*, 98, 1984, 183-190.
- [102] K. C. Ludema, *Wear*, 100, 1984, 315-331.
- [103] H. K. Yoon, T. K. Sheiretov, and C. Cusano, *Wear* 337, 2000, 163-175.
- [104] M. P. Cavatorta and C. Cusano, *Wear*, 342, 2000, 133-139.
- [105] Y. Z. Lee, and B. T. Kirn, *Wear*, 232, 1999, 116-121.
- [106] G. C. Barber, J. J. Mathews, and S. Jafry, *Lubrication Eng.*, 47, 1991, 421-430.
- [107] T. K. Sheiretov, H. K. Yoon and C. Cusano, *Tribol. Trans.*, 41 (4), 1998, 435-446.
- [108] A. Somi, Reddy, A. B. Pramila Bai, K. S. S. Murthy and S. K. Biswas, *Wear*, 171, 1994, 115-127.
- [109] K. M. Jasim and E. S. Dwarakadasa, *J. Mat. Sci. Lett.*, 11 (7), 1993, 421-433.
- [110] A. R. Riahi and A. T. Alpas, *Wear*, 251, 2001, 1396-1407.

- [111] R. Shivanath, P. K. Sengupta and T. S. Eyre, *The British Foundryman*, 70, 1977, 349-356.
- [112] W. Hirst and J. K. Lancaster, *J. Appl. Phys*, 1956, 27, 1057-1065.
- [113] K. Mohammed Jasim and E. S. Dwarakadasa, *Wear*, 119, 1987, 119-130.
- [114] H. Torabian, J. P. Pathak, and S. N. Tiwari, *Wear*, 172, 1994, 49-58.
- [115] A. Somi Reddy, B. N. Pramila, K. S. S. murthy and S. K. Biswas, 171, *Wear*, 1994, 115-127.
- [116] S. Wilson and A. T. Alpas, *Wear*, 229, 1999, 440-449.
- [117] S. Jahanmir and N. P. Suh, *Wear*, 44, 1, 1977, 17-38.
- [118] J. Zhang and A. T. Alpas, *Mater. Sci. Eng.*, A160, 1993, 25-35.
- [119] F. M. Hosking, F. Folgar Portillo, R. Wunderli and R. Mehrabian, *J. Mater. Sci.*, 17, 1982, 477-498.
- [120] J. Zhang and A. T. Alpas, *Mater. Sci. Eng.*, A161, 1994, 273-284.
- [121] A. G. Wang and H. J. Rack, *Mater. Sci. Eng.*, A147, 1991, 211-224.
- [122] A. T. Alpas and J. Zhang, *Scripta Metall. Mater.*, 26, 1992, 505-509.
- [123] S. F. Moustafa, *Wear*, 185, 1995, 189-195.
- [124] I. Hoff, *Finishing*, 20, 12, 1996, 34-35.
- [125] S. Sampath, and H. Heman, *Journal of Thermal Spray Technology*, 5, No 4, 1996, 445-456.

- [126] V. V. Sobolev, J. M. Guilemany, J. Nutting, and J. R. Miquel, *International Materials Reviews*, 42, No. 3, 1997, 117-136.
- [127] M. L. Berndt and C. C Berndt, ASM International Materials Park, OH, 2003, 803-813.
- [128] F. Rastegar and A. Craft, *Surface and Coatings Technology*, 61, no. 1-3, 1993, 36-42.
- [129] W. R. Smith and R. Knight, *JOM*, August 1995, 32-39.
- [130] R. McPherson, *Thin Solid Films*, 83, 1981, 297-310.
- [131] C. C. Berndt, J. Karthikeyan, R. Ratnaraj, and Y. D. Jun, in *Thermal Spray Coatings: Properties, Processes and Applications, Proceedings, 4th National Thermal Spray Conference*, T.F.Bernecki (ed), 1992, 199-203.
- [132] R. A. Neiser, M. F. Smith, and R. C. Dykhuizen, *Journal of Thermal Spray Technology*, Christopher C. Berndt (eds.), 7, No. 4, 1998, 538-545.
- [133] C. M. Hackett and Settels G. S., *Thermal Spray Industrial Applications, Proceedings, 7th National Thermal Spray Conference*, Boston, MA, 20-24 June, C. C. Berndt, and S. Sampath (eds.), 1994, 307-312.
- [134] J. Matejicek, S. Sampath and H. Herman, In proceeding of the 15th International Thermal Spray Conference, Materials Park, OH, ASM International, 1998, 419-424.
- [135] L. C. Erickson, R. Westergard, U. Wiklund, N. Axen, H. M. Hawthorne and S. Hogmark, *Wear*, 214, 1998, 30-37.

- [136] R. C. McCune, M. J. Zaluzec, L. V. Reatherford, and E. L. Cartwright, in proceeding of the 7th National Thermal Spray Conference 20-24 June 1994, Boston, Massachusetts, 25-31.
- [137] J. B. Heywood, Internal Combustion Engine, McGraw- Hill Series in Mechanical Engineering, 1988.
- [138] S. P. Parker, Encyclopaedia of Science and Technology, McGraw-Hill, 1982, p 545.
- [139] S. D. Henry, in ASM Handbook, Vol. 18, Friction, Lubrication, and Wear Technology, The Materials Information Society, 1992, 162-171.
- [140] A. Kearney and E. Rooy, Aluminum Foundry Products, Metals Handbook, Vol. 12, 10th edition, ASM International, 1990, 123-151.
- [141] L. L. Ting, in Wear Control Handbook, ASME, 1980, 609-665
- [142] J. Nadel and T. S. Eyre, Tribology International, 1978, 267-271.
- [143] K. C. Ludema, Wear, 100, 1984, 315-331.
- [144] A. Dyson, Journal of Tribology International, 1975, 77-87.
- [145] A. Dyson, Journal of Tribology International, 1975, 117-122
- [146] J. Galligan, A. Torance and G. Liraut, Wear, 236, 1999, 199-209
- [147] R. A. Young, P. E. Mackie, and R. B. Von Dreele, J. Appl. Crystal., 10, 1977, 262-269.
- [148] R. A. Young and D.B. Wiles, J. Appl. Crystal., 15, 1982, 430-438.
- [149] H. M. Rietveld Aust., J. Phys.41, 1988, 113-116.

- [150] Metals Handbook 9th Edition, Properties and Selection: Iron and Steels, B. P. Bardes, H. Baker and D. Benjamin (eds.), 1, 1978, 148.
- [151] D. R. Poirier, G. H. Geiger, Transport Phenomena in Materials Processing, Warrendale, Minerals, Metals & Materials Society, 1994, 208-210.
- [152] CRC Handbook of Chemistry and Physics, CRC Press, 82nd Edition, D. R. Lide (ed.), Section 12, 2001-2002, 223.
- [153] G. E. Dieter, Mechanical Metallurgy, McCraw Hill, Third edition, 1986, 189-191.
- [154] L. E. Samuels, in ASM Handbook (Friction, Lubrication and Wear Technology), Vol. 18, ASM International, Metals Park, 1998, 191-197.
- [155] L. L. VanKuiken Jr., G. Rapids, L. E. Byrnes, R. Hills: M. S. Kramer, "High Pressure Water Jet Method of Blasting Low Density Metallic Surfaces", United States Patent, No. 5, 380, 564, Jan. 10, 1995.
- [156] X. Wu, N. Tao, Y. Hong, B. Xu, J. Lu, K. Lu, Acta Materialia 50, 2002, 2075-2084.
- [157] N. Hansen, Materials Science and Technology, 6, 1990, 1039-1047.

LIST OF PUBLICATIONS RESULTING FROM THIS WORK

1. Edrisy, A. and Alpas, A. T., "Microstructures and Sliding Wear Resistances of 0.2% Carbon Steel Coatings Deposited by HVOF and PTWA Thermal Spray Processes," *Thin Solid Films*, Volume 420-421, 2002, 338-344.
2. Edrisy, A., Perry, T., Cheng, Y. T. and Alpas, A. T., "The Effect of Humidity on the Sliding Wear of Plasma Transfer Wire Arc Thermal Sprayed (PTWA) Low Carbon Steel Coatings," *Surface and Coatings Technology*, Volume: 146-147, 2001, 571-577.
3. Edrisy, A., Perry, T., Cheng, Y. T. and Alpas, A. T., "Wear of Thermal Spray Deposited Low Carbon Steel Coatings on Aluminum Alloys," *Wear*, Volume: 251, 2001, 1023-1033.
4. Edrisy, A., Perry, T., Cheng, Y. T. and Alpas, A. T., "Wear Map for a Thermal Sprayed Low Carbon Steel Coating," in *Handbook of Tribology and Lubrication*, Wilfried J. Bartz (ed.), Volume 10, 2002, 12-16.
5. Edrisy, A. and Alpas, A. T., "Wear Behaviour of PTWA and HVOF Iron Based Thermal Spray Coatings: Effects of Composition and Microstructures," *Society of Manufacturing Engineers, Technical Paper No. FC03-161*, Dearborn, MI, U.S.A., 2003, 1-14.

LIST OF CONFERENCE PRESENTATIONS RESULTING FROM THIS WORK

1. Edrisy A., Perry T., Cheng Y. T. and Alpas A. T., "Construction and Applications of Wear Maps for Ferrous Thermal Spray Coatings", TMS Annual Meeting and Exhibitions, March 14-18, 2004.
2. Edrisy A., Perry T., Cheng Y. T., and Alpas A. T., "Wear Mechanisms in Thermal Spray Steel Coatings on Aluminum," in Dawson, D. (ed.), 29th Leeds-Lyon Symposium on Tribology, Leeds, England, September 3-6, 2002.
3. Edrisy, A., and Alpas, A. T., "Microstructures and Sliding Wear Resistances of 0.2% Carbon Steel Coatings Deposited by HVOF and PTWA Thermal Spray Processes," 29th International Conference on Metallurgical Coatings and Thin Films, San Diego, California, U.S.A., April 22-26, 2002.
4. Edrisy, A., Perry, T., Cheng, Y. T. and Alpas, A. T., "The Effect of Humidity on the Sliding Wear of Plasma Transfer Wire Arc Thermal Sprayed (PTWA) Low Carbon Steel Coatings," 28th International Conference on Metallurgical Coatings and Thin Films, San Diego, California, U.S.A., April 30-May 4, 2001.
5. Edrisy, A., Perry, T., Cheng, Y. T. and Alpas, A. T., "Wear of Thermal Spray Deposited Low Carbon Steel Coatings on Aluminum Alloys," 13th International Conference on Wear of Materials, Vancouver, British Columbia, Canada, April 22-26, 2001.
6. Edrisy, A., Perry, T., Cheng, Y. T. and Alpas, A. T., "Sliding Wear of Plasma Transfer Wire Arc Thermal Sprayed Low Carbon Steel Coatings," Materials and Research Society (MRS), Boston, U.S.A., November 26-29, 2001.
7. Edrisy, A., Perry, T., Cheng, Y. T. and Alpas, A. T., "Wear Map for A Thermal Sprayed Low Carbon Steel Coating," 2nd World Tribology Conference, Vienna, Austria, September 3-7, 2001.
8. Edrisy, A., Perry, T., Cheng, Y. T. and Alpas, A. T., "Wear Behaviour of Plasma Transfer Wire Arc (PTWA) Low Carbon Steel Coatings under Dry Sliding Conditions," in 50th Canadian Metal Physics Conference, Kingston, ON, Canada, June 6-9, 2000.

VITA AUCTORIS

NAME: Afsaneh Edrisy

PLACE OF BIRTH: Arak, Iran

YEAR OF BIRTH: 1972

EDUCATION: University of Windsor, Windsor, Ontario, Canada
Department of Mechanical, Automotive and Materials Engineering
Ph.D in Engineering Materials
1999-2004

Isfahan University of Technology, Isfahan, Iran
Department of Materials Engineering
B.A.Sc. in Engineering Materials
1991-1995